Modelling, Control and System Performance Analysis of A Partially Power Decoupled AC-DC Hybrid Shipboard Power System for More-Electric Ships

by

Kai Ni

B.Eng.

A thesis submitted in accordance with the requirements for the award of the degree of *Doctor of Philosophy* of the University of Liverpool

July 2019

Declaration

I hereby declare that except where specific reference is made to the work of others, the contents of this dissertation are original and have not been submitted in whole or in part for consideration for any other degree or qualification in this, or any other University. This dissertation is the result of my own work and includes nothing which is the outcome of work done in collaboration, except where specifically indicated in the text.

Kai Ni

2019

Acknowledgements

First of all, I would like to show my greatest gratitude to my supervisor Dr. Yihua Hu for offering me such a precious opportunity to pursue a high level of academic study in electrical engineering and electronics. You put the maximum patience not only in supervising me on my research but also on guiding the direction for my career. During my PhD study, you always try your best to help me, and come up with fantastic ideas for me to follow, as well as provide me with many valuable chances of attending academic events and applying for rewards. Most importantly, your keen ambition and enthusiasm in carrying out world-leading research and your rigorous working attitude always stimulate me to study hard. You deserve my deepest and sincerest respect, since I could not obtain such great research achievements in the short period of PhD study without your generous supervision and selfless contribution. In addition, I want to express my hearty appreciation to Dr. Lin Jiang and Dr. Kai Shi for providing guidance on my undergraduate final year project, which inspired my interest in being a researcher. Moreover, the comments and suggestions from Prof. Joseph Yan and Dr. Jiafeng Zhou in annual assessments are quite helpful and meaningful for me to improve my research skills.

I also would like to thank my parents and my grandma for your unconditional support and understanding. You always show the warmest care for me and pay the closest attention to my physical and mental health. What's more, you spend a lot of time in searching for any useful information on my study and keep me updated. You share your valuable life experience with me. When we have different opinions, you always patiently listen to my points of view and discuss with me in the most reasonable way. Your understanding is critical for me to carry out my research intently.

I am also grateful to my brilliant and lovely colleagues and friends, with special thanks to Sen Song, Tianhao Wu, Xinhua Li, Zhiyi Zhao, Lujia Xie, Sokol Kuka, Zuyu Wu, Mohammed Alkahtani, Yixuan Zhang, Haochen Shi, Dr. Chunmin Yang, Prof. Zheng Wang, Prof. Quan Xu, Prof. Zhongning Zhou, Prof. Rui Liang, and Dr. Xianming Ye for many fruitful discussions and enjoyable moments. I want to particularly thank my best friend Chao Wu, who sits next to me in the same office, as we encourage, support and motivate each other every day, and I hope we can both finally achieve our targets in academia. I also want to devote my special thanks to my good friend, colleague, as well as housemate Chao Gong for regular in-depth discussions on academic and philosophical problems. Besides, I want to express my special gratitude to Dr. Guipeng Chen, Dr. Yang Liu and Dr. Jiadong Lu for your valuable guidance and suggestions on academic problems for me, which are significant for accelerating my progress in academic research. In addition, I would like to thank the researchers at SmartRUE, ICCS-NTUA, with special thanks to Prof. Nikos D. Hatziargyriou for offering me this valuable opportunity, and to Dimitris T. Lagos for providing support and guidance for me on carrying out real-time simulations in RTDS with CHIL setup.

Last but not the least, the support from the Department of Electrical Engineering and Electronics at the University of Liverpool is gratefully acknowledged.

Table of Contents

List of Figures

Acronyms

AC	Alternating Current
ANPC	Active Neutral-Point-Clamped
AVM	Average-Value Modelling
BTBPC	Back-To-Back Power Converter
CHB	Cascaded H-Bridge
CHIL	Control-Hardware-In-The-Loop
CPL	Constant Power Load
CSA	Clonal Selection Algorithm
DC	Direct Current
DFIM	Doubly-Fed Induction Machine
DSTATCOM	Distribution Static Compensator
div	Division
ESS	Energy Storage System
ESVO	Emulated Stator Voltage Oriented
EXS	Excitation System
FC	Fuel Cell
FPD	Fully Power Decoupled
GVO	Grid Voltage Oriented
IEEE	Institute of Electrical and Electronics Engineers
IM	Induction Machine

IMU	Impedance Measurement Unit
IPS	Integrated Power System
LSC	Load-Side Converter
MAS	Multi-Agent System
MES	More-Electric Ship
MIT	Massachusetts Institute of Technology
MMC	Modular Multilevel Converter
MPC	Model Predictive Control
MVDC	Medium Voltage Direct Current
MVAC	Medium Voltage Alternating Current
NPC	Neutral-Point-Clamped
PC	Personal Computer
PCM	Power Conversion Module
PDEI	Parameter Deviation Effect Indicator
PDM	Power Distribution Module
PI	Proportional-Integral
PLL	Phase-Locked Loop
PGU	Power Generation Unit
PPD	Partially Power Decoupled
PSS	Power System Stabilizer
PSO	Particle Swarm Optimization
PWM	Pulse Width Modulation
pu	Per unit

RTDS	Real-Time Digital Simulator
SC	Super-Capacitor
SFO	Stator Flux Oriented
SG	Synchronous Generator
SiC	Silicon-Carbide
SIVV	Synthetic Internal Voltage Vector
SM	Submodule
SPPSO	Small-Population-Based Particle Swarm Optimization
SPS	Shipboard Power System
SSC	Source-Side Converter
SST	Solid-State Transformer
SoC	State of Charge
THD	Total Harmonic Distortion
TX	Transmitter
VC	Vector Control
WT	Wind Turbine

Nomenclature

C	Capacitance
com	Compensating term
E	Internal voltage magnitude
E_{rr}	Energy dissipation during the reverse recovery period
E_{sw}	Energy dissipation during the switching period
e	Internal voltage
F	Friction factor
f	Frequency
H	Inertia constant
I	Current magnitude
i	Current
i_{CE}	Collector-emitter current
i_F	Diode forward current
$K_{i,d}$	Exponent for current dependence of diode switching losses
$K_{v,d}$	Exponent for voltage dependence of diode switching losses
$K_{v,T}$	Exponent for voltage dependence of transistor switching losses
K_a	Regulator gain
K_d	Damping factor
K_f	Feedback gain
K_e	Exciter gain

k_s	Stator coupling factor
L	Inductance
L_{lr}	Rotor leakage inductance
L_{ls}	Stator leakage inductance
L_m	Mutual inductance
L_r	Rotor inductance: $L_r = L_m + L_{lr}$
L_s	Stator inductance: $L_s = L_m + L_{ls}$
L_{ss}	Source side inductance
n_p	Number of pole pairs
P	Active power
p	Differential calculator d/dt
P_{cl}	Copper losses
$P_{cond,T}$	Transistor conduction power loss
$P_{cond,D}$	Diode conduction power loss
P_{dc}	DC-bus power losses
P_T	Terminal active power
$P_{sw,T}$	Power loss during the switching period
$P_{sw,rr}$	Power loss during the reverse recovery period
PF	Power factor
Q	Reactive power
R	Resistance
r_{CE}	Collector-emitter on-state slope resistance
r_F	Diode forward on-state slope resistance

S	Switching function
s	Complex frequency in frequency domain
T_a	Regulator time constant
T_D	Damping torque
T_d	*d*-axis short-circuit time constant
T_{do}	*d*-axis open-circuit time constant
T_e	Exciter time constant
T_{em}	Electromagnetic torque
T_f	Feedback time constant
T_j	Junction temperature
T_{kd}	*d*-axis damping time constant
T_L	Load torque
T_m	Mechanical torque
T_q	*q*-axis short-circuit time constant
T_{qo}	*q*-axis open-circuit time constant
T_S	Synchronizing torque
T_s	Sampling period
T_{sw}	Switching period
$T_{sw,T}$	Temperature coefficient of transistor switching loss
$T_{rr,d}$	Temperature coefficient of diode switching loss
t	Time
U	Control signal magnitude
u	Control signal

V	Voltage magnitude
V_{CE0}	Collector-emitter threshold voltage
V_{F0}	Diode forward threshold voltage
V_T	Terminal voltage
v	Voltage
ψ	Flux
X	Reactance
X_k	Damping reactance
X_l	Leakage reactance
X_m	Mutual reactance
Z	Impedance
σ	Leakage flux factor: $\sigma = 1 - [L_m^2/(L_r L_s)]$
θ_E	Synthetic internal voltage phase
θ_e	Stator internal voltage phase
θ_m	Mechanical rotor angle
θ_p	Phase-locked loop (PLL) angle
θ_s	Synchronous angle
θ_ψ	Flux angle
ω_b	Base angular frequency
ω_e	Grid angular frequency
ω_m	Mechanical rotor angular speed
ω_r	Electrical rotor angular speed
ω_{slip}	Slip angular frequency

Δ	Small-signal value
δ	Rotor angle deviation

Subscripts

A	Point A
a	Phase A
B	Point B
b	Phase B
C	Point C
c	Phase C
d	Direct component referred to synchrnous reference frame
dc	DC-bus related variable
f	Field winding related variable
i	Rotor current related variable
k	Damper winding related variable
L	Load variable
l	Leakage winding related variable
ls	Load side converter related variable
nom	Nominal value
o	Open-circuit variables
p	PLL related variable
Q	Reactive power related variable
q	Quadrature component referred to synchrnous reference frame
r	Rotor related variable

req	Required value
SC	Supercapacitor related variable
SG	Sychronous generator related variable
s	Stator related variable
ss	Source-side converter related variable
stab	Stablizing value
T	Terminal variable
t	Total variable
ub	Difference between variables
v	Voltage related variable
0	Variable value at a specific operation point
α	Direct component referred to stationary reference frame
β	Quadrature component referred to stationary reference frame
ω	Rotor speed related variable

Superscripts

p	Variables represented in PLL reference frame
*	Reference value
’	Transient variable
’’	Sub-transient variable

Note: (1) If not specified in the text, the descriptions in Nomenclature are applied for the symbols throughout this thesis. (2) The specific definitions of some symbols in the figures in Chapter 2 should be found from the corresponding references. (3) The descriptions of the variables in Section 3.4 are defined in a different way, and the readers should refer to the texts in Section 3.4 for detailed information. (4) Vectors and matrices are expressed in **bold**.

List of Publications

During my PhD study, I have published 3 journal articles and 1 conference paper on the topic of more-electric ships, which are included as a part of the contents in this thesis.

Journal Articles *(*correspondence)*

1. **Kai Ni**, Yihua Hu*, Zheng Wang, Huiqing Wen, and Chun Gan, "Asynchronized Synchronous Motor-Based More Electric Ship – Less Power Electronics for More System Reliability," *IEEE/ASME Transactions on Mechatronics*, DOI: 10.1109/TMECH.2019.2929074
2. **Kai Ni**, Yihua Hu*, Rui Liang, Huiqing Wen, and Mohammed Alkahtani, "Internal Voltage Phase-Amplitude Dynamic Analysis with Interface Friendly Back-To-Back Power Converter Average Model for Less Power Electronics Based More-Electric Ship," *IEEE Access*, vol. 7, pp. 93339-93351, Jul. 2019.
3. **Kai Ni**, Yihua Hu*, Xinhua Li, "An Overview of Design, Control, Power Management, System Stability and Reliability in Electric Ships," *Power Electronics and Drives*, vol.2, no.2, pp.5-29, 2017.

Conference Paper *(*correspondence)*

1. **Kai Ni**, Lujia Xie*, Yihua Hu, "Cost Effective Electric Ship Energy Regulation System Based on Asynchronized Synchronous Motor", 2018 IEEE International Conference on Electrical Systems for Aircraft, Railway, Ship Propulsion and Road Vehicles & International Transportation Electrification Conference (ESARS-ITEC), Nottingham, United Kingdom, Nov. 2018.

Awards

- The award winner of 2019 Hong Kong Graduate Association Yu Scholarship
- "The best oral speech" in "The 8th CSSA-UK Academic Forum and the 1st Manchester China-UK Forum of International Young Scholars" on 5th July 2019
- The award winner of 2018 Hong Kong Graduate Association Postgraduate Scholarship

- The runner up in IET "Presentation Around The World (PATW)" in the Merseyside and Western Cheshire Network Heat on 27th March 2017
- The recipient of The Merit Poster Presentation at Decarbonisation of Transport through Electrification Summit organised by IEEE UK and Ireland Power Electronics Chapter on 20th March 2019
- Being selected to present a Poster at the STEM for Britain Exhibition in the Engineering Section held at the House of Commons on Wednesday 13th March 2019

Reviewer

IEEE Transactions on Industrial Electronics, IEEE Transactions on Power Electronics, IEEE Transactions on Power Systems, IEEE Transactions on Power Delivery, IEEE Transactions on Systems, Man and Cybernetics: Systems, IET Power Electronics, IET Renewable Power Generation, International Journal of Electrical Power and Energy Systems, Measurement and Control, Journal of Power Electronics, Energies, Sustainability, Inventions, Applied Sciences, Power Electronics and Drives

Abstract

Thanks to the fast development of power electronics technology, the world ship industry greets the rise of more-electric ships (MES) in recent years. The wide use of power electronic interfaces enhances the modularity of shipboard power system (SPS) and enables flexible on-board power regulation, leading the trend of fully power decoupled SPS (FPD-SPS). The FPD-SPS is based on direct current (DC) power distribution, which has high requirements of fault protection. Besides, owing to the fragility and high switching speeds of solid-state power switches, the power electronic converters prone to break down, which threatens the SPS safety. Moreover, precise fault isolation should be implemented to avoid affecting the normal operation of the other on-board sections, which is a difficult task. Furthermore, the extensive use of expensive DC circuit breakers increases the cost of fault protection.

In this thesis, a partially power decoupled SPS (PPD-SPS) architecture with doubly-fed induction machine (DFIM) as the propulsion motor is proposed to mitigate the dominant status of power electronics in MES. The proposed PPD-SPS is based on the alternating current (AC)-DC (AC-DC) hybrid power regulation structure, reducing the difficulty and cost in fault protection. The MES based on PPD-SPS has the ability to easily ride through power electronic device faults to realize continuous sailing, thus ensuring the safety of passengers and crew. A review of the state-of-the-art technologies in design, control, power management, system stability and reliability for MES is presented to familiarize the readers with the development and challenges in this field. Then, targeting at the proposed intrinsically safe PPD-SPS, the research activities in modelling, control, and system performance analysis are carried out. The basic models of power generation unit (PGU), DFIM, back-to-back power converter (BTBPC), and energy storage system (ESS), along with their control strategies, are illustrated in detail. The average model of BTBPC is presented for system-level analysis, which shortens the simulation time without sacrificing the main features of system operation. With the proposed emulated stator voltage oriented vector control (ESVO-VC) strategy, normal system operation can be achieved with frequent load variations taken into consideration, where almost identical system performance can be obtained when comparing with the case of applying the traditional stator flux oriented (SFO) VC strategy for DFIM. Besides, two small-signal modelling methods of PPD-SPS propulsion subsystem by focusing on separate DFIM and BTBPC models, and by regarding the propulsion subsystem as a synthetic internal voltage vector (SIVV) respectively in the electromechanical control timescale are proposed. The internal voltage vector phase-amplitude dynamics are studied with respect to the corresponding controller gain setup. Furthermore, the PPD-SPS performance is analysed by taking the parameter deviation of 16 PGU system and control parameters into account. Three parameter deviation effect indicators (PDEIs) are defined to identify the most critical parameters. The proposed strategies are implemented and verified by simulations in Matlab/Simulink, and the control methods are further verified in control-hardware-in-the-loop (CHIL) setup by building up the power circuits of synchronous generator (SG) with BTBPC in the real-time digital simulator (RTDS) software, which imitates almost exactly an actual operation environment.

Chapter 1 Introduction

1.1 Motivation

Electric ship propulsion has a history of over one century, but it was rarely applied before the emergence of modern power electronics technology. Recently, the increasing shipboard electric power demand and environment protection requirements have accelerated the development of more-electric ships (MES) [1-3]. The breakthrough in the electrification of marine vessels was achieved by applying power electronic converters in the 1990s [4, 5], which gave a sharp rise in the trend towards the fully power decoupled shipboard power system (FPD-SPS) [6-9]. Direct current (DC) power distribution is commonly used in FPD-SPS, where the following advantages are presented: 1) high power efficiency; 2) random speeds for prime movers; 3) fast power generation response time; 4) easy energy storage system (ESS) integration; 5) reduced overall space, cost and weight. By using FPD-SPS for MES, flexible regulation of electrical power among power sources, ESSs, propulsion and service loads can be easily obtained.

One typical representative of FPD-SPS is medium voltage direct current (MVDC) SPS architecture [10-13]. By employing a large number of power electronic converters, the purposes of on-board space and weight reduction and flexible equipment arrangement are realized, and the system efficiency, survivability and maintainability are improved. However, the challenges of fault detection, location and isolation are encountered for MVDC-SPS [14-16]. For example, the faulty section has to be completely isolated to ensure normal operation of the other power components, and the simple “unit-based” protection scheme is no longer feasible [13]. Besides, compared with alternating current (AC) power distribution, extremely

fast fault detection and isolation are required for FPD-SPS based on DC power distribution, which are difficult and costly to achieve. Since there is a lack of regular zero-crossings in a DC FPD-SPS, the arcing faults are not likely to extinguish early, and enormous fault currents may be caused if the fault isolation is not executed fast enough [17]. By employing solid-state circuit breakers, ultrafast protection speed can be achieved, while high cost and power losses are inevitable. In [18], an optimized solid-state circuit breaker-based DC protection system design has been implemented to obtain a compromise of the protection speed and cost. Nevertheless, the coordination of circuit breakers for a selective protection method is challenging. Besides, a communication-assisted fault detection method has been proposed in [19] to precisely detect the faulty part of the DC network, while the requirement and complexity of control algorithm are high. In order to alleviate the dependence of communication between elements, a fault detection method has been put forward in [20] that coordinates the actions of power converters with that of bus contractors, and they only rely on independent local measurements. However, there are a large number of different scenarios to be considered, and it is difficult to verify that tripping is conducted quickly enough in each case.

According to the above discussion, there are still several challenges in developing circuit breaker-based protection methods for DC power systems. Additionally, since the performance of MVDC-SPS mainly depends on the operation of power electronic converters, a nonlinear dynamic is induced because of switching behaviours. If the switching frequencies for the power switches are not high enough, the produced current harmonics can seriously affect the power quality. However, if the switching frequencies are too high, the lifetime of power switches can be short, which further shortens the lifetime of MES. The health condition of power electronic converters are difficult to assess, and more power electronic converters result in more complicated electromagnetic compatibility and electromagnetic interference problems. Furthermore, many system reliability issues are actually caused by the high failure rate of

power electronic converters [21, 22]. In MVDC-SPS, full power decoupling is obtained by applying power converters, and the power distribution is realized by using DC buses. In this case, the overall system reliability is made worse due to the fragility of solid-state devices [21], and additional power losses are encountered.

A large number of researchers have focused on improving the system safety level by proposing different control strategies for power electronic converters to improve the stability and reliability of MVDC-SPS [23-26]. Although these methods are applicable for certain cases, they do not deal with the intrinsic safety issues caused by applying DC power distribution and extensive use of power electronics. Therefore, from the intrinsic safety point of view, we propose a partially power decoupled SPS (PPD-SPS) based on doubly-fed induction machine (DFIM) propulsion load to mitigate the dominant status of power electronics to obtain a higher system safety level, and reduce the volume of DC power distribution to decrease the difficulty and cost of fault protection. A back-to-back power converter (BTBPC) is connected between the rotor and power generation unit (PGU), with the stator directly connected to PGU [27]. The system structures of MVDC-SPS and the proposed PPD-SPS are displayed in Fig. 1.1. It can be seen that compared with MVDC-SPS, power regulation is not only dependent on power converters for PPD-SPS, but is also achieved by direct AC power delivery between the DFIM stator and PGU. In this case, the volume of on-board power electronics can be reduced, and the power delivery path is not isolated even if the BTBPC breaks down, and the on-board power regulation can still be achieved by generator control. Continuous operation of MES can be obtained after the faulty BTBPC is isolated, making sure the passengers and crew are sent to safe places. Besides, the trade-off between AC and DC power system architectures can be flexibly adjusted to achieve the optimal overall performance in terms of reliability and controllability. Moreover, the requirement of fault protection becomes lower, and decreased

fault protection cost by replacing some of the DC circuit breakers by cheap and mature AC ones is presented.

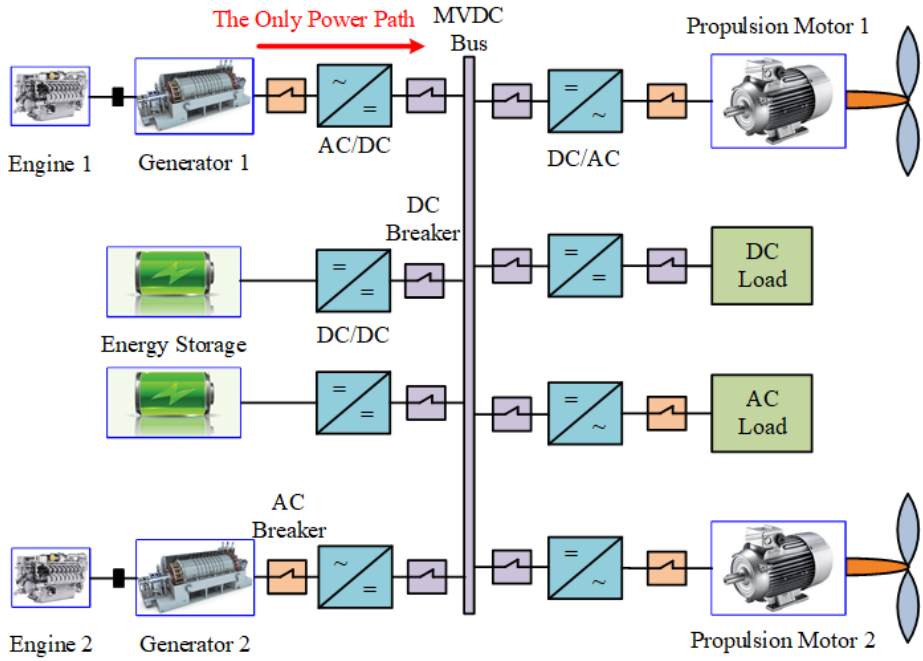

(a)

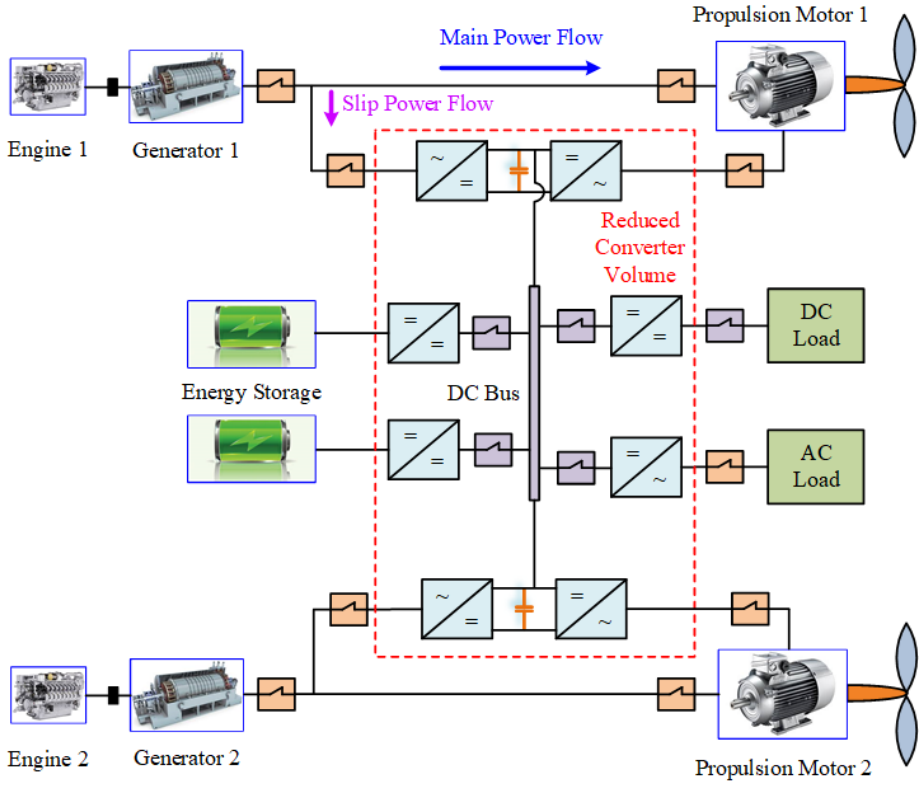

(b)

Fig. 1.1. The system structures of (a) MVDC-SPS (b) PPD-SPS.

In the proposed PPD-SPS, the power is supplied by an SG, and the system synchronous angle tracking performance of the phase-locked loop (PLL) can deteriorate if the PLL controller gain setup is not appropriate [28]. Therefore, in this thesis, an emulated stator voltage oriented vector control (ESVO-VC) strategy that does not employ a PLL is proposed for PPD-SPS to achieve robust control performance. Besides, the transfer function of the input voltage to the field voltage in the SG excitation system (EXS) is obtained, and its stability is analysed referring to the changes in the regulator and exciter gains.

For the conventional wind power application of DFIM, i.e. DFIM-based wind turbine (DFIM-WT), a number of studies have been carried out to investigate the system stability issue from the motion equation point of view. Following the concept of "virtual synchronous generator" [29-31] that exhibits some of the desired properties of SG for short-term frequency support, the virtual synchronous control has been first investigated for DFIM-WT in [32, 33]. By defining the synthetic internal voltage of DFIM-WT, it has been found in [34] that the PLL and active power control loop simultaneously dominate the phase motion. In [28], a modified synchronized control strategy has been proposed to improve both the synchronous and small-signal stability of DFIM-WT. However, the control method has to be modified, which is detrimental for obtaining a general understanding of control effects. In order to better understand the operation mechanism, extensive studies on modelling of DFIM-WT for specific purposes have been conducted in [35-39], while the effects of external grid have not been taken into account. Besides, the characteristics of DFIM-WT have been explored in [40] under transient control, with its impact on the first-swing stability of SGs analysed. Furthermore, the impact of DFIM-WT inertia control on the electromechanical oscillation damping of SG in a grid-connected power system has been investigated in [41]. The interaction was found to be mainly between the internal voltage phase angle of DFIM-WT and the rotor swing of SG. Nevertheless, the investigated systems are all connected to the power grid. In the case of

standalone power systems like SPS, the system dynamics can be quite different, as indicated in [42].

With the purpose of carrying out system-level studies, average-value modelling (AVM) methods for power converters have been presented [43-45] to release the computational burden and thus reduce the simulation time. More importantly, dynamic average models can be applied as powerful computation tools for large- and small-signal analysis for power systems [46]. However, the validity of such models depends on the frequency range used. In order to properly investigate the system stability, linearization is one of the commonly applied methods. Generally, there are three categories of AVM methods for linearizing power converter models, including traditional averaging methods [47, 48], generalized-averaging or dynamic phasor methods [49, 50], harmonic domain-based and harmonic state-space modelling methods [51-53]. A comprehensive review and comparison of these linearized modelling methods for AC-DC power converters can be found in [54]. However, these methods are emulated in a mathematical way, which are not straightforward for physical understanding. The use of AVM methods in SPS has also been widely investigated. The modelling and simulation of low-voltage DC MES by comparing and discussing different AVM methods have been carried out in [55]. In [56], a novel AVM approach for MVDC-SPS in the form of differential algebraic equation has been put forward to derive a more precise approximation of the system dynamic behaviours when comparing with the conventional AVM method. However, as the propulsion module was assumed as a constant power load, the effects of propulsion motor dynamics were neglected. Moreover, the dynamic assessment of source-load interactions in MVDC-SPS has been accomplished in [57] by investigating the effects of applying three different source-side converters. Although the effect of source-side converter control strategy was well researched, the impacts caused by the load-side inverter control were not discussed.

In this thesis, the average model of BTBPC is applied for system-level study of the proposed PPD-SPS. In addition, a small-signal model is established in the electromechanical control timescale to analyse the internal voltage phase-amplitude dynamics, with the effects of rotor speed control, reactive power control and PLL taken into account. Moreover, the DFIM stator and power converter are regarded as a synthetic internal voltage vector (SIVV) to better describe the external characteristics of the propulsion subsystem of PPD-SPS by the internal voltage motion equation [58]. Based on this concept, the transfer function of the torque difference to SIVV phase and that from the reactive power difference to SIVV amplitude are derived in the small-signal model. Furthermore, the proposed ESVO-VC is applied to avoid tuning the PLL controller gains, and it greatly simplifies the expression of the equivalent inertia of DFIM in the electromechanical control timescale.

In a PPD-SPS, the on-board power supply is mainly provided by SGs. Due to multiple reasons such as aging and high temperature, the variations in SG parameters like the reactance, short-circuit and open-circuit time constants may occur, which can seriously affect the system operation. In addition, the parameter deviations of its EXS also influence the overall system performance. The fundamental concepts of synchronous machine stability have been investigated in detail by taking the effects of excitation control into account in [59], which provided guidance for the research in synchronous machine-based power systems. In addition, the parameter determination method for synchronous machine by studying its modelling process without simplifying assumptions has been proposed in [60]. In addition, some techniques used for exploring synchronous machine-based power system transients have been put forward by making necessary simplifications [61-63]. In order to provide satisfactory voltage control performance for an SG when there are uncertainties in the system operation conditions [64] and exciter parameters [65], the design approaches for EXS have been proposed. Moreover, an online measurement strategy based on a multistage genetic algorithm

for simultaneously identifying the SG and EXS parameters online has been illustrated in [66]. Furthermore, with the purpose of overcoming the difficulty in the conventional parameter identification method when the saturation effect is presented, a new method using $d-q$ axes tests by considering saturation effect has been presented to improve both the accuracy and precision of SG parameter estimation [67]. However, most of the aforementioned studies only consider the single-machine infinite bus system, and none of the existing research investigated the effects of parameter deviations in SG and EXS on the performance of a PPD-SPS with DFIM functioning as the propulsion load. In this thesis, by taking the detailed models of SG and its EXS into consideration, the deviation of the corresponding parameters is implemented for the proposed PPD-SPS in the high-speed operation mode. The effects of parameter deviations for 16 SG and EXS parameters on the SG terminal voltage and active power output are studied in detail by analysing three parameter deviation effect indicators (PDEIs), with different degrees of parameter deviations applied. Moreover, the overall system performance is investigated for the two most influential parameters. Furthermore, the performance of PPD-SPS is evaluated by building up the power circuits in real-time digital simulator (RTDS) and implementing the control strategies in control-hardware-in-the-loop (CHIL) setup.

The target of this thesis is to propose a PPD-SPS as an intrinsically safe alternative to the existing SPS architectures to increase the MES safety level by using less power electronics. The overall scheme of the conducted research work in this thesis is illustrated in Fig. 1.2.

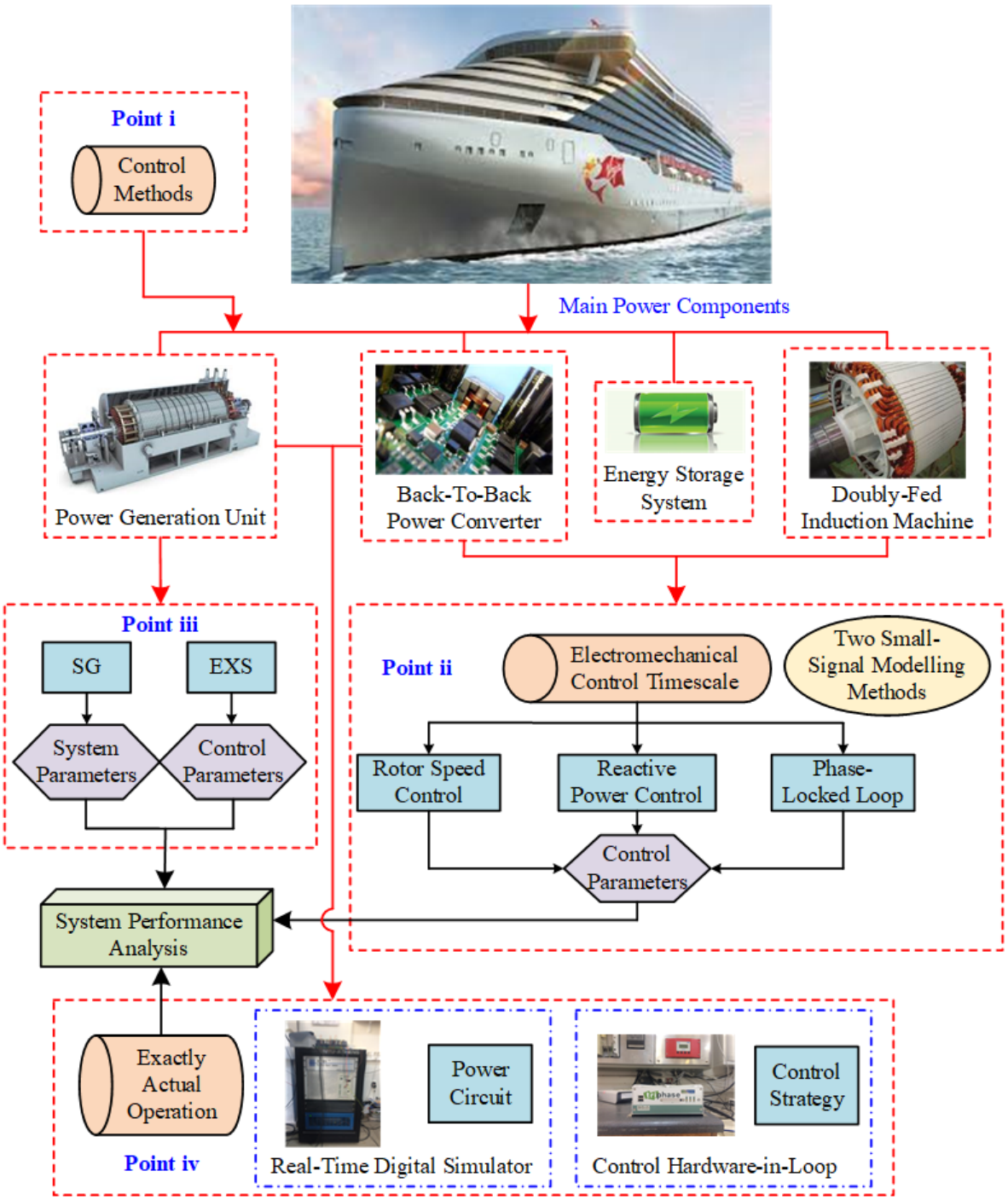

Fig. 1.2. Overall research scheme of the thesis.

The work is carried out from the following points of view:

i. To provide **control methods for the main on-board power components, including PGU, DFIM, BTBPC and EES,** to accomplish good system performance when frequent load variations are presented. An ESVO-VC strategy is proposed for DFIM to

eliminate the potential threats to system stability caused by the inappropriate PLL controller gain setup. The system variables can swiftly and precisely track the reference values, and SC banks can be efficiently used in balancing the input and output power.

ii. To establish **the small-signal models of PPD-SPS propulsion subsystem in the electromechanical control timescale** that are based on separate DFIM and BTBPC models, and an SIVV, respectively. The two models can respectively reveal the internal and external behaviours of the DFIM-based ship propulsion subsystem in PPD-SPS, and the internal voltage phase-amplitude dynamics are studied with respect to the controller parameter setup for rotor speed control, reactive power control and PLL.

iii. To develop **a performance analysis scheme by evaluating the PDEIs for 16 parameters in PGU,** which can guide the other researchers in choosing system and control parameters for the PGU in such an SPS. The most critical parameters that influence the system performance are determined according to the simulation study.

iv. To evaluate **the system performance in almost exactly an actual operation environment that is emulated by RTDS with the CHIL setup**. The focus is on the control of BTBPC and SG, with different parts of the system simulated step by step in the RTDS software, and the control strategies implemented in the CHIL. The circuit of SG with BTBPC is finally tested to verify its good control performance in both the lock mode and free mode.

1.2 Dissertation Outline

This work focuses on the modelling, control and performance analysis of a partially power decoupled AC-DC hybrid SPS for MES. The dissertation consists of seven chapters and the structure is organized as follows:

Chapter 1 describes the challenges of applying FPD-SPS for MES, which motivate us to carry out the proposed research. The proposed PPD-SPS is introduced, with the detailed tasks and main contributions of this work presented.

Chapter 2 reviews the history of MES and the state-of-the-art technologies in the field of MES. The previous research efforts are categorized according to the aspects of design, control, power management, system stability and reliability.

Chapter 3 presents the basic models for the main power components in the proposed PPD-SPS. The PGU consists of an SG and EXS, and it is the main power source. The DFIM acts as the propulsion load, whose model is established in the *dq* synchronous reference frame. Besides, the BTBPC plays an important role in controlling the on-board power flow, and its detailed and average models are respectively introduced. Moreover, the models of three types of commonly applied energy storage devices are given.

Chapter 4 illustrates the control strategies for the main power components of PPD-SPS. The control of PGU is based on the field voltage control by EXS, and its stability is assessed. An ESVO-VC strategy is proposed to omit the use of a PLL, which eliminates the risk of inappropriate PLL controller gain setup. In addition, the control strategy for SC bank is depicted to realize source-load power balance. Simulations in Matlab/Simulink are conducted to verify the good performance of PPD-SPS by applying the proposed control strategies when presenting frequent load variations.

Chapter 5 focuses on the small-signal modelling methods of PPD-SPS propulsion subsystem by employing the concept of internal voltage vector in power system study. The small-signal models are established in the electromechanical control timescale to investigate the interaction between electrical and mechanical behaviours of PPD-SPS. The phase-amplitude dynamics of PPD-SPS propulsion subsystem are investigated by establishing the small-signal models in two

different ways: 1) treating the DFIM and BTBPC as two separate parts; 2) regarding the DFIM and BTBPC as an SIVV. The internal and external behaviours of PPD-SPS propulsion subsystem in the electromechanical control timescale can be analysed by using these two different models respectively. The effects of control parameter setup in the interested control timescale are examined by simulations in Matlab/Simulink.

Chapter 6 proposes three PDEIs to assess the system performance when different degrees of parameter deviations are presented in the PGU of PPD-SPS. Simulations are carried out in Matlab/Simulink to investigate the effects of parameter deviations for 16 PGU system and control parameters on the terminal power and voltage values, and the most critical parameters are sorted out for further analysis on the overall system performance. Moreover, simulation studies in RTDS with CHIL setup are carried out to validate the system performance in almost exactly an actual operation environment to provide the basis of applying the proposed PPD-SPS in practice. Simulations are presented at different circuit complexity levels to evaluate the performance of each part in detail.

Chapter 7 gives a summary of the research achievements in this thesis, and the main contributions and future work are presented as well.

Chapter 2 Review of More-Electric Ships

In recent years, electric propulsion is being developed for various types of vessels and the concept of the "More-Electric Ship" (MES) becomes well-known for the large shipyards all over the world. Thanks to the rapid development of semiconductor switching devices, which are widely used to fabricate power electronic converters, the high power drives in MES can be effectively controlled, leading to flexible on-board power regulation. Owing to the requirement of saving fuel consumption, electric propulsion in commercial ship applications is being widely used, which substitutes the original mechanical counterpart. In future MES, multiple energy sources, independent operation of individual power producers, and energy storage for different types of applications will be available.

The history of the MES dates back to over a century ago [68], where a limited number of such applications have been presented. Massive production of MES was not realized until the 1990s, since at that time the maturity of semiconductor technology was high enough for the variable speed control of electrical motors. The electric propulsion system utilizes a number of small units for power generation instead of a big prime mover, so the generator engines are always loaded close to their optimal operating points [1]. By applying the MES architecture, the placement of on-board equipment becomes much more flexible than the conventional mechanical ones, which eliminates the negative impacts caused by using long shaft-lines to the propellers. In [69], the past, present, and future challenges of the marine vessel's electric power system have been discussed. There are a number of variants for electric propulsion solutions, which are dependent on the type of vessel, operational profiles, and the current available technologies for construction. The history of the MES is shown in Fig. 2.1.

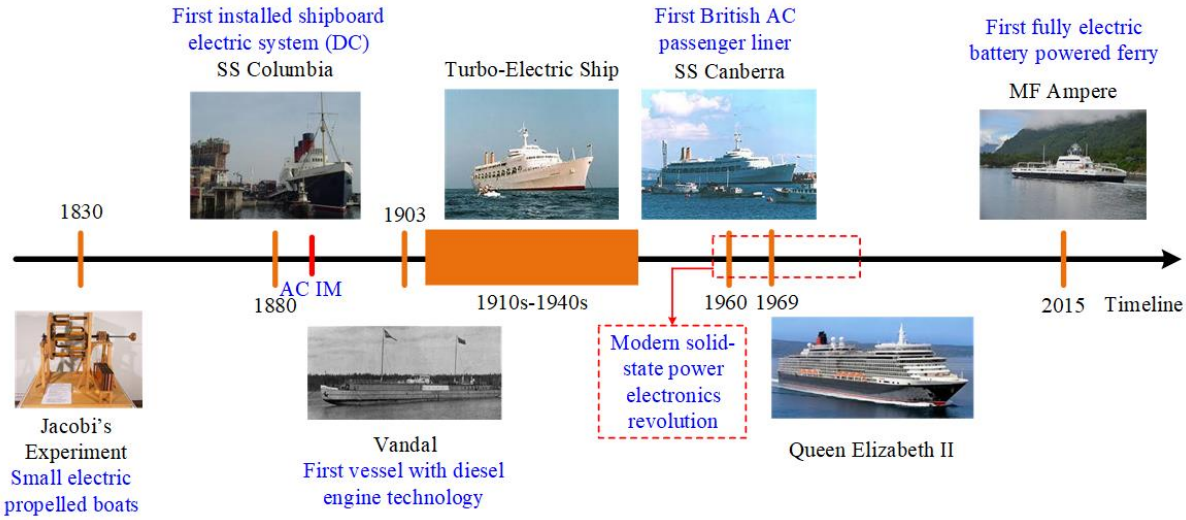

Fig. 2.1. The history of the MES.

It can be seen from Fig. 2.1 that the history of the MES can be dated back to Jacobi's experiment on an electrical machine in 1830s, which was firstly applied to propel small electric boats. After about 50 years, the first formally installed SPS emerged in *SS Columbia*, which was based on DC power regulation. Then, the alternating current (AC) induction machine (IM) was invented and put onto market, popularizing the AC powered MES. *Vandal* was the first vessel equipped with the diesel engine technology, and different types of turbo-electric ships emerged during 1910s and 1940s. Then, within the period of modern solid-state power electronics revolution, the first AC British passenger liner called *SS Canberra* was developed, followed by the birth of one of the largest cruise ships in the UK, *Queen Elizabeth II*. In recent years, the first fully electric power propelled ship named *MF Ampere* appeared.

Three different application areas of electric propulsion systems for ships were introduced in [1], which are 1) ocean going, where the criteria of propulsion design is a certain vessel speed with flexibility in operating at different speeds; 2) station keeping, whose main target is operating the shipboard power system (SPS) safely by keeping position; 3) icebreaking, where a propulsion design trade-off has to be considered among a high bollard pull demand, propeller over-torque, and open water efficiency [1]. It was also indicated that the future trends and

technologies for MES involve direct current (DC) power grid, energy storage, hybrid propulsion and dynamic position closed bus. Furthermore, future electrical energy sources can be accommodated for MES, since the relevant necessary on-board infrastructures are available. According to [8], the following advantages have been proven by applying electric propulsion: 1) electrical motors are likely to be more flexibly accommodated without using extremely long shaft lines, and the rudder may be omitted by possible installation of outer rotating pods; 2) the fuel consumption is reduced; 3) higher comfort level is derived since vibrations are mitigated; 4) a higher level of automation is presented for the engine rooms. Furthermore, the concept of MES has been raised as the use of electric power equipment is able to replace the traditional power sources in mechanical or hydraulic form [2].

The MES concept has become a standard in the field of large cruise ships, which has been accepted by the major shipyards all over the world [2]. Electric propulsion is now applied in various types of ships, including ferries, gas carriers, vessels, icebreakers, and offshore oil and gas platforms [2].

This chapter gives a comprehensive overview on the design, control, power management, system stability and reliability of MES in the following sections. The most recent technologies and research achievements in these fields are presented and discussed.

2.1 Design

In [70], an overview has been carried out for the design stages of US navy ships, where the design procedures can be classified as concept design, engineering design, and production design. In the concept design procedure, the expressed need is to be met by considering the defined gap in operational capability, and the future evaluation of ship design alternatives are produced with the consideration of the mission requirements, concept of operation, and

operational environment. In addition, the possible ship concepts are derived in the analysis of alternatives phase to meet the high-level mission requirements and capabilities. Preliminary design and contract design are included in the engineering design process, where the basic architectures are built up, and more details are added to the preliminary design in the contract design process. Afterwards, the engineering data are applied in the process of verifying if all the specifications are met for the ship in the product design process, which aims to complete the detailed design and construction. The design stages are depicted in Fig. 2.2.

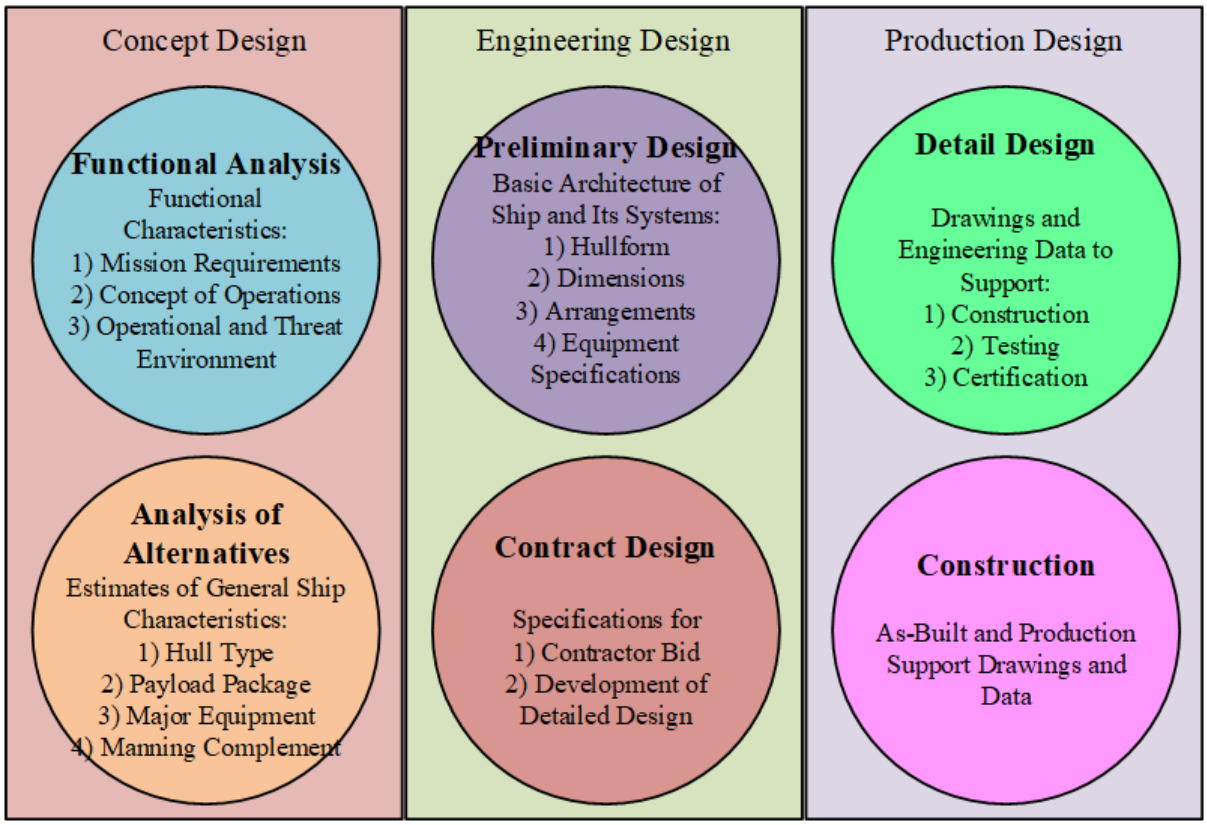

Fig. 2.2. The design stages for US Navy MES [70].

As presented in [70], the inside-out ship design concept has been raised in [71]. If the design is made following the process of designing the external structure first, then an extremely dense ship design may be caused due to the external constraints, which results in difficult production and maintenance, and it increases the life-cycle cost of the ship class [71]. Following this concept, several projects have been taken at MIT Sea Grant, including the projects regarding a

functional arrangement by selecting modular blocks for payload and machinery [72], creating additional permutations based on prearranged machinery spaces [73], and hydro dynamically optimized hulls produced within the user-specified constraints [74]. In addition, an objective function was maximized to improve the packing density, and the components and compartments were located in the places as close to the ideal ones as possible in [75], which has been completed by a packing approach. Furthermore, the evolutionary process of configurations for merchant ships, cruise ships and military ships is displayed in Table 2.1 over the past few decades, at present and in the possible future [76].

Table 2.1. Ship Configurations [76]

	Merchant Ships	Cruise Ships	Military Ships
Half of the last century	Stream Plants – Mechanical Propulsion		
Present	2 Strokes Diesel Engine Mechanical Propulsion	Electric Generators Electric Propulsion	Gas Turbines Mechanical Propulsion
Possible Future	Electric Generators and New Generation Power Distribution – Electric Propulsion		

MES have been developed for a long time, and with the emergence of power electronic converters and the rapid progress made in this field, the SPSs utilized in MES is transferring from ordinary electrical propulsion based ones to integrated electrical and electronic ones. The importance of design methods of integrated electrical and electronic power systems for MES has been demonstrated in [8] through an overview of the latest results derived in technological research. A large number of design methodologies have been proposed in [70, 77-82], where the simplest and the most relevant one is called the design spiral [70]. By utilizing this method, the most general details are derived first, and then more detailed design levels are developed, in which case the current iteration can be revised by using the information obtained from the previous design cycles.

2.2 Control

In advanced MES, the control of SPS highly relies on the control of power electronic devices, which are capable of coordinating the power flows between AC and DC subsystems. In addition, with the evolution of integrated power system (IPS) in MES, the requirement of saving on-board space and flexible power delivery becomes stricter, which can be met by developing more advanced power electronics technologies and control strategies.

2.2.1 Power Electronics Techniques

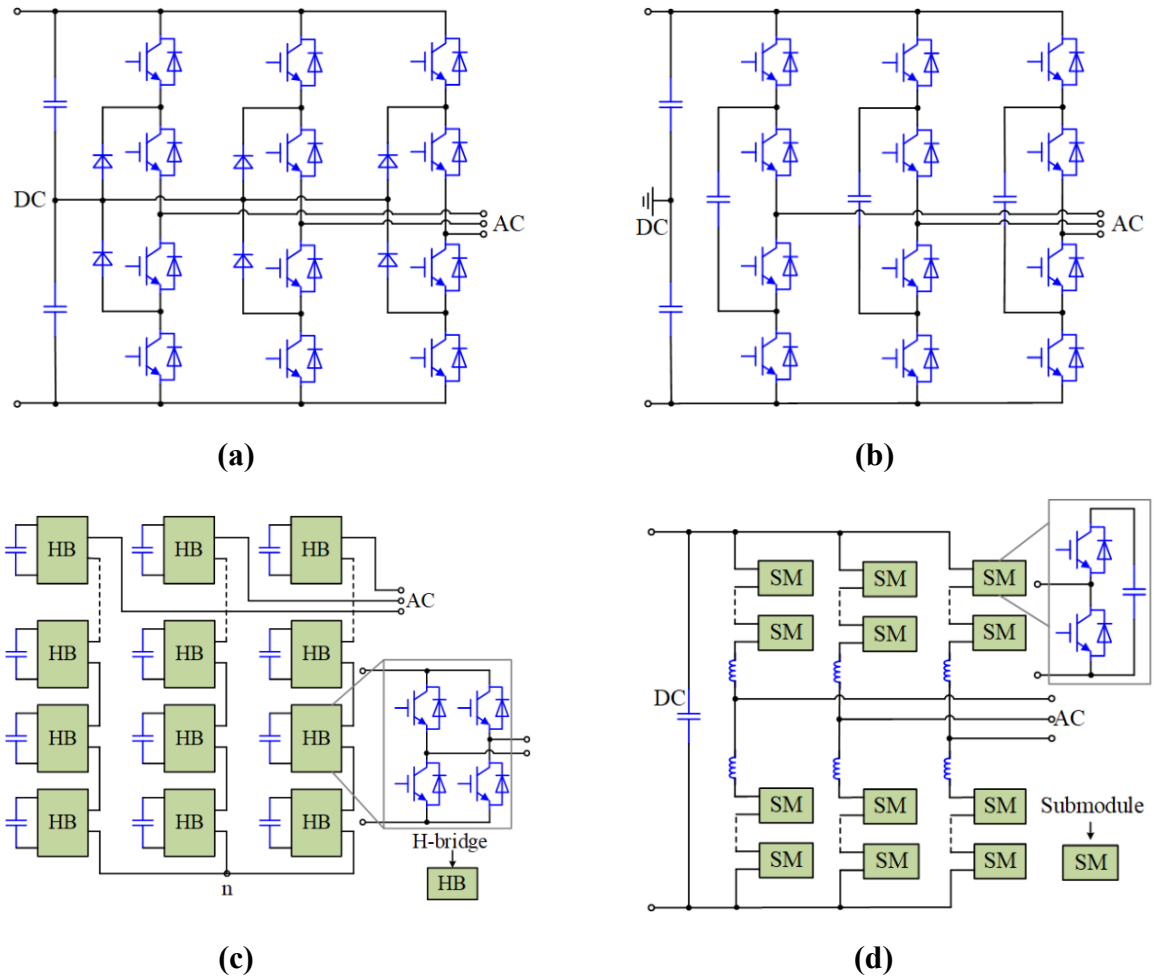

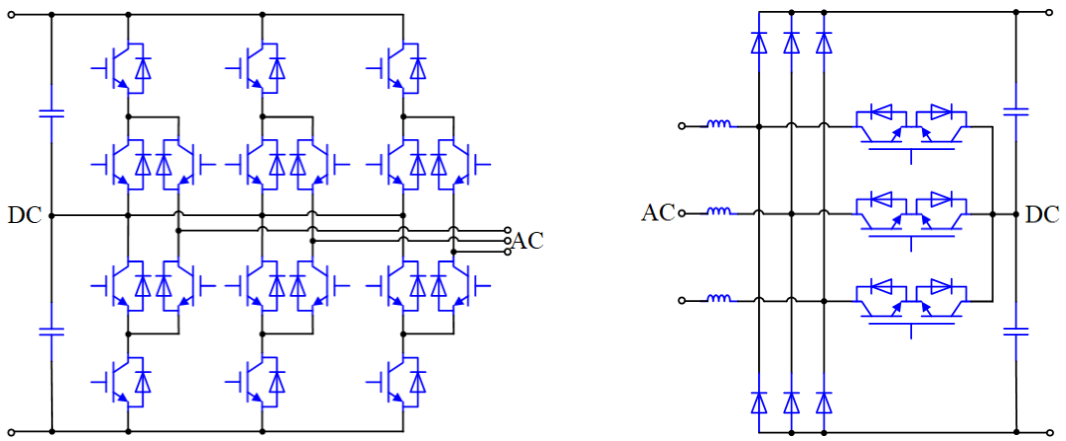

(e) **(f)**

Fig. 2.3. Multilevel converters: (a) Three-level neutral-point-clamped (NPC) inverter; (b) three-level flying capacitor converter; (c) cascaded H-bridge (CHB) converter; (d) modular multilevel converter (MMC); (e) three-level active NPC (ANPC); and (f) Vienna-type rectifier [83].

As the demand of electricity in MES is constantly increasing, a higher power rating is desired. Apart from that, increasing the power density and system reliability is also of paramount importance. Therefore, instead of basic voltage source converters, a number of advanced topologies are investigated for applications in power conversion modules in MES. In general, the possible advanced voltage source converter topologies to be used in shipboard IPSs include multilevel converters [84-86], interleaved converters [87], multiphase converters [88, 89], soft-switched converters [90], and power electronics building blocks [91, 92]. In [83], the authors summarized the typical topologies for multilevel converters, which are already widely used in a variety of power systems. The main categories of multilevel converter structures are shown in Fig. 2.3, with the comparison among them displayed in Table 2.2.

Table 2.2. Summary on Multilevel Converter Comparison [83]

	NPC	Flying Capacitor	CHB	MMC	Vienna-type	ANPC
Device Utilization	1.25	1	1	1 to 2	1	1.5
Modularity	No	No	Yes	Yes	No	No
Capacitor Volume	Low	Medium	High	High	Low	Low
Inductor Volume	Low	Low	Low	High	Low	Low

* Assume two-level voltage source converter is 1.

Owing to the superiority of modular multilevel converter (MMC) over other multilevel converter topologies in terms of high modularity, high scalability, high efficiency, excellent harmonic performance, and elimination of DC-link capacitors, it has been widely investigated [93, 94]. An approach to developing a scalable meta-model for compatible MMCs has been presented in [95], and the size/weight/efficiency was produced to achieve the required voltage and power ratings. In [96], a hybrid energy storage system (ESS) based on isolated modular multilevel DC-DC converter has been proposed with active filter function for shipboard medium-voltage direct current (MVDC) system applications to improve the bus power quality and achieve superior fault response. In [97], the modelling and control of an isolated DC-DC MMC with a medium-frequency AC-link transformer has been investigated for MVDC-SPS. The proposed DC-DC MMC system in [97] is displayed in Fig. 2.4.

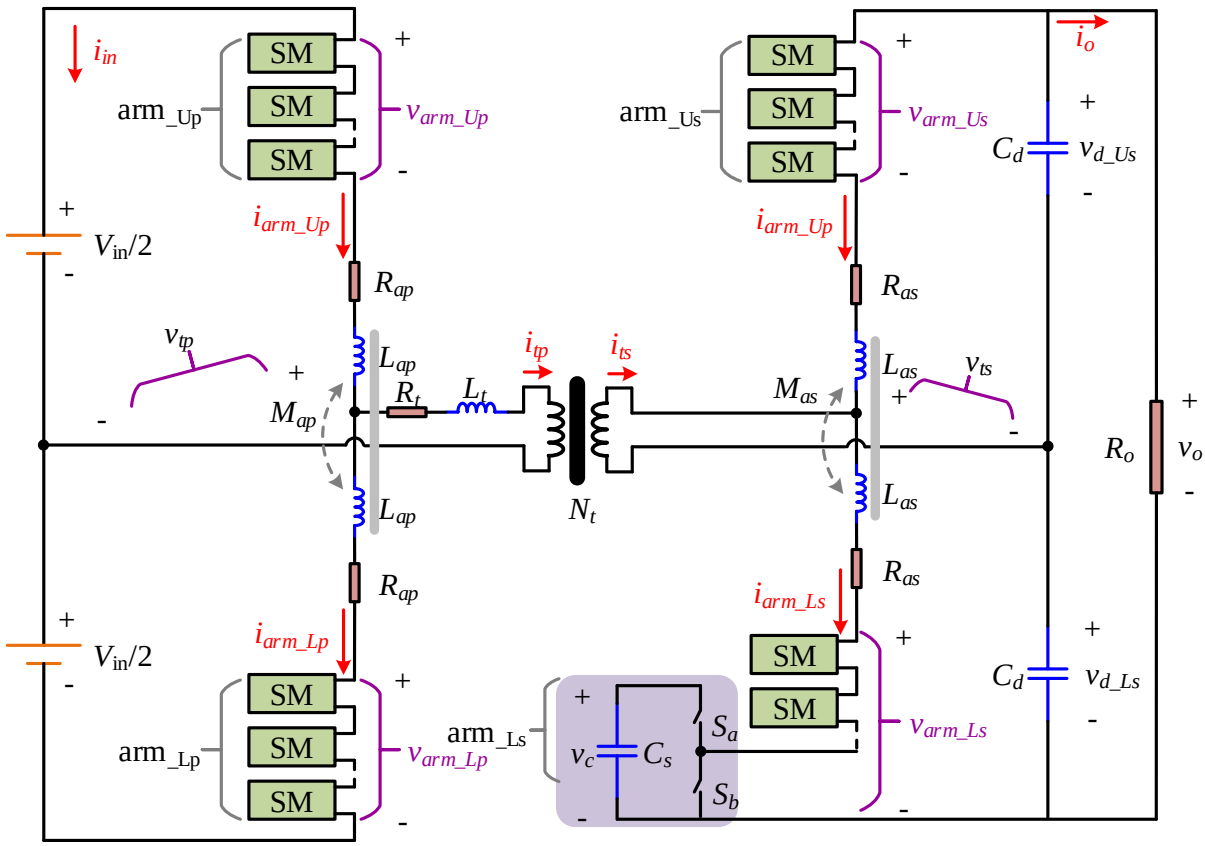

Fig. 2.4. Proposed DC-DC MMC system for MES MVDC application [97].

In an isolated DC-DC MMC, the bridge arms are formed by using several submodules. Therefore, different voltage levels are derived in this topology. In addition, the fundamental frequency modulation technique in [98] has been employed for minimizing the switching losses of each submodule (SM) by reducing the switching times, which allows further alleviation of the leakage current. Moreover, the useful model information for control purposes has been maintained, which enables both the steady-state and transient system performance analysis.

The theoretical limits of the commonly used silicon power semiconductor devices restrict the use of power electronic converters in harsh operation environments [83]. Under such a circumstance, the wide-bandgap semiconductor devices [99], including silicon-carbide [100] and gallium-nitride [101] based ones, are emerging to replace the traditional silicon-based ones.

2.2.2 Control Schemes

The control strategies for various applications in MES have been investigated, and some of them will be reviewed in this section to illustrate the development in this field.

For MES applications, the power quality may be seriously deteriorated by pulse loads, which require a large amount of energy during an extremely short period of time [102]. Therefore, the approaches to improving the power quality in an SPS are required after the occurrence of pulse loads. The high power quality is to be achieved with the premise of good voltage regulation. In [103], a distribution static compensator (DSTATCOM) based on an artificial immune system has been applied in order to compensate the insufficient reactive power and regulate the voltage at the point of common coupling in an SPS with respect to pulse loads. Besides, an adaptive control strategy has been proposed, in which the particle swarm optimization (PSO) algorithm was first applied for deriving the optimal parameters of the

controller. In this case, online adaptive system identification and control are possible to be achieved, which do not rely on any prior knowledge. By using the proposed PSO algorithm based control strategy for DSTATCOM in artificial immune system based MES, good voltage regulation at the point of common coupling can be guaranteed since proper tuning of DSTATCOM has been accomplished. Meanwhile, when the system returns to the normal stage after experiencing the impacts from the pulse loads, the original optimal controller parameters can still be reserved. In order to mitigate the influence on the voltages at neighbouring buses in a diesel-electric ship by applying an active power filter, a model predictive control strategy has been proposed in [104] to minimize the harmonic distortions of the whole system with a given active power filter rating.

Apart from obtaining a good voltage regulation capability, other control strategies have also been proposed to deal with the issues caused by pulse power loads. Focusing on isolating the negative impacts produced by the pulse power loads in an SPS, cooperative controls of the generation control and ESS charging control have been presented in [105]. The PI-based and feedback linearization based control algorithms have been respectively performed and analysed in that paper. In [106], by taking multiple impact factors into consideration, the detailed modelling and analysis of the active foldback control have been illustrated. The thyristor rectifier system in a DC powered electric ship is able to deal with the surge current without a DC inductor, if a proper active foldback control is available.

In order to further improve the power quality of an SPS, the optimal design and control of the excitation system are required. An online design and laboratory hardware implementation of an optimal excitation controller based on an artificial immune system algorithm has been proposed for improving the performance of future MES used for navy applications in [107]. The demand for the capacity of energy storage devices can be reduced by applying an improved excitation control to minimize the effects of pulsed loads, which is based on a clonal selection

algorithm (CSA). In [107], the possibility of energy storage reduction has been explored by considering the situation that high-power pulsed loads are directly powered from the DC side. Additionally, the PSO based algorithm implemented in [108] has been compared with the proposed CSA method, focusing on the performance and computational complexity for real-time tuning. The general comparison of these two algorithms for excitation controller design is illustrated in Table 2.3.

Table 2.3. General Comparison of CSA and PSO Algorithms for Excitation Controller Design [107]

	PSO	CSA
Computational functional complexity	Small, mainly "add, subtract, multiply" operation 3.3M clock cycles per particle in one iteration with 150MHz frequency	Large, contains "sorting, round, exponential, and division operation" 9.6M clock cycles per antibody in one iteration with 150MHz frequency
Computational memory requirements	Small, mainly "particles position and velocity"	Medium, "antibody, affinity, new group of antibody and affinity"
Hardware requirements	Low. Many microcontrollers such as PIC, DSP are available to be implemented on; Shallow memory requirements	High. High processing speed is needed; Memory requirements high.
Convergence	Good	Better
Algorithm code execution time	Small	Large – nearly 3 times larger than PSO

In addition, an artificial immune system-based control of generator excitation systems for the US Navy's MES has been proposed in [109], which aims at solving the high-energy load related problems that deteriorate the power quality. The computational intelligence methods are widely used at present, including fuzzy set theory [110], PSO theory [111], online trained neuro-controllers [112], and genetic algorithms [90]. However, the optimal performance cannot be ensured when it is out of the range of operation conditions considered in the design. Moreover, adaptive excitation controllers should be used in the cases when the performance

degrades, while it is challenging to design multiple excitation controllers to obtain the optimal performance when the operating conditions vary. The proposed artificial immune system-based control of excitation controllers for MES applications in [109] have been employed to minimize the voltage deviation and power losses when the pulse loads are directly energized by SPS. Optimal performance is achieved when known disturbances are injected, and better performance can be obtained by adapting the parameters for unknown disturbances, which demonstrated its innate and adaptive immunities.

The smart grid and DC micro-grid technologies have been introduced into shipboard electrical networks in [113], indicating the developing trend of the next-generation DC SPS. In such a complicated system, with the purpose of obtaining different control functions, the hierarchical control scheme has been proposed, which can be divided into the following control levels [113]: (1) primary control, aiming at locally controlling the output voltage and current of the power electronic interfaces; (2) secondary control, which handles the restoration of voltage or frequency, manages the power quality and deals with power exchange with the external grids in the same layer; (3) tertiary control, which is responsible for managing the power exchange between the micro-grid and its upper-layer grid. A typical scheme of hierarchy control is displayed in Fig. 2.5.

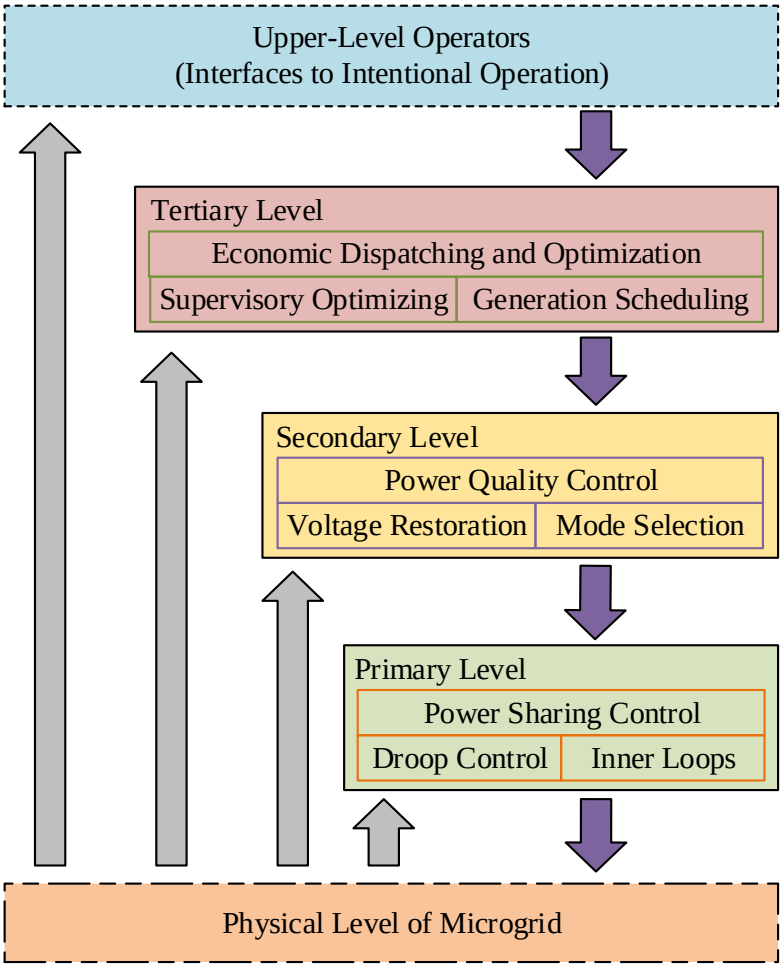

Fig. 2.5. Different levels in hierarchical control [113].

2.3 Power Management

The AC power grid has been commonly used in current MES applications. The typical representative of AC power distribution systems in MES is the medium-voltage AC (MVAC) architecture, which was applied in [114], and the power conversion has been completed by using solid-state transformers [115, 116]. However, the challenge of applying such MVAC power systems induces several problems. For example, the volume of solid-state transformer is large, and synchronous generators are required, and it is necessary to implement reactive compensation. As a promising alternative, the MVDC [4, 7, 117-119] power distribution architecture can be used, which adopts power converters for power regulation, instead of

applying solid-state transformers. Additionally, since there is no frequency limitation for the generators, it is possible to eliminate the gearboxes between the prime mover and synchronous generator (SG), which reduces the overall cost and increases the system reliability. Moreover, the system losses are reduced due to the fact that no reactive power transmission and skin effect need to be considered [97]. To clearly illustrate the difference between these two categories of SPS, their structures are shown in Fig. 2.6(a) and (b), respectively.

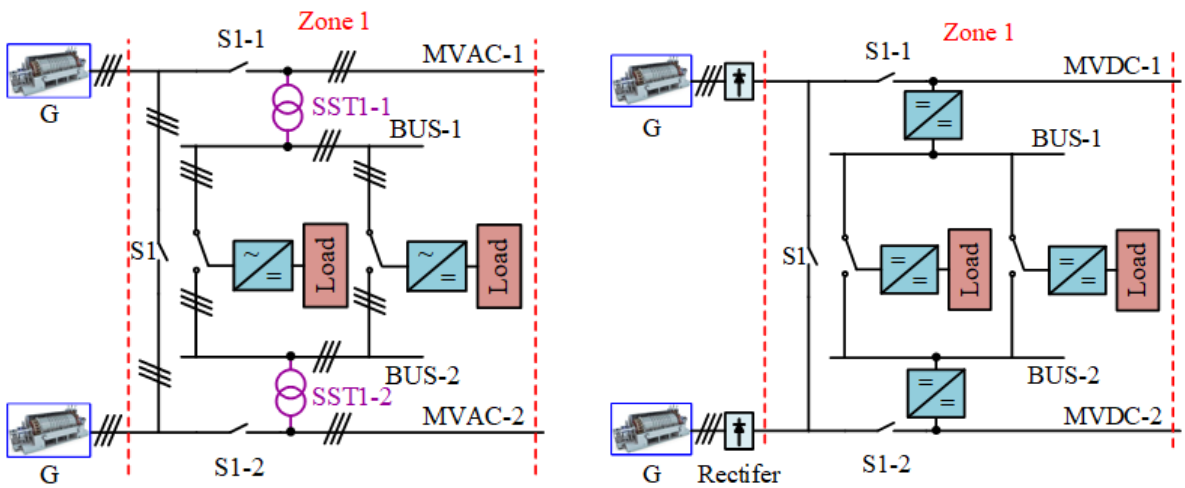

(a) (b)

Fig. 2.6. Power systems for MES (a) MVAC power system with SSTs (b) MVDC power system with DC-DC converters [97].

The MVDC-SPS architecture has been extensively investigated owing to the above mentioned advantages, and the reason why DC distribution contributes to the most efficient ship has been explained in [120] with a comprehensive review of the challenges, state of the art and future prospects. For a determined MVDC system, the settings of DC voltage reference and the optimal power reference have to be defined in advance for the voltage source converters operating in the voltage regulator mode and power dispatcher mode, respectively [121]. The system architecture of MVDC-SPS is shown in Fig. 2.7.

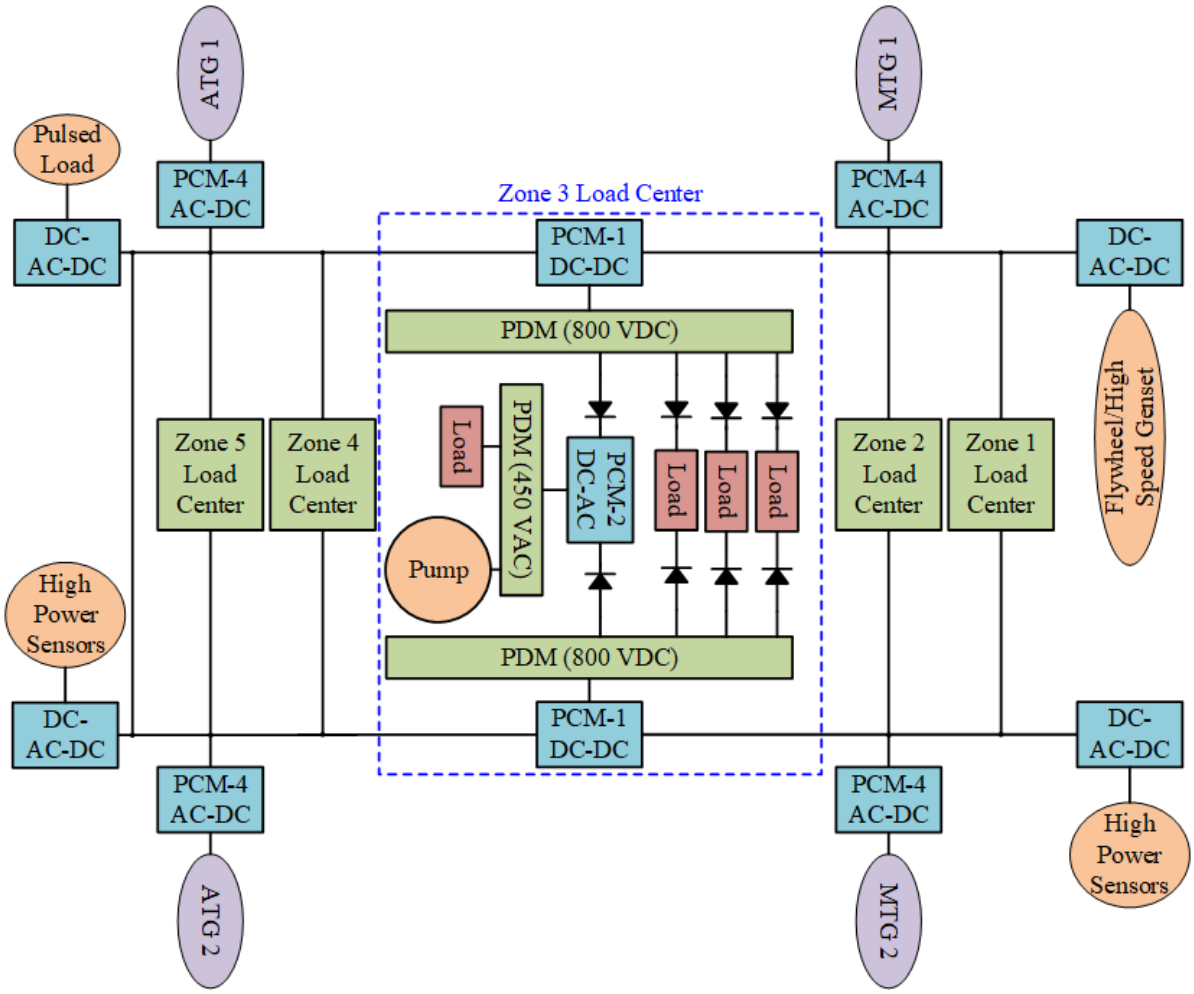

Fig. 2.7. MVDC architecture of SPS [122].

There are four generators in this MVDC architecture, including two main generators (MTG1 & 2) and two auxiliary ones (ATG1 & 2). The power delivery in this SPS is generally realized by a MVDC ring bus, which is fed by the SGs through transformers and AC-DC converters, and it operates at 5kV. In this SPS, the DC power is distributed among five zones including the loads, voltage source converters, power conversion modules (PCMs), and power distribution modules (PDMs). The 5000V DC voltage is stepped down to an 800V one by PCM-1, while PCM-2 is used to perform DC-AC conversion to supply AC zonal loads such as the propulsion motor. In addition, PCM-4 is usually connected to a generator, playing the roles of AC-DC converters. Moreover, energy storage devices, a pulsed load device, a pump, and high power sensors are involved in this system [123]. Furthermore, a methodology for power flow studies

in ship MVDC distribution systems for system planning has been proposed in [124] to determine the proper shipboard generator-power converter scheme.

An IPS is usually favoured in MES, which eliminates the use of separated internal combustion engines [2]. In this case, electric power can be distributed to wherever it is needed, and the size of the ship can be optimized, along with the on-board combustion. The typical IPS layout of MES is displayed in Fig. 2.8.

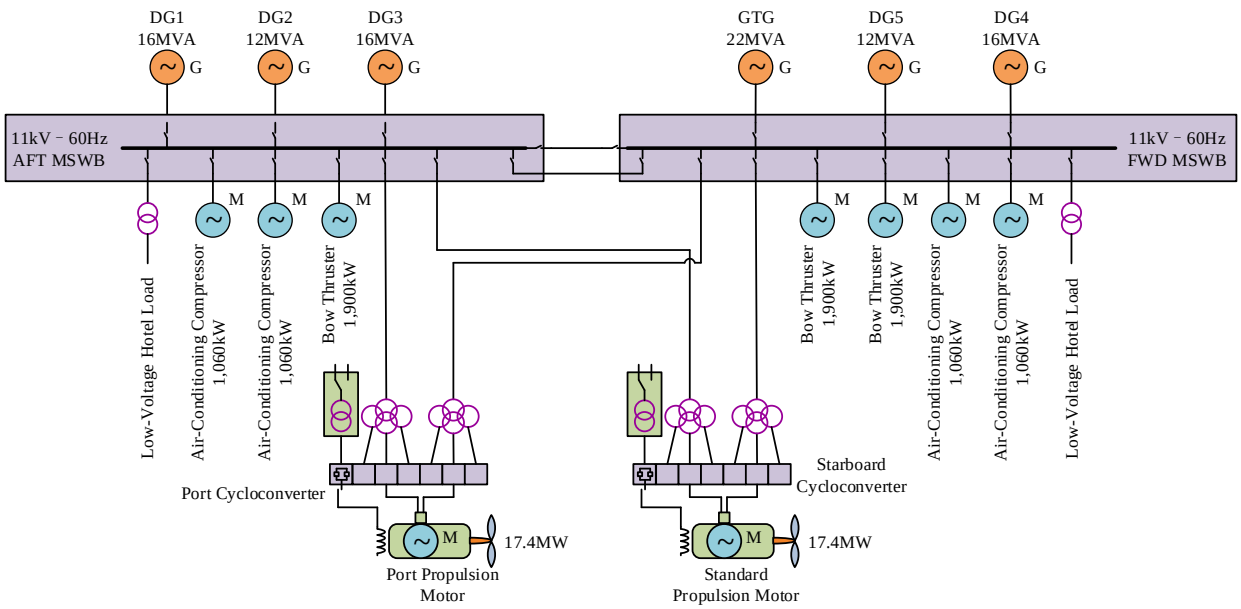

Fig. 2.8. The typical IPS layout of MES [2].

The electric power in MES is usually supplied from more than one separate power station, and at least two generator sets are used in each of them in order to allow enough redundancy for the SPS to achieve high fault tolerance. A prime mover, an SG, and the corresponding subsystems needed are contained in each set of power generation unit. From Fig. 2.8, it can be seen that a conjunction breaker is applied to make it possible for the power stations to operate separately when feeding the separate bus bars. The ship's loads can be fed by several means, where the bus bars and transformers are commonly employed for this purpose [2].

Since an IPS is a commonly used system configuration for MES to meet the increasing shipboard power demand and the requirement of sustainable development, power management of IPSs in MES with time scale separation for real-time large scale optimization has been investigated in [6]. Gas turbine/generator and fuel cell were considered as the power sources and the optimal power split between them was to be achieved with respect to energy efficiency, power tracking, and component safety. The optimization methodology was based on the sensitivity function method [125], where the main idea is to make the control solutions at each level available in real time by leveraging the multi time scale property of the IPS and solving a two-level simplified optimization problem. By applying the sensitivity function method, the computational effort can be reduced, and simplification of the IPS model can be achieved to some extent.

The multi-agent system (MAS) technologies are promising candidates to address challenging issues in power systems. In [126], a novel MAS-based real-time load management technique has been proposed to determine the switch status of loads in DC zones and satisfy the operating constraints of the system in real time simultaneously. A reduced-order agent model and an artificial potential function of the MAS were utilized as the basis for the developing the cooperative control protocol. The developed MAS framework was illustrated by using a two-zone notional shipboard power system. By using the proposed real-time load management technique based on MAS framework, the amount of load shedding is dynamically minimized when the available power source capacity constraint is violated. In addition, the disconnected loads can be dynamically restored if more power is available in the system, in which case the restoration time for loads is greatly decreased. Furthermore, the nominal system frequency can always be obtained. The diagram of a general multi-agent distributed control system for real-time load management in shipboard power systems is shown in Fig. 2.9.

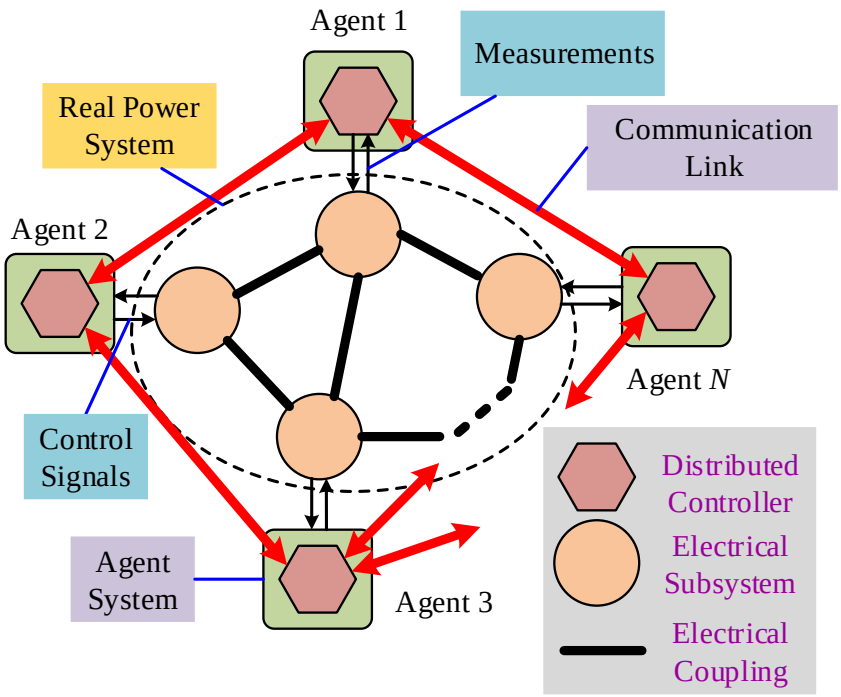

Fig. 2.9. Diagram of a general multi-agent distributed control system for real-time load management in shipboard power systems [126].

On the other hand, an MAS-based system cooperative controller for real-time electric load management in MVAC shipboard power systems has been proposed in [127] to balance the power consumption and generation. Meanwhile, the system's operational constraints were satisfied with the load priorities taken into consideration. The decentralized MAS cooperative control method has been first applied for solving the secondary control problem in SPS in [127]. In the proposed method, there is no need to change the existing system design when integrating new components into the MAS. Additionally, the mission-critical loads such as high energy weapon loads in Navy applications, are always served during emergency conditions. On top of that, the pulse and propulsion loads have been successfully coordinated so that the impact of pulse load on the system power quality is reduced. Moreover, the system can still be controlled by the decentralized control framework as that in normal cases when the communication system failure is encountered [127].

Aiming at reducing the fuel consumption and greenhouse gas emissions for MES, the optimal operation of a ship electric power system with full electric propulsion and energy storage system has been analysed to minimize the cost, limit greenhouse gas emissions, and obey the corresponding technical and operational constraints at the same time in [128]. In the proposed power management strategy, the optimization goals have been obtained by the means of energy storage and propulsion power adjustment. Three stages are needed in the proposed method owing to the complexity of the examined problem. Different from the method proposed in [128], no ESS and investment capital is required for SPS operation optimization in the optimal demand-side power management method for the MES raised in [129]. In this approach, the dynamic programming is employed as a solution, and the ship load forecasting is assumed to be available. In addition, the proposed method has been applied to a cruise ferry with integrated full electric propulsion, with the simulations under realistic operation situations presented. In [130], the dynamic positioning system has been applied as dynamic energy storage on diesel-electric ships, and new simple formulas have been derived to relate the dynamic energy storage capacity to the maximum allowed ship position deviation. The operational availability and safety are maintained by applying the integrated approach, and the power consumption is also minimized.

A novel integrated security-constrained model-based power management approach has been proposed in [131], which was used in isolated micro-grids in MES during the normal/alert operating state. The novelty of the study is that the objectives for various control methods are combined together by formulating the integrated security-constrained power management method as a multi-objective optimization problem. In addition, the dynamic security of the system is guaranteed in the proposed integrated security-constrained power management formulation when planned and unpredicted scenarios are encountered. The proposed method

has been applied in a notional isolated micro-grid power system model for MES, whose structure is displayed in Fig. 2.10.

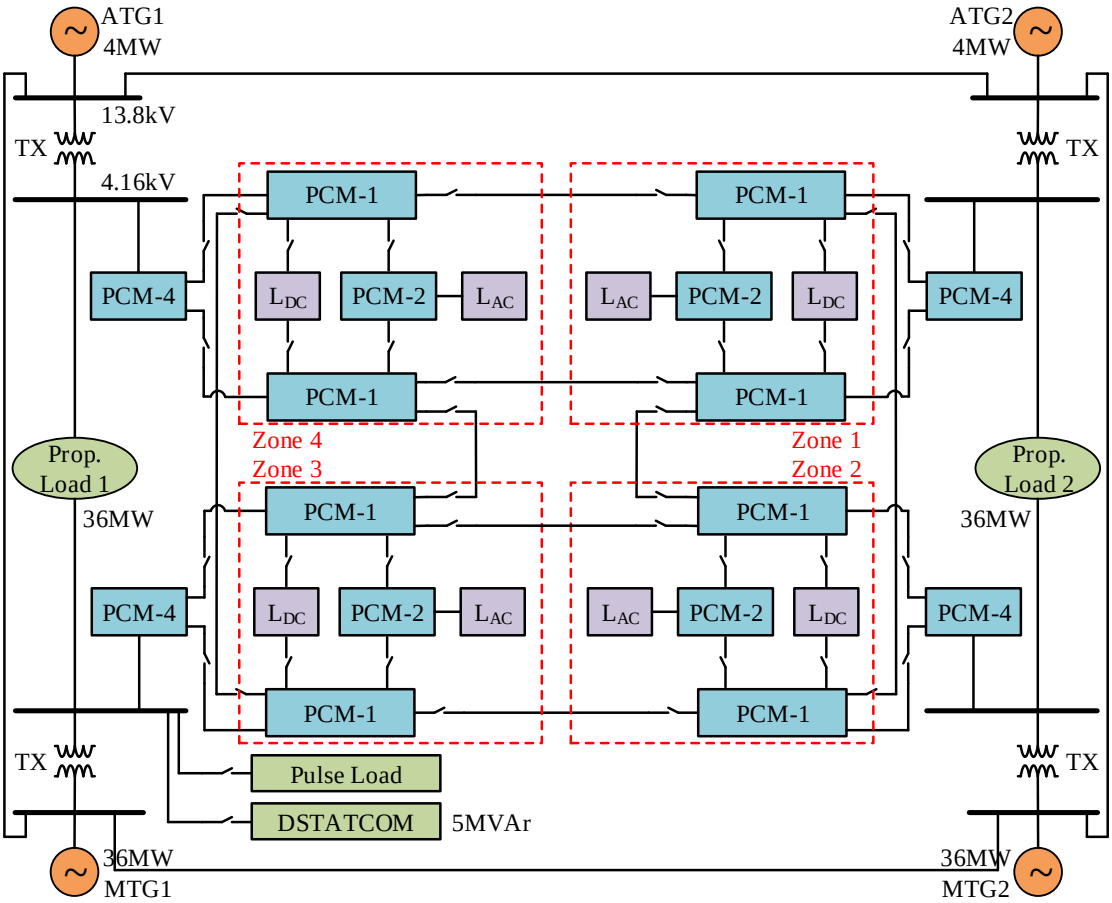

Fig. 2.10. Single line diagram of the notional MES model [131].

The ESS [132] in MES plays an important role for coordinating the power flow in IPS, and a methodology for power generation controls of fuel cells (FCs)/energy storage hybrid SPS has been presented in [133]. In order to support the MVDC-SPS, a fuzzy logic based energy storage management system has been proposed in [134] and compared with a PI based one. Instantaneous reference powers for charging and discharging of these energy storage devices have been provided, with two power sharing strategies designed in this study. Compared with the PI controller based energy storage management system, no extra deep discharging and overcharging protection controller is required for the proposed fuzzy logic based one, which mitigates the damage to the MVDC-SPS of MES. Besides, an energy management system

using PSO has been proposed in [135] aiming at reducing fuel consumption in optimization of the vessel's machinery systems during its voyage. Additionally, a novel FC power management scheme without employing DC-DC interfacing converters has been proposed in [136], which maintains the high performance of FC, and thus the optimal power sharing between the FC and the lithium-ion battery in MES application is achieved. Furthermore, an IPS based on FC, battery, photovoltaic panels, and two diesel generators has been proposed and modelled for MES in [137]. The appropriate control strategies of the nonlinear models for different modules in the hybrid power system of MES and the corresponding power management approaches are focused on. With the application of the proposed decentralized model predictive control method in different parts of the SPS, the reference values are precisely followed, and the DC-link voltage variation is maintained within an acceptable range by employing the hierarchical-droop control strategy.

2.4 System Stability and Reliability

In order to widely adopt DC SPS for MES, new fault protection strategies are required, consisting of fault detection, protection device coordination, system reconfiguration, and fault isolation [138]. Since a DC zonal electric distribution system is a promising candidate for surface combatant, the rationale for the DC zonal system has been described in [139], along with the description of the stability issues, discussion on fault detection and load shedding problems. When MVDC power systems are applied for MES, the constant power load (CPL) behaviour occurs when large control bandwidths are employed for load converters, and a destabilizing effect can be produced, which should be taken into consideration when analysing the system stability [4]. In [140], a control method based on linearization via state feedback has been proposed to solve the problem of CPL instability for multi-converter MVDC-SPS. A new comprehensive model has been applied for analysing the multi-converter shipboard DC

grid, and the overall behaviour was captured in a second-order nonlinear differential equation. In the proposed method, the system nonlinearities are compensated by the linearization via state feedback technique and then the traditional linear control techniques can be used for deriving a desired pole placement [140]. The original system model has been simplified for the sake of providing a complete voltage control design procedure for DC radial grids. In addition, the shipboard plant requirements are to be met by considering the implementation aspects in the proposed control design. Moreover, the first medium-voltage impedance measurement unit (IMU) has been designed and implemented in [87] to characterize in-situ source and load impedances of AC and DC networks in a specific frequency range, with the aim of assessing the system stability of MES. A single-phase wide-bandwidth injection algorithm has been employed for identifying small-signal *dq* impedances of MVAC and MVDC systems of MES. Besides, the minimized hardware size, weight and complexity have been obtained with the single-phase injection of perturbation current or voltage by using a modular SiC converter. The proposed IMU is applicable at several different low and medium voltage levels since the modularity and scalability are presented in the proposed injection converter solution. The simplified structure of the illustration displaying IMU insertion into the MES MVDC distribution system is shown in Fig. 2.11.

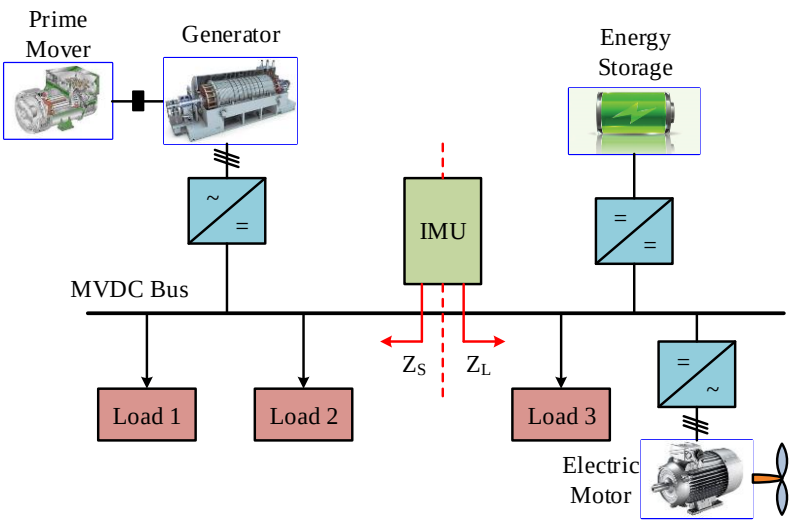

Fig. 2.11. Illustration showing IMU insertion into the MES MVDC distribution system (simplified) [87].

In terms of the ways of dealing with faults and failure of the components in MES, it is possible to use intelligent reconfiguration of system function and connectivity, which is based on the system-level knowledge of component failure when the intelligent power distribution is in the faulty modes [141]. The intelligent diagnostic requirements of future MES IPS have been illustrated in [141], along with the introduction of emerging technologies that are available to be integrated into the future ship IPSs. Particularly for recent navy ships, both survivability and affordability are required, where the crew intensive functions should be reallocated for intelligent automation. In [141], the opinion that diagnostic knowledge management should begin at the earliest stages of ship design and continue throughout the vessel's life has been raised. In addition, the accuracy of embedded diagnostics is of importance for implementing advanced reconfigurable control algorithms. Some major types of IPS components that are taken into consideration in the diagnostic management strategies are illustrated in Fig. 2.12.

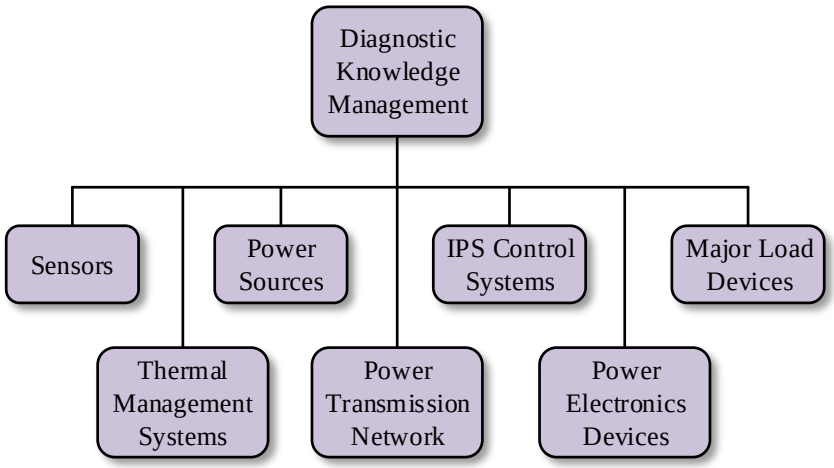

Fig. 2.12. Diagnostic knowledge management of IPS components [141].

From Fig. 2.12, the following points can be summarized [141]: 1) A huge potential exists in the process of diagnostic development; 2) most of the diagnostic technologies are not

demonstrated in real-world service; 3) the evolution of diagnostics in the whole lifecycle of the ship is inevitable; 4) further improvement in system reliability and affordability have to be achieved with upgrade mechanisms based on new diagnostic technologies. Furthermore, the embedded diagnostic knowledge should be up-to-date and accurate.

In [142], a fast intelligent reconfiguration algorithm based on small-population-based particle swarm optimization (SPPSO) has been proposed to maintain the proper power balance in the SPS when severe damages or faults are encountered during battle conditions for navy MES. The problem is first formulated as a single objective optimization one to obtain a fast execution speed for the algorithm, where the unique solution is derived directly with SPPSO. While in the cases that two conflicting objectives arise, the problem is formulated as a multi-objective one, where a set of Pareto optimal solutions are extracted by SPPSO from two conflicting objectives. Then by passing the solutions through a number of questions that represent user preferences with respect to mission-specific requirements, the final solution can be obtained based on the response to those questions [142].

The optimal reconfiguration of SPS has been analysed in [143], and a new balanced AC-DC hybrid SPS has been considered for optimizing the status of switches to maximize the power delivered to loads after the occurrence of a fault. In addition, the discussion on the trade-off between power delivered and number of switching operations at steady state has been presented after reconfiguration. The traditional reconfiguration methods for terrestrial systems are usually regarded as optimization problems by considering different types of objectives. However, these existing approaches typically require running a complete power flow algorithm after each switching step, which slows down the process, and under certain situations they are not feasible. Therefore, by considering optimization of the objective function and satisfying the power flow constrains, better solutions can be proposed [143]. The methods proposed are with low complexity with the aid of a new MVDC ship model, and a near-optimal solution can

be derived within milliseconds. The schematic views of SPS under both the pre-fault and post-fault conditions are displayed in Fig. 2.13.

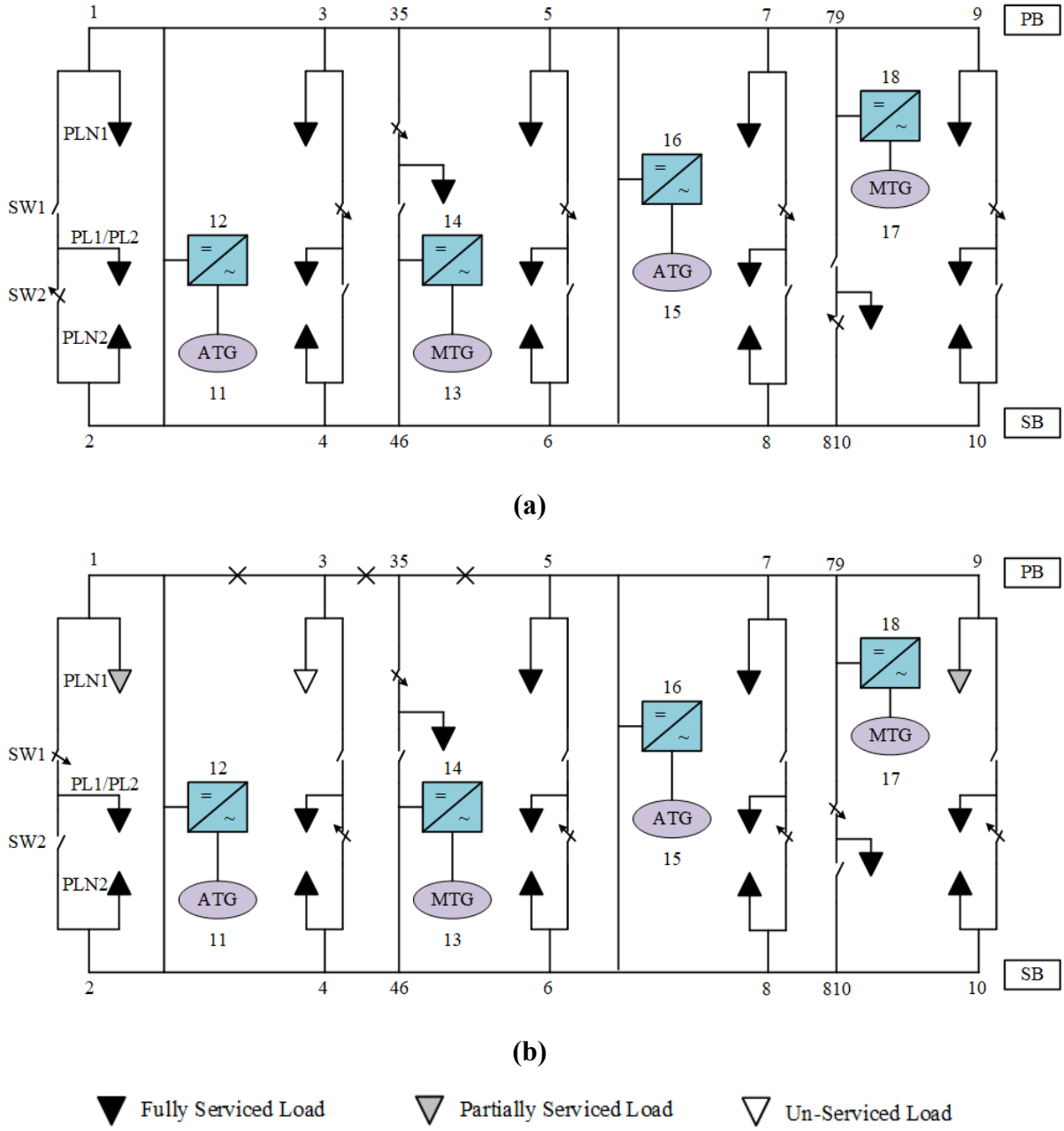

Fig. 2.13. Schematic views of SPS (a) under pre-fault condition; (b) under faults occurring at 1-3, 3-35, and 35-5 [143].

In the proposed method, two centralized optimization solutions have been evaluated, which deliver near-optimal power to loads in SPS. Compared with the global solver using "branch and bound" method, much lower complexity is presented in the proposed one. It is illustrated

that the vital and semi-vital loads are serviced properly in 50% of the fault cases, where up to four random faults are included [143].

Since the DC power distribution architecture is becoming popular due to its high power efficiency and flexible power regulation capability, some efforts have been devoted to the fault protection in DC-SPS. An active impedance estimation scheme has been proposed in [144] to accurately determine the fault location in a zonal DC-SPS, where the injection of a short-duration disturbance onto the MPSs is required. Then the transient response measured at the point of coupling is utilized to monitor the power system impedance, which can be used to detect a change of system state. In addition, the effective operation of active impedance estimation scheme in terms of identifying changes in bus impedance caused by short-circuit faults is demonstrated in a 30-kW experimental zonal DC distribution system. Moreover, the employment of the proposed technique in a DC-SPS for obtaining more intelligent reconfigurations for faulty cases has been discussed. The main advantage of the proposed fault location identification scheme is that system-wide communications are not needed, which creates the possibility for the equipment in each zone to accurately locate the faults and reconfigure the power system automatically.

An MMC with hierarchical redundancy ability has been designed and implemented for shipboard MVDC systems in [98]. The proposed hierarchical redundant strategy has been realized smoothly by the design of pre-treatment units, which fails to compromise the modulation and sort-and-selection strategies designed for the normal condition. Besides, the fault detection circuit and mechanical switch for each SM have been presented, and the faulty SM can be isolated very quickly. In addition, the MMC can still work properly with the “hot-reserved” SMs, and even when a number of SMs are in fault, the MMC can persist to work. Moreover, the devices are not damaged when the voltage and current overshoots occur during the fault and redundancy processes. The redundancy strategy can make the MMC recover to

the safe operation condition effectively, and the satisfactory output voltage is ensured. Three arrangements are contained in the DC-AC MMC suitable for MVDC-SPS, where the top and bottom arms consist of each arrangement. The configuration suitable for MVDC-based MES application is displayed in Fig. 2.14.

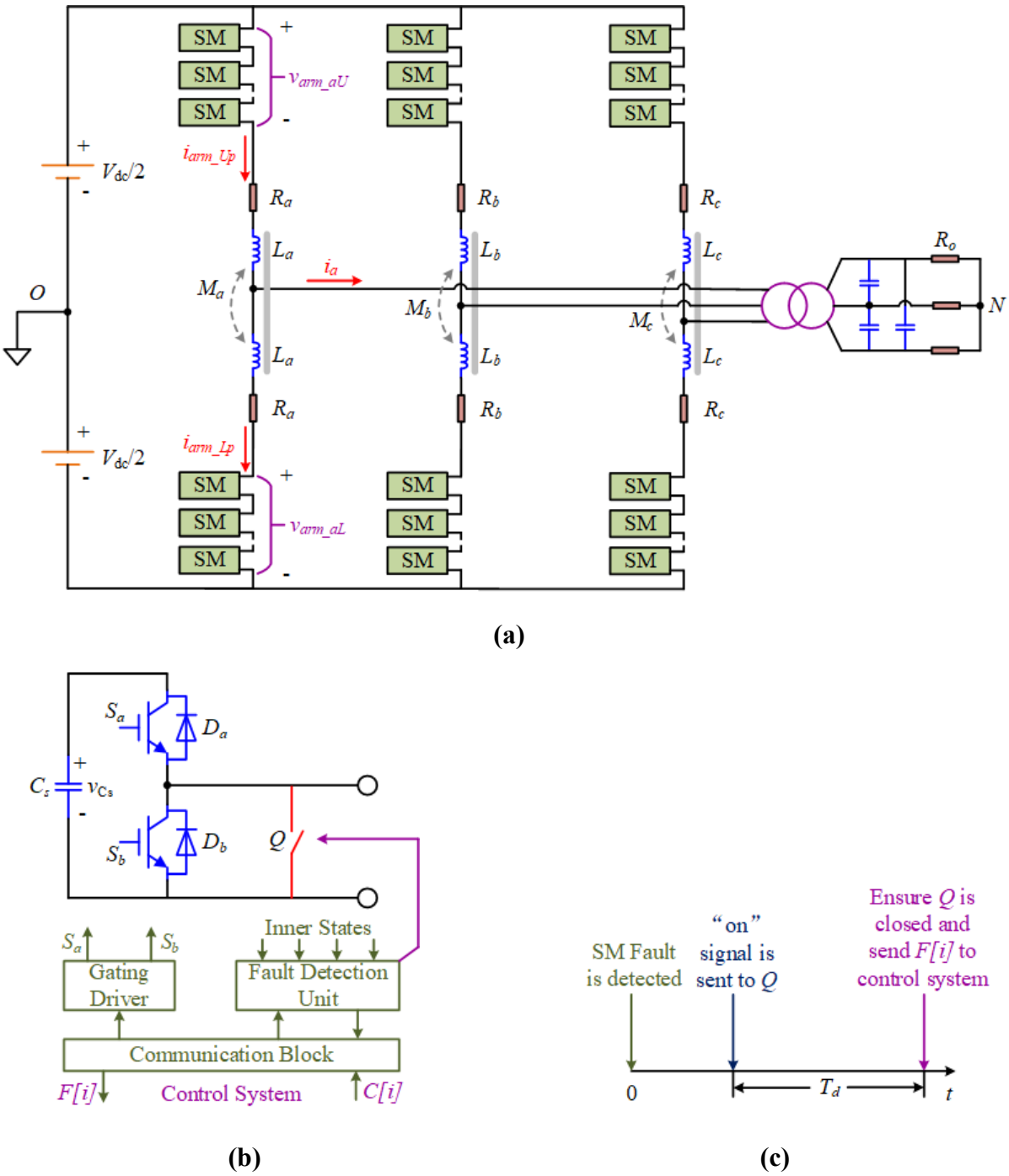

Fig. 2.14. Configuration of MMC suitable for MVDC application. (a) Topology of the MMC; (b) SM with diagnosis unit; (c) time sequence of the SM operation [98].

2.5 Summary

This chapter gives a comprehensive overview of MES in terms of the design, control, power management, system stability and reliability. With the propose of meeting the increasing electricity demand and achieving flexible power delivery in MES, MVDC-SPS is being widely used in various categories of vessels. With such a promising architecture, electric propulsion is likely to be completely realized for the next generation of merchant, cruise, and military ships. In addition, the rapid development of MES depends on the emergence of advanced power electronics techniques, where multilevel converters have been extensively investigated for large-scale micro-grid applications. Besides, the hierarchical control scheme has been proposed to integrate the smart grid and DC micro-grid technologies into SPS to obtain different control functions. Furthermore, some novel fault protection strategies have been presented to ensure DC SPS stability and reliability.

Chapter 3 Modelling of Main Power Components in A Partially Power Decoupled AC-DC Hybrid Shipboard Power System

In this chapter, the models of the main power components in the proposed partially power decoupled shipboard power system (PPD-SPS) are illustrated in detail. The basic power components consist of the power generation unit (PGU), doubly-fed induction machine (DFIM), back-to-back power converter (BTBPC), energy storage devices and service loads. Since around 80% of the on-board power is supplied to propulsion loads [145], the service loads are not taken into consideration in the presented study. The effects of cables are also neglected as the distance between the power source and load is much shorter than that of an onshore grid. Therefore, only the models of PGU, DFIM, BTBPC and energy storage devices are presented for study in this chapter. The synchronous generator (SG) acts as the power source in the proposed PPD-SPS to provide power supply and determine the SPS frequency. The modelling of SG and DFIM is based on the use of synchronous reference frame, and the *dq* models are derived to accomplish decoupling the mutual effects among the three-phase variables, therefore alternating current (AC) machines can be controlled a similar way to direct current (DC) ones. All the rotor-side parameters are transferred to the stator side for the convenience of clearly illustrating the model. The on-board power flow is delivered from the power source to the load through two paths, which are the AC transmission line and BTBPC based power paths. The SPS power flow control is realized by controlling the BTBPC, whose proportion in the total volume of the on-board power rating determines the flexibility in bidirectional power regulation. Moreover, energy storage systems (ESS) are needed to compensate for the power imbalance between the source and load of the proposed PPD-SPS,

where the battery, super-capacitor (SC), and fuel cell (FC) are the most commonly used devices in an ESS.

3.1 PGU

In this chapter, a salient-pole SG and a type DC1A excitation system (EXS) are applied at the power generation side of SPS as the PGU. The dynamics of stator, field and damper windings are taken into consideration, and the rotor parameters are seen from the stator side. In the *dq* reference frame, the field winding only exists in the *d* axis. The electrical model of SG in the *dq* frame is displayed in Fig. 3.1.

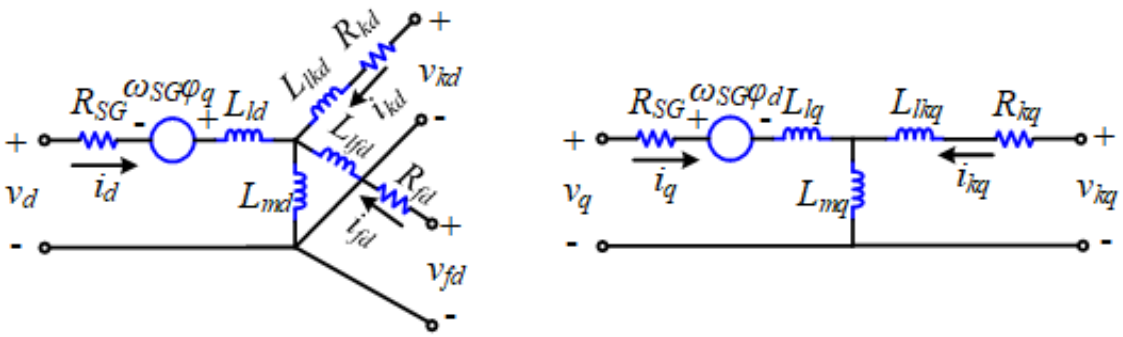

(a) **(b)**

Fig. 3.1. SG electrical model in *dq* frame (a) *d*-axis (b) *q*-axis.

The voltage and flux equations of a standard SG in the *dq* frame are expressed as shown below:

$$\begin{cases} v_d = R_{SG} i_d + p\psi_d - \omega_{SG}\psi_q \\ v_q = R_{SG} i_q + p\psi_q + \omega_{SG}\psi_d \\ v_f = R_f i_f + p\psi_f \\ v_{kd} = R_{kd} i_{kd} + p\psi_{kd} \\ v_{kq} = R_{kq} i_{kq} + p\psi_{kq} \end{cases} \tag{3-1}$$

$$\begin{cases} \psi_d = L_d i_d + L_{md}(i_f + i_{kd}) \\ \psi_q = L_q i_q + L_{mq} i_{kq} \\ \psi_f = L_f i_f + L_{md}(i_d + i_{kd}) \\ \psi_{kd} = L_{kd} i_{kd} + L_{md}(i_d + i_f) \\ \psi_{kq} = L_{kq} i_{kq} + L_{mq} i_q \end{cases} \tag{3-2}$$

where v_d and v_q are the d-axis and q-axis stator voltages in V; v_f is the field voltage in V; v_{kd} and v_{kq} are the d-axis and q-axis damper voltages in V; i_d and i_q are the d-axis and q-axis stator currents in A; i_f is the field current in A; i_{kd} and i_{kq} are the d-axis and q-axis damper currents in A; ψ_d and ψ_q are the d-axis and q-axis fluxes in Wb; ψ_f is the field flux in Wb; ψ_{kd} and ψ_{kq} are the d-axis and q-axis damper fluxes in Wb; R_{SG} is the stator resistance in Ω; R_f is the field resistance in Ω; R_{kd} and R_{kq} are the d-axis and q-axis damper resistances in Ω; L_d and L_q are the d-axis and q-axis stator inductances in H; L_f is the field inductance in H; L_{kd} and L_{kq} are the d-axis and q-axis damper inductances in H; L_{md} and L_{mq} are the d-axis and q-axis mutual inductances in H; ω_{SG} is the rotor speed in rad/s; p represents the differential operator d/dt.

The mechanical behaviour of SG can be illustrated by the following equations:

$$\Delta\omega_{SG}(t) = \frac{1}{2H}\int_0^t (T_m - T_{em})dt - K_d \Delta\omega_{SG}(t) \tag{3-3}$$

$$\omega_{SG}(t) = \Delta\omega_{SG}(t) + \omega_{SG0} \tag{3-4}$$

where $\Delta\omega_{SG}$ indicates the rotor speed variation in rad/s; ω_{SG0} is the initial rotor speed in rad/s; T_m is the mechanical torque in N/m; T_{em} is the electromechanical torque in N/m; H is the inertia constant in s; K_d is the damping constant.

The reactance, transient reactance and sub-transient reactance of SG in the dq reference frame are calculated as shown below:

$$\begin{cases} X_d = X_{ld} + X_{md} \\ X_d' = X_{ld} + (X_{md} \parallel X_{lf}) \\ X_d'' = X_{ld} + (X_{md} \parallel X_{lf} \parallel X_{lkd}) \\ X_q = X_{lq} + X_{mq} \\ X_q'' = X_{lq} + (X_{mq} \parallel X_{lkq}) \end{cases} \tag{3-5}$$

where X_d, X_d', X_d'' are the d-axis reactance, transient reactance, and sub-transient reactance in Ω; X_q and X_q'' are the q-axis reactance and sub-transient reactance in Ω; X_{ld} and X_{lq} are the d-axis and q-axis leakage reactance in Ω; X_{md} and X_{mq} are the d-axis and q-axis mutual reactance in Ω; X_{lkd} and X_{lkq} are the d-axis and q-axis leakage damper reactance in Ω; X_{lf} is the leakage field reactance in Ω.

A general SG EXS usually consists of an exciter, a terminal voltage transducer and load compensator, excitation control elements, and a power system stabilizer (PSS) and the supplementary discontinuous excitation controls [146]. The functional block diagram for a general SG EXS is displayed in Fig. 3.2.

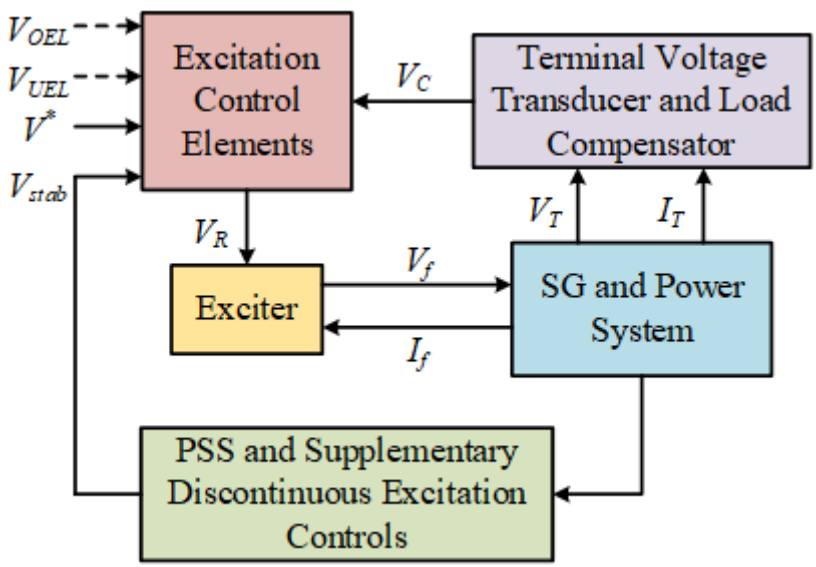

Fig. 3.2. General SG EXS functional block diagram.

where V_{OEL} and V_{UEL} are the over excitation and under excitation voltage limits in V; V^* is the reference voltage in V; V_{stab} is the stabilizing voltage in V; V_R is the regulated voltage in V; V_C is the compensated voltage in V; V_T and I_T are the terminal voltage in V and current in A, respectively.

The inputs for the excitation control elements include the reference, stabilizing and compensating voltages, and the over excitation and under excitation limiters may be presented to implement the saturations. The exciter is employed to produce the field voltage for the SG. Meanwhile, the voltage sensing and compensation are realized by using the terminal voltage transducer and load compensator, respectively. On top of that, the stabilizing function is obtained by PSS and supplementary discontinuous excitation controls.

3.2 DFIM *dq* Model

In the *dq* model, a vector **x** is in the format of $[x_d\ x_q]^T$. For example, $\mathbf{V_s} = [V_{sd}\ V_{sq}]^T$.

With a constant rotor speed, the stator voltage of SG remains constant, therefore the stator voltage of DFIM does not change. By orienting the *d*-axis in the same direction as that of the stator voltage vector, the voltage equations for DFIM *dq* model in the synchronous reference frame are derived as:

$$\begin{cases} \mathbf{V_s} = R_s\mathbf{I_s} + \dfrac{d\boldsymbol{\psi}_\mathbf{s}}{dt} + \mathrm{j}\omega_e\boldsymbol{\psi}_\mathbf{s} \\ \mathbf{V_r} = R_r\mathbf{I_r} + \dfrac{d\boldsymbol{\psi}_\mathbf{r}}{dt} + \mathrm{j}\omega_{slip}\boldsymbol{\psi}_\mathbf{r} \end{cases} \tag{3-6}$$

where $\mathbf{V_s}$, $\mathbf{V_r}$ are the stator and rotor voltage vectors in V; R_s, R_r are the stator and rotor resistances in Ω; $\mathbf{I_s}$, $\mathbf{I_r}$ are the stator and rotor current vectors in A; $\boldsymbol{\psi}_\mathbf{s}$, $\boldsymbol{\psi}_\mathbf{r}$ are the stator and rotor flux vectors in Wb; ω_e and ω_{slip} are the grid and slip angular speeds in rad/s, respectively.

The stator and rotor flux equations are expressed as:

$$\begin{cases} \boldsymbol{\psi}_\mathbf{s} = L_s\mathbf{I}_\mathbf{s} + L_m\mathbf{I}_\mathbf{r} \\ \boldsymbol{\psi}_\mathbf{r} = L_m\mathbf{I}_\mathbf{s} + L_r\mathbf{I}_\mathbf{r} \end{cases} \tag{3-7}$$

where L_s, L_r and L_m are the stator, rotor, and mutual inductances in H, respectively.

According to (3-6) and (3-7), the equivalent circuit of DFIM *dq* model can be obtained as shown in Fig. 3.3.

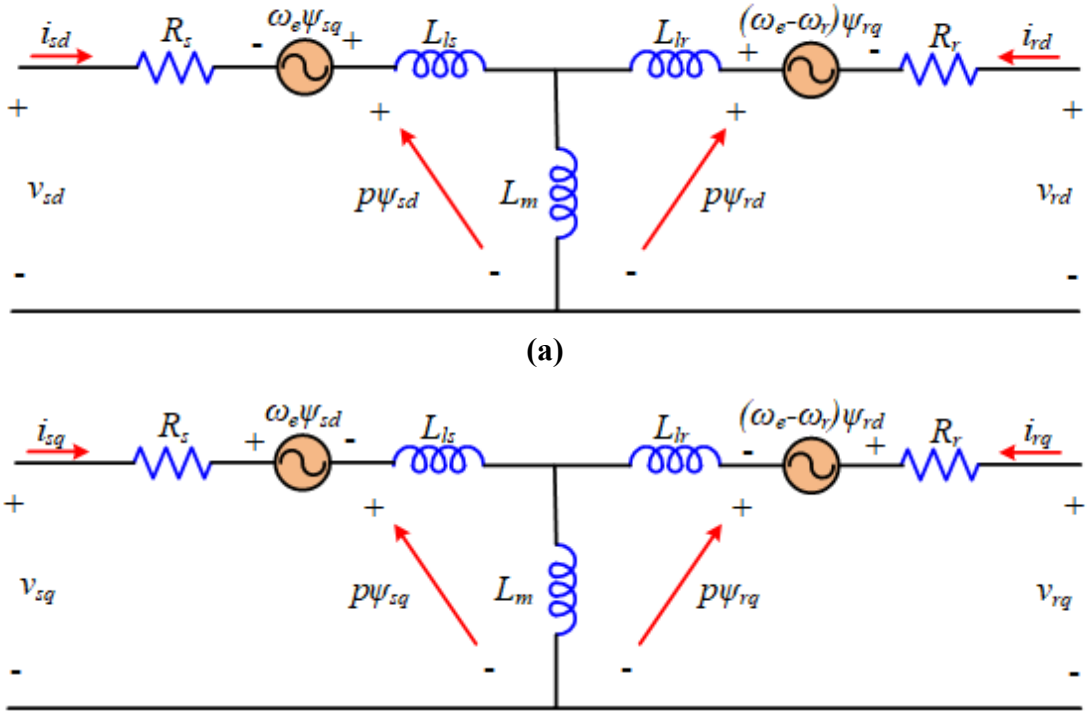

Fig. 3.3. Equivalent circuits for DFIM *dq* model (a) *d*-axis (b) *q*-axis.

To reveal the field current effect more clearly, the stator flux can also be illustrated as:

$$\boldsymbol{\psi}_\mathbf{s} = L_s\mathbf{I}_\mathbf{s} + L_m\mathbf{I}_\mathbf{r} = L_m\mathbf{I}_\mathbf{ms} \tag{3-8}$$

where $\mathbf{I}_\mathbf{ms}$ indicates the equivalent field current vector, and the rotor flux can be expressed by:

$$\boldsymbol{\psi}_\mathbf{r} = \frac{L_m^{\ 2}}{L_s}\mathbf{I}_\mathbf{ms} + \sigma L_r \mathbf{I}_\mathbf{r} \tag{3-9}$$

where σ = 1 – [$L_m^2/(L_rL_s)$] is the leakage flux factor. Substitute (3-8) and (3-9) into (3-6), the following equations are derived:

$$\begin{cases} \mathbf{V}_\mathbf{s} = R_s\mathbf{I}_\mathbf{s} + L_m p\mathbf{I}_\mathbf{ms} + \mathrm{j}\omega_e\boldsymbol{\psi}_\mathbf{s} \\ \mathbf{V}_r = R_r\mathbf{I}_\mathbf{r} + \sigma L_r p\mathbf{I}_\mathbf{r} + \dfrac{L_m^{\ 2}}{L_s}p\mathbf{I}_\mathbf{ms} + \mathrm{j}\omega_{slip}\boldsymbol{\psi}_\mathbf{r} \end{cases} \tag{3-10}$$

If the dynamic process of stator field currents is neglected, (3-10) can be updated as:

$$\begin{cases} \mathbf{V}_\mathbf{s} = R_s\mathbf{I}_\mathbf{s} + \mathrm{j}\omega_e\boldsymbol{\psi}_\mathbf{s} \\ \mathbf{V}_r = R_r\mathbf{I}_\mathbf{r} + \sigma L_r p\mathbf{I}_\mathbf{r} + \mathrm{j}\omega_{slip}\boldsymbol{\psi}_\mathbf{r} \end{cases} \tag{3-11}$$

The electromagnetic torque and the kinetic equation of DFIM are expressed as:

$$T_{em} = 1.5 n_p L_m (i_{rd} i_{sq} - i_{rq} i_{sd}) \tag{3-12}$$

$$\frac{d\omega_m}{dt} = \frac{1}{2H}(T_{em} - T_L) \tag{3-13}$$

where n_p is the number of pole pairs; ω_m is the mechanical rotor angular speed in rad/s; T_{em} and T_L are the electromagnetic and load torques in N/m, respectively.

The concept of "slip" is important for the operation of DFIM, which is defined by:

$$slip = \frac{\omega_e - \omega_r}{\omega_e} = \frac{\omega_{slip}}{\omega_e} \tag{3-14}$$

where ω_e is the grid angular speed in rad/s and ω_r is the electrical rotor angular speed in rad/s. With the premise that the motor or generator mode of a DFIM is determined, the operation

mode of DFIM can be determined according to the sign of slip. The details of DFIM operation modes are displayed in Table 3.1.

Table 3.1. Operation Modes of DFIM

Operation Mode	*slip*	Description
Subsynchronous (Motor)	> 0	The DFIM feeds the slip power back to the power source through BTBPC.
Supersynchronous (Motor)	< 0	The power source delivers power to the DFIM through two paths.
Synchronous	= 0	The power source delivers power to the DFIM only through AC transmission.
Subsynchronous (Generator)	> 0	The power source feeds the slip power back to the DFIM through BTBPC.
Supersynchronous (Generator)	< 0	The DFIM delivers power to the power source through two paths.

3.3 BTBPC

3.3.1 Detailed Model

There are two power converters in the BTBPC, which are the source-side converter (SSC) and load-side converter (LSC). The SSC is directly connected to the AC transmission line, while the LSC is connected to the rotor of DFIM. The topology of BTBPC is displayed in Fig. 3.4.

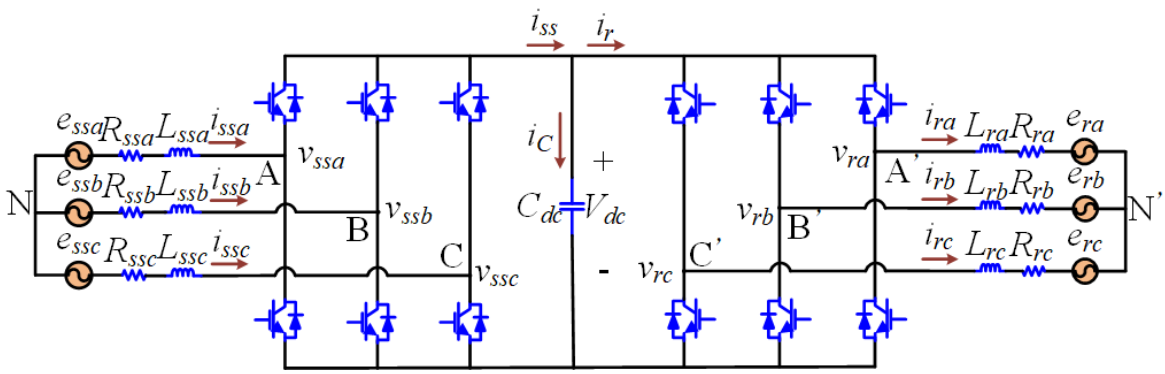

Fig. 3.4. BTBPC topology.

The DC-link capacitor is installed to decouple the power regulation of SSC and LSC, and in Fig. 3.4 the positive direction of power flow is assumed from the SSC to LSC, which corresponds to the supersynchronous mode when the DFIM operates as a propulsion motor. S_{ssa}, S_{ssb} and S_{ssc} are defined as the switching functions of power switches in the three phases of SSC, while S_{lsa}, S_{lsb} and S_{lsc} are defined as the switching functions of the power switches in the three phases of LSC. Therefore, the three-phase model of BTBPC can be expressed as:

$$\begin{cases} L_{ssx}\dfrac{di_{ssx}}{dt} = e_{ssx} - R_{ssx}i_{ssx} - \dfrac{e_{ssa}+e_{ssb}+e_{ssc}}{3} - [S_{ssx} - \dfrac{S_{ssa}+S_{ssb}+S_{ssc}}{3}]V_{dc}, & x = a,b,c \\ L_{rx}\dfrac{di_{rx}}{dt} = -e_{rx} - R_{rx}i_{rx} + \dfrac{e_{ra}+e_{rb}+e_{rc}}{3} + [S_{lsx} - \dfrac{S_{lsa}+S_{lsb}+S_{lsc}}{3}]V_{dc}, & x = a,b,c \\ C_{dc}\dfrac{V_{dc}}{dt} = (S_{ssa}i_{ssa} + S_{ssb}i_{ssb} + S_{ssc}i_{ssc}) - i_r = i_{ss} - (S_{lsa}i_{ra} + S_{lsb}i_{rb} + S_{lsc}i_{rc}) \end{cases} \tag{3-15}$$

$$\begin{cases} v_{ssx} = [S_{ssx} - \dfrac{S_{ssa}+S_{ssb}+S_{ssc}}{3}]V_{dc}, & x = a,b,c \\ v_{rx} = [S_{lsx} - \dfrac{S_{lsa}+S_{lsb}+S_{lsc}}{3}]V_{dc}, & x = a,b,c \\ i_{ss} = S_{ssa}i_{ssa} + S_{ssb}i_{ssb} + S_{ssc}i_{ssc} \\ i_r = S_{lsa}i_{ra} + S_{lsb}i_{rb} + S_{lsc}i_{rc} \end{cases} \tag{3-16}$$

where L_{ss}, R_{ss}, i_{ss}, v_{ss} and e_{ss} are the source-side inductance, resistance, current, voltage and internal voltage values in H, Ω, A, V and V, respectively; e_r is the rotor-side internal voltage in V; i_{ss} and i_r are the DC-side currents for the SSC and LSC in A; C_{dc} is the DC-link capacitance in F; and V_{dc} is the DC-bus voltage in V.

Substituting (3-16) into (3-15), the three-phase model can be updated as:

$$\begin{cases} L_{ssx}\dfrac{di_{ssx}}{dt} = e_{ssx} - R_{ssx}i_{ssx} - \dfrac{e_{ssa}+e_{ssb}+e_{ssc}}{3} - v_{ssx}, & x = a,b,c \\ L_{rx}\dfrac{di_{rx}}{dt} = -e_{rx} - R_{rx}i_{rx} + \dfrac{e_{ra}+e_{rb}+e_{rc}}{3} + v_{rx}, & x = a,b,c \\ C_{dc}\dfrac{V_{dc}}{dt} = i_{ss} - i_r \end{cases} \tag{3-17}$$

Assume that the three phases on both the source and load sides are balanced ($R_{ssa} = R_{ssb} = R_{ssc} = R_{ss}$; $L_{ssa} = L_{ssb} = L_{ssc} = L_{ss}$; $R_{ra} = R_{rb} = R_{rc} = R_r$; $L_{ra} = L_{rb} = L_{rc} = L_r$). The dq model of BTBPC can be expressed as:

$$\begin{cases} L_{ss}\dfrac{d\mathbf{I_{ss}}}{dt} = \mathbf{E_{ss}} - R_{ss}\mathbf{I_{ss}} - \mathbf{V_{ss}} - \mathrm{j}\omega_e L_{ss}\mathbf{I_{ss}} \\ L_r\dfrac{d\mathbf{I_r}}{dt} = -\mathbf{E_r} - R_r\mathbf{I_r} + \mathbf{V_r} + \mathrm{j}\omega_{slip}L_r\mathbf{I_r} \\ C_{dc}\dfrac{V_{dc}}{dt} = i_{ss} - i_r \end{cases} \tag{3-18}$$

In order to investigate the power efficiency of BTBPC, the power loss model is established, which contains the copper losses, switching losses, conduction losses, and DC-bus losses. Taking the case of supersynchronous operation as an example, the power loss model of BTBPC is illustrated in Fig. 3.5.

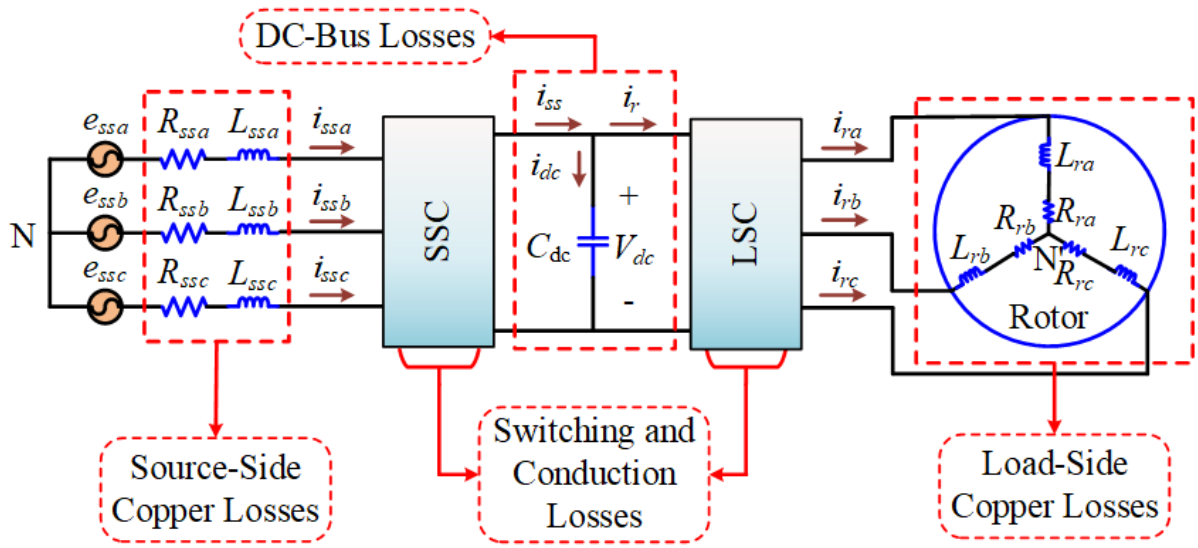

Fig. 3.5. BTBPC power loss model.

The copper losses are calculated as:

$$P_{cl} = \frac{3}{2}(R_r I_r^2 + R_{ss} I_{ss}^2) \tag{3-19}$$

According to [147], assuming the duty cycles are related to time in a sinusoidal way, the conduction losses in an active power device and its freewheeling diode during a fundamental period are expressed as:

$$\begin{cases} P_{cond,T} = V_{CE0} i_{CE}(\frac{1}{2} + \frac{m\cos\phi}{8}) + r_{CE} i_{CE}^2(\frac{1}{8} + \frac{m\cos\phi}{3\pi}) \\ P_{cond,D} = V_{F0} i_F(\frac{1}{2} + \frac{m\cos\phi}{8}) + r_F i_F^2(\frac{1}{8} - \frac{m\cos\phi}{3\pi}) \end{cases} \tag{3-20}$$

where $P_{cond,T}$ and $P_{cond,D}$ are the conduction losses on the transistor and diode in W, respectively; V_{CE0} and V_{F0} are the collector-emitter and diode forward threshold voltages in V, respectively; i_{CE} and i_F are the collector-emitter and diode forward currents in A, respectively; r_{CE} and r_F are the on-state slope resistances for the transistor and diode in Ω, respectively; m is the modulation index; Φ is the angle difference between the voltage and current in degree.

The switching losses during the switching and reverse recovery periods of a power switch are described by the following equations:

$$\begin{cases} P_{sw,T} = \frac{\sqrt{2} I_m E_{sw}}{\pi T_{sw} I^*}(\frac{V_{dc}}{V_{dc}^*})^{K_{v,T}} \times [1 + T_{sw,T}(T_j - T^*)] \\ P_{sw,rr} = \frac{\sqrt{2} E_{rr}}{\pi T_{sw}}(\frac{I}{\sqrt{2} I^*})^{K_{i,d}}(\frac{V_{dc}}{V_{dc}^*})^{K_{v,d}} \times [1 + T_{rr,d}(T_j - T^*)] \end{cases} \tag{3-21}$$

where $P_{sw,T}$ and $P_{sw,rr}$ are the power losses during the switching and reverse recovery periods in W, respectively; E_{sw} and E_{rr} are the energy dissipation during the switching and reverse recovery periods in J, respectively; T_{sw} is the switching period in s; $K_{v,T}$ and $K_{i,d}$ are the exponents for the voltage and current dependence of the diode switching losses; T_j is the junction temperature in K; T^* is the reference temperature value in K; $T_{sw,T}$ and $T_{rr,d}$ are the temperature coefficients of the transistor and diode switching losses.

The DC-bus loss is modelled by the power loss in the DC-link capacitor, which is mainly caused by the existence of equivalent series resistance R_{esr} and leakage resistance R_l in Ω. The DC-bus losses can be calculated by:

$$P_{dc} = (R_{esr} + R_l) I_{dc}^2 \tag{3-22}$$

Taking the copper losses, DC-bus losses, switching and conduction losses into consideration, and since there are 12 switches in a BTBPC, the whole power loss model of BTBPC can be expressed as:

$$P_{loss} = P_{cl} + P_{dc} + \frac{12T_s}{T_{sw}}(P_{sw,T} + P_{sw,rr} + P_{cond,T} + P_{cond,D}) \tag{3-23}$$

3.3.2 Average Model

In the detailed BTBPC model, the switching functions are obtained by comparing the instantaneous values of carrier wave u_c and modulated wave u_m according to:

$$S = \begin{cases} 1, & u_m > u_c \\ 0, & u_m \le u_c \end{cases} \tag{3-24}$$

Since the switching frequency of AC-DC power converter is at the level of several thousands to tens of thousands of Hz, the step time used in the simulation needs to be small enough to construct the valid carrier wave.

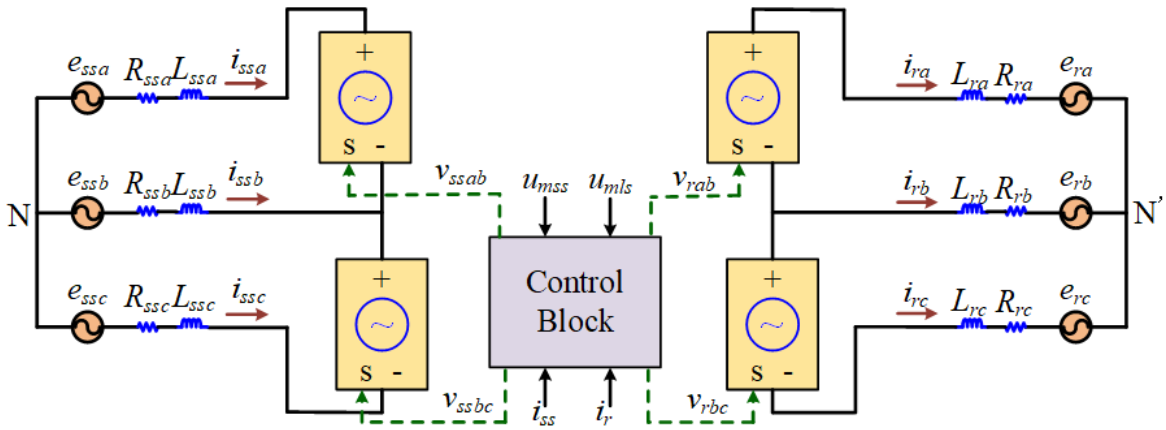

Fig. 3.6. BTBPC topology.

When it comes to the system-level analysis, the details of switching functions are not important. Instead of using the detailed BTBPC model that illustrates the switching details, the average model is applied to represent the BTBPC as four controlled voltage sources, which are presented between phases A and B, B and C at the SSC and LSC sides, respectively. The three-phase modulated signals and current values are the inputs for the control block to obtain the phase-to-phase voltages. The equivalent circuit for BTBPC average model is displayed in Fig. 3.6, and the phase-to-phase voltages for the four controlled voltage sources are calculated by

$$\begin{cases} v_{ssab} = 0.5V_{dc}(u_{mssa} - u_{mssb}) \\ v_{ssbc} = 0.5V_{dc}(u_{mssb} - u_{mssc}) \\ v_{rab} = 0.5V_{dc}(u_{mlsa} - u_{mlsb}) \\ v_{rbc} = 0.5V_{dc}(u_{mlsb} - u_{mlsc}) \end{cases} \tag{3-25}$$

where u_{mssa}, u_{mssb}, u_{mssc} and u_{mlsa}, u_{mlsb}, u_{mlsc} are the three-phase modulated waves at the SSC and LSC sides, respectively; v_{ssab}, v_{ssbc} and v_{rab}, v_{rbc} are the phase-to-phase voltages in V between phases A and B, B and C at the SSC and LSC sides, respectively.

In addition, the magnitude for any of these voltage values should be smaller than V_{dc}. The value of V_{dc} can be derived according to the following equation:

$$V_{dc} = \sqrt{\frac{1}{C_{dc}} \int (P_{ss} - P_r) dt} \tag{3-26}$$

Where:

$$P_{ss} = v_{ssab} i_{ssa} - v_{ssbc} i_{ssc} \tag{3-27}$$

$$P_r = v_{rab} i_{ra} - v_{rbc} i_{rc} \tag{3-28}$$

3.4 Energy Storage

During the operation process of PPD-SPS, the power generation from PGU is adjusted according to the load demand. When the propulsion load is remained at a constant value, the power generation can meet the load demand with the highest efficiency. However, variations in the load torque are inevitable in practical sailing, which may result in instantaneous power imbalance between the power source and propulsion load. Usually, additional energy storage devices are needed to compensate for the power imbalance. Battery, SC, and FC are the three categories of commonly applied energy storage devices in SPS, and their models are to be illustrated in the following paragraphs.

3.4.1 Battery

A battery used for automotive applications like MES is usually endowed with high energy density, and it is used to deal with the long-term energy imbalance in the SPS during the sailing process. There are mainly four types of batteries, which are the lead-acid battery, lithium-ion

(Li-ion) battery, nickel-cadmium and nickel-metal-hydride battery. All of these batteries have charge and discharge models, which are illustrated in Table 3.2.

Table 3.2. Battery Models

Battery Type	Model Type	Expression of Battery Voltage
Lead-Acid	Discharge Model	$V_{bat} = V_{bat0} - K \cdot \frac{Q}{Q-it} \cdot \hat{i} - K \cdot \frac{Q}{Q-it} \cdot it + \text{Laplace}^{-1}(\frac{Exp(s)}{Sel(s)} \cdot 0)$
	Charge Model	$V_{bat} = V_{bat0} - K \cdot \frac{Q}{it+0.1 \cdot Q} \cdot \hat{i} - K \cdot \frac{Q}{Q-it} \cdot it + \text{Laplace}^{-1}(\frac{Exp(s)}{Sel(s)} \cdot \frac{1}{s})$
Li-ion	Discharge Model	$V_{bat} = V_{bat0} - K \cdot \frac{Q}{Q-it} \cdot \hat{i} - K \cdot \frac{Q}{Q-it} \cdot it + A \cdot \exp(-B \cdot it)$
	Charge Model	$V_{bat} = V_{bat0} - K \cdot \frac{Q}{it+0.1 \cdot Q} \cdot \hat{i} - K \cdot \frac{Q}{Q-it} \cdot it + A \cdot \exp(-B \cdot it)$
Nickel-Cadmium and Nickel-Metal-Hydride	Discharge Model	$V_{bat} = V_{bat0} - K \cdot \frac{Q}{Q-it} \cdot \hat{i} - K \cdot \frac{Q}{Q-it} \cdot it + \text{Laplace}^{-1}(\frac{Exp(s)}{Sel(s)} \cdot 0)$
	Charge Model	$V_{bat} = V_{bat0} - K \cdot \frac{Q}{\lvert it \rvert + 0.1 \cdot Q} \cdot \hat{i} - K \cdot \frac{Q}{Q-it} \cdot it + \text{Laplace}^{-1}(\frac{Exp(s)}{Sel(s)} \cdot \frac{1}{s})$

In Table 3.2, Laplace^{-1} indicates the Inverse Laplace Transformation. For the equations in Table 3.2, V_{bat} is the nonlinear battery voltage in V; V_{bat0} is the initial value of V_{bat} in V; $Exp(s)$ is exponential zone dynamics; $Sel(s)$ indicates the state variable of battery mode, where $Sel(s) = 0$ during the battery discharge process and $Sel(s) = 1$ during the battery charging process; K is the polarization constant in AH^{-1} (Ampere•Henery^{-1}) or polarization resistance in Ohm; $\hat{i}$ is low frequency current dynamics in A; i is battery current in A; it is the extracted capacity in C; Q is the maximum battery capacity in C; A and B are the exponential voltage and capacity, respectively.

More detailed battery models include the temperature and aging effects, which are neglected in this chapter for simplicity.

3.4.2 SC

The SC banks have high power density, and they are efficient in compensating the transient power imbalance between the power source and load of SPS. The output voltage of SC is expressed by the Stern equation.

$$V_{SC} = \frac{N_s Q_T d}{N_p N_e \varepsilon\varepsilon_0 A_i} + \frac{2 N_e N_s R T}{F} \sinh^{-1}\left(\frac{Q_T}{N_p N_e^2 A_i \sqrt{8RT\varepsilon\varepsilon_0 c}}\right) - R_{SC} \cdot i_{SC} \tag{3-29}$$

with

$$Q_T = \int i_{SC} dt \tag{3-30}$$

If the self-discharge phenomenon is taken into account, the SC electric charge can be modified as (when i_{SC} = 0 A)

$$Q_T = \int i_{self\_dis} dt \tag{3-31}$$

where

$$i_{self\_dis} = \begin{cases} \dfrac{C_T \alpha_1}{1 + s R_{SC} C_T}, & t - t_{oc} \le t_3 \\ \dfrac{C_T \alpha_2}{1 + s R_{SC} C_T}, & t_3 < t - t_{oc} \le t_4 \\ \dfrac{C_T \alpha_3}{1 + s R_{SC} C_T}, & t - t_{oc} > t_4 \end{cases} \tag{3-32}$$

The descriptions of the variables used for SC model are given in Table 3.3.

Table 3.3. Descriptions of Variables for SC Model

Variable	Description
A_i	Interface area between electronics and electrolyte (m^2)

c	Molar concentration (mol/m^3) that is equal to $1/(8N_A r^3)$
F	Faraday constant
i_{SC}	SC current (A)
V_{SC}	SC voltage (V)
C_T	Total capacitance (F)
R_{SC}	Total SC resistance (Ohm)
N_e	Number of layers of electrodes
N_A	Avogadro constant
N_p	Number of parallel SCs
N_s	Number of series SCs
Q_T	Electric charge (C)
R	Ideal gas constant
d	Molecular radius (m)
T	Operating temperature (K)
ε	Permittivity of material
ε_0	Permittivity of free space

In this chapter, SCs are integrated to the DC bus of the proposed PPD-SPS through a DC-DC power converter, as shown in Fig. 3.7.

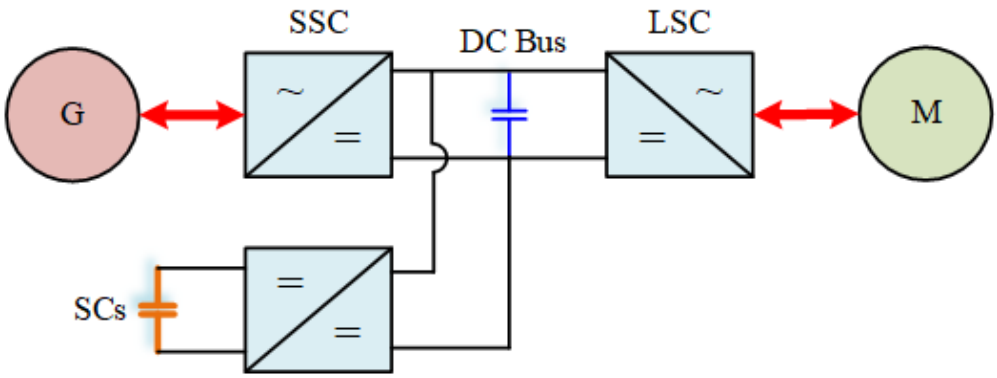

Fig. 3.7. SC connected to the DC bus of DFIM-SPS (G: Generator; M: Motor).

The SCs are endowed with good transient performance, and they can be accessed at any operation point [148]. More importantly, they assist in regulating the DC-bus voltage to improve the system control performance and enhance the system stability. The ESS that is established by SC banks functions as either a source or sink to complement the power difference between the active powers at the source and load sides. The capacitance of SC is determined by

$$C_{SC} = \frac{2P_{nom}T_{SC}}{V_{SCnom}^{2}} \tag{3-33}$$

where P_{nom} indicates the rated power of DFIM in W; T_{SC} is the desired time period in s for the SC bank to exchange energy when DFIM operates at the rated power; V_{SCnom} is the rated voltage of SC bank in V.

3.4.3 FC

The model of FC is represented by the following three variables: the open circuit voltage E_{oc}, the exchange current i_0, and the Tafel slope A. Their expressions are shown as follows.

$$E_{oc} = K_c E_n \tag{3-34}$$

$$i_0 = \frac{zFk(P_{H2} + P_{O2})}{Rh} e^{\frac{-\Delta G}{RT}} \tag{3-35}$$

$$A = \frac{RT}{z\alpha F} \tag{3-36}$$

where K_c is the voltage constant at nominal condition of operation; E_n is the Nernst voltage in V; z is the number of moving electrons; F is the Faraday constant; k is the Boltzmann's constant = $1.38*10^{-23}$J/K; P_{H2} and P_{O2} are the partial pressure of hydrogen and oxygen inside the stack, respectively; R is the ideal gas constant; h is the Planck's constant = $6.626*10^{-34}$Js; ΔG is the size of the activation barrier; T is the temperature of operation in K; α is the charge transfer coefficient.

3.5 Summary

This chapter presents the models of the main power components including PGU, DFIM, BTBPC, and energy storage device in the proposed PPD-SPS. The SG works as the power source for the whole MES, and its correct modelling is important for the stable operation of PPD-SPS. The commonly used salient-pole SG and a type DC1A EXS are applied in the PGU of the proposed SPS. The SG *dq* model with the *d*-axis aligned in the direction of the magnetic field is illustrated. In addition, the expressions for the *dq* reactance, transient reactance and sub-transient reactance are also presented. The DFIM *dq* model is illustrated briefly with the *d*-axis oriented in the direction of the stator voltage vector, which is the most widely used orientation method. The voltage, flux, and motion equations are given to summarize the overall electrical and mechanical characteristics of DFIM. Besides, the descriptions for the subsynchronous, synchronous, and supersynchronous operation modes when DFIM is applied either as a motor or generator are presented, and the corresponding relationships with the slip are shown. In addition, the modelling of BTBPC is carried out by presenting the detailed and average models with the main focus on the switching behaviours and system-level features, respectively. The overall power loss model of BTBPC is also illustrated in detail. Furthermore, the models of three main categories of energy storage devices are presented, including battery, SC and FC. The SC banks are chosen as the energy storage devices in the proposed work as it has high power density for compensating the power imbalance in transient states, which are to be clearly simulated and discussed in the following chapters.

Chapter 4 Control of A Partially Power Decoupled AC-DC Hybrid Shipboard Power System

This chapter aims to illustrate the control strategies for the synchronous generator (SG), doubly-fed induction machine (DFIM), back-to-back power converter (BTBPC), and super-capacitor (SC) in the proposed partially power decoupled shipboard power system (PPD-SPS). The power is supplied by an SG, and good synchronous angle tracking performance of phase-locked loop (PLL) is to be obtained by careful PLL controller parameter setup [28]. If the PLL controller parameter setup is not appropriate, the SPS may not operate by following the command values, resulting in system instability. The stator flux oriented vector control (SFO-VC) method is commonly used for the case without grid voltage orientation by applying PLL, but its decoupling performance depends on the accuracy of flux estimation. As the stator resistance is much smaller than the stator reactance in practice, an emulated stator voltage orientated vector control (ESVO-VC) strategy that does not employ PLL can be applied for PPD-SPS. On top of that, the transfer function of the input voltage to the field voltage of the SG excitation system (EXS) is obtained, and its stability is analysed referring to the changes in the regulator and exciter gains. Furthermore, an ESS established by parallel SCs and a DC-DC buck/boost converter is presented to eliminate the active power imbalance between the power generation unit (PGU) and propulsion load during sailing, enabling the PPD-SPS to operate smoothly. The performance of the proposed PPD-SPS is evaluated for both the cases adopting ESVO-VC and SFO-VC schemes. Frequent propulsion load variations are taken into consideration to verify that the proposed control strategy can work properly under different operation modes of SPS.

4.1 Control of PGU

The PGU consists of an SG and the corresponding EXS for field voltage control. The SG stator voltage is regulated by an excitation system to provide the field voltage V_f. In addition to V_s, a reference voltage V^* and a stabilizing voltage V_{stab} are used as the input variables. The field voltage is produced by the exciter. Moreover, a stabilizer is added to feed the field voltage component back. The transfer functions for the regulator, exciter and stabilizer in the EXS are expressed as:

$$G_{regulator} = K_a / (T_a s + 1) \tag{4-1}$$

$$G_{exciter} = K_e / (T_e s + 1) \tag{4-2}$$

$$G_{stabilizer} = K_f s / (T_f s + 1) \tag{4-3}$$

The EXS voltage control block diagram is shown in Fig. 4.1.

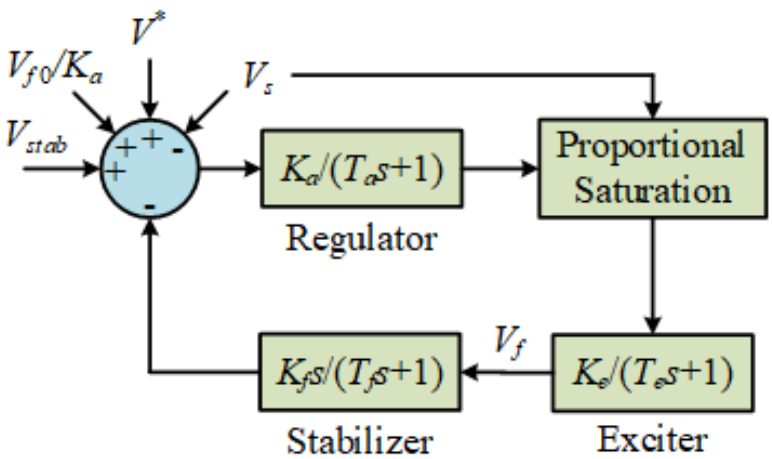

Fig. 4.1. EXS voltage control block diagram.

In order to conveniently express the transfer function $G(s)$ of the input voltage to the field voltage, the input voltage is defined as:

$$V_{in} = V^{*} + \frac{V_{f0}}{K_a} + V_{stab} - V_s \tag{4-4}$$

where V^* is the reference voltage; V_{f0} is the initial field voltage; V_{stab} is the stabilizing voltage; V_s is the terminal voltage; and K_a is the regulator gain.

According to Fig. 4.1, the relationship between V_f and V_{in} can be expressed as:

$$V_f = (V_{in} - \frac{K_f s}{T_f s + 1} V_f) \frac{K_a K_e}{(T_a s + 1)(T_e s + 1)} \tag{4-5}$$

where K_e, K_f are the exciter and feedback gains; T_a, T_e and T_f are the regulator, exciter and feedback time constants, respectively.

Therefore, the transfer function $G(s)$ can be derived as:

$$G(s) = \frac{V_f}{V_{in}} = \frac{Xs^3 + Ys^2 + Zs + W}{As^5 + Bs^4 + Cs^3 + Ds^2 + Es + 1} \tag{4-6}$$

The time constants have the following values: $T_a = 10^{-3}$s, $T_e = 10^{-4}$s, and $T_d = 10^{-1}$s. The details of A, B, C, D, E, X, Y, Z and W are displayed in Table 4.1. Compared with the other parameters, A is small enough to be neglected. Therefore, the s^5 term in the denominator can be ignored, and (4-6) can be updated as:

$$\begin{aligned} G(s) \approx & \frac{10^{-8} K_a K_e s^3 + 1.1\times10^{-4} K_a K_e s^2 + 0.1 K_a K_e s + K_a K_e}{[2.2\times10^{-11} s^4 + (10^{-7} K_a K_e K_f + 4.122\times10^{-8}) s^3} \\ & +(1.1\times10^{-3} K_a K_e K_f + 2.1\times10^{-4}) s^2 + (K_a K_e K_f + 0.1) s + 1] \end{aligned} \tag{4-7}$$

From (4-7), $G(s)$ can be further modified by setting $K_{ae} = K_a K_e$.

$$\begin{aligned} G(s) \approx & \frac{10^{-8} K_{ae} s^3 + 1.1\times10^{-4} K_{ae} s^2 + 0.1 K_{ae} s + K_{ae}}{[2.2\times10^{-11} s^4 + (10^{-7} K_{ae} K_f + 4.122\times10^{-8}) s^3} \\ & +(1.1\times10^{-3} K_{ae} K_f + 2.1\times10^{-4}) s^2 + (K_{ae} K_f + 0.1) s + 1] \end{aligned} \tag{4-8}$$

Table 4.1. Details of the parameters in *G*(*s*)

Parameters	Values
A	$T_a^2 T_e^2 T_f = 10^{-15}$
B	$T_a T_e (T_a T_e + 2T_a T_f + 2T_e T_f) \approx 2.2\times 10^{-11}$
C	$2T_a^2 T_e + 2T_a T_e^2 + 4T_a T_e T_f + T_e^2 T_f + T_a T_e K_a K_e K_f = 10^{-7} K_a K_e K_f + 4.122\times 10^{-8}$
D	$(T_a + T_e)^2 + 2(T_a T_e + T_a T_f + T_e T_f) + (T_a + T_e) K_a K_e K_f \approx 1.1\times 10^{-3} K_a K_e K_f + 2.1\times 10^{-4}$
E	$2T_a + 2T_e + T_f + K_a K_e K_f \approx K_a K_e K_f + 0.1$
X	$T_a T_e T_f K_a K_e = 10^{-8} K_a K_e$
Y	$(T_a T_e + T_a T_f + T_e T_f) K_a K_e \approx 1.1\times 10^{-4} K_a K_e$
Z	$(T_a + T_e + T_f) K_a K_e \approx 0.1 K_a K_e$
W	$K_a K_e$

In this chapter, the feedback gain K_f is chosen as 10^{-4}, and the effect of change in K_{ae} on the transfer function is investigated. The values of 30, 300 and 3000 are selected for stability analysis. The root locus of $G(s)$ is derived as shown in Fig. 4.2.

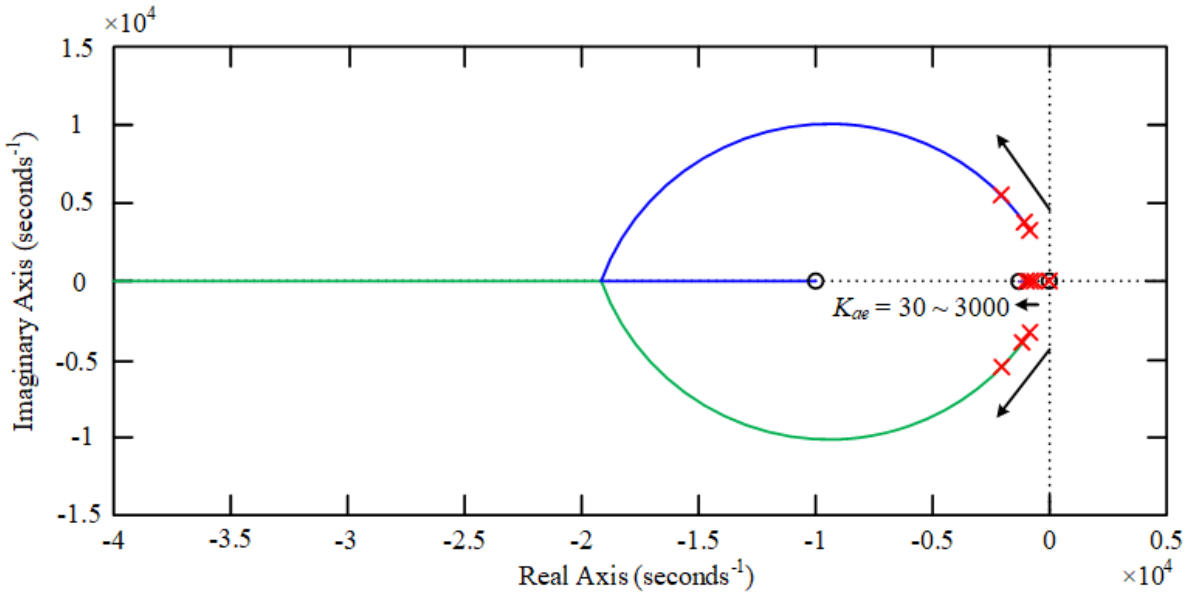

Fig. 4.2. Root locus of *G*(*s*).

According to the root locus shown in Fig. 4.2, the system is stable when the value of K_{ae} varies from 30 to 3000. The dominant poles are all on the real axis, with the values between around (-0.1) and 0. The Bode plots of $G(s)$ with different values of K_{ae} are depicted in Fig. 4.3.

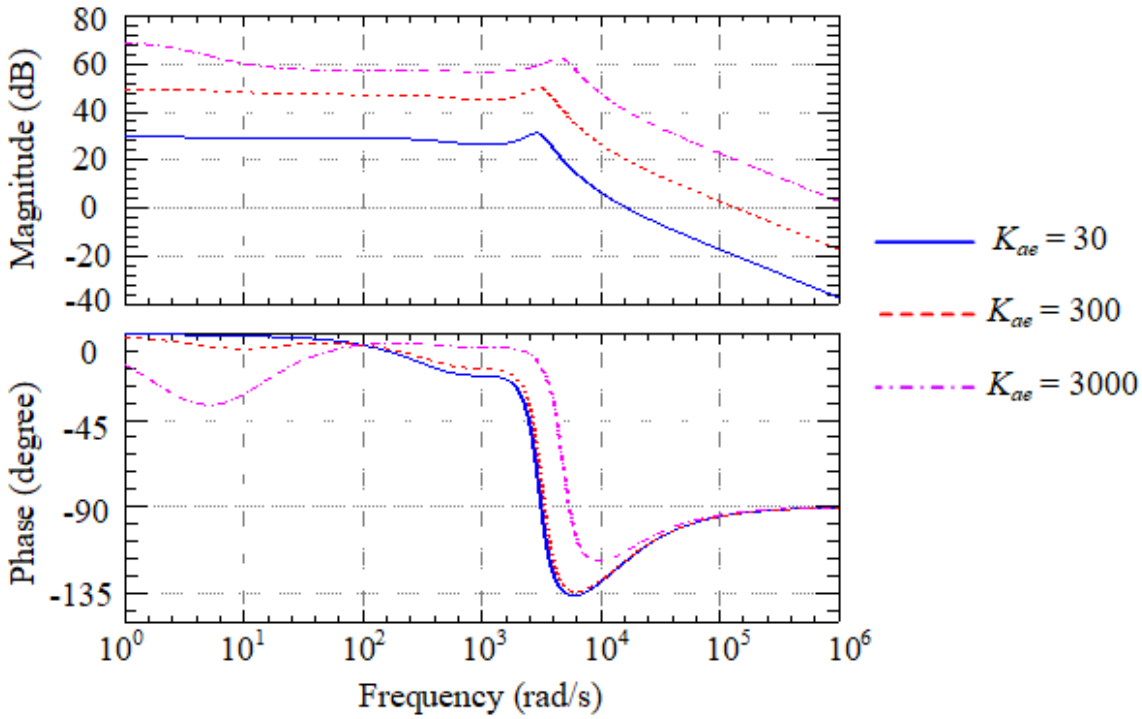

Fig. 4.3. Magnitude and phase responses of *G*(*s*).

It can be seen from the magnitude response that the magnitude starts to decrease between 10^3rad/s and 10^4rad/s for each case, and it approaches zero at around 10^4rad/s, 10^5rad/s, and 10^6rad/s for K_{ae} = 30, 300 and 3000, respectively. For the phase response, with the increase in K_{ae}, the phase drop in the low frequency region becomes deeper, which makes the generator prone to instability. On the other hand, the phase value is closer to 0 between 10^3rad/s and 10^4rad/s and it recovers to (-90°) faster when K_{ae} is higher. With the overall consideration of stability margins in both low and high frequency ranges, 300 is chosen as the value for K_{ae}.

4.2 Control of PPD-SPS

The PPD-SPS can be regarded as an islanded micro-grid, and the only power source is SG. In this case, deteriorated tracking performance for the angle of source-side voltage or stator flux can be encountered if the PLL controller parameter setup is not appropriate. In this chapter, the flux angle θ_φ is directly estimated, and then 90° is added to it to derive the synchronous angle θ_s. If the stator resistance is small enough to be neglected, then the tracking performance is good enough. The control block diagram based on the proposed ESVO-VC for PPD-SPS is displayed in Fig. 4.4.

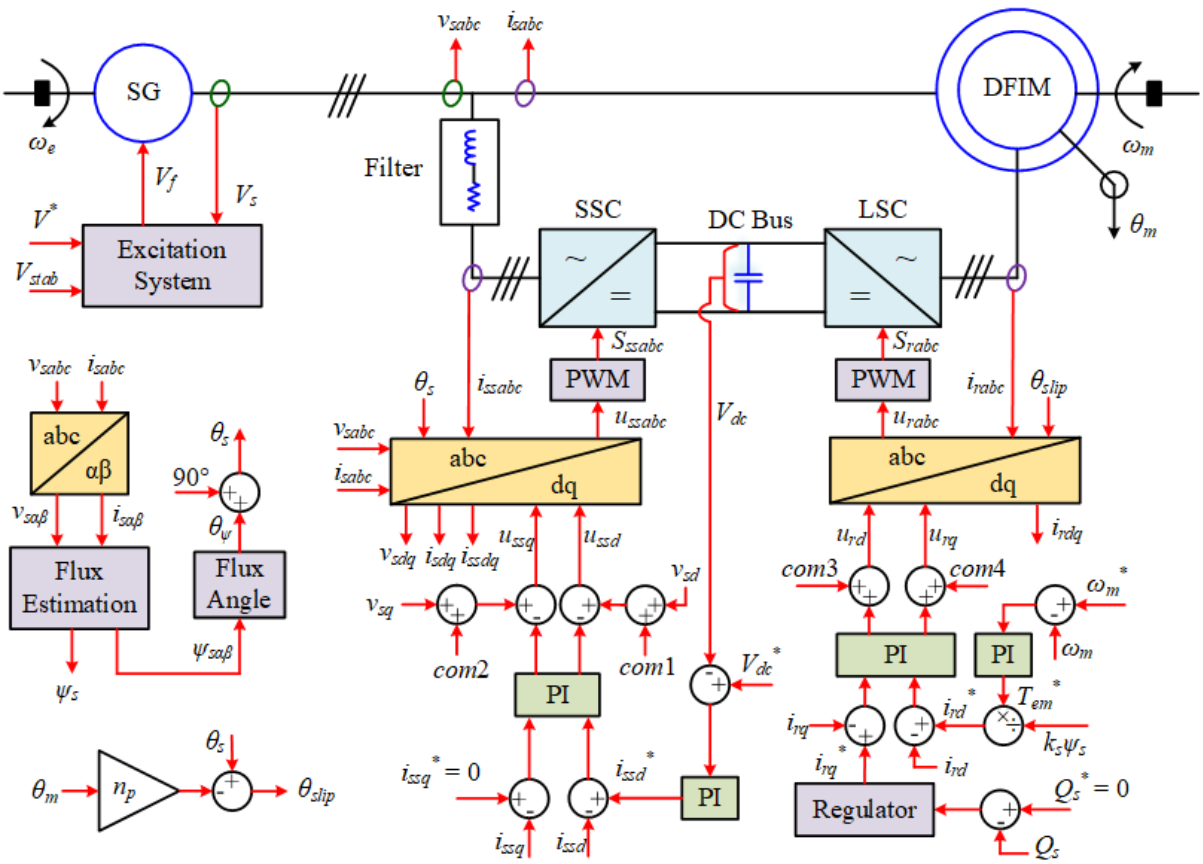

Fig. 4.4. ESVO-VC for PPD-SPS.

The control of SSC and that of LSC are decoupled by the DC-link capacitor on the DC bus. In the SSC control process, the *d*-axis source-side reference current component i_{ssd}^* is derived by regulating the DC-bus voltage V_{dc}. The SSC control aims to keep V_{dc} constant. In addition, the

value of q-axis source-side reference current component i_{ssq}^* is set as 0 to obtain a unity power factor. Besides, the quality of SSC currents is dependent on the current control performance. The dq voltage equations at the source side are expressed as:

$$\begin{cases} v_{ssd} = v_{sd} - R_{ss} i_{ssd} - L_{ss} \dfrac{di_{ssd}}{dt} + \omega_e L_{ss} i_{ssq} \\ v_{ssq} = v_{sq} - R_{ss} i_{ssq} - L_{ss} \dfrac{di_{ssq}}{dt} - \omega_e L_{ss} i_{ssd} \end{cases} \tag{4-9}$$

According to (4-9), the source-side compensating terms $com1$ and $com2$ can be derived as:

$$\begin{cases} com1 = -R_{ss} i_{ssd} + \omega_e L_{ss} i_{ssq} \\ com2 = -R_{ss} i_{ssq} - \omega_e L_{ss} i_{ssd} \end{cases} \tag{4-10}$$

For LSC, the d-axis rotor current component i_{rd} is controlled to regulate the electromagnetic torque T_{em}, thus controlling the stator active power P_s and the rotor speed ω_m. On the other hand, the q-axis rotor reference current component i_{rq}^* is achieved by regulating the stator reactive power Q_s, and the control of i_{rq} is related to the control of air-gap field, which ultimately affects the reactive power output. Similar to (4-9), the rotor-side dq voltage equations are obtained as:

$$\begin{cases} v_{rd} = R_r i_{rd} + \sigma L_r \dfrac{di_{rd}}{dt} - \omega_{slip} \psi_{rq} \\ v_{rq} = R_r i_{rq} + \sigma L_r \dfrac{di_{rq}}{dt} + \omega_{slip} \psi_{rd} \end{cases} \tag{4-11}$$

where σ is the leakage flux factor ($\sigma = 1 - [L_m L_m/(L_r L_s)]$); ω_{slip} is the slip angular speed, and it is calculated by:

$$\omega_{slip} = \omega_e - \omega_r \tag{4-12}$$

Different from the source side, mutual effects exist between the stator and rotor of DFIM, and the expressions of ψ_{rd} and ψ_{rq} are not directly available from the rotor-side parameters and variables. Instead, the mutual components produced by the stator flux should be taken into consideration. When the d-axis of synchronous reference frame is in the same direction as that of the stator voltage vector, ψ_{rd} and ψ_{rq} can be obtained as:

$$\begin{cases} \psi_{rd} = \sigma L_r i_{rd} \\ \psi_{rq} = -\dfrac{k_s}{\omega_e} + \sigma L_r i_{rq} \end{cases} \tag{4-13}$$

where $k_s = L_m/L_s$ is the stator coupling factor.

Substitute (4-13) into (4-11), the rotor voltage equations can be updated as:

$$\begin{cases} v_{rd} = R_r i_{rd} + \sigma L_r \dfrac{di_{rd}}{dt} - \omega_{slip}(-\dfrac{k_s}{\omega_e} + \sigma L_r i_{rq}) \\ v_{rq} = R_r i_{rq} + \sigma L_r \dfrac{di_{rq}}{dt} + \omega_{slip}\sigma L_r i_{rd} \end{cases} \tag{4-14}$$

The rotor-side compensating terms $com3$ and $com4$ are:

$$\begin{cases} com3 = R_r i_{rd} - \omega_{slip}(-\dfrac{k_s}{\omega_e} + \sigma L_r i_{rq}) \\ com4 = R_r i_{rq} + \omega_{slip}\sigma L_r i_{rd} \end{cases} \tag{4-15}$$

Alternatively, the control strategy for DFIM also can be adopted as SFO-VC. In this case, the orientation of the dq frame is based on the direction of the stator flux. The control block diagram for PPD-SPS with SFO-VC is displayed in Fig. 4.5.

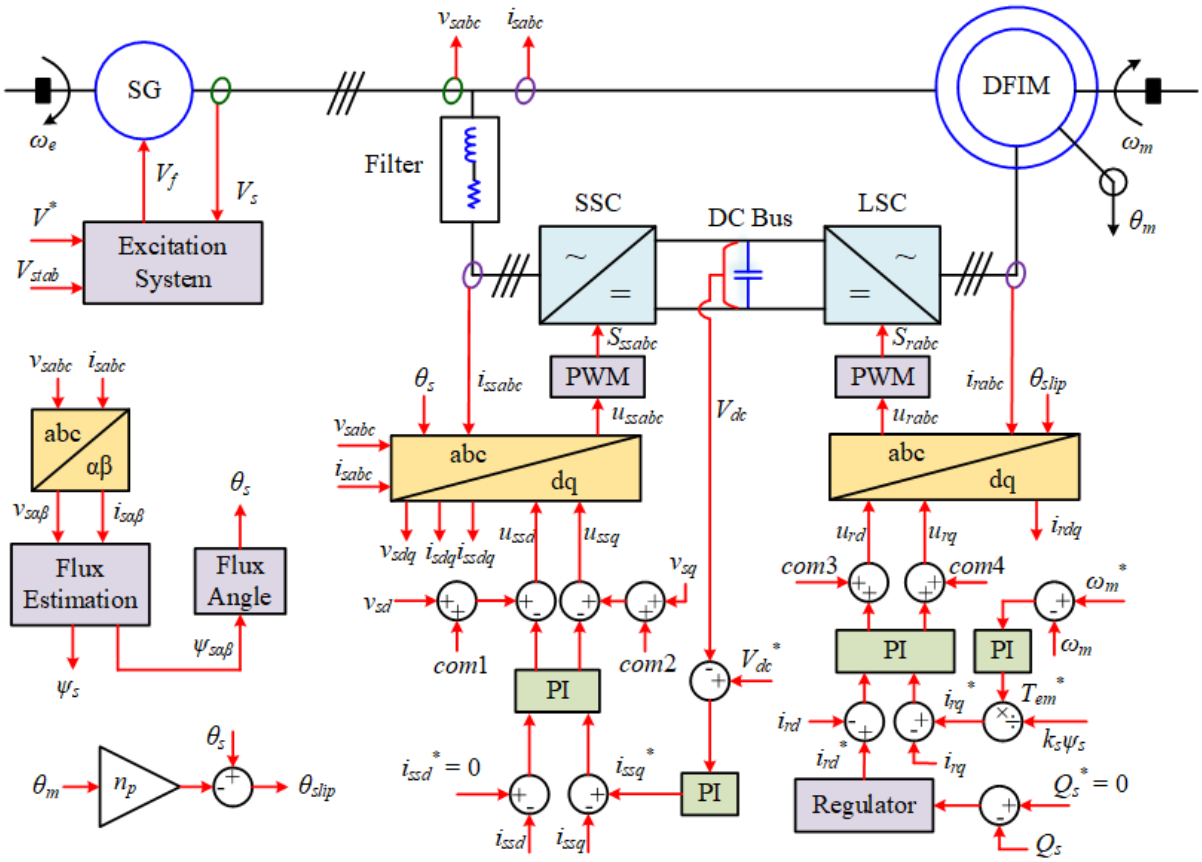

Fig. 4.5. SFO-VC for PPD-SPS.

4.3 Control of SC Bank

The SC bank is connected to the DC bus via a DC-DC buck/boost converter. Two power switches are included in the bridge arm of this DC-DC converter, and their duty ratios are controlled separately in the buck and boost operation modes. The operation mode of DC-DC converter and the behaviour of SC bank can be determined according to Table 4.2 when the DFIM operates in different modes.

Table 4.2. DC-DC converter and SC bank behaviour determination

DFIM	Situation	DC-DC Converter	SC Bank
Subsynchronous	$P_r > P_{ss}$	Boost	Supply Power
	$P_r < P_{ss}$	Buck	Absorb Power
Supersynchronous	$P_r > P_{ss}$	Buck	Absorb Power

$P_r < P_{ss}$	Boost	Supply Power

The positive power flow direction is from SSC to LSC, which corresponds to that in the supersynchronous mode for the case where the DFIM operates as a motor, and the active power required from SC bank is defined as P_{req}.

$$P_{req} = P_r - P_{ss} \tag{4-16}$$

Then, as the signs of power flows are considered in the calculation process, the determination of the DC-DC converter and SC bank behaviours is not restricted by the operation mode of DFIM, and Table 4.2 can be updated as Table 4.3.

Table 4.3. Updated version of Table 4.2 by introducing P_{req}

P_{req}	DC-DC Converter	SC Bank
> 0	Boost	Supply Power
< 0	Buck	Absorb Power

In the control process, proportional-integral (PI) controllers are applied for controlling the current through the SC inductor L_{SC}. The pulse width modulation (PWM) signal is produced from a PWM generator. When the converter operates in the buck mode, the duty ratio of the upper switch is controlled to absorb active power. In contrast, when the converter operates in the boost mode, the duty ratio of the lower switch is controlled to supply active power. The control block diagram for the SC bank is shown in Fig. 4.6.

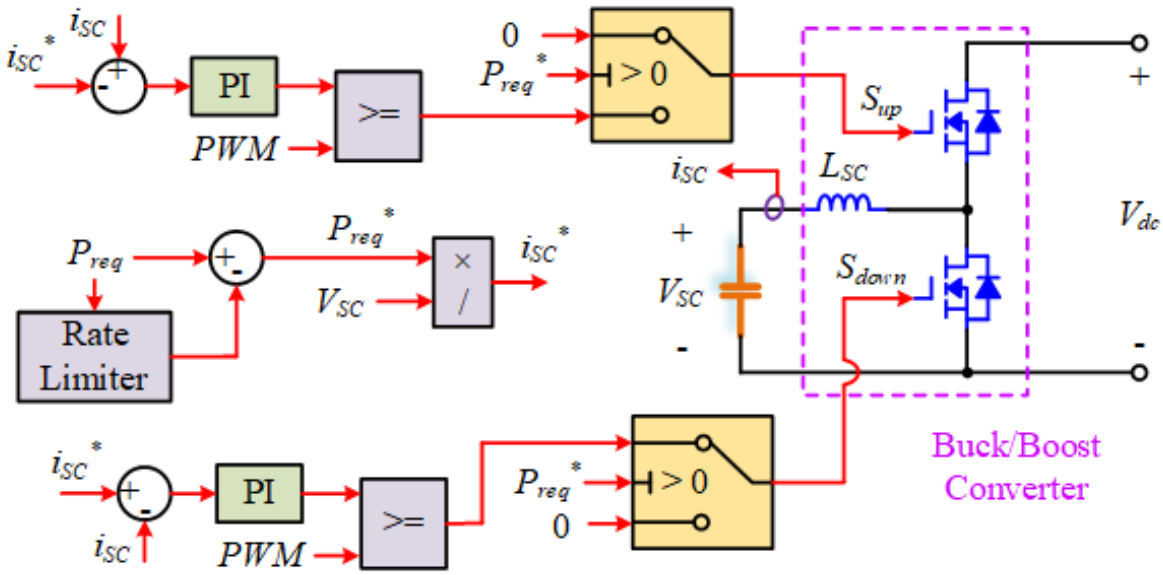

Fig. 4.6. Control of the buck/boost converter of SC bank.

4.4 Simulation Study

4.4.1 Simulation Setup

The operation of the proposed PPD-SPS is verified in Matlab/Simulink2017a. The system operation with the proposed ESVO-VC scheme is compared with that using the traditional SFO-VC strategy. In the simulation study, the propulsion load variation is taken into consideration (0 ~ 1s: T_L = 1pu; 1 ~ 3s: T_L = 0.8pu; 3 ~ 5s: T_L = 1.2pu). The sampling time of simulation is set as 5μs. The parameters used for SG and DFIM are listed in the Appendix.

4.4.2 Simulation Results

With the control scheme for SG illustrated in the previous section, the SG can continuously supply power to the propulsion subsystem. The SG stator voltages and currents are displayed in Fig. 4.7, and the output power is displayed in Fig. 4.8.

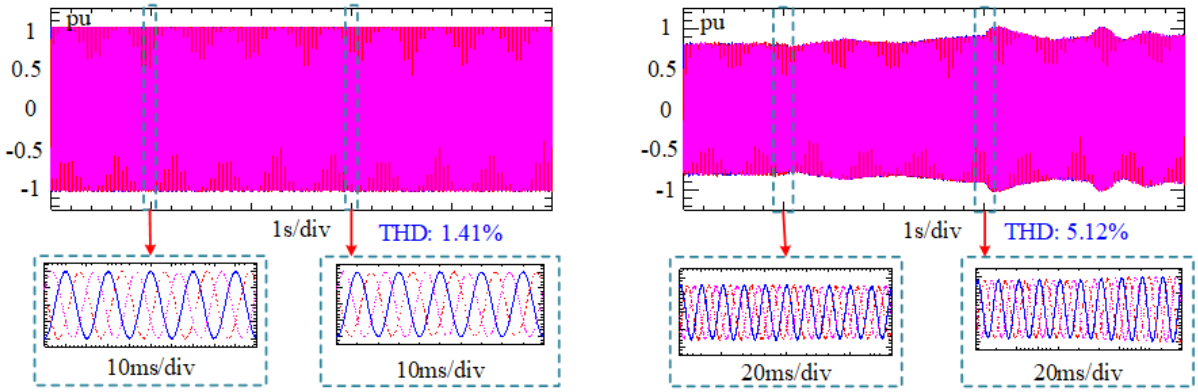

(a) PPD-SPS with ESVO-VC

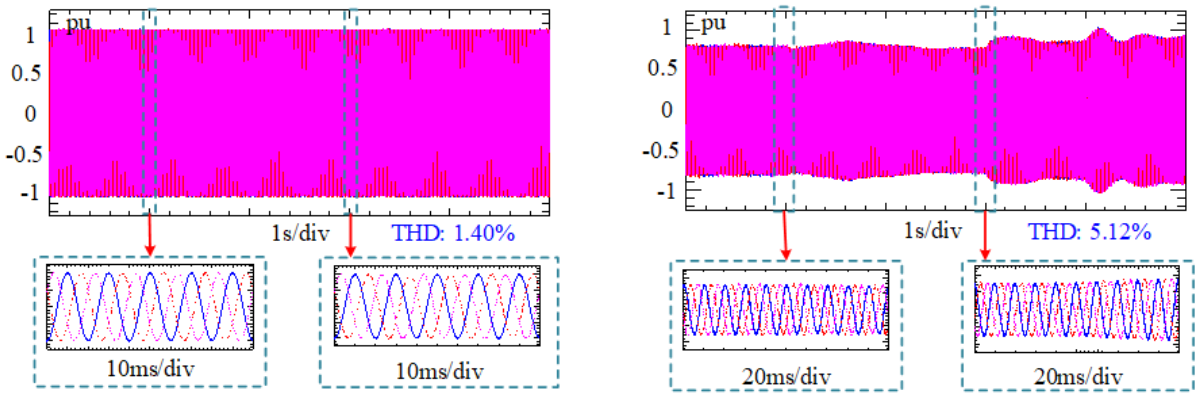

(b) PPD-SPS with SFO-VC

Fig. 4.7. SG stator voltages V_{SG} (left) and currents I_{SG} (right).

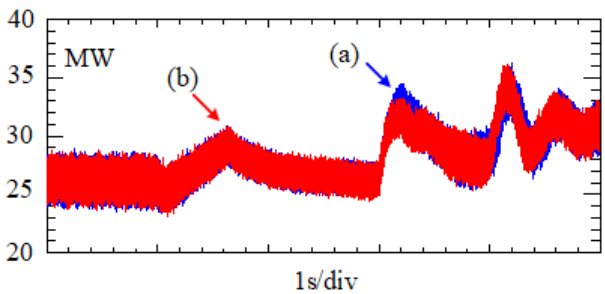

Fig. 4.8. SG power generation P_{SG} for PPD-SPS (a) with ESVO-VC; (b) with SFO-VC.

From Fig. 4.7, it can be seen that the stable operation of SG is achieved with almost sinusoidal three-phase stator voltage waveforms for both scenarios, and the three-phase SG currents can track the load changes at 1s and 3s. In addition, it can be seen that the total harmonic distortions (THDs) for the SG stator voltages in both cases are at the same level, which are 1.41% and 1.40%, respectively. On the other hand, the THDs for the SG stator currents are both 5.12%.

Therefore, the performance of the power generation unit is hardly affected by using different vector control methods at the load side.

The change in the generated power from the SG follows the load variation for each case, as can be seen in Fig. 4.8. At the instants of load variations, obvious fluctuations are observed, and the overall degrees of fluctuations of SG power generation are the same for both cases.

The performance of SSC is verified by illustrating the stator and SSC three-phase AC currents and the DC-bus voltage for the DFIM cases, and the corresponding waveforms are displayed in Figs. 4.9 and 4.10 for the two cases.

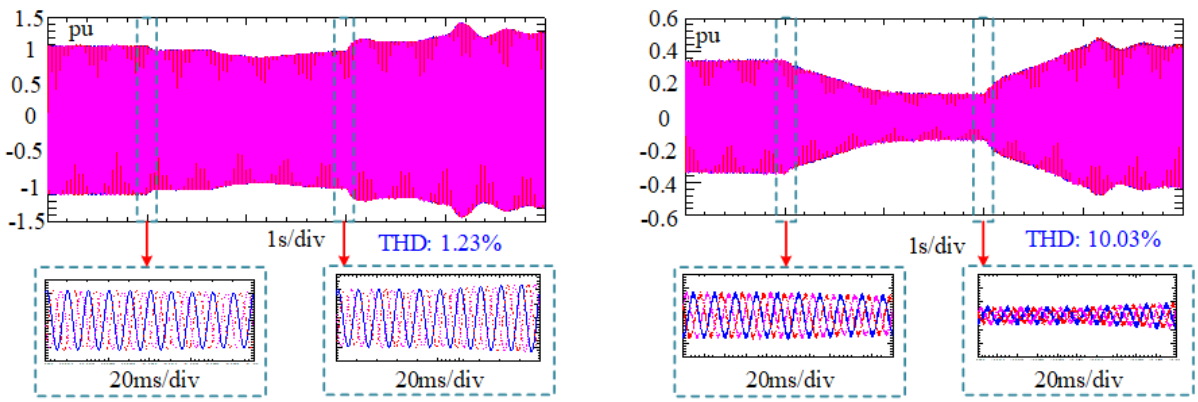

(a) PPD-SPS with ESVO-VC

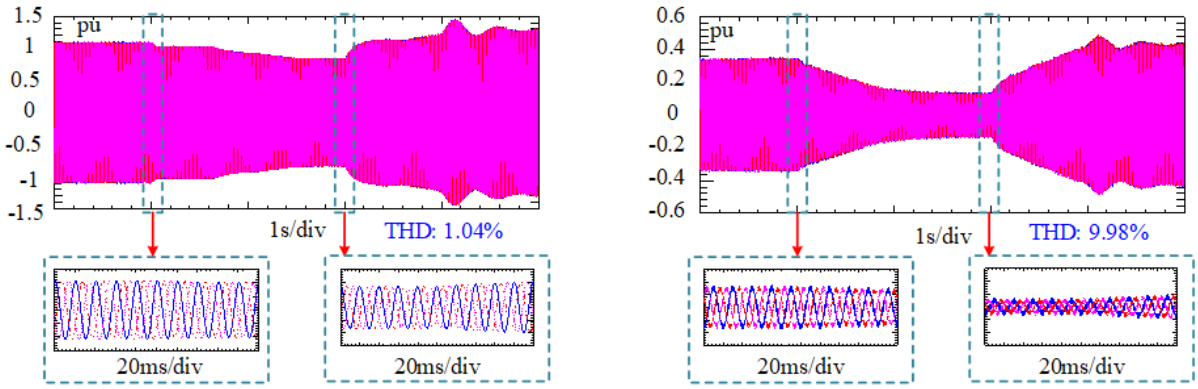

(b) PPD-SPS with SFO-VC

Fig. 4.9. The DFIM stator currents I_s (left) and SSC currents I_{ss} (right)

From Fig. 4.9, the waveform quality of DFIM stator-side three-phase currents by applying SFO-VC (THD: 1.04%) is slightly better than that in the ESVO-VC case (THD: 1.23%). This

is because the stator resistance of DFIM exists in the simulation process, which deteriorates the decoupling performance of the stator currents when applying the proposed ESVO-VC. However, for the SSC currents, almost identical tracking performances are obtained for both cases, and a slightly lower THD level (THD: 9.98%) is presented for the SFO-VC case when comparing with the case of applying ESVO-VC (THD: 10.03%). These results indicate that identical control performances of SSC are achieved by applying both control methods. Therefore, the proposed ESVO-VC is also applicable for controlling the proposed PPD-SPS to achieve normal operation.

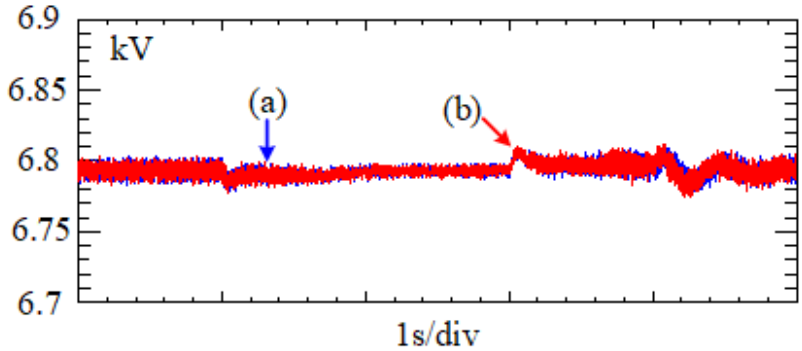

Fig. 4.10. The DC-bus voltage V_{dc} for PPD-SPS (a) with ESVO VC; (b) with SFO-VC.

The DC-bus voltage V_{dc} should be regulated to maintain at a constant value to provide a stable DC voltage supply for the LSC, thus achieving good DFIM control performance. As the SSC current regulation performances for the two cases are almost identical, it can be inferred that identical voltage regulation performances will be achieved. From Fig. 4.10, it can be seen that the DC-bus voltage values in both cases are maintained around a certain value with minor fluctuations in the steady state, which validates good voltage regulation performances for both cases.

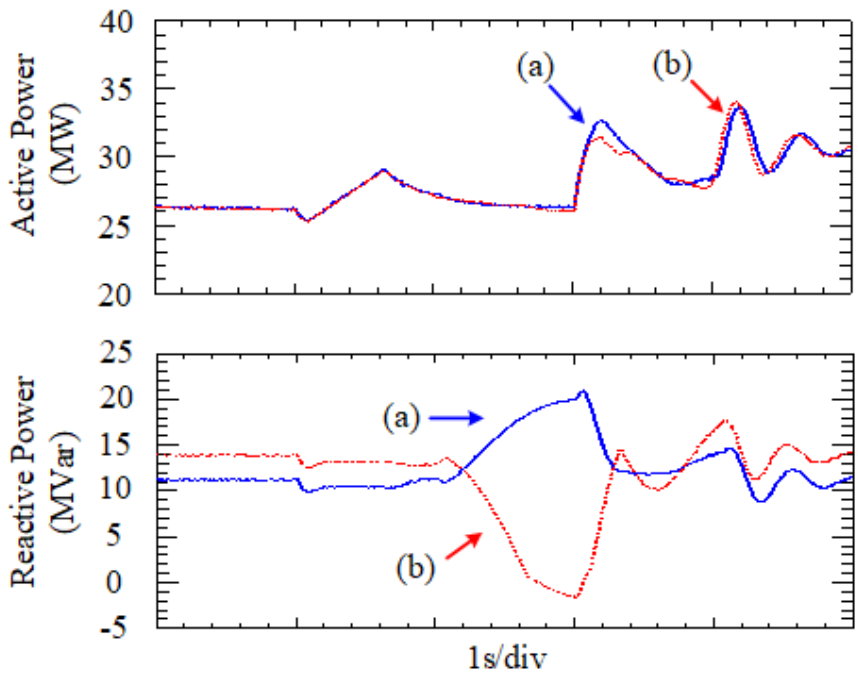

Fig. 4.11. Active and reactive powers P_t & Q_t for PPD-SPS (a) with ESVO-VC; (b) with SFO-VC.

The active and reactive powers delivered to the power loads are illustrated in Fig. 4.11 for the three cases, and the corresponding waveforms for power factor are shown in Fig. 4.12.

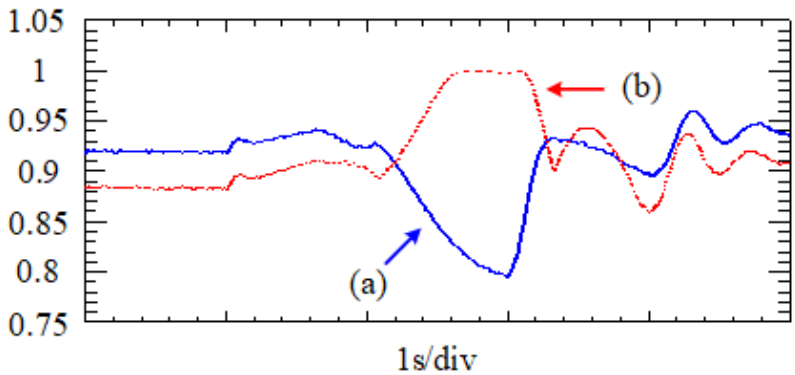

Fig. 4.12. Power factor *PF* for PPD-SPS (a) with ESVO-VC; (b) with SFO-VC.

From Fig. 4.11, the active power supplied to DFIM is almost the average value of the power generated by SG for each scenario at each sampling point due to the filtering effect introduced by the inductance in the power circuit. The main difference is encountered in the reactive power Q_t and thus the power factor *PF* for these two cases. It can be seen that the reactive power for

the ESVO-VC case is lower than that for the SFO-VC case when the load torque is large, while higher reactive power (lower power factor) is presented for the ESVO-VC case during the period of low load torque. It is to be noticed that the power factor can be different when using different system parameters, and the results obtained in Figs. 4.11 and 4.12 are only applicable for the chosen system parameters in this thesis.

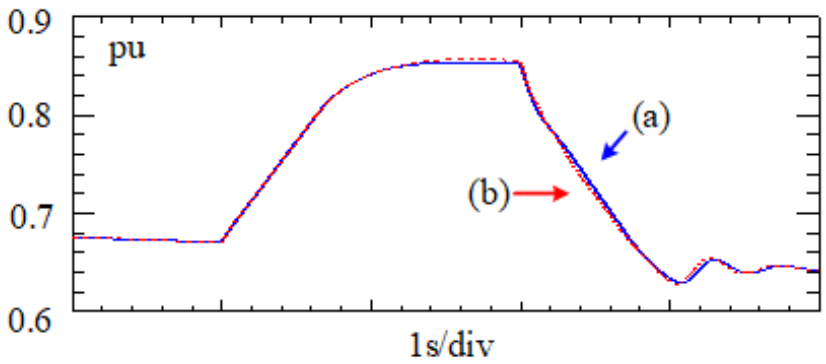

Fig. 4.13. Rotor speed ω_m for PPD-SPS (a) with ESVO-VC; (b) with SFO-VC.

It can be seen from Fig. 4.13 that the rotor speeds in the two cases have almost identical waveforms, and they track the load changes well to balance the power input and output. Furthermore, according to Fig. 4.14, the electromagnetic torques in both cases can track the changes in the load torque. Some delays in achieving the stable values are observed after the instants of load changes, since the inertia constant of DFIM is comparable to the time period of load change.

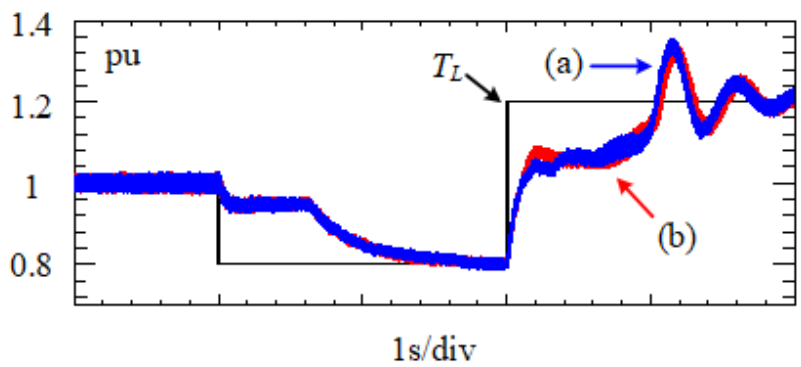

Fig. 4.14. Electromagnetic torque T_{em} for PPD-SPS (a) with ESVO-VC; (b) PPD-SPS with SFO-VC.

According to the simulation results, effective slip power control can be obtained by using the proposed ESVO-VC scheme, and good system performance in terms of the SG stator power control and DFIM torque control is obtained by comparison with the case of applying SFO-VC. Therefore, in order to eliminate the possible negative effects caused by inappropriate PLL controller gain setup, the proposed ESVO-VC is a promising alternative to the traditional SFO-VC, under the circumstance of negligible stator resistance.

Furthermore, in order to complement the active power required by the load side, 50 SCs with the capacitance of 50F and rated voltage of 6.8kV are connected in parallel to function as the ESS. The initial state of charge (SoC) for each SC is around 49.4%. With the aforementioned propulsion load profile (0 ~ 1s: T_L = 1pu; 1 ~ 3s: T_L = 0.8pu; 3 ~ 5s: T_L = 1.2pu), the active power required from the propulsion load and that supplied from the SC bank are shown in Fig. 4.15, and the SoC of SC bank is displayed in Fig. 4.16. The proposed ESVO-VC scheme is applied in this case.

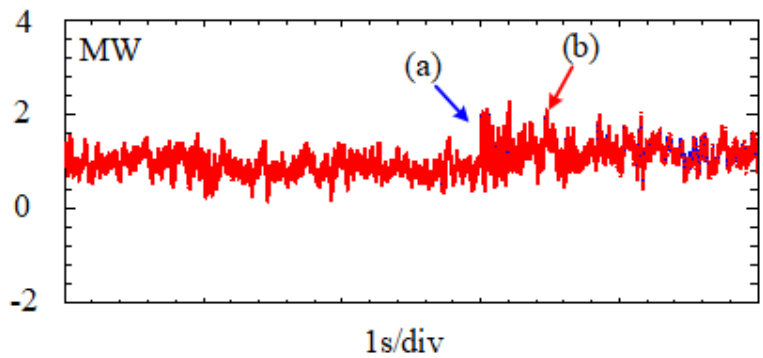

Fig. 4.15. The active power (a) required by the propulsion load (blue solid line); (b) supplied by the SC bank (read dash line).

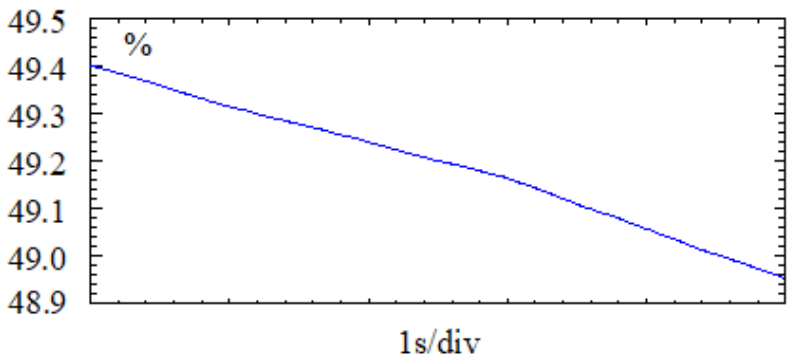

Fig. 4.16. SoC of SC bank.

It can be seen that the active power supplied from energy storage can complement that required by the load, and at the same time, the SoC keeps decreasing, indicating the discharge process of the SC bank.

4.5 Summary

The control methods of SG, DFIM, BTBPC and SC bank are presented in this chapter. In addition, the transfer function of the input voltage to the field voltage of the SG excitation system is derived, and the root locus and bode diagrams are analysed. Moreover, the ESVO-VC strategy without using PLL is illustrated to control the PPD-SPS propulsion subsystem in the working condition with frequent load changes. Almost identical performances can be obtained for the proposed ESVO-VC and the traditional SFO-VC, and the proposed ESVO-VC can be used as a promising alternative when the issue of inappropriate PPL controller gain tuning is to be avoided. Furthermore, the implementation of SC bank as the ESS complements the power insufficiency at the propulsion load. According to the simulation results, the following points can be obtained:

1) Effective slip power regulation can be obtained by using the proposed ESVO-VC strategy.

2) Good SG stator power control performances are derived for both the ESVO-VC and SFO-VC cases.

3) The three-phase voltage and current waveforms achieved by employing the ESVO-VC strategy have high quality.

4) The speed control performance is good enough for the investigated working condition and the electromagnetic torque can precisely track the mechanical load torque change.

Overall, by applying the proposed ESVO-VC strategy for PPD-SPS, cost effective shipboard energy management is obtained even if frequent load variations are presented.

Chapter 5 Small-Signal Modelling for Internal Voltage Vector Phase-Amplitude Dynamics Analysis of A Partially Power Decoupled AC-DC Hybrid Shipboard Power System

For system-level analysis, the power components such as electrical machines and power converters can be regarded as internal voltage vectors. This chapter presents the small-signal modelling of the ship propulsion subsystem of a partially power decoupled shipboard power system (PPD-SPS) for internal voltage vector phase-amplitude dynamics study in the electromechanical control timescale, which reveals the interactions between the electrical and mechanical behaviours of PPD-SPS. The controller parameters of the relevant control loops including rotor speed control, reactive power control and phase-locked loop (PLL) are taken into consideration when evaluating the system performance in the electromechanical control timescale. Firstly, the average model of back-to-back power converter (BTBPC) in PPD-SPS is used for system-level dynamic study, which reduces the simulation time and is easier for physical understanding. The stator and BTBPC of doubly-fed induction machine (DFIM) are regarded as separate models that are represented by an internal voltage vector and controlled voltage sources, respectively. Secondly, by regarding the DFIM stator and source-side converter (SSC) as a synthetic internal voltage vector (SIVV), a small-signal model of PPD-SPS propulsion subsystem is established in the electromechanical control timescale to illustrate the SIVV phase-amplitude dynamics. The external characteristics of DFIM are described by the internal voltage motion equation, which is similar to the swing equation [58]. Based on this concept, the transfer function of the torque difference to SIVV phase and that from the reactive

power difference to SIVV amplitude are derived in the small-signal model. The voltage phase and amplitude dynamics are studied in the electromechanical control timescale by analysing the effects of PLL, rotor speed control and reactive power control to describe the system operation mechanism. Additionally, an emulated stator voltage oriented vector control (ESVO-VC) is proposed to avoid tuning the PLL controller gains, and it greatly simplifies the expression of the equivalent inertia of PPD-SPS propulsion subsystem small-signal model in the electromechanical control timescale.

5.1 Multi-Timescale Control Loops for PPD-SPS

The SG and DFIM are regarded as the source and load of PPD-SPS, and they need to be properly controlled to maintain the power balance of the system, thus ensuring the stable system operation. In a PPD-SPS, there are multiple control loops, which have different control timescales, as shown in Fig. 5.1.

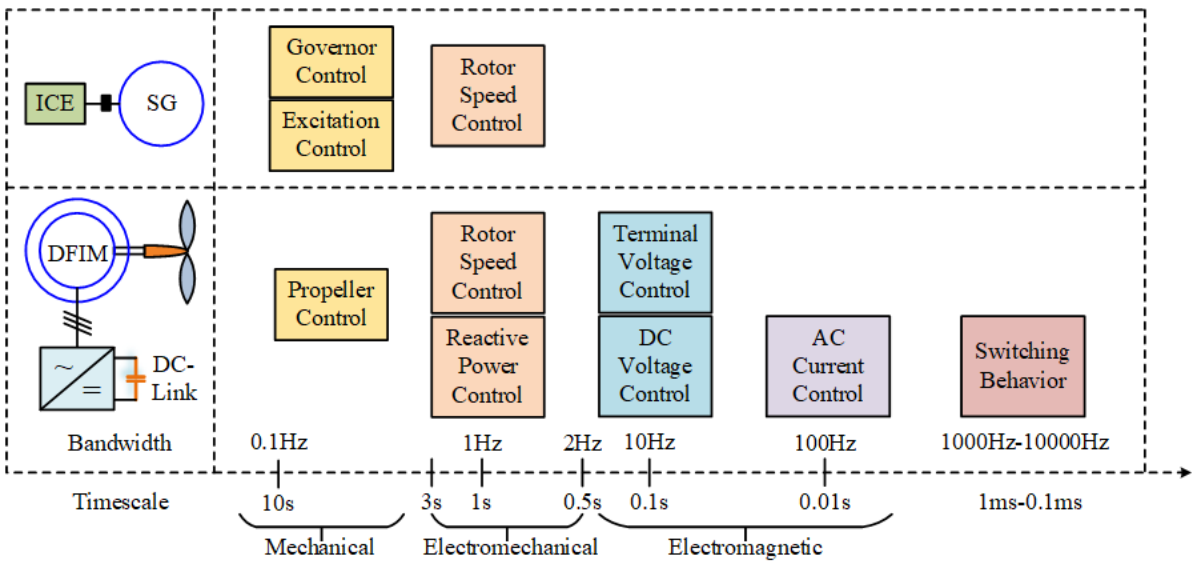

Fig. 5.1. Control loops of PPD-SPS with multiple control timescales.

As can be seen from Fig. 5.1, there are two main components to be controlled, which are the SG driven by an internal combustion engine, and the DFIM loaded by a propeller. The system-level analysis can be carried out mainly in three control timescales, which are the mechanical, electromechanical and electromagnetic control timescales. However, the high switching speed for power converters greatly prolongs the simulation time if the detailed power converter model is applied. Therefore, with the purpose of conducting system-level studies, where the details of switching behaviours are not required, the average model of BTBPC is used in PPD-SPS to shorten the simulation time. For the power source, the governor and excitation controls are typically in the mechanical control timescale, which represents a large time constant of seconds. In terms of the propulsion load, the propeller control is accomplished in the mechanical control timescale. These modules respond slowly, and they can be assumed to operate in steady states when referring to the electromechanical control timescale. On the other hand, the DC-bus voltage is to be kept at a constant value by using the SSC, whose response time is around 0.1s. Moreover, the current control loop responds faster, which has a bandwidth of around 100Hz. These responses are too fast, so that they do not affect the concerned interactions between the power source and load in this study. In this chapter, the rotor speed control and reactive power control that are in the electromechanical control timescale are the main focus, and they play the most important role in assessing the system dynamics of PPD-SPS propulsion subsystem with respect to the source-load interactions. Since around 80% of the on-board power is supplied to propulsion loads [145], service loads are not taken into consideration in this chapter. The effects of cables are also neglected as the distance between the power source and load is much shorter than that of an onshore grid. Therefore, only the effects of SG, BTBPC, and DFIM on system performance are taken into consideration.

When studying the system dynamic performance in the electromechanical control timescale, the dynamics in the other timescales are neglected, and the following assumptions are made:

1) The reference values of rotor speed and reactive power are constant. 2) The DC-bus voltage can track its reference all the time. 3) The SSC currents can track their references instantly. 4) The transient dynamics of stator flux, rotor flux, and inductor currents are neglected.

5.2 Small-Signal Modelling of PPD-SPS Propulsion Subsystem with Separate DFIM and BTBPC

A DFIM is deemed as a two-port electric machine that regulates power by two paths, the AC power path is directly connected to its stator, and the power electronic path is connected to its rotor through BTBPC. Therefore, the stator, rotor, SSC and LSC can all be regarded as voltage vectors to show their external characteristics in the PPD-SPS. The resistances in the circuit are neglected as they are small compared to the corresponding reactance counterparts. The equivalent DFIM and BTBPC circuits represented by voltage vectors are displayed in Fig. 5.2.

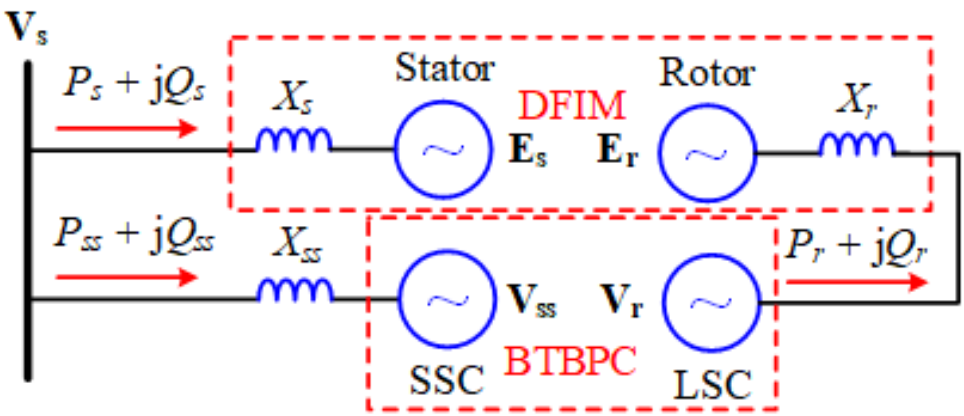

Fig. 5.2. Equivalent circuits of DFIM and BTBPC represented by voltage vectors.

As defined in [37], $\mathbf{E_s}$ is the internal voltage of DFIM, which is expressed as:

$$\mathbf{E_s} = \mathrm{j}X_m\mathbf{I_r} \tag{5-1}$$

5.2.1 Linearization of Internal Voltage Vector

As the stator of DFIM is directly connected to the power source, and the main power flow is injected to the propulsion subsystem through the stator, it is of paramount importance to investigate the phase-amplitude dynamics of $\mathbf{E_s}$.

The *dq* components of $\mathbf{E_s}$ are expressed as:

$$\begin{cases} E_{sd}{}^{p} = E_s \cos\theta_e{}^{p} = -X_m i_{rq}{}^{p} \\ E_{sq}{}^{p} = E_s \sin\theta_e{}^{p} = X_m i_{rd}{}^{p} \end{cases} \tag{5-2}$$

where θ_e is the DFIM internal voltage phase. The superscript "*p*" indicates that the *dq* components project into the *dq* reference frame defined by PLL. Taking the partial derivative of $\theta_e{}^p$ at some operation point and combine the two equations, $\Delta\theta_e{}^p$ can be derived as:

$$\Delta\theta_e{}^{p} = \frac{X_m \Delta i_{rq}{}^{p} \sin\theta_{e0}{}^{p} + X_m \Delta i_{rd}{}^{p} \cos\theta_{e0}{}^{p}}{E_{s0}} \tag{5-3}$$

At a specific operation point, the amplitude of $\mathbf{E_s}$ is expressed as E_{s0}, as shown in (5-3). In the steady state, $\theta_{e0}{}^p = -\pi/2$, so $\sin\theta_{e0}{}^p = -1$ and $\cos\theta_{e0}{}^p = 0$, and (5-3) is updated as:

$$\Delta\theta_e{}^{p} = -\frac{X_m \Delta i_{rq}{}^{p}}{E_{s0}} \tag{5-4}$$

By applying the similar process, ΔE_s can be obtained as:

$$\Delta E_s = -X_m \Delta i_{rq}{}^{p} \cos\theta_{e0}{}^{p} + X_m \Delta i_{rd}{}^{p} \sin\theta_{e0}{}^{p} \tag{5-5}$$

By applying $\sin\theta_{e0}{}^p = -1$ and $\cos\theta_{e0}{}^p = 0$, (5-5) is updated as:

$$\Delta E_s = -X_m \Delta i_{rd}{}^{p} \tag{5-6}$$

5.2.2 Linearization of rotor speed control and reactive power control

As this chapter focuses on the system dynamics of PPD-SPS in the electromechanical control timescale, the DC-bus voltage V_{dc} is assumed to be stable, thus only the control of LSC is considered. The d and q axis rotor currents are controlled respectively for controlling the electromagnetic torque T_{em} and the terminal voltage V_s, whose reference values are derived from the rotor speed and reactive power controllers, respectively, which are:

$$i_{rd}^{*} = \frac{(\omega_m - \omega_m^{*})(k_{p\omega} + k_{i\omega}/s)}{k_s \varphi_s} \tag{5-7}$$

$$i_{rq}^{*} = [(Q_t^{*} - Q_t)k_{iq}/s - V_s]k_{iv}/s \tag{5-8}$$

where $k_s = L_m/L_s$ is the stator coupling factor. The control block diagram including rotor speed control and reactive power control is displayed in Fig. 5.3.

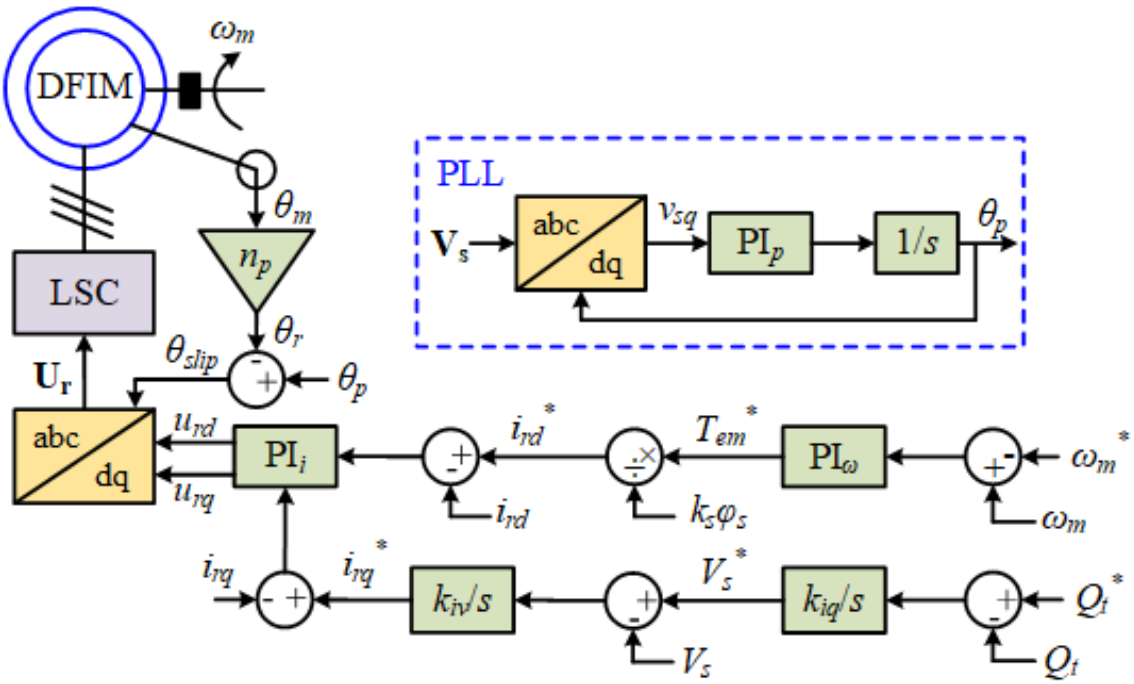

Fig. 5.3. Control block diagram including reactive power control and rotor speed control for DFIM.

The rotor speed control and reactive power control are linearized to describe the small-signal values of *dq* rotor currents.

$$\Delta i_{rd}{}^{p} = (\Delta\omega_m - \Delta\omega_m{}^{*})(k_{p\omega}' + k_{i\omega}'/s) \tag{5-9}$$

$$\Delta i_{rq}{}^{p} = (\Delta Q_t^{*} - \Delta Q_t)k_{iq}k_{iv}/s^2 \tag{5-10}$$

where $k_{p\omega}' = (k_{p\omega}/k_s\varphi_{s0})$ and $k_{i\omega}' = (k_{i\omega}/k_s\varphi_{s0})$.

5.2.3 Linearization of PLL

The output angle of PLL θ_p is obtained by implementing PI control and another integration for the *q*-axis component of $\mathbf{V_s}$.

$$\theta_p = v_{sq}(k_{pp} + k_{ip}/s)/s = V_s \sin\theta_s{}^{p}(k_{pp} + k_{ip}/s)/s \tag{5-11}$$

Linearizing it at some operation point,

$$\Delta\theta_p = V_{s0}\cos\theta_{s0}{}^{p}\Delta\theta_s{}^{p}(k_{pp}/s + k_{ip}/s^2) \tag{5-12}$$

In the steady state, the difference between synchronous angle θ_s and PLL angle θ_p is 0, thus (5-13) can be modified as:

$$\Delta\theta_p = V_{s0}\Delta\theta_s{}^{p}(k_{pp}/s + k_{ip}/s^2) \tag{5-13}$$

The internal voltage phase and amplitude dynamics can be obtained based on (5-4) to (5-6) and (5-9) to (5-13) by taking PLL, rotor speed control and reactive power control into account. As the small-signal model is established in the electromechanical control timescale, the SSC *dq* currents i_{ssd} and i_{ssq} can track their reference values, so does the terminal voltage V_s. Therefore, the small-signal model of DFIM internal voltage phase-amplitude dynamics is illustrated in

Fig. 5.4.

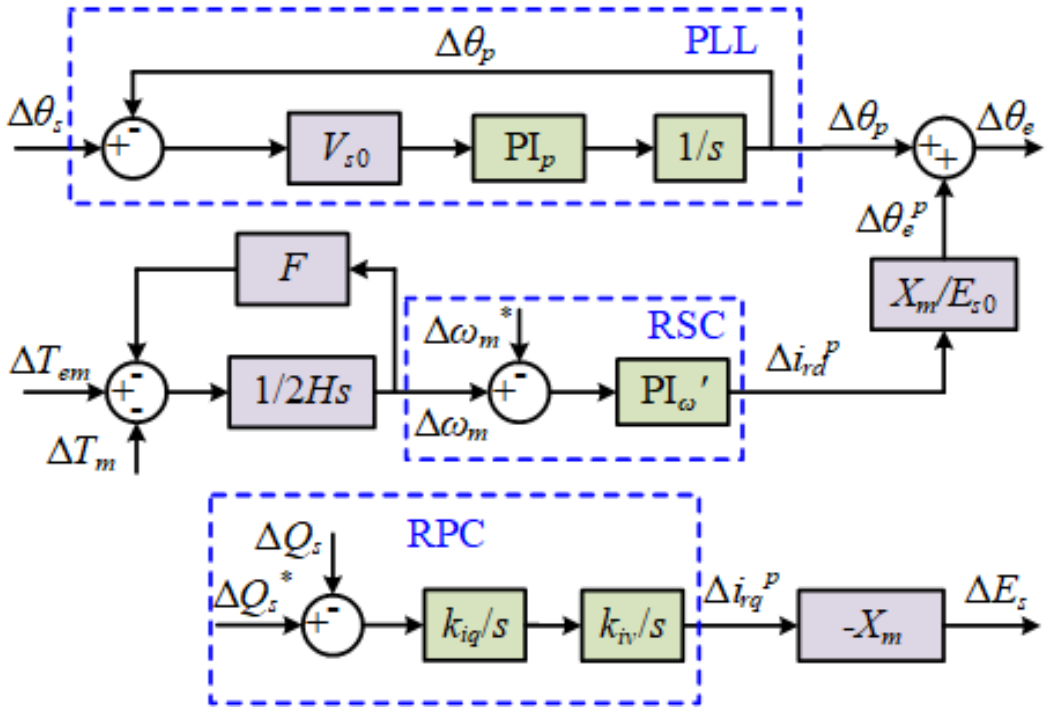

Fig. 5.4. Block diagram of small-signal model of DFIM internal voltage phase-amplitude dynamics.

5.2.4 Transfer Functions for $\Delta\theta_e$ and ΔE_s

The final step in small-signal modelling for internal voltage phase-amplitude dynamics study is to derive the transfer functions for $\Delta\theta_e$ and ΔE_s. Therefore, the synchronous angle $\Delta\theta_s$ needs to be eliminated.

The expressions of the active and reactive powers delivered to the stator of DFIM are shown below:

$$P_s = \frac{E_s V_s \sin(\theta_s - \theta_e)}{X_s} \tag{5-14}$$

$$Q_s = \frac{E_s^2 - E_s V_s \cos(\theta_s - \theta_e)}{X_s} \tag{5-15}$$

Linearizing the above two equations, and since $\theta_s = \theta_p$ at a specific operation point, the following equations are derived:

$$\begin{aligned} X_s\Delta P_s &= -V_{s0}\Delta E_s \sin\theta_{e0}{}^p - E_{s0}\Delta V_s \sin\theta_{e0}{}^p \\ &+E_{s0}V_{s0}\Delta\theta_s \cos\theta_{e0}{}^p - E_{s0}V_{s0}\Delta\theta_e \cos\theta_{e0}{}^p \end{aligned} \tag{5-16}$$

$$\begin{aligned} X_s\Delta Q_s &= 2E_{s0}\Delta E_s - V_{s0}\Delta E_s \cos\theta_{e0}{}^p - E_{s0}\Delta V_s \cos\theta_{e0}{}^p \\ &-E_{s0}V_{s0}\Delta\theta_s \sin\theta_{e0}{}^p + E_{s0}V_{s0}\Delta\theta_e \sin\theta_{e0}{}^p \end{aligned} \tag{5-17}$$

Combining (5-16) and (5-17), the synchronous angle $\Delta\theta_s$ can be replaced by the following expression:

$$\Delta\theta_s = \Delta\theta_e + \frac{2\Delta E_s \sin\theta_{e0}{}^p}{E_{s0}} + \frac{X_s\Delta P_s \cos\theta_{e0}{}^p - X_s\Delta Q_s \sin\theta_{e0}{}^p}{E_{s0}V_{s0}} \tag{5-18}$$

The simplification of (5-18) can be achieved by assuming that $\sin\theta_{e0}{}^p \approx -1$ and $\cos\theta_{e0}{}^p \approx 0$.

$$\Delta\theta_s = \Delta\theta_e - \frac{2\Delta E_s}{E_{s0}} + \frac{X_s\Delta Q_s}{E_{s0}V_{s0}} \tag{5-19}$$

Therefore, $\Delta\theta_s$ is a function of $\Delta\theta_e$, ΔE_s and ΔQ_s.

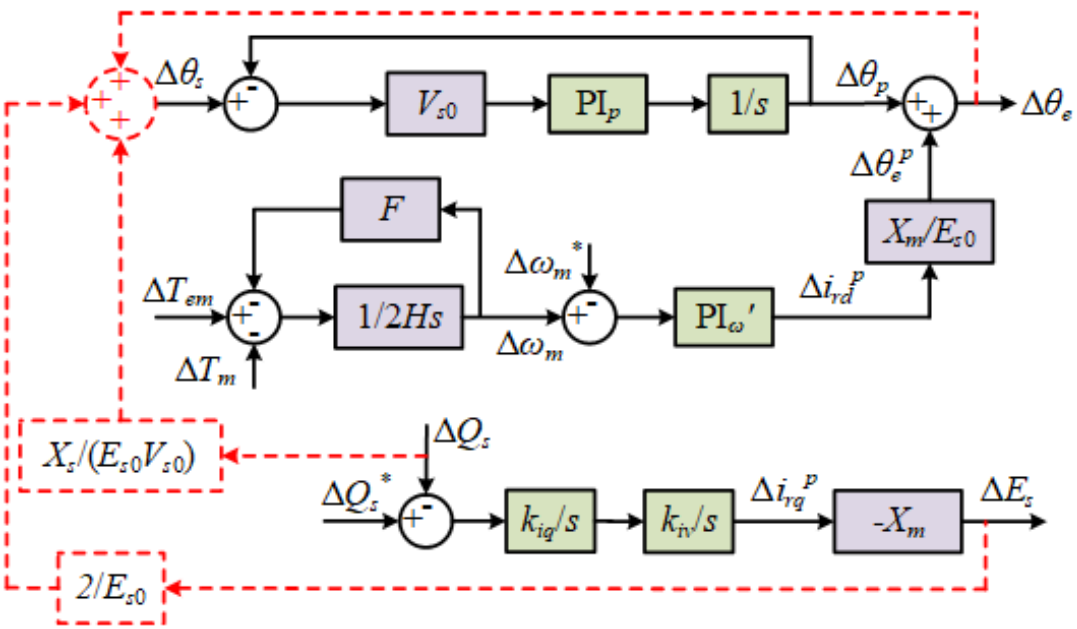

Fig. 5.5. Updated DFIM internal voltage phase-amplitude dynamics.

By applying (5-19), the DFIM internal voltage phase-amplitude dynamics can be updated as shown in Fig. 5.5. Then, the internal voltage amplitude ΔE_s is to be removed from (5-19). Since the reactive power through BTBPC is kept at 0, the stator reactive power Q_s is almost equal to the total input reactive power Q_t. Therefore, the transfer function of the reactive power difference ΔQ_{ub} to the internal voltage amplitude ΔE_s is expressed as:

$$\Delta E_s = -X_m k_{iq} k_{iv} \Delta Q_{ub} / s^2 \tag{5-20}$$

Where:

$$\Delta Q_{ub} = \Delta Q_s^* - \Delta Q_s = -\Delta Q_s \tag{5-21}$$

Substitute (5-20) and (5-21) into (5-19),

$$\Delta \theta_s = \Delta \theta_e + \left(\frac{2 X_m k_{iq} k_{iv}}{E_{s0} s^2} - \frac{X_s}{E_{s0} V_{s0}}\right) \Delta Q_{ub} \tag{5-22}$$

Based on (5-22), the DFIM internal voltage phase-amplitude dynamics can be further updated, which is displayed in Fig. 5.6. Furthermore, the transfer functions for $\Delta\theta_e$ and ΔE_s are obtained by following the deduction process in Fig. 5.7.

$$\Delta \theta_e = (G_1 + G_1 G_4) \Delta T_{ub} + G_3 G_4 \Delta Q_{ub} \tag{5-23}$$

$$\Delta E_s = G_2 \Delta Q_{ub} \tag{5-24}$$

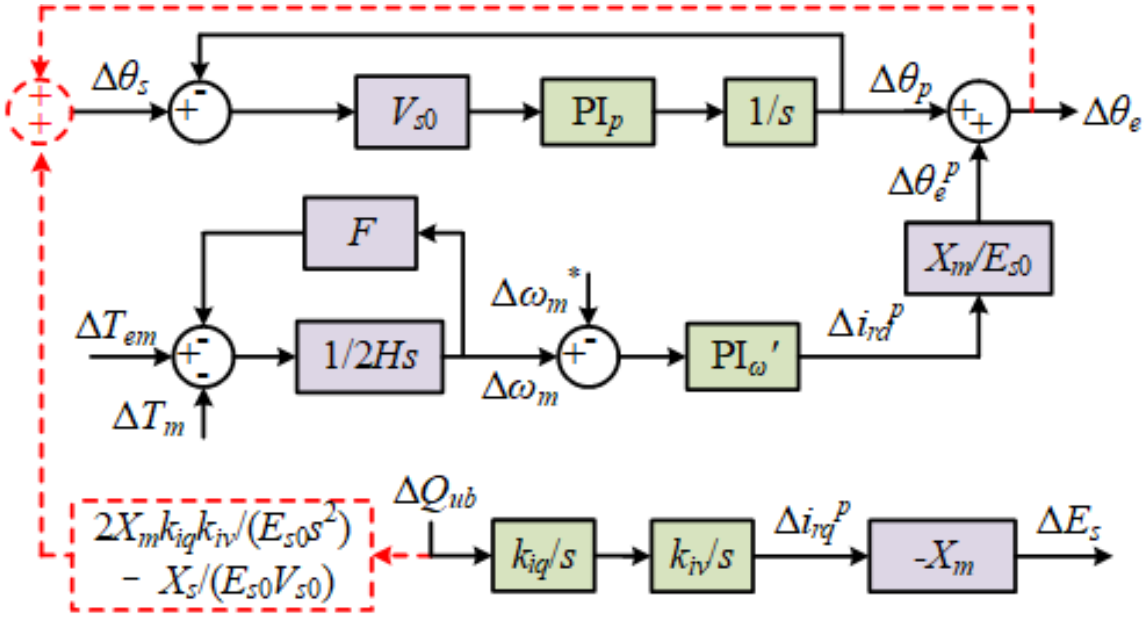

Fig. 5.6. Further updated DFIM internal voltage phase-amplitude dynamics.

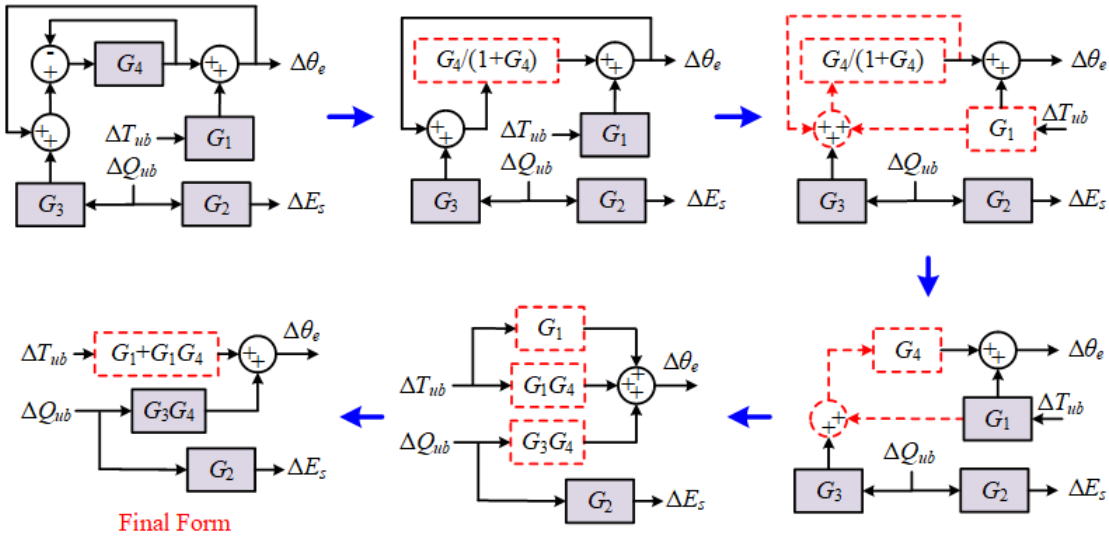

Fig. 5.7. Deduction process for the transfer functions for $\Delta\theta_e$ and ΔE_s.

The expressions of $G_1 \sim G_4$ are shown in the Appendix. G_1 is related to rotor speed control; G_2 and G_3 are linked with reactive power control; G_4 is related to PLL. According to (5-23) and (5-24), it can be summarized that $\Delta\theta_e$ is determined by rotor speed control, reactive power control and PLL, while ΔE_s is dependent on reactive power control. Therefore, it is valuable to investigate the effects of rotor speed control, reactive power control and PLL on DFIM internal

voltage phase-amplitude dynamics in the electromechanical control timescale.

5.3 Small-Signal Modelling of PPD-SPS with Synthetic Internal Voltage Vector for Ship Propulsion Subsystem

For the convenience of investigating the external characteristics of grid-connected devices and the response of each grid node, the concept of internal voltage is used to represent the device as an equivalent voltage source. Different from a synchronous machine, there are two electrical ports for a DFIM, which are the stator and SSC. In this case, it is complicated to analyse the external effects, thus necessitating the definition of SIVV.

The whole PPD-SPS propulsion subsystem can be expressed according to the principle of Thevenin-Norton equivalent circuit, and the equivalent impedance is calculated by:

$$Z_t = \frac{1}{1/Z_s + 1/Z_{ss}} \tag{5-25}$$

The equivalent circuit of the two electrical input ports for PPD-SPS is displayed in Fig. 5.8.

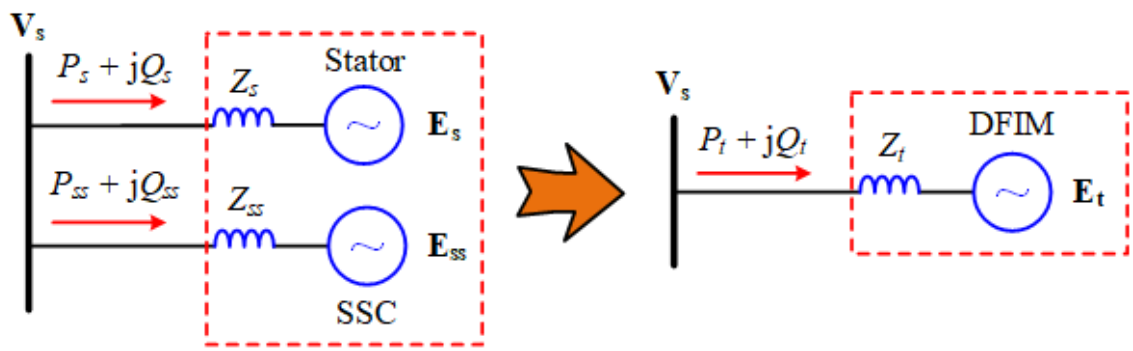

Fig. 5.8. The equivalent circuit of two electrical input ports for PPD-SPS propulsion subsystem.

With the terminal voltage vector $\mathbf{V_s}$ oriented in the positive direction of *d*-axis for vector control, the voltage and flux equations of DFIM are expressed as:

$$\begin{cases} \mathbf{V_s} = R_s\mathbf{I_s} + \mathrm{j}\omega_e\boldsymbol{\psi}_\mathbf{s} \\ \mathbf{V_r} = R_r\mathbf{I_r} + \mathrm{j}(\omega_e - \omega_r)\boldsymbol{\psi}_\mathbf{r} \end{cases} \tag{5-26}$$

$$\begin{cases} \boldsymbol{\psi}_\mathbf{s} = L_s\mathbf{I_s} + L_m\mathbf{I_r} \\ \boldsymbol{\psi}_\mathbf{r} = L_r\mathbf{I_r} + L_m\mathbf{I_s} \end{cases} \tag{5-27}$$

The proposed PPD-SPS is composed of SG and the equivalent internal voltages of the stator and SSC ($\mathbf{E_s}$ and $\mathbf{E_{ss}}$), which can be replaced by the SIVV $\mathbf{E_t}$:

$$\mathbf{E_t} = \frac{Z_{ss}}{Z_s + Z_{ss}}\mathbf{E_s} + \frac{Z_s}{Z_s + Z_{ss}}\mathbf{E_{ss}} \tag{5-28}$$

Substituting (5-25) into (5-28), $\mathbf{E_t}$ is updated as:

$$\mathbf{E_t} = Z_t[(1/Z_s)\mathbf{E_s} + (1/Z_{ss})\mathbf{E_{ss}}] \tag{5-29}$$

Therefore, the dynamics of $\mathbf{E_t}$ can be used to reveal the external characteristics of PPD-SPS propulsion subsystem.

With the purpose of revealing the physical meaning of the model of PPD-SPS propulsion subsystem, the concept of motion equation is described to illustrate the system dynamic behaviour. This concept is familiar to power engineers, which has been widely applied in explaining the mechanism of rotor motion for a synchronous machine. The small-signal model is first established by considering PLL-VC, and then the corresponding model without the control effects of PLL is presented for ESVO-VC.

5.3.1 Concept of Motion Equation

The rotor dynamic process of a synchronous machine under small disturbances can be clearly depicted from a physical point of view by applying the rotor motion equation, which is also

called the swing equation. It describes the relationship between the torque difference and rotor speed, which is shown as follows:

$$\omega_m = \frac{1}{2H}\int_0^t (T_{em} - T_m - F\omega_m)dt \tag{5-30}$$

The rotor motion equation of a conventional synchronous machine is displayed in Fig. 5.9. In the motor mode for synchronous machine, the electromagnetic torque T_{em} is the input, while the mechanical torque T_m is the output. The synchronizing torque T_S and damping torque T_D, which play important roles in achieving power system stability, are in phase with the rotor angle θ_m and rotor speed ω_m, respectively.

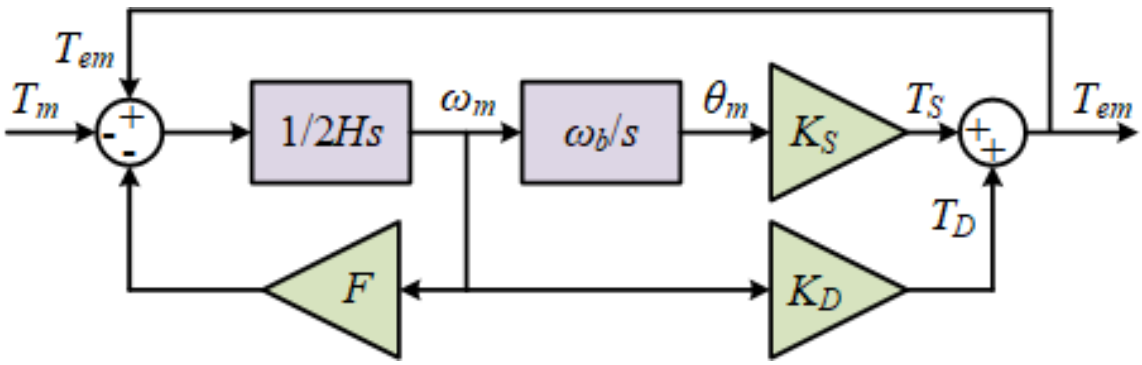

Fig. 5.9. Rotor motion equation of conventional synchronous machine (in motor mode).

5.3.2 Linearization of SIVV

The SIVV $\mathbf{E_t}$ is used to represent the external characteristic of PPD-SPS propulsion subsystem. Linearization should be performed to obtain both the small-signal values of the SIVV phase $\Delta\theta_E$ and amplitude ΔE_t. By neglecting the resistive components, (5-29) can be updated to be:

$$\mathbf{E_t} = X_t[(1/X_s)\mathbf{E_s} + (1/X_{ss})\mathbf{E_{ss}}] \tag{5-30}$$

Additionally, the internal voltage vector for SSC can be expressed by the following equation:

$$\mathbf{E_{ss}} = \mathbf{V_s} - \mathrm{j}X_{ss}\mathbf{I_{ss}} \tag{5-31}$$

By substituting (5-25) and (5-31) into (5-30),

$$\mathbf{E_t} = (X_t / X_{ss})\mathbf{V_s} + \mathrm{j}X_t[(X_m / X_s)\mathbf{I_r} - \mathbf{I_{ss}}] \tag{5-32}$$

Let

$$\begin{cases} g = X_t / X_{ss} \\ \mathbf{I} = (X_m / X_s)\mathbf{I_r} - \mathbf{I_{ss}} \end{cases} \tag{5-33}$$

Then the expression of $\mathbf{E_t}$ can be obtained as:

$$\mathbf{E_t} = g\mathbf{V}_s + \mathrm{j}X_t\mathbf{I} \tag{5-34}$$

The *dq* components of $\mathbf{E_t}$ are expressed as:

$$\begin{cases} e_{td}{}^p = gv_{sd} - X_t i_q{}^p \\ e_{tq}{}^p = gv_{sq} + X_t i_d{}^p \end{cases} \tag{5-35}$$

which is equivalent to:

$$\begin{cases} E_t \cos\theta_E{}^p = gV_s \cos\theta_s{}^p - X_t i_q{}^p \\ E_t \sin\theta_E{}^p = gV_s \sin\theta_s{}^p + X_t i_d{}^p \end{cases} \tag{5-36}$$

Take the partial derivative of $\theta_E{}^p$ at some operation point and combining the two equations, $\Delta\theta_E{}^p$ can be derived as:

$$\begin{aligned} \Delta\theta_E{}^p = & \frac{\cos\theta_{E0}{}^p}{E_{t0}}(gV_{s0}\cos\theta_{s0}{}^p\Delta\theta_s{}^p + g\Delta V_s \sin\theta_{s0}{}^p + X_t\Delta i_d{}^p) \\ & + \frac{\sin\theta_{E0}{}^p}{E_{t0}}(gV_{s0}\sin\theta_{s0}{}^p\Delta\theta_s{}^p - g\Delta V_s \cos\theta_{s0}{}^p + X_t\Delta i_q{}^p) \end{aligned} \tag{5-37}$$

In the steady state, θ_{s0}^p equals 0, therefore

$$\Delta\theta_E{}^p = \frac{\cos\theta_{E0}{}^p}{E_{t0}}(gV_{s0}\Delta\theta_s{}^p + X_t\Delta i_d{}^p) + \frac{\sin\theta_{E0}{}^p}{E_{t0}}(X_t\Delta i_q{}^p - g\Delta V_s) \tag{5-38}$$

The process can be repeated for E_t to obtain ΔE_t:

$$\Delta E_t = \cos\theta_{E0}{}^p(g\Delta V_s - X_t\Delta i_q{}^p) + \sin\theta_{E0}{}^p(gV_{s0}\Delta\theta_s{}^p + X_t\Delta i_d{}^p) \tag{5-39}$$

As the value of θ_{E0}^p is usually smaller than 10 degrees [36], a reasonable approximation can be made that $\sin\theta_{E0}^p \approx 0$ and $\cos\theta_{E0}^p \approx 1$. Therefore, (5-38) and (5-39) are updated as:

$$\Delta\theta_E{}^p = (gV_{s0}/E_{t0})\Delta\theta_s{}^p + (X_t/E_{t0})\Delta i_d{}^p \tag{5-40}$$

$$\Delta E_t = g\Delta V_s - X_t\Delta i_q{}^p \tag{5-41}$$

The SIVV phase and amplitude dynamics can be obtained by considering PLL, rotor speed control and reactive power control based on (5-9), (5-10), (5-13), (5-33), (5-40), and (5-41). Since the small-signal model is established in the electromechanical control timescale, the SSC *dq* currents i_{ssd} and i_{ssq} track their reference values, so does the terminal voltage V_s. Therefore, the small-signal model of PPD-SPS describing the SIVV phase-amplitude dynamics is illustrated in Fig. 5.10.

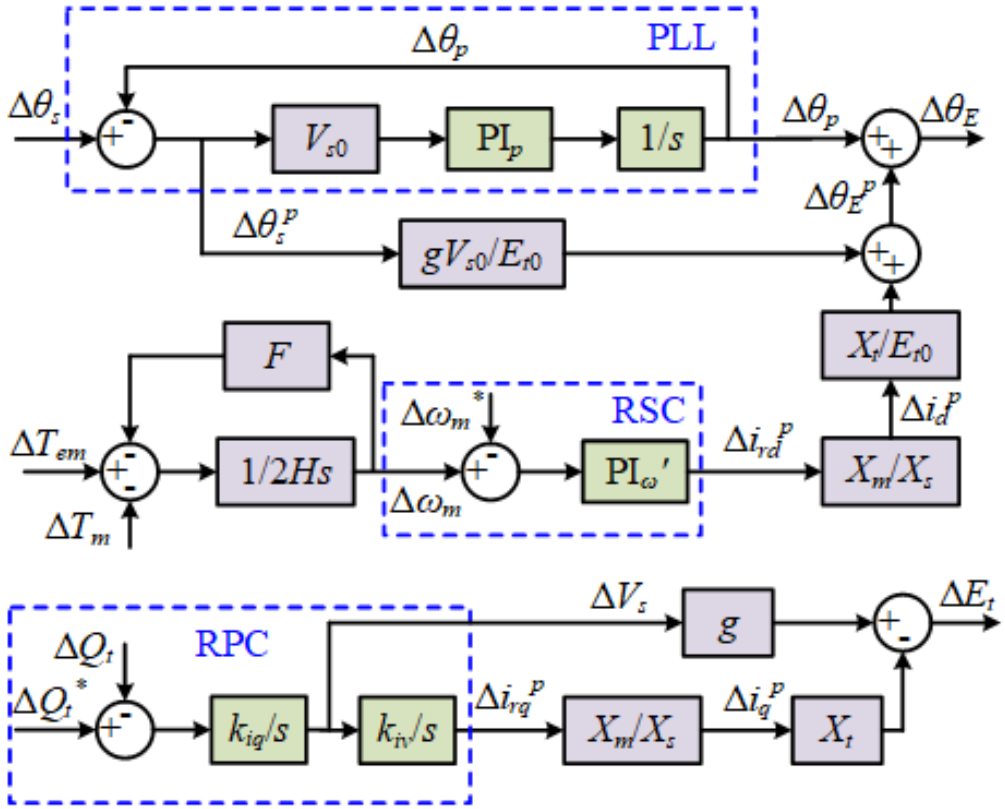

Fig. 5.10. PPD-SPS small-signal model describing the SIVV phase-amplitude dynamics.

5.4 Derivation of the Motion Equation based Model

In order to figure out the direct relationship between the SIVV phase $\Delta\theta_E$ and torque difference ΔT_{ub}, and that between the SIVV amplitude ΔE_t and reactive power difference ΔQ_{ub}, the block diagram shown in Fig. 5.10 needs to be modified.

Since the current dynamics in the path with power converters are neglected, the assumption of $\Delta P_t \approx \Delta P_s$ can be made. Therefore, the following relationship is obtained:

$$\Delta P_t \approx \Delta P_s = \omega_{m0}\Delta T_{em} \tag{5-42}$$

The expressions of active and reactive powers delivered from the connection node to DFIM are shown below.

$$P_t = E_t V_s \sin(\theta_s - \theta_E) / X_t \tag{5-43}$$

$$Q_t = E_t^2 / X_t - E_t V_s \cos(\theta_s - \theta_E) / X_t \tag{5-44}$$

Linearizing the above two equations, and since $\theta_s = \theta_p$ at a specific operation point, the following equations are derived.

$$\begin{aligned} X_t \Delta P_t &= -V_{s0} \Delta E_t \sin \theta_{E0}{}^p - E_{t0} \Delta V_s \sin \theta_{E0}{}^p \\ &+ E_{t0} V_{s0} \Delta \theta_s \cos \theta_{E0}{}^p - E_{t0} V_{s0} \Delta \theta_E \cos \theta_{E0}{}^p \end{aligned} \tag{5-45}$$

$$\begin{aligned} X_t \Delta Q_t &= 2E_{t0} \Delta E_t - V_{s0} \Delta E_t \cos \theta_{E0}{}^p - E_{t0} \Delta V_s \cos \theta_{E0}{}^p \\ &- E_{t0} V_{s0} \Delta \theta_s \sin \theta_{E0}{}^p + E_{t0} V_{s0} \Delta \theta_E \sin \theta_{E0}{}^p \end{aligned} \tag{5-46}$$

5.4.1 Replacing $\Delta\theta_s$ by the Expressions with ΔT_{em} and $\Delta\theta_E$

Combining (5-45) and (5-46), the terminal voltage phase variation can be obtained as:

$$\begin{aligned} \Delta\theta_s &= \Delta\theta_E + (2 \sin \theta_{E0}{}^p / E_{t0}) \Delta E_t + \\ &[X_t \cos \theta_{E0}{}^p / (E_{t0} V_{s0})] \Delta P_t - [X_t \sin \theta_{E0}{}^p / (E_{t0} V_{s0})] \Delta Q_t \end{aligned} \tag{5-47}$$

The simplification of (5-47) can be achieved by assuming that $\sin\theta_{E0}{}^p \approx 0$ and $\cos\theta_{E0}{}^p \approx 1$.

$$\Delta\theta_s = \Delta\theta_E + [X_t / (E_{t0} V_{s0})] \Delta P_t \tag{5-48}$$

Substituting (5-42) into (5-48), the relationship between $\Delta\theta_s$ and ΔT_{em} is obtained as:

$$\Delta\theta_s = \Delta\theta_E + [X_t \omega_{m0} / (E_{t0} V_{s0})] \Delta T_{em} \tag{5-49}$$

Then the phase dynamics can be expressed by the updated block diagram as shown in Fig. 5.11.

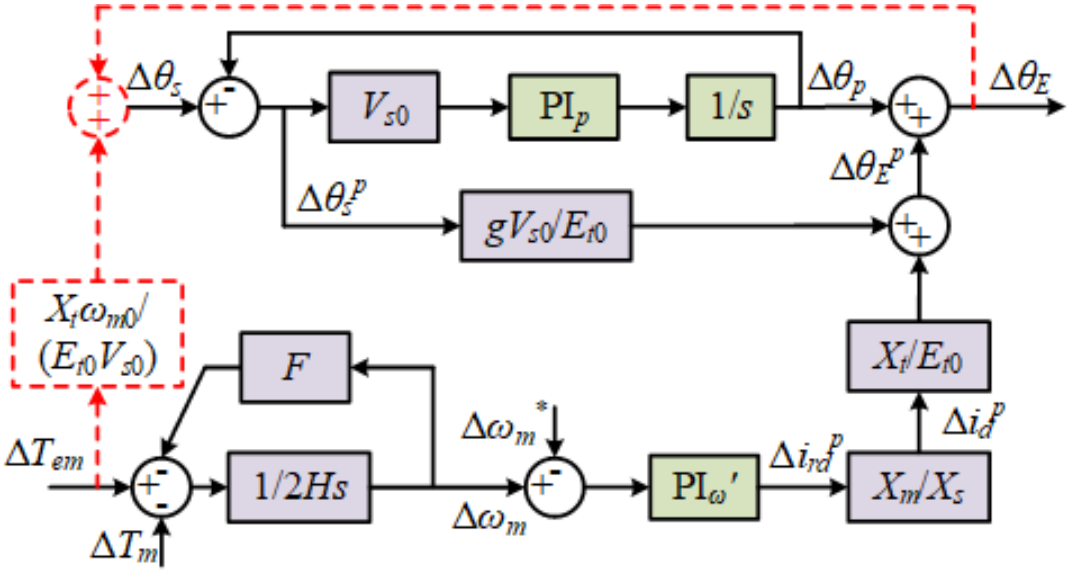

Fig. 5.11. Updated phase dynamics by eliminating $\Delta\theta_s$.

In the steady state, the mechanical torque ΔT_m and the reference value of the rotor speed $\Delta\omega_m^*$ are both equal to 0. Then, the whole deduction process of the transfer function of the torque difference ΔT_{ub} (= $\Delta T_{em} - \Delta T_m$) to the SIVV phase $\Delta\theta_E$ can be derived as shown in Fig. 5.12. The expressions of $G_{\theta 1} \sim G_{\theta 4}$ are shown in the Appendix.

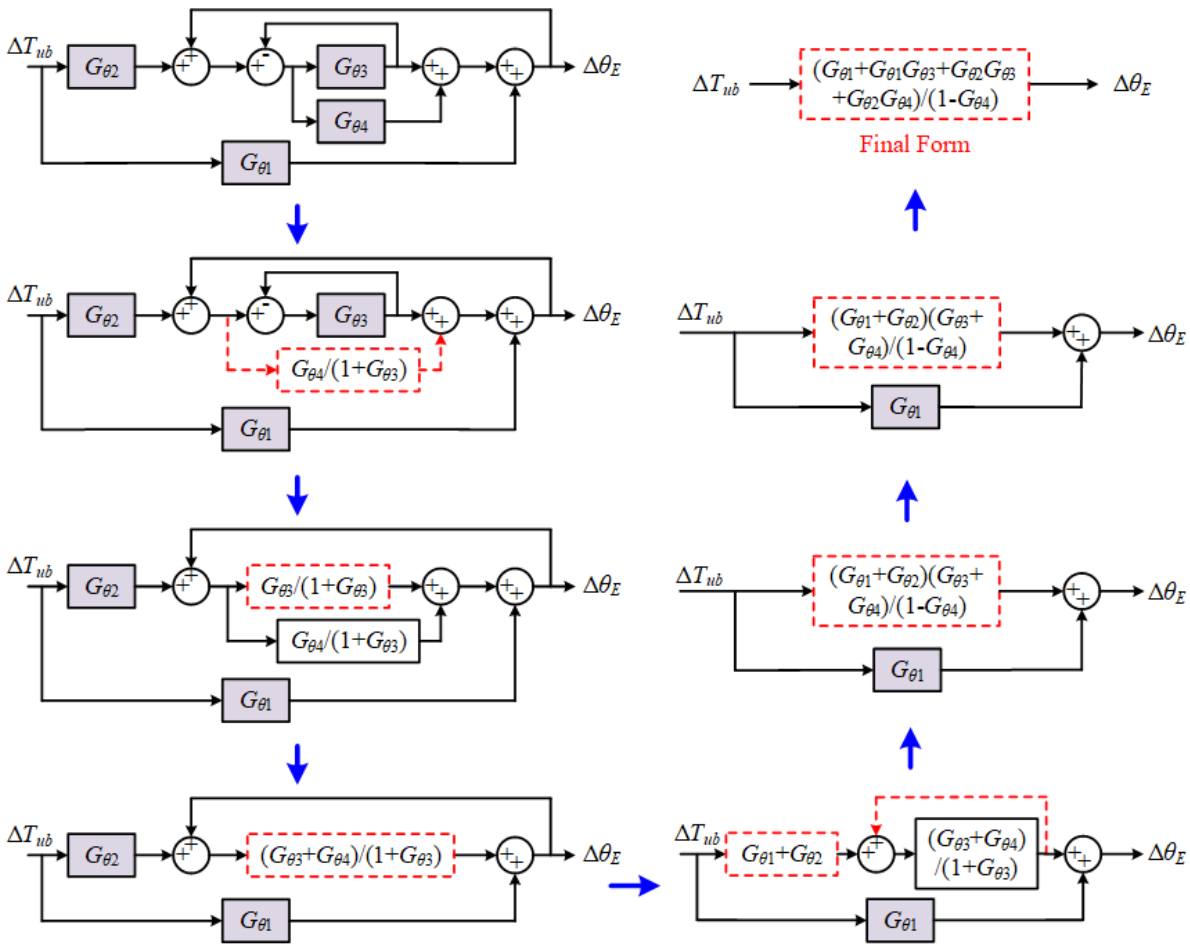

Fig. 5.12. Derivation process of the transfer function of ΔT_{ub} to $\Delta\theta_E$.

Substitute the expressions of $G_{\theta1} \sim G_{\theta4}$ into the final transfer function in Fig. 5.12, the following equation is obtained:

$$\Delta\theta_E = \frac{1}{B}\frac{K_4 s^4 + K_3 s^3 + K_2 s^2 + K_1 s + K_0}{(D_2 s^2 + D_1 s)s^2}\Delta T_{ub} \tag{5-50}$$

The expressions for B, $K_0 \sim K_4$, and $D_1 \sim D_2$ are displayed in the Appendix. Furthermore, the transfer function is rearranged to be in the form of motion equation to describe the SIVV phase dynamics of PPD-SPS propulsion subsystem. The updated phase motion equation is shown as follows:

$$\Delta\theta_E = \frac{1}{M_\theta(s)}\frac{1}{s^2}\Delta T_{ub} \tag{5-51}$$

where $M_\theta(s)$ is the equivalent inertia,

$$M_\theta(s) = B\frac{D_2 s^2 + D_1 s}{K_4 s^4 + K_3 s^3 + K_2 s^2 + K_1 s + K_0} \tag{5-52}$$

5.4.2 Obtaining the SIVV Amplitude Motion Equation

According to the lower part of Fig. 5.10, the relationship between the SIVV amplitude ΔE_t and the total reactive power error ΔQ_{ub} (ΔQ_t^* - ΔQ_t) can be obtained. The corresponding derivation process is shown in Fig. 5.13. The expressions of G_{E1} ~ G_{E3} are displayed in Appendix. Substitute the expressions of G_{E1} ~ G_{E3} into the final transfer function obtained in Fig. 5.13, the following equation is obtained:

$$\Delta E_t = \frac{1}{X_s}\frac{N_1 s + N_0}{s^2}\Delta Q_{ub} \tag{5-53}$$

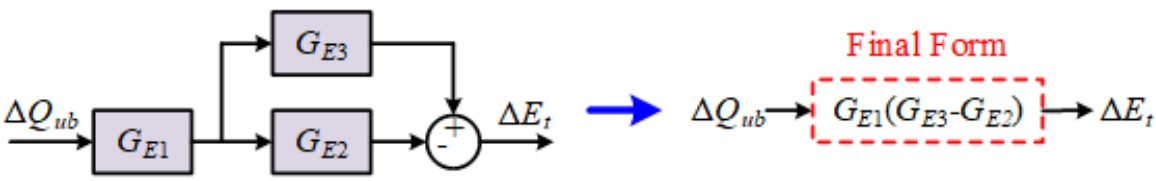

Fig. 5.13. Derivation process of the transfer function of ΔQ_{ub} to ΔE_t.

The expressions of N_1 and N_0 are shown in the Appendix. Moreover, (5-53) can be further updated to express the linkage between ΔE_t and ΔQ_{ub} based on the motion equation concept,

$$\Delta E_t = \frac{1}{M_E(s)}\frac{1}{s}\Delta Q_{ub} \tag{5-54}$$

Where:

$$M_E(s) = \frac{X_s s}{N_1 s + N_0} \tag{5-55}$$

To this point, the SIVV phase-amplitude dynamics of PPD-SPS propulsion subsystem in the electromechanical control timescale are obtained from (5-51) and (5-54).

5.4.3 The Motion Equation based Model for ESVO-VC

Different from the traditional PLL-VC, the proposed ESVO-VC estimates the terminal voltage angle by using a stator flux estimator, and the stator resistance is small enough to be neglected. In this case, the terminal voltage angle always aligns with the *d*-axis. Therefore, the control effects of PLL are eliminated, where $G_{\theta 3}$ and $G_{\theta 4}$ are not taken into consideration. The transfer function of ΔT_{ub} to $\Delta\theta_E$ can be updated as:

$$\Delta\theta_E = \frac{1}{W}\frac{T_1 s + T_0}{2FHs + 1}\Delta T_{ub} \tag{5-62}$$

The expressions of W, T_1 and T_0 are shown in the Appendix, and the updated phase motion equation is derived as:

$$\Delta\theta_E = \frac{1}{M_\theta'(s)}\frac{1}{s^2}\Delta T_{ub} \tag{5-63}$$

where $M_\theta'(s)$ is the simplified equivalent inertia,

$$M_\theta'(s) = \frac{W(2FHs + 1)}{T_1/s + T_0/s^2} \tag{5-64}$$

Compared with (5-58), it can be seen that the expression of (5-64) becomes much simpler. Besides, according to the expressions for $K_0 \sim K_4$, and $D_1 \sim D_2$, the control effects of the PLL significantly influence the SIVV phase dynamics. For the voltage amplitude dynamics, the same characteristics remain, since ΔE_t is only related to reactive power control.

The purposes of establishing these two small-signal models for the propulsion subsystem of PPD-SPS are to investigate the internal system dynamics between the DFIM and BTBPC, and to study the external system dynamics between the propulsion subsystem and the rest part of PPD-SPS. The derived transfer functions clearly illustrate the system dynamics in the electromechanical control timescale, where the effects of rotor speed control, reactive power control and PLL are taken into consideration. The results of above theoretical analysis in the *s*-domain will be utilized in the further small-signal stability analysis of the proposed PPD-SPS.

5.5 Simulation Results and Discussion

The simulation studies are carried out in Matlab/Simulink with discrete time-step simulation to verify the operation of a PPD-SPS by applying the BTBPC average and detailed switching models, respectively, and the effects of PLL, rotor speed control and reactive power control on DFIM stator phase-amplitude dynamics are investigated. The time steps of 100μs and 50μs are applied for the PPD-SPS with the BTBPC average and detailed switching models, respectively. The mechanical/load torque input for DFIM torque is 0.8pu, and the reference rotor speed is 0.8pu. The simulation parameters for the DFIM and SG, along with the primitive controller gains for rotor speed control, reactive power control and PLL are displayed in the Appendix.

5.5.1 Control Parameter Effects on System Operation with BTBPC Average Model

The BTBPC average model is first applied in PPD-SPS to reduce the time used for simulation, and the model is verified by comparing its performance to that of the detailed one. The key variables are compared for these two models, which are shown in Fig. 5. 14. It can be seen that oscillations are eliminated for the values derived by using the proposed average model of

BTBPC, as the switching behaviors are omitted by replacing the switches with controlled voltage sources. The stator voltage V_s, electromagnetic torque T_{em}, rotor speed ω_m, and DC-bus voltage V_{dc} are all kept at nominal values when the ship operates at a specific operation point. The internal voltage phase θ_e is around (-π/2), which is shown as a value close to 3π/2 in the figure, and the internal voltage amplitude E_s is about 0.9pu, since the DFIM operates as a propulsion motor in the system.

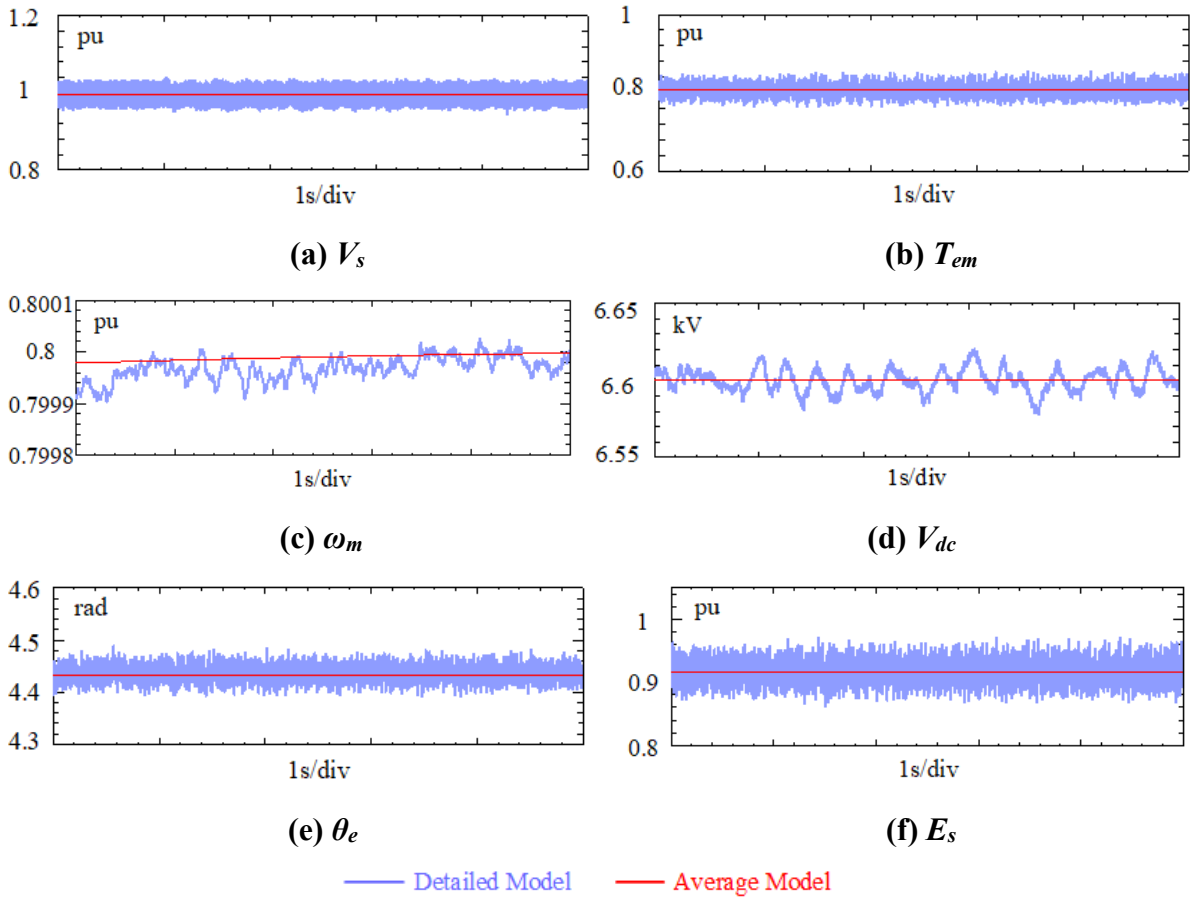

Fig. 5.14. Comparison between the values of key variables derived by using the detailed and average BTBPC models.

In the electromechanical control time scale, the effects of PLL, rotor speed control and reactive power control are focused on. All of these control loops are related to the internal voltage phase dynamics, while only reactive power control affects the dynamics of internal voltage amplitude. The effects of varying PLL, rotor speed and reactive power controller gains on the

system performance by applying the BTBPC average model are displayed in Figs. 5.15 & 5.16, Figs. 5.17 & 5.18, and Figs. 5.19 & 5.20, respectively. When varying one of the controller gains, the others are kept at the primitive values, which are shown in the Appendix.

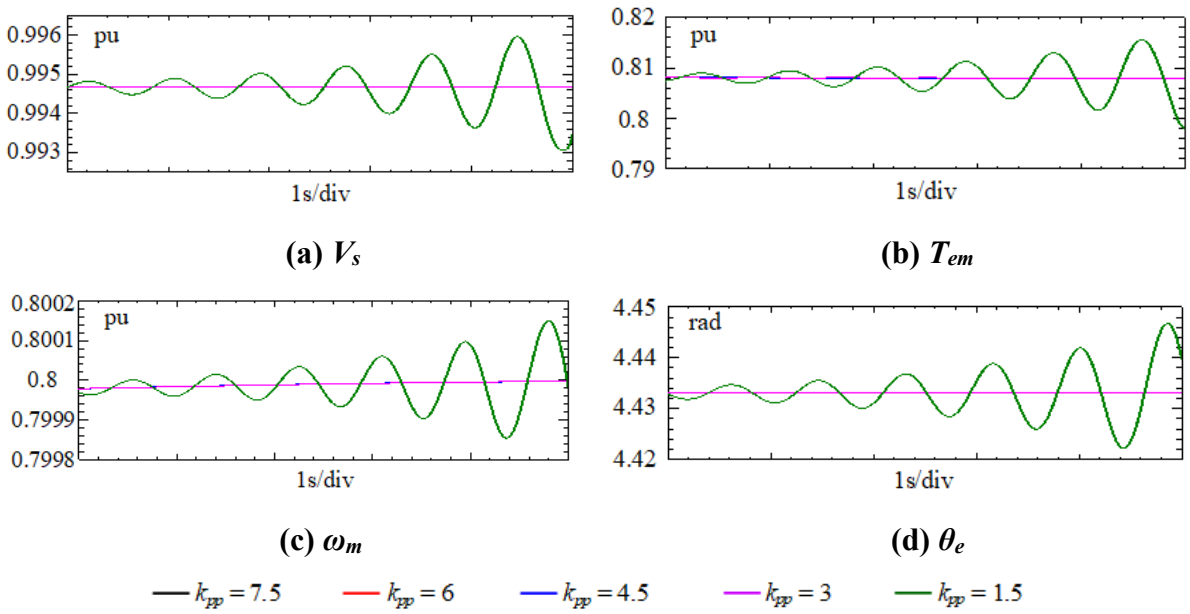

Fig. 5.15. Control effects of varying k_{pp} on (a) V_s (b) T_{em} (c) ω_m (d) θ_e.

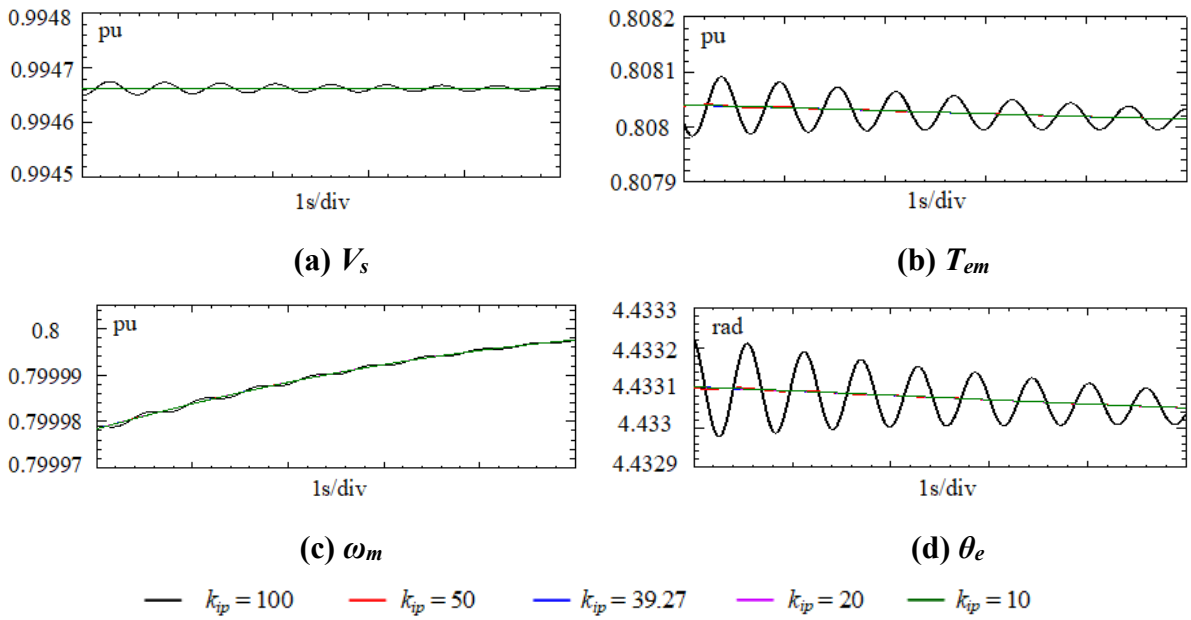

Fig. 5.16. Control effects of varying k_{ip} on (a) V_s (b) T_{em} (c) ω_m (d) θ_e.

It can be seen from Fig. 5.15 that the PLL proportional gain k_{pp} is decreased from 7.5 to 1.5, with the step change of 1.5 to observe the effects on V_s, T_{em}, ω_m and the internal voltage phase

θ_e. When the value of k_{pp} is large enough, the values of all these variables are kept stable. However, once k_{pp} is decreased to 1.5, the oscillation becomes more evident as the time goes, and eventually instable performance will be caused, which is not desirable. On the contrary, as can be seen from Fig. 5.16, when the value of k_{ip} is small enough, the values of system variables track the corresponding values at a specific operation point very well. While obvious fluctuations with decreasing amplitudes are presented when k_{ip} reaches 100, and it takes much longer time for the system to achieve the stable operation.

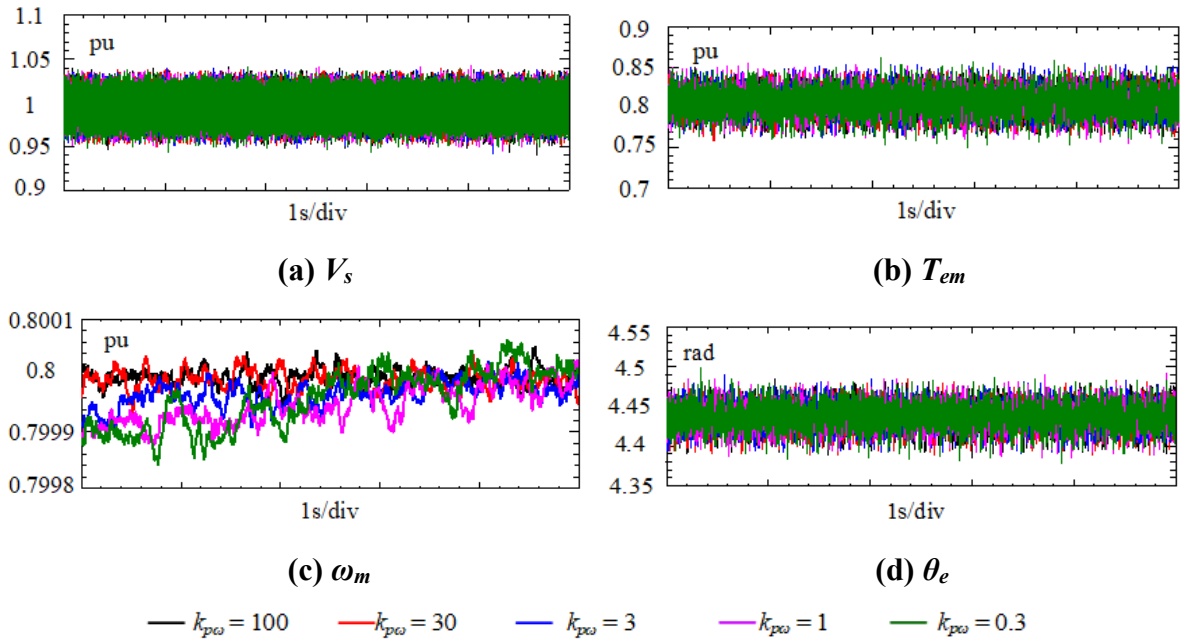

Fig. 5.17. Control effects of varying $k_{p\omega}$ on (a) V_s (b) T_{em} (c) ω_m (d) θ_e.

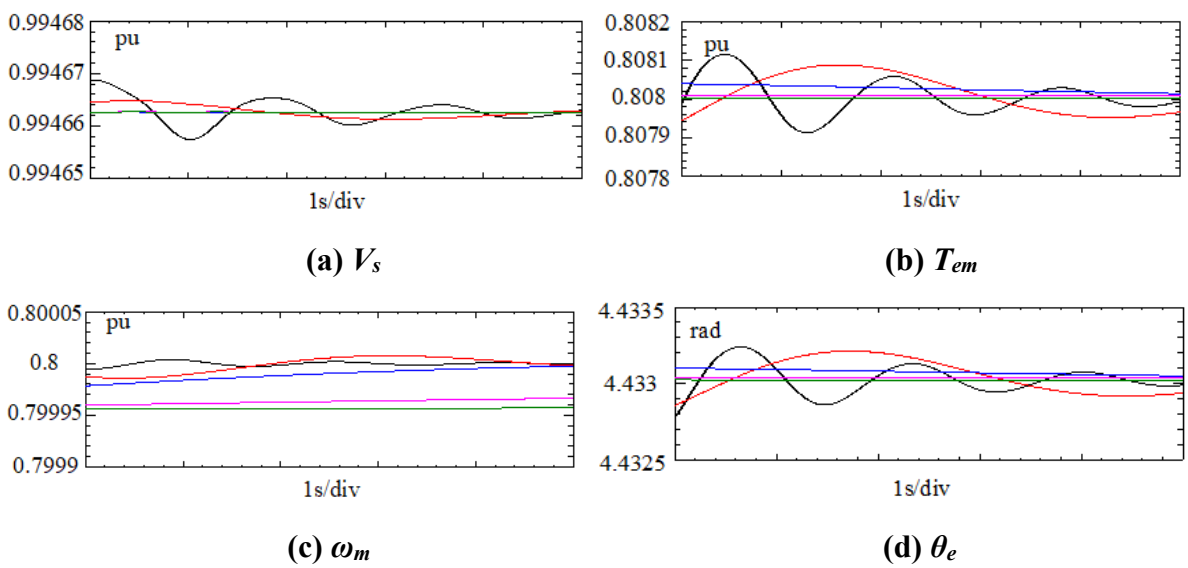

— $k_{i\omega} = 100$ — $k_{i\omega} = 10$ — $k_{i\omega} = 0.6$ — $k_{i\omega} = 0.1$ — $k_{i\omega} = 0.01$

Fig. 5.18. Control effects of varying $k_{i\omega}$ on (a) V_s (b) T_{em} (c) ω_m (d) θ_e.

The effects of rotor speed controller gain variations are presented in Figs. 5.17 & 5.18. It can be seen that by changing the proportional gain $k_{p\omega}$, the values of these variables can track their reference values with some fluctuations, but good tracking performance is perserved. As the average BTBPC model is applied, the electromachenical torque tracking accuracy is a little bit lower than using the detailed model, and the derived value of T_{em} is slightly higher than 0.8pu. From Fig. 5.18, some distinctions in the system performance by using different integral gains are presented. Larger $k_{i\omega}$ results in more serious oscillations and longer time to achieve the steady operation point. However, as can be seen from Fig. 5.18(c), the tracking accuracy is higher when the rotor speed controller integral gain becomes higher.

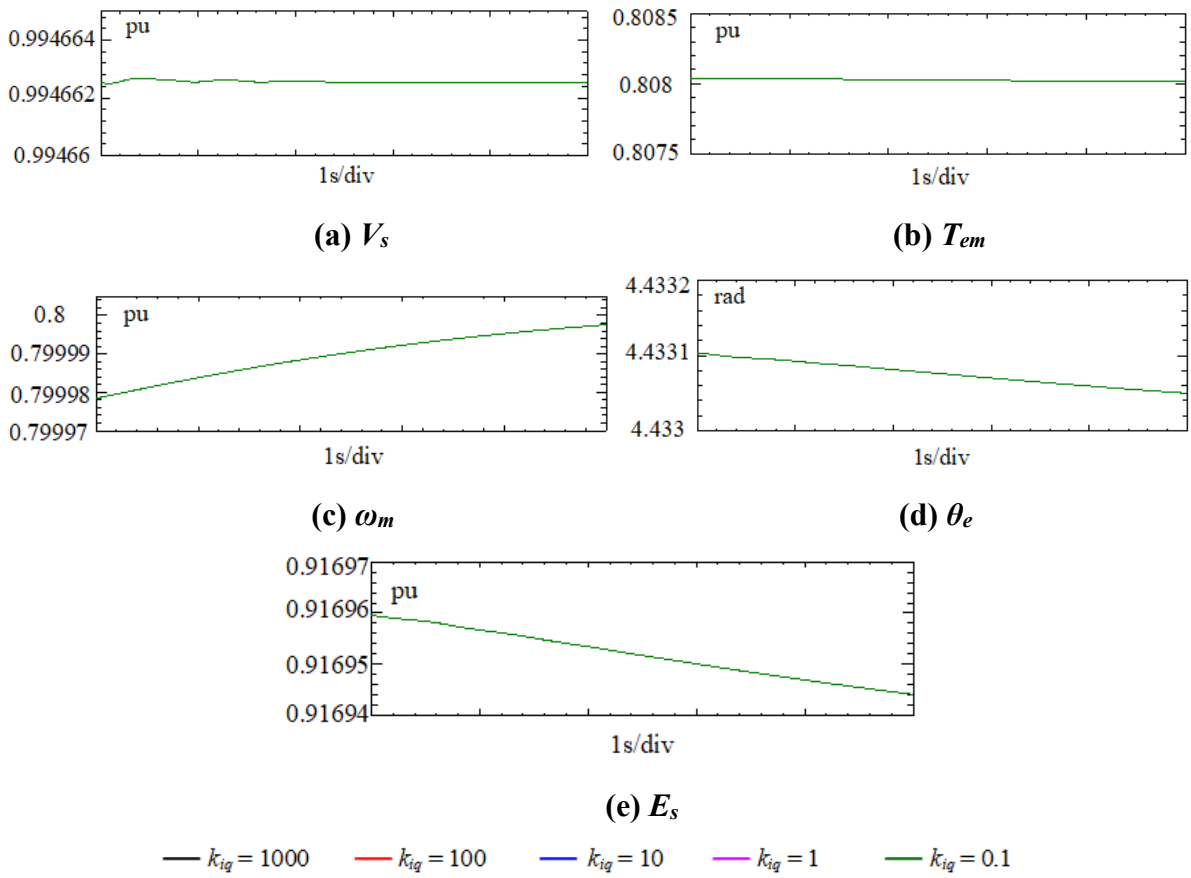

Fig. 5.19. Control effects of varying k_{iq} on (a) V_s (b) T_{em} (c) ω_m (d) θ_e (e) E_s.

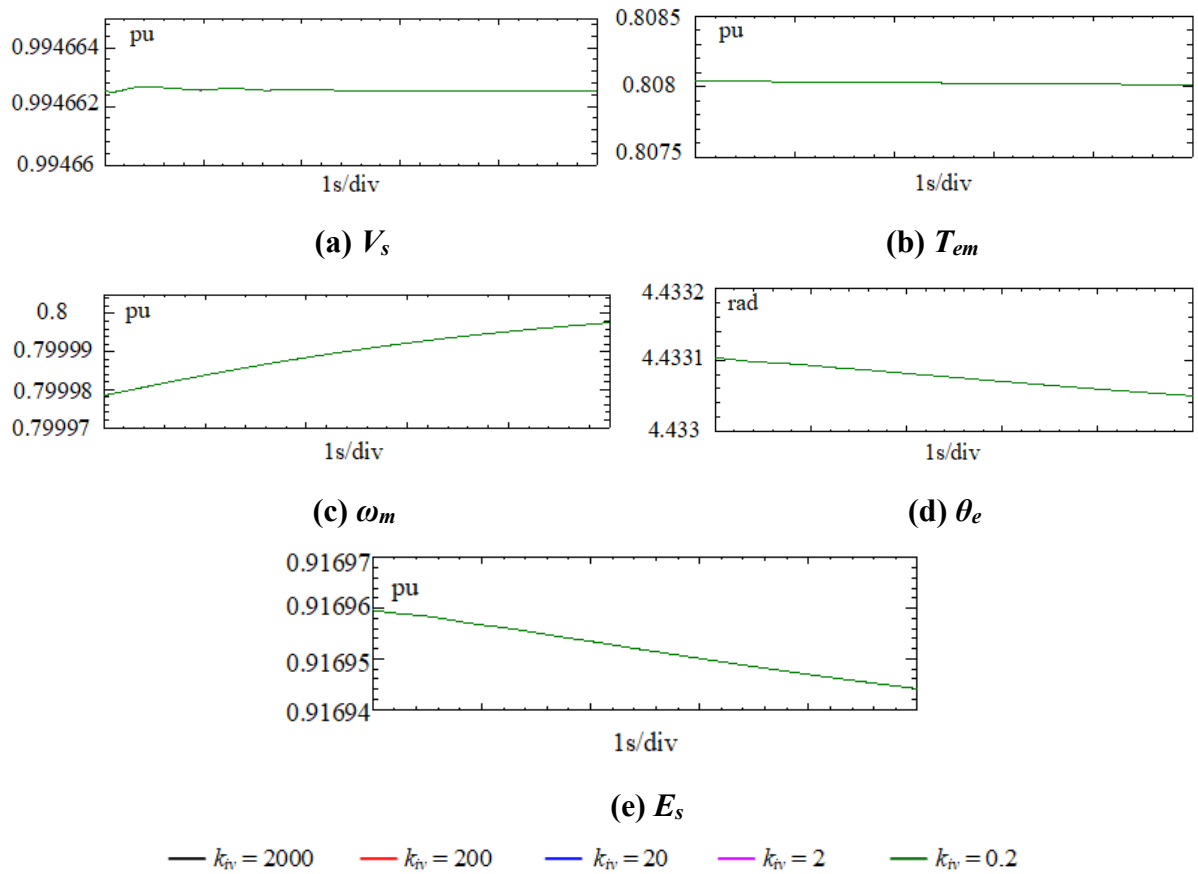

Fig. 5.20. Control effects of varying k_{iv} on (a) V_s (b) T_{em} (c) ω_m (d) θ_e (e) E_s.

From (5-23) and (5-24), since the integral controller gains k_{iq} and k_{iv} always appear in the form of $k_{iq}k_{iv}$, the effect of varying the value of k_{iq} is the same as that of varying the value of k_{iv}. From Figs. 5.19 & 5.20, the variations in k_{iq} and k_{iv} for reactive power control almost have no effects on the system performance, since the values of each variable when applying different values of k_{iq} and k_{iv} are equal to each other. This is because the calculation of stator reactive power Q_s is only dependent on the stator voltage and current, whose transient behaviours are eliminated due to the use of the BTBPC average model, thus $\Delta Q_{ub} = 0$. According to (5-23) and (5-24), the effects of G_2 and G_3, which correspond to those of reactive power control, are therefore not reflected. Contrarily, as mentioned above, there are differences between the actual and reference electromechanical torque values, thus ΔT_{ub} is not 0, and the effects of G_1 (related to rotor speed control) and G_4 (related to PLL) can be observed based on (5-23) when adjusting the values of k_{pp}, k_{ip}, $k_{p\omega}$ and $k_{i\omega}$.

5.5.2 Control Parameter Effects on System Operation with BTBPC Detailed Switching Model

Since the DFIM functions as the propulsion load, it operates in the motor mode, thus the SIVV angle θ_E lags the stator voltage angle θ_s. Since PLL and rotor speed control loops are correlated with the SIVV phase dynamics, while reactive power control is responsible for the SIVV amplitude dynamics, their effects on the system performance are studied separately. In addition, the effects of applying ESVO-VC are investigated for comparison. The simulation results for SIVV phase study are presented in Figs. 5.21 - 5.24 for PLL-VC by changing the PLL and rotor speed control proportional and integral gains, respecitvely. Besides, the corresponding simulation results by applying ESVO-VC are displayed in Fig. 5.25.

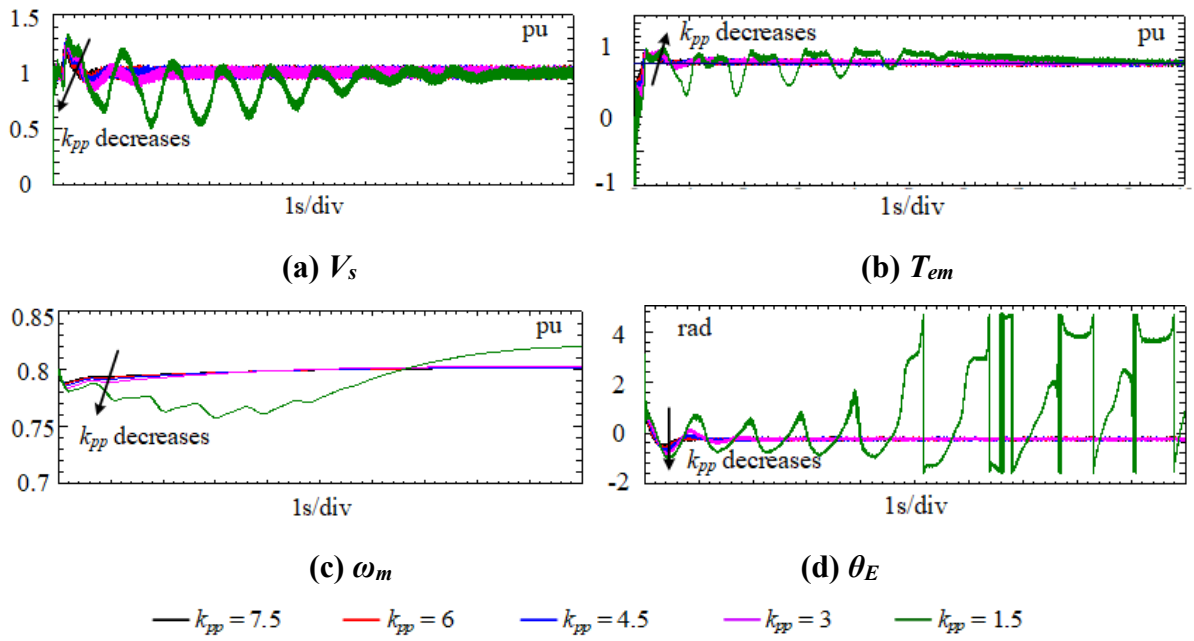

Fig. 5.21. Control effects of k_{pp} for PLL-VC on (a) V_s (b) T_{em} (c) ω_m (d) θ_E.

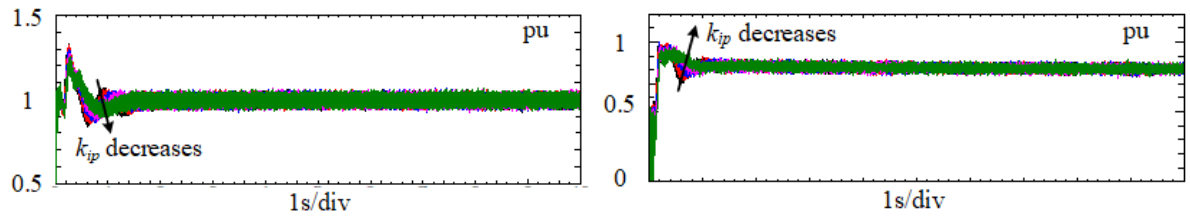

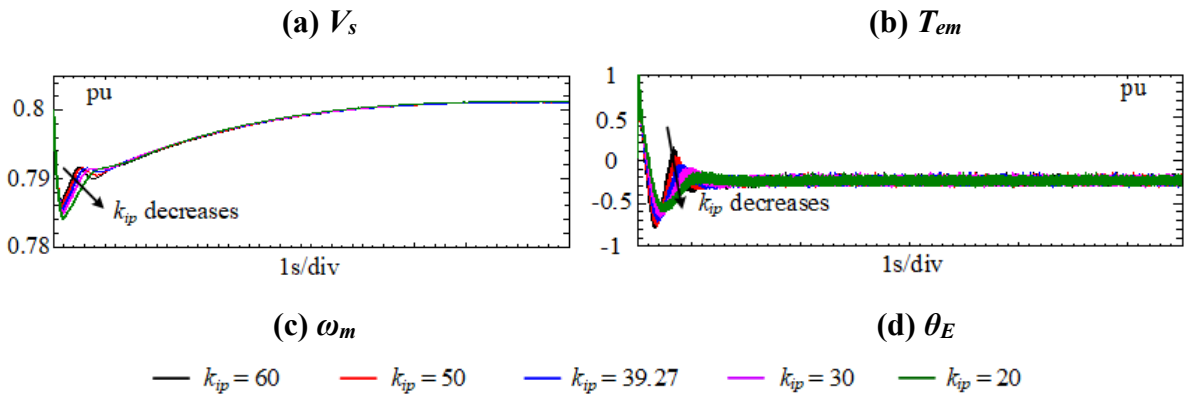

Fig. 5.22. Control effects of k_{ip} for PLL-VC on (a) V_s (b) T_{em} (c) ω_m (d) θ_E.

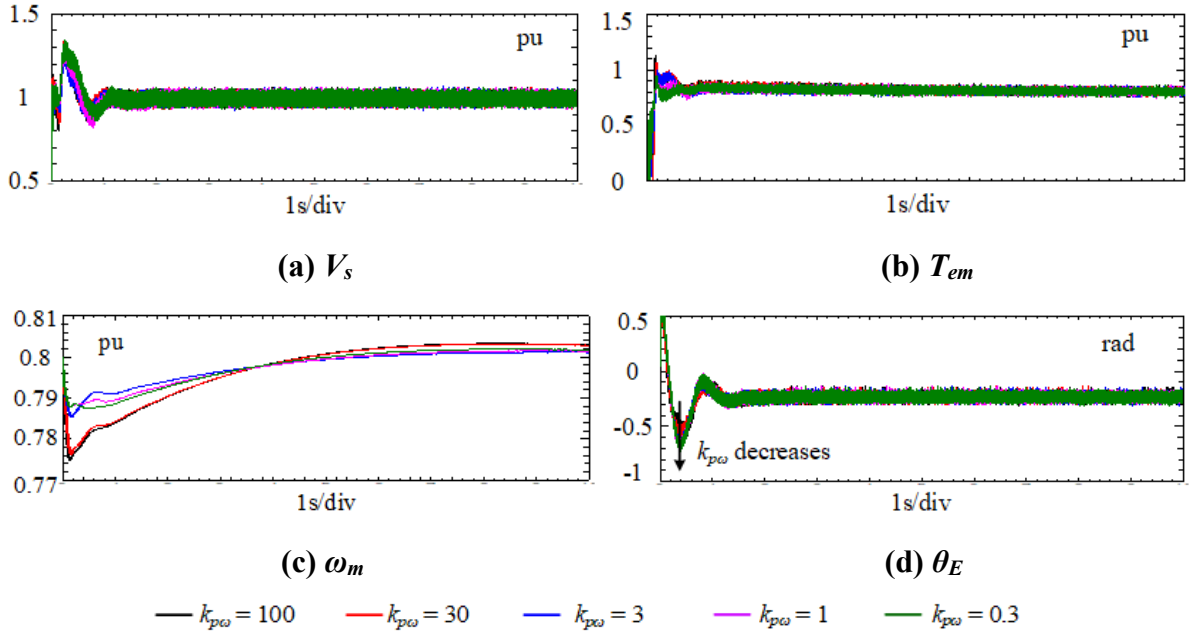

Fig. 5.23. Control effects of $k_{p\omega}$ for PLL-VC on (a) V_s (b) T_{em} (c) ω_m (d) θ_E.

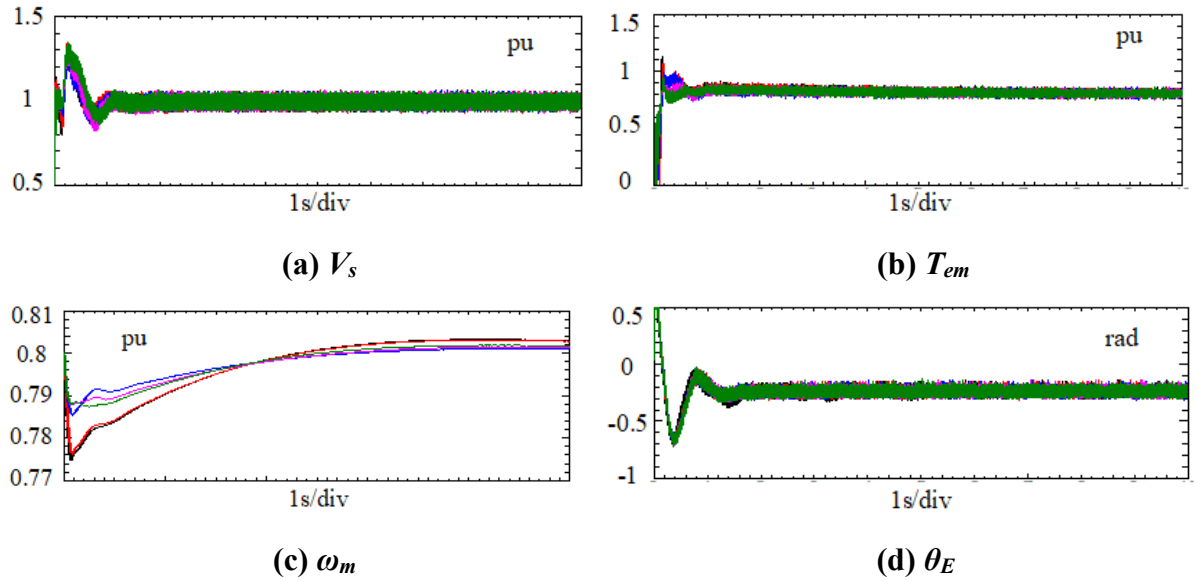

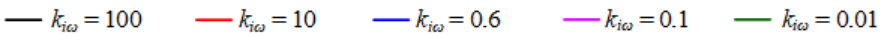

Fig. 5.24. Control effects of $k_{i\omega}$ for PLL-VC on (a) V_s (b) T_{em} (c) ω_m (d) θ_E.

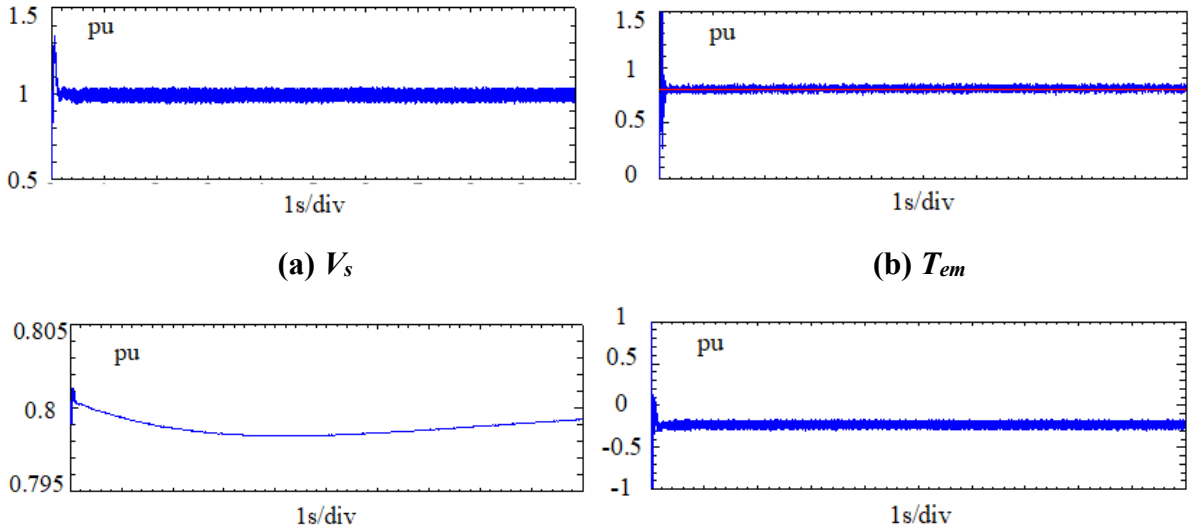

(a) V_s **(b) T_{em}**

(c) ω_m **(d) θ_E**

Fig. 5.25. Simulation results by applying ESVO-VC (a) V_s (b) T_{em} (c) ω_m (d) θ_E.

It can be seen from Fig. 5.21 that by decreasing k_{pp} from 7.5 to 1.5, with the step change of 1.5, it takes longer time for the variables to achieve steady states. Besides, when $k_{pp} = 1.5$, there are obvious fluctuations in V_s, T_{em}, ω_m and θ_E, and the final values of ω_m and θ_E deviate from the desired ones, in which case the stable operation of PPD-SPS propulsion subsystem is no longer available. In contrast, as can be seen from Fig. 5.22, the variation of k_{ip} hardly affects the tracking performance. From Figs. 5.23 and 5.24, it can be observed that the effects of varying $k_{p\omega}$ and $k_{i\omega}$ are not distinct on the overall performance of PPD-SPS. However, as can be seen from Figs. 5.23(c) and 5.24(c), the smaller the controller gain is, the more precise the actual rotor speed tracks the reference value. Moreover, by applying the proposed ESVO-VC, there is no need to worry about setting the values for PLL and rotor speed controller gains, and good tracking performance still can be obtained.

In order to investigate the effects of reactive power control on the SIVV amplitude dynamics, simulations are carried out by applying different controller gains (k_{iq} & k_{iv}) for the reactive

power and voltage controllers. The corresponding simulations for ESVO-VC by changing the reactive power controller gain values are not carried out, as the effects on voltage amplitude dynamics are similar for PLL-VC and ESVO-VC. The corresponding simulation results are shown in Figs. 5.26 & 5.27.

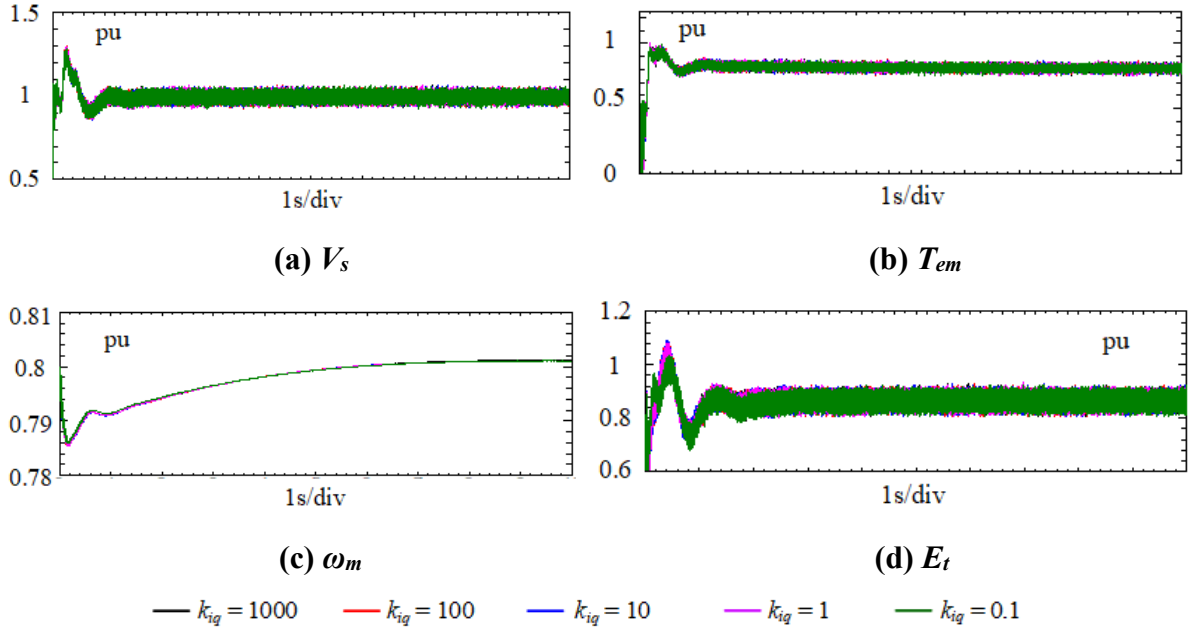

Fig. 5.26. Control effects of k_{iq} for PLL-VC on (a) V_s (b) T_{em} (c) ω_m (d) E_t.

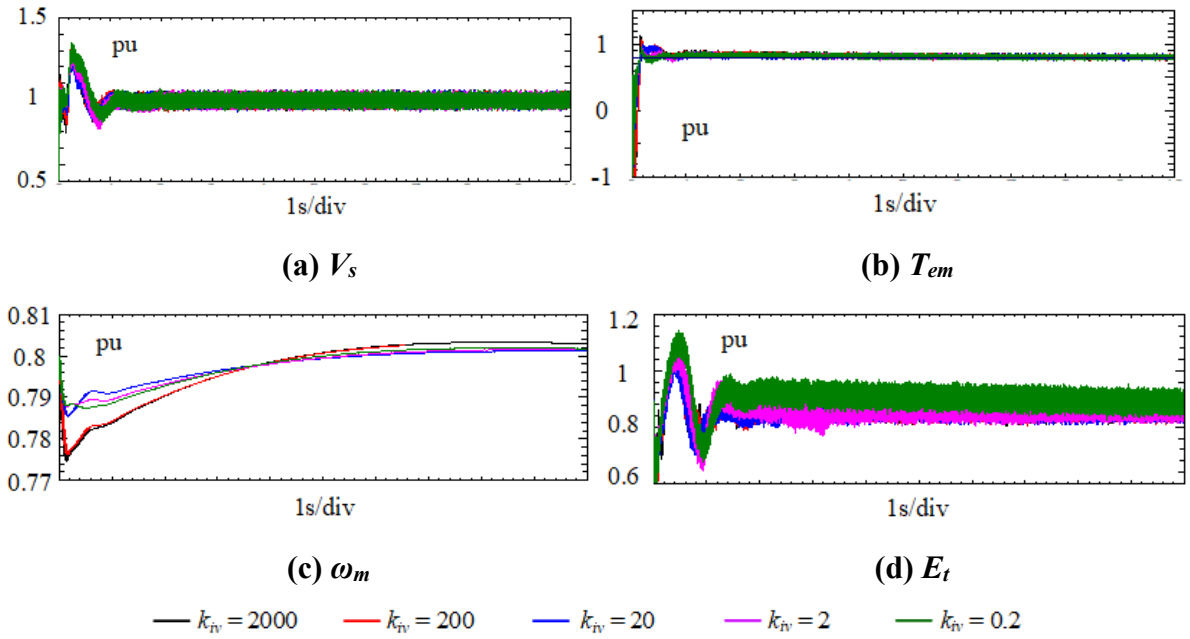

Fig. 5.27. Control effects of k_{iv} for PLL-VC on (a) V_s (b) T_{em} (c) ω_m (d) E_t.

It can be seen from Figs. 5.26 and 5.27 that except slight differences in the tracking speeds and final values, no matter how k_{iq} and k_{iv} change, the SIVV amplitude dynamics and system performance are almost maintained at a constant level.

Therefore, the control parameter that mainly affects the system performance is k_{pp}, and it has to be carefully designed for PPD-SPS control. As an alternative, ESVO-VC can be applied to simplify the equivalent inertia of SIVV to handle the challenge of tuning PLL controller gain.

5.6 Summary

In this chapter, the small-signal models for PPD-SPS propulsion subsystem are presented in two different ways based on the internal voltage vector concept. Firstly, the BTBPC average model is used for system-level analysis with controlled voltage sources, and a small-signal model for studying the internal voltage phase-amplitude dynamics in the electromechanical control timescale is proposed and illustrated. Secondly, this chapter proposes a small-signal PPD-SPS propulsion subsystem model in the electromechanical control timescale by regarding the DFIM stator and converter as an SIVV. The effects of rotor speed control, reactive power control and PLL are taken into consideration for deriving the transfer functions for the internal voltage phase-amplitude dynamics in the electromechanical control timescale. Moreover, as an alternative to the traditional PLL-VC, ESVO-VC is proposed to properly control the system without tuning the PLL controller gains.

From the derived DFIM internal voltage and SIVV phase-amplitude motion equations, and from the obtained simulation results, the following key points are obtained:

For the simulation study with the average BTBPC model:

1) The PPD-SPS propulsion subsystem with the BTBPC average model can correctly simulate the system operation without considering the fast transients caused by switching behaviours.

2) The PLL proportional gain k_{pp} should be large enough to avoid unstable operation, while the PLL integral gain k_{ip} needs to be small enough to ensure fast tracking performance.

3) A larger rotor speed controller integral gain $k_{i\omega}$ leads to more serious oscillations and longer time to achieve stable operation, but higher speed tracking performance is obtained.

4) The effects of reactive power control cannot be explicitly investigated when the BTBPC average model is used.

For the small-signal model with the propulsion subsystem functioning as an SIVV, and the simulation study with the detailed switching model for BTBPC:

1) In the electromechanical control timescale, the SIVV phase dynamics is related to both PLL control and rotor speed control, while the SIVV amplitude dynamics is relevant with reactive power control.

2) The PLL proportional controller gain k_{pp} needs to be carefully designed in order to obtain satisfactory SIVV phase dynamics and tracking performance.

3) Smaller values of $k_{p\omega}$ and $k_{i\omega}$ contribute to more precise tracking of the rotor speed.

4) The changes in the integral gains k_{ip}, k_{iq} and k_{iv} do not significantly influence the PPD-SPS propulsion subsystem operation characteristics.

5) Applying ESVO-VC simplifies the equivalent inertia of SIVV and avoids tuning PLL controller gains. At the same time, good system performance still can be achieved.

Chapter 6 Performance Analysis of A Partially Power Decoupled AC-DC Hybrid Shipboard Power System

In this chapter, the system performance analysis of the proposed partially power decoupled shipboard power system (PPD-SPS) is carried out in both Matlab/Simulink and real-time digital simulator (RTDS) with control-hardware-in-the-loop (CHIL) setup. As the power generation unit (PGU) of PPD-SPS plays an important role of providing main power supply to the system, its stable operation is of great significance for maintaining good overall system performance. However, due to the effects of aging and harsh operating environments, deviations may occur in PGU parameters, which influences its output characteristics and further deteriorates the PPD-SPS system performance. The parameter deviations in the synchronous generator (SG) and its excitation system (EXS) are studied to evaluate the effects on system performance. Different degrees of parameter deviations are applied to 16 important parameters of PGU for parameter sensitivity analysis. Three parameter deviation effect indicators (PDEIs) are defined to illustrate the effects on the SG terminal voltage and output active power. Meanwhile, the increasing rates of PDEIs when applying different degrees of parameter deviations for the key parameters are analysed. Then, simulation studies are carried out in Matlab/Simulink to investigate the parameter deviation effects on system performance in detail when varying the values of the two most critical system parameters. Deviations in the corresponding parameters are implemented for a PPD-SPS in the high-speed operation mode. Therefore, some vital clues on SG and EXS parameter identification for PPD-SPS are obtained.

On the other hand, the system performance of PPD-SPS is to be evaluated in a simulation environment established by RTDS with CHIL setup, which imitates exactly an actual operation scenario. In the work described, the power circuits of SG and back-to-back power converter (BTBPC) are built up in RTDS software, with the rotor of doubly-fed induction machine (DFIM) simulated as a three-phase voltage source, and the stator of DFIM is not taken into consideration. The corresponding control algorithms for the BTBPC are implemented in CHIL set-up. The verification process is carried out step by step for the control of SSC, control of LSC, and control of the whole BTBPC in the proposed PPD-SPS with noises and time delays.

6.1 Parameter Deviation Effect Indicator

The accuracy of SG and EXS parameters is of paramount importance for the steady and reliable operation of the proposed PPD-SPS. However, variations in theses parameters are inevitable in practice. In this section, 16 important parameters for SG (X_d, X_d', X_d'', X_q, X_q'', X_l, T_{do}', T_{do}'' and T_{qo}'') and its EXS (K_a, T_a, K_e, T_e, K_f, T_f, T_r) are taken into account. Different degrees of deviations of each parameter are applied to study the effects on the output terminal voltage V_T and active power P_T of SG. Since the input of SG is the rotor angular speed, there is no need to define the inertia and friction factor. In addition, the rotor type of the applied SG is salient-pole, under which circumstance the q-axis transient reactance X_q' is not available. The parameter values used for the SG and its EXS are displayed in the Appendix.

The evaluation of parameter deviation effects is carried out according to three PDEIs, which are the average deviation (*AVGD*), standard deviation (*STDEV*), and the average square root of quadratic sum (*ASRQS*). The output signals are measured for the cases with and without deviations for a specific parameter in Matlab/Simulink, and 50001 points are sampled to obtain the PDEIs for parameter sensitivity analysis.

AVGD is used to evaluate the average error between the output signal value (*OSV*) with parameter deviation and that without parameter deviation:

$$AVGD = \frac{1}{N}\sum_{i=1}^{N}(OSV_i - OSV_{iPD}) \tag{6-1}$$

where *N* is 50001 in this chapter; *i* indicates the specific sampling point; and *iPD* is used to represent the value with parameter deviation at the sampling point *i*.

Besides, *STDEV* is applied to measure the overall deviation of *OSV* at different time points from the average error obtained in (6-1). Therefore, the dispersion degree of samples can be obtained for different degrees of parameter deviation in each parameter.

$$STDEV = \sqrt{\frac{1}{N}\sum_{i=1}^{N}[(OSV_i - OSV_{iPD}) - AVGD]^2} \tag{6-2}$$

Moreover, in order to determine the absolute error between the values of *OSV* with and without parameter deviation, the definition of *ASRQS* is put forward, which has a positive correlation with the absolute error.

$$ASRQS = \frac{1}{N}\sqrt{\sum_{i=1}^{N}(OSV_i - OSV_{iPD})^2} \tag{6-3}$$

During the simulation process, *OSV* is replaced by either V_T or P_T.

The results to be derived from the simulation studies on the parameter deviation effects of PGU in the proposed PPD-SPS can be useful for identifying the most critical PGU parameters for keeping stable system operation. By combining the obtained results with parameter identification strategies, non-ideal system performance can be predicted and the respective remedial measures are likely to be undertaken in advance, which is beneficial for achieving reliable and safe system operation.

6.2 Simulation Results in Matlab/Simulink and Discussion

The PPD-SPS discrete model with the time step of 5μs is simulated in Matlab/Simulink to investigate its operation with SG and EXS parameter deviations. Since the transmission lines for PPD-SPS are much shorter than those of a grid connected power system, the impedances of transmission lines are neglected. The details of system parameters are displayed in the Appendix.

With all the three aforementioned PDEIs taken into account, the parameter deviation effects can be studied in detail. The simulation results of *AVGD*, *STDEV* and *ASRQS* for V_T and P_T in the cases of different degrees of parameter deviations for SG and its EXS are shown in Figs. 6.1 – 6.3. The PDEIs for V_T and P_T are illustrated as blue squares and red dots, respectively. The units of all these values are in pu.

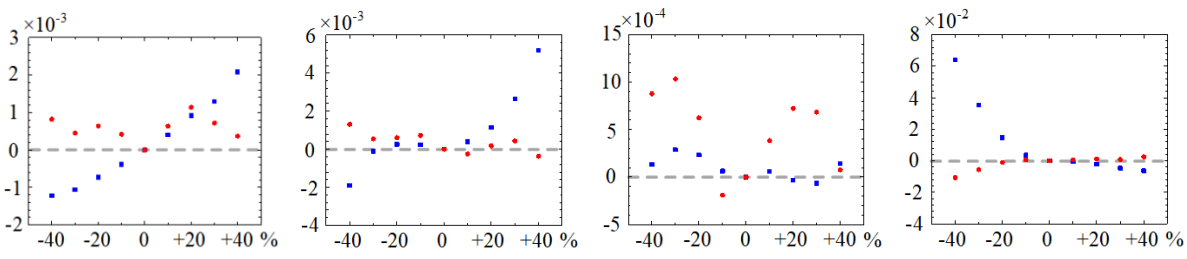

(a) X_d **(b)** X_d' **(c)** X_d'' **(d)** X_q

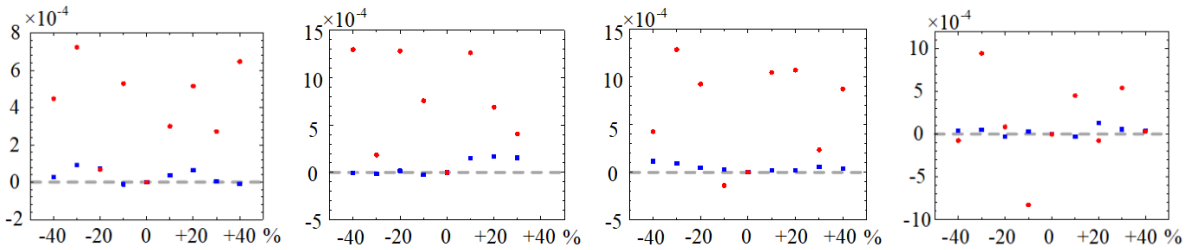

(e) X_q'' **(f)** X_l **(g)** T_{do}' **(h)** T_{do}''

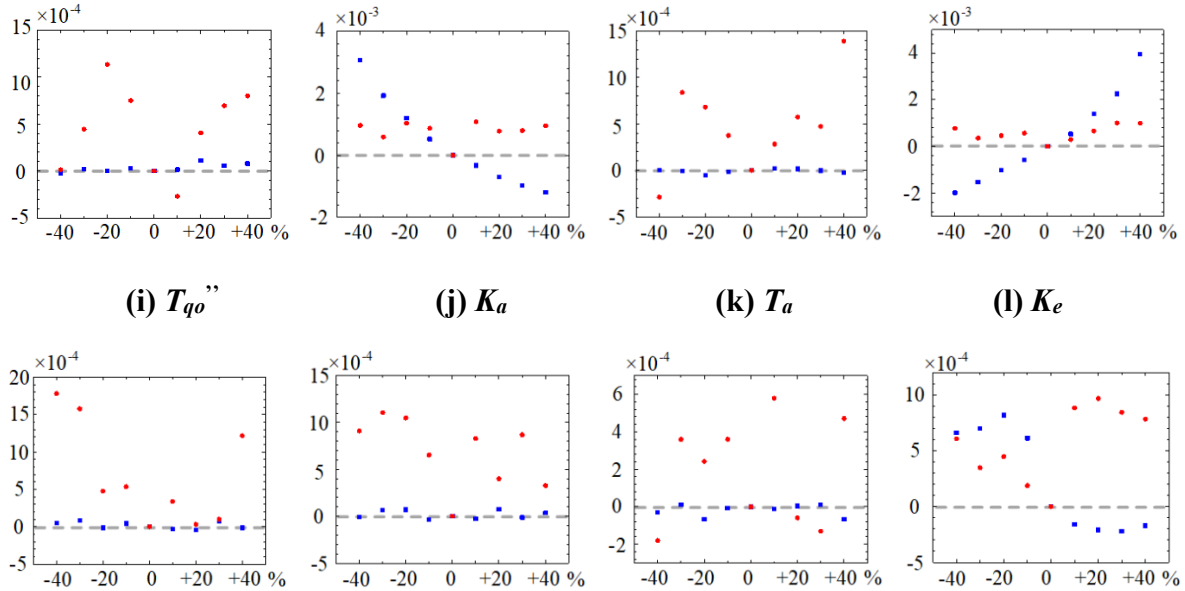

(i) T_{qo}'' (j) K_a (k) T_a (l) K_e

(m) T_e (n) K_f (o) T_f (p) T_r

Fig. 6.1. *AVGD* for different degrees of parameter deviations of the 16 SG and EXS parameters for V_T (blue squares) and P_T (red dots).

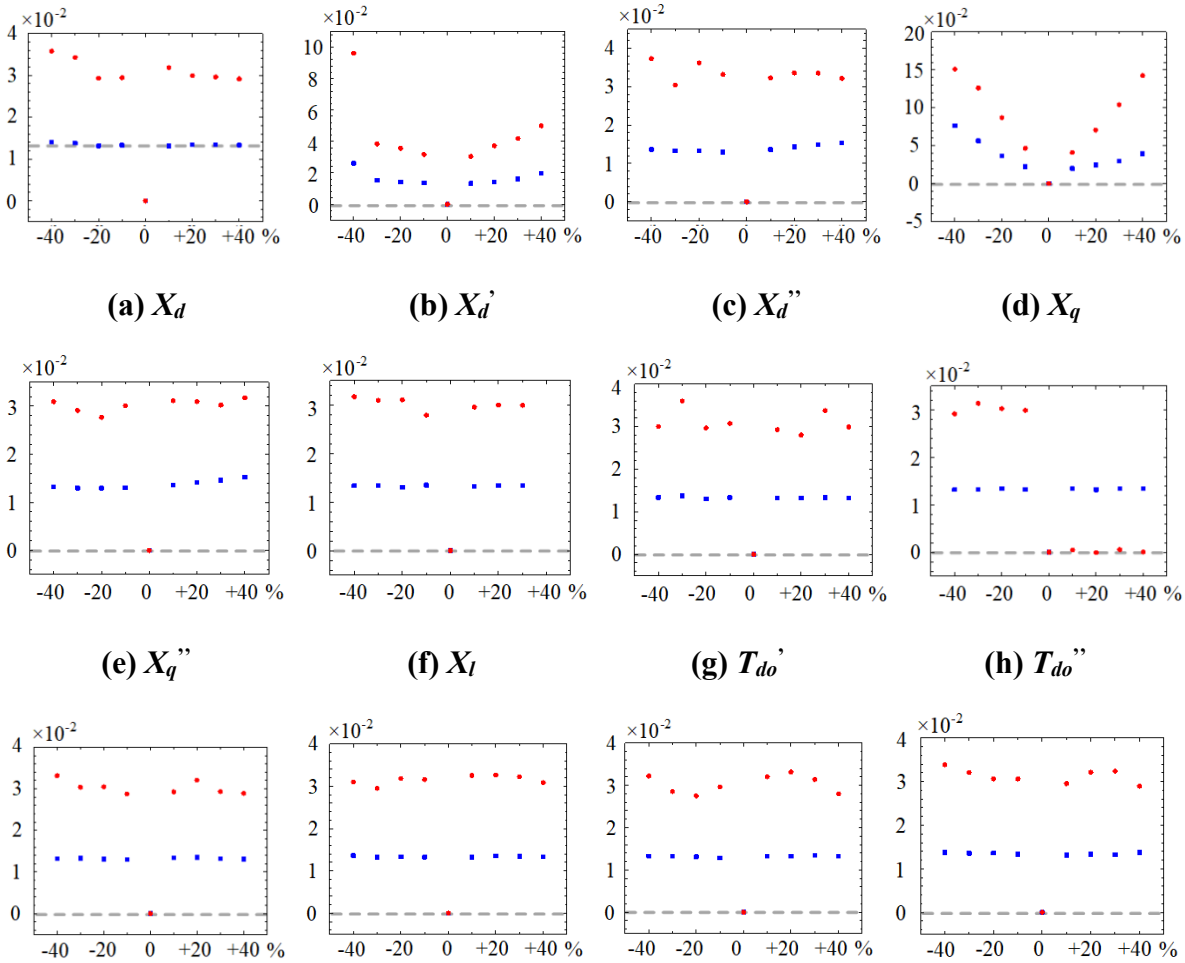

(a) X_d (b) X_d' (c) X_d'' (d) X_q

(e) X_q'' (f) X_l (g) T_{do}' (h) T_{do}''

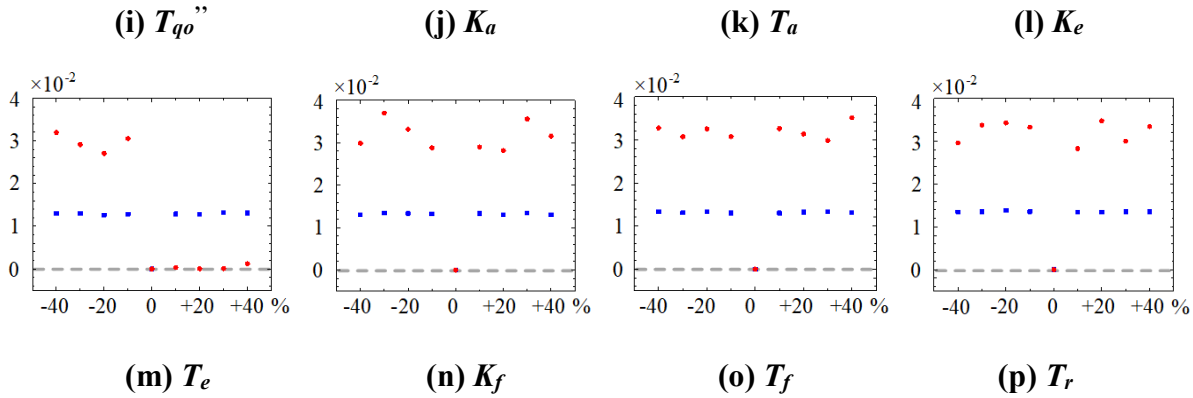

Fig. 6.2. *STDEV* for different degrees of parameter deviations of the 16 SG and EXS parameters for V_T (blue squares) and P_T (red dots).

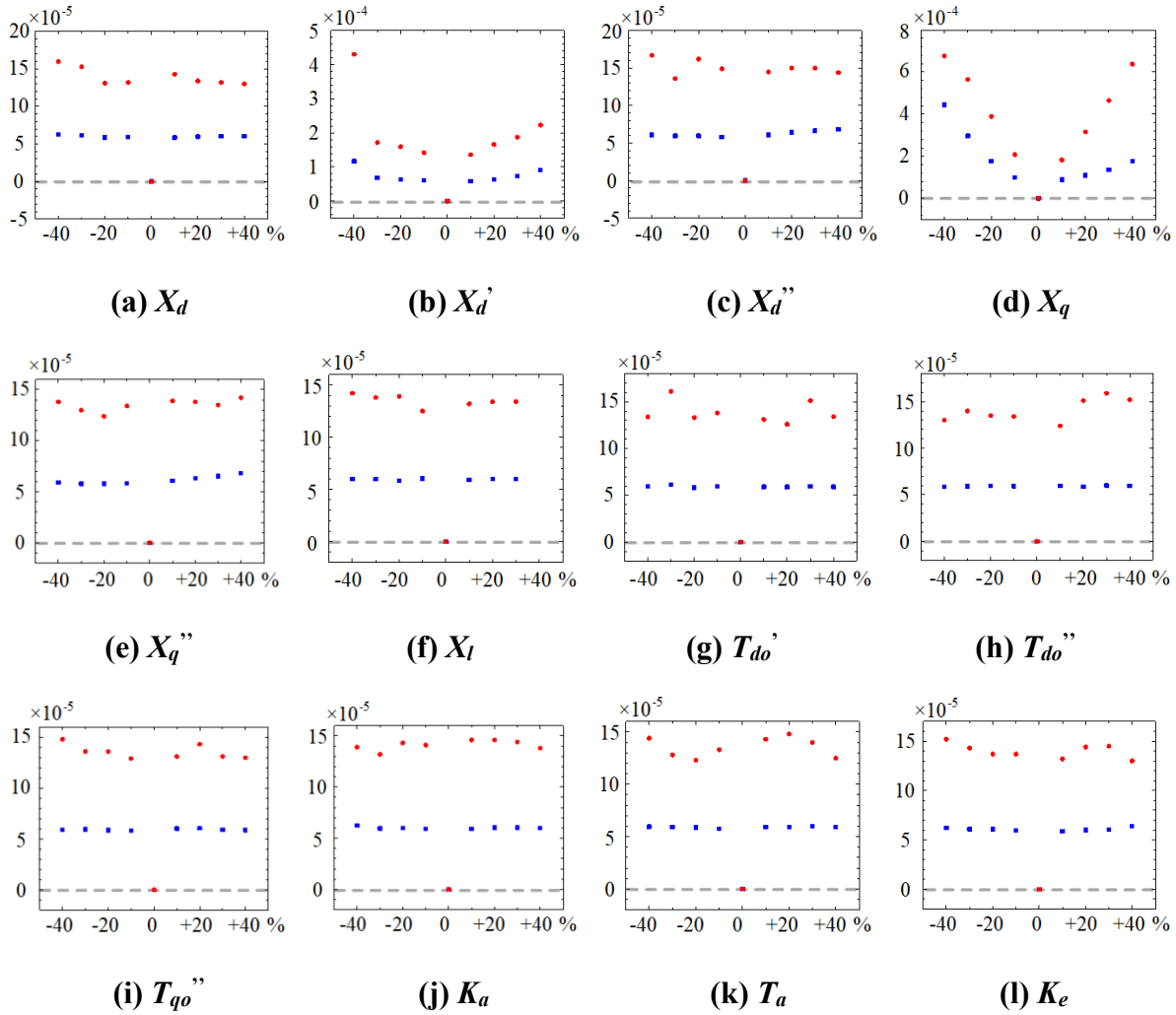

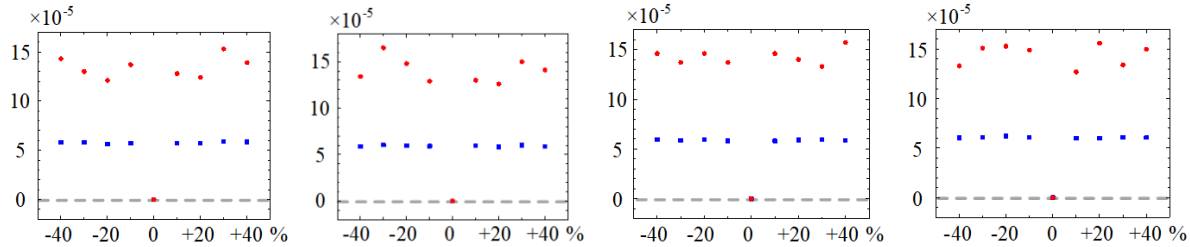

(m) T_e **(n) K_f** **(o) T_f** **(p) T_r**

Fig. 6.3. *ASRQS* for different degrees of parameter deviations of the 16 SG and EXS parameters for V_T (blue squares) and P_T (red dots).

The degrees of parameter deviations for each parameter are set as -40%, -30%, -20%, -10%, +10%, +20%, +30% and +40% respectively from the actual value to study the effects of parameter deviation on the stator terminal voltage V_T and output active power P_T. It can be seen from Figs. 6.1 – 6.3 that varying the degrees of parameter deviations of X_d' and X_q affects the values of PDEIs for V_T and P_T significantly, and the degrees of parameter deviations of X_d'' and K_e are mainly related to the variations of PDEIs for V_T. In addition, when applying different degrees of parameter deviations for X_d and K_a, the values of *AVGD* for V_T are obviously changed. Nevertheless, parameter deviations in the other parameters hardly influence the SG output performance. Therefore, the key parameters to be further discussed are X_d', X_q, X_d'', K_e, X_d and K_a. Moreover, the effects of parameter deviation on P_T are generally more significant than those on V_T, as can be seen from most diagrams in Figs. 6.1 – 6.3, especially for *STDEV* and *ASRQS*.

The parameter deviations of X_d' obviously influence *STDEV* and *ASRQS* for both V_T and P_T of SG. When applying different degrees of parameter deviations for X_q, *AVGD* for V_T is also significantly affected. In addition, the parameters X_d'', K_e, X_d and K_a only have obvious impacts on the increasing rates of some PDEIs for V_T when the degree of parameter deviation varies. By increasing the degree of parameter deviation in either the negative or positive way, the increasing rates of these PDEIs vary for different regions of degrees of parameter deviation

variations for each parameter. In order to analyse the phenomenon in detail, the increasing rates of PDEIs with respect to degrees of parameter deviation variations of X_d', X_q, X_d'', K_e, X_d and K_a are displayed in Figs. 6.4 – 6.6, respectively.

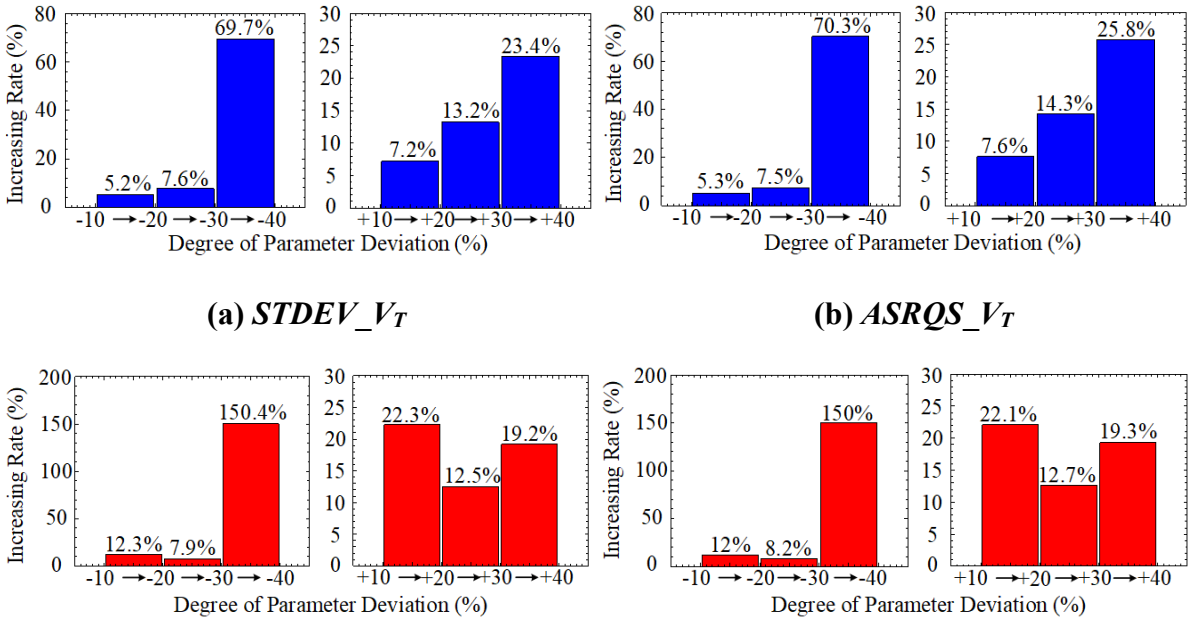

(a) *STDEV_V_T* **(b) *ASRQS_V_T***

(c) *STDEV_P_T* **(d) *ASRQS_P_T***

Fig. 6.4. PDEI increasing rates with respect to the degree of parameter deviation variations of X_d'.

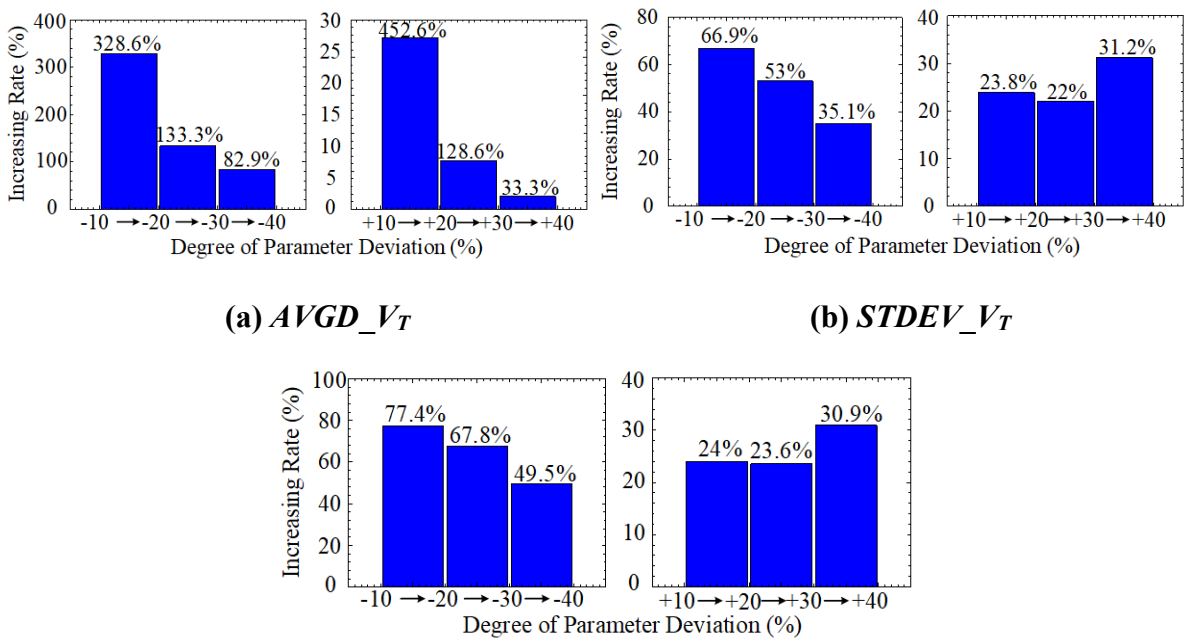

(a) *AVGD_V_T* **(b) *STDEV_V_T***

(c) *ASRQS_V_T*

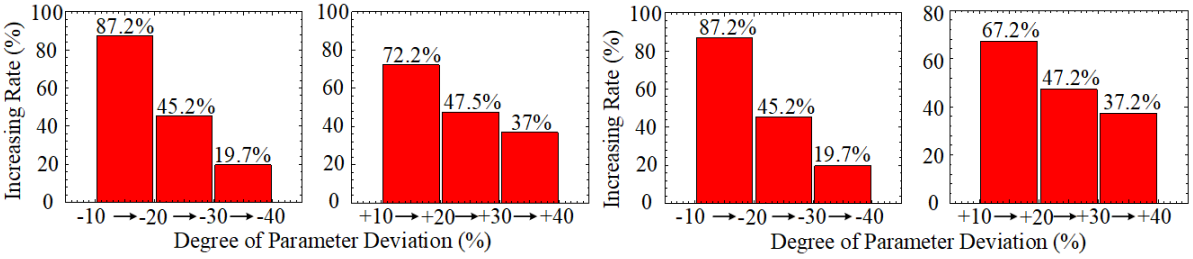

(d) *STDEV_PT* **(e) *ASRQS_PT***

Fig. 6.5. PDEI increasing rates with respect to the degree of parameter deviation variations of X_q.

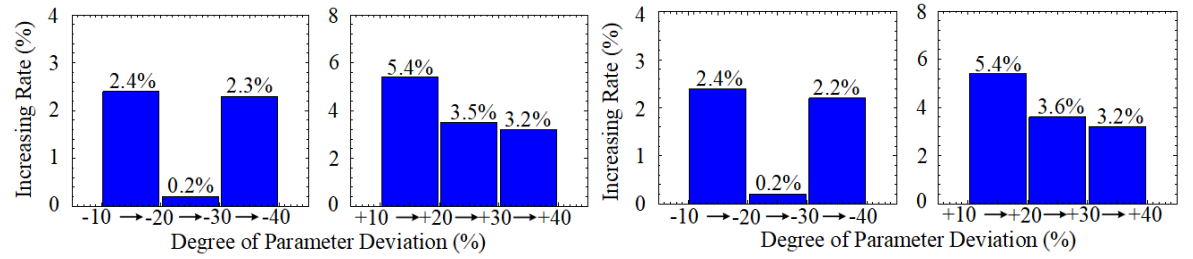

(a) *STDEV_VT* of X_d" **(b) *ASRQS_VT* of X_d"**

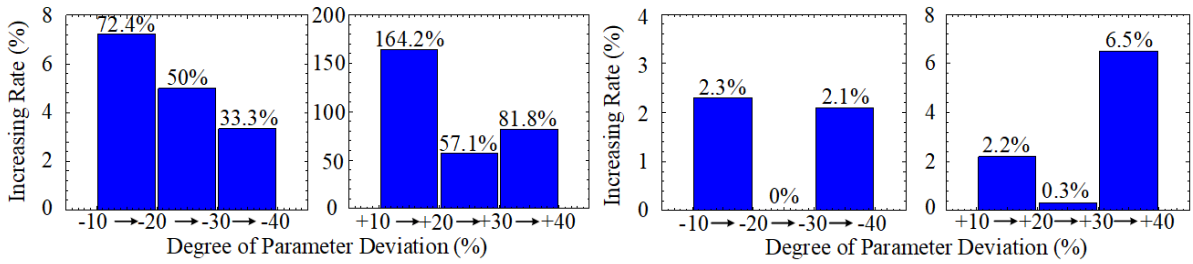

(c) *AVGD_VT* of K_e **(d) *ASRQS_VT* of K_e**

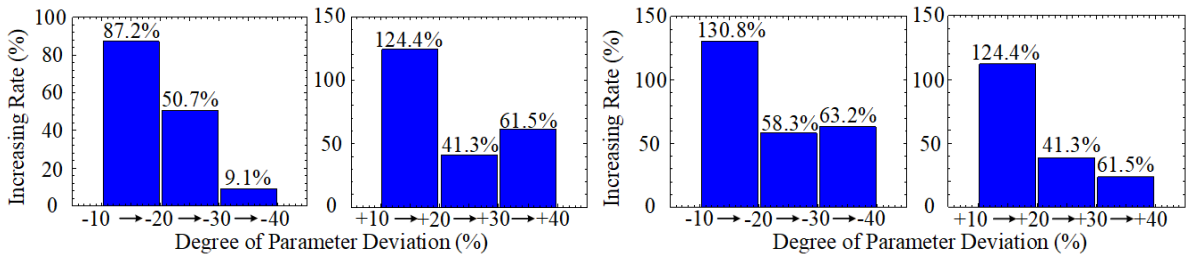

(e) *AVGD_VT* of X_d **(f) *AVGD_VT* of K_a**

Fig. 6.6. PDEI increasing rates with respect to the degree of parameter deviation variations of X_d", K_e, X_d and K_a.

It can be seen from Fig. 6.4 that with the increase of degree of parameter deviation for X_d', the increasing rates of *STDEV* and *ASRQS* for V_T keep rising, while those in the variation regions of (-20%) to (-30%) and (+20%) to (+30%) are the lowest ones for P_T. Additionally, the increasing rates in the variations regions of (-30%) to (-40%) are much higher than the others for both the cases of PDEIs for V_T and P_T. In terms of X_q, the increasing rates keep falling for all the PDEIs shown in Fig. 6.5 except the positive variation directions for *STDEV* and *ASRQS* for V_T. Besides, the increasing rates of *AVGD* for V_T are astonishingly high for the variation regions of (-10%) to (-20%) and (+10%) to (+20%). Therefore, it can be deduced that the system performance will be significantly affected even if a slight degree of parameter deviation is applied to X_q.

From Fig. 6.6, it can be seen that changing the degree of parameter deviation of X_d'' has little impact on the increasing rates of the corresponding PDEIs. In addition, in spite of a slightly high increasing rate (6.5%) in the region of (+30%) to (+40%) for the degrees of parameter deviation of K_e in the case of *ASRQS* for V_T, the overall impact of degrees of parameter deviation of K_e on the PDEI is negligible. The trends of increasing rate variation are the same for *AVGD* for V_T of K_e and X_d, and the highest values appear in the regions that are closest to the points of actual values, which is also the case for *AVGD* for V_T of K_a. Therefore, the deviations of V_T from the actual value will be obvious when applying a small degree of parameter deviation for K_e, X_d and K_a.

Since the parameter deviations of X_d' and X_q play the most important role in affecting the output voltage and active power of SG, the system performance is strongly related to the degrees of deviation of these two parameters. The simulation results of key system variables in the proposed PPD-SPS are obtained when applying different degrees of parameter deviations for X_d' and X_q, which are displayed in Figs. 6.7 and 6.8, respectively. Note that the SG variables are endowed with the subscript "*_SG*", while the others correspond to the DFIM variables.

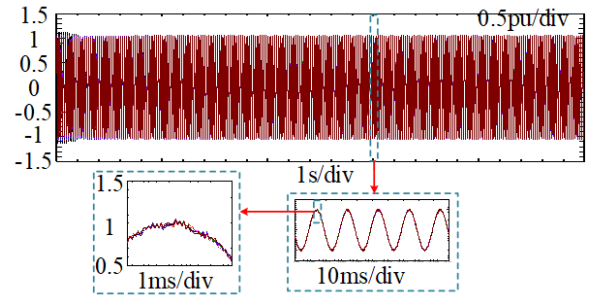

(a) v_{sa_SG}

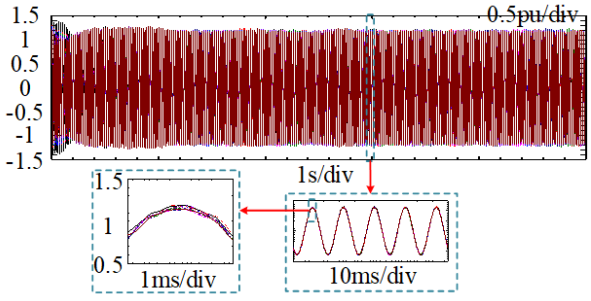

(b) i_{sa_SG}

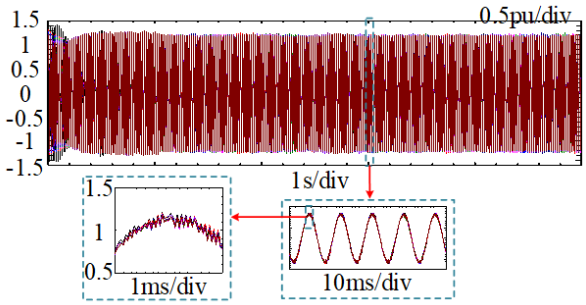

(c) i_{ra}

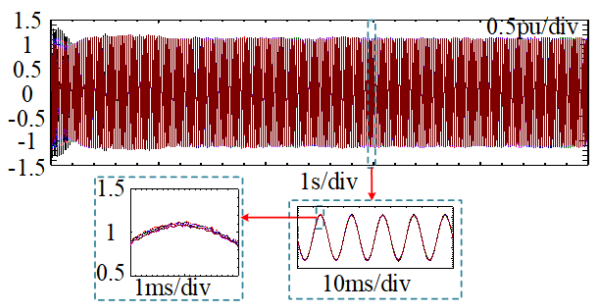

(d) i_{sa}

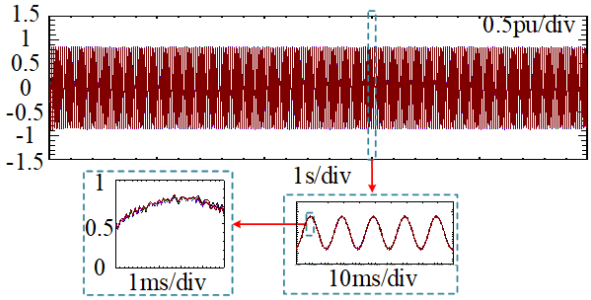

(e) i_{ssa}

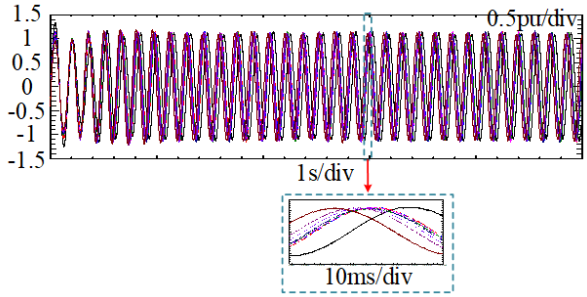

(f) i_{ra}

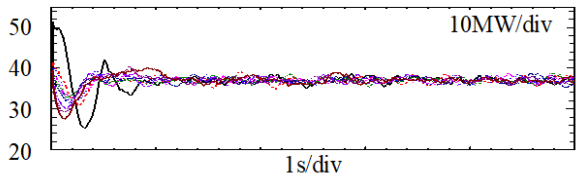

(g) P_t

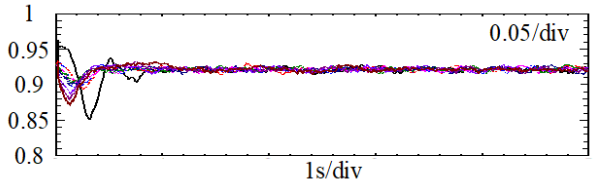

(h) PF

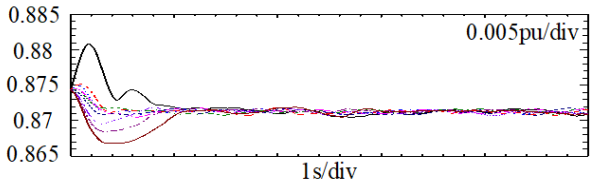

(i) ω_m

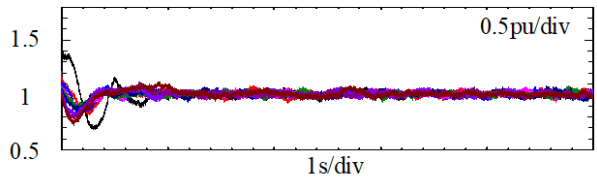

(j) T_{em}

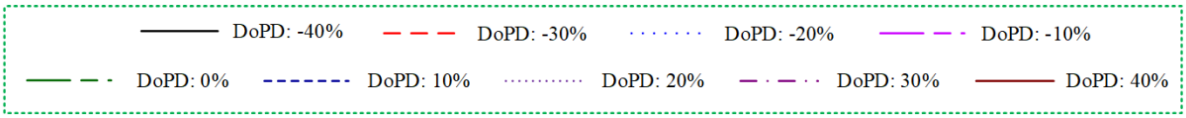

Fig. 6.7. Simulation results of PPD-SPS with different degrees of parameter deviations (DoPD) for X_d'.

For the convenience and simplicity of analysis, only the phase-A voltage and current waveforms are used to illustrate the system operation. As can be seen from Fig. 6.7(a), the phase-A stator voltages with different degrees of parameter deviations align with each other very well, except that the fluctuations in the signals with larger degrees of parameter deviations are larger, which caters to the deductions in the previous paragraphs. As a result, the current waveforms also have the similar performance, as can be seen from Figs. 6.7(b) – (e). Owing to the low frequency of three-phase rotor currents, the deviations of i_{ra} with the degrees of parameter deviations of (-40%) and (+40%) from those with other values are obvious. From Figs. 6.7 (g) and (h), the oscillations of P_t and PF can be clearly observed at the beginning for the cases with large degrees of parameter deviations, while their values with different degrees of parameter deviations converge as time goes by. The situations are similar for the DFIM rotor speed ω_m and electromagnetic torque T_{em}, which are displayed in Figs. 6.7(i) and (j).

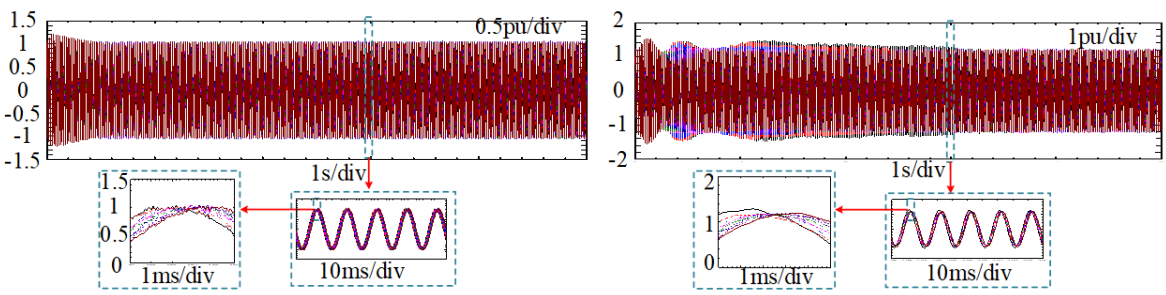

(a) v_{sa_SG} **(b) i_{sa_SG}**

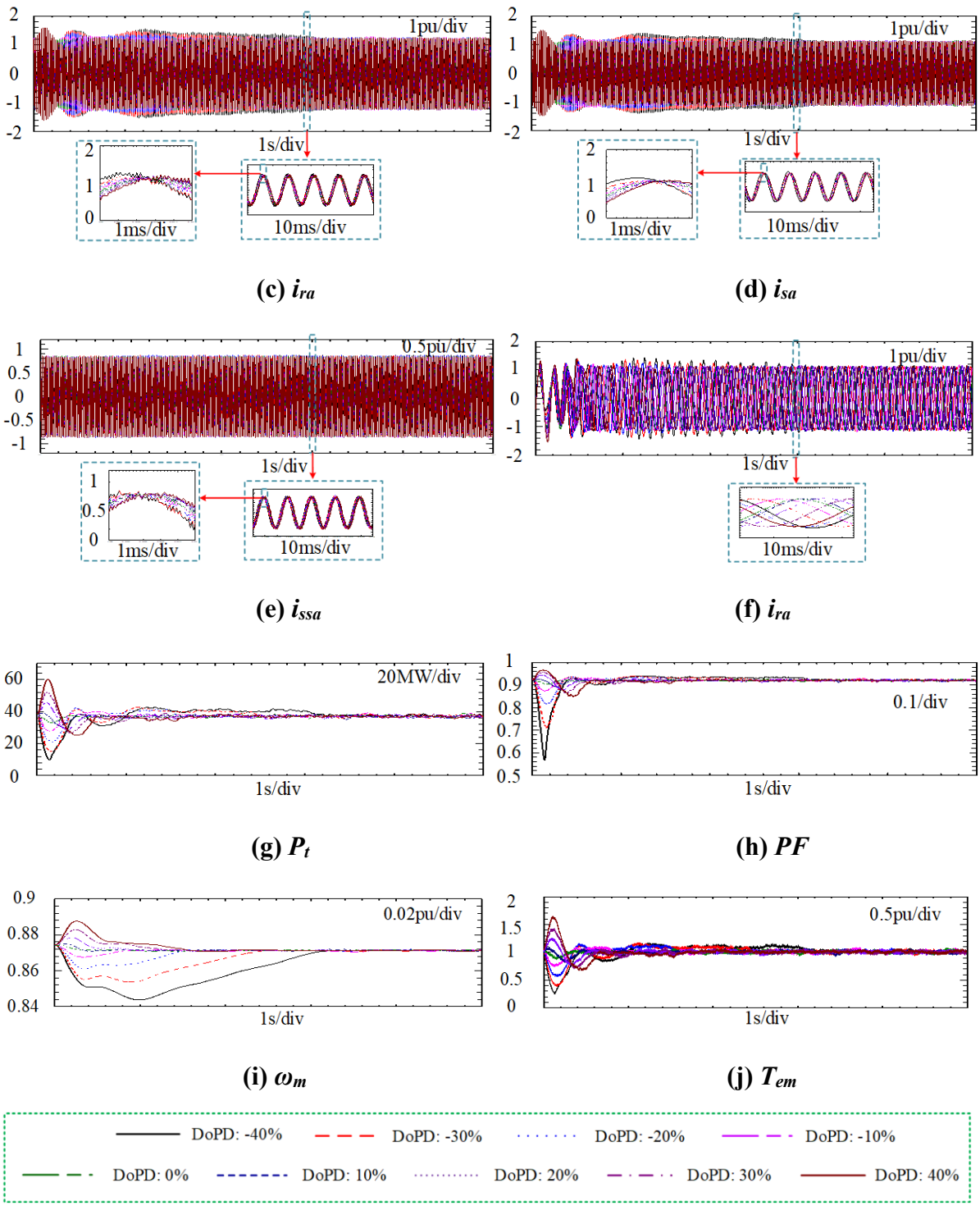

Fig. 6.8. Simulation results of PPD-SPS with different degrees of parameter deviations (DoPD) for X_q.

Compared with the simulation results in Fig. 6.7, it can be seen from Fig. 6.8 that the phase-A voltage and current waveforms with different degrees of parameter deviations distinctly deviate from each other, as the degrees of parameter deviation of X_q is positively correlated with *AVGD*

for V_T. In addition, the oscillations in the total active power P_t, power factor PF, rotor speed ω_m and electromagnetic torque T_{em} are much larger than those in the previous case for each degree of parameter deviation. Moreover, it takes longer time for ω_m and T_{em} to return back to the steady-state values. Therefore, the simulation results in Fig. 6.8 correspond to the descriptions for Figs. 6.1– 6.6.

6.3 RTDS Results with CHIL Setup

To evaluate the control performance of the proposed PPD-SPS in almost exactly an actual operation environment, the power circuits of SG and BTBPC are simulated in RTDS software, with the control strategy implemented in the CHIL setup at SmartRUE, ICCS-NTUA, Greece. The variables to be used for controlling the BTBPC are output from RTDS software to the target PC, and at the same time, the control signals for the power switches in the BTBPC in the power circuit are input to RTDS software from the target PC. The setup of the simulation platform is shown in Fig. 6.9.

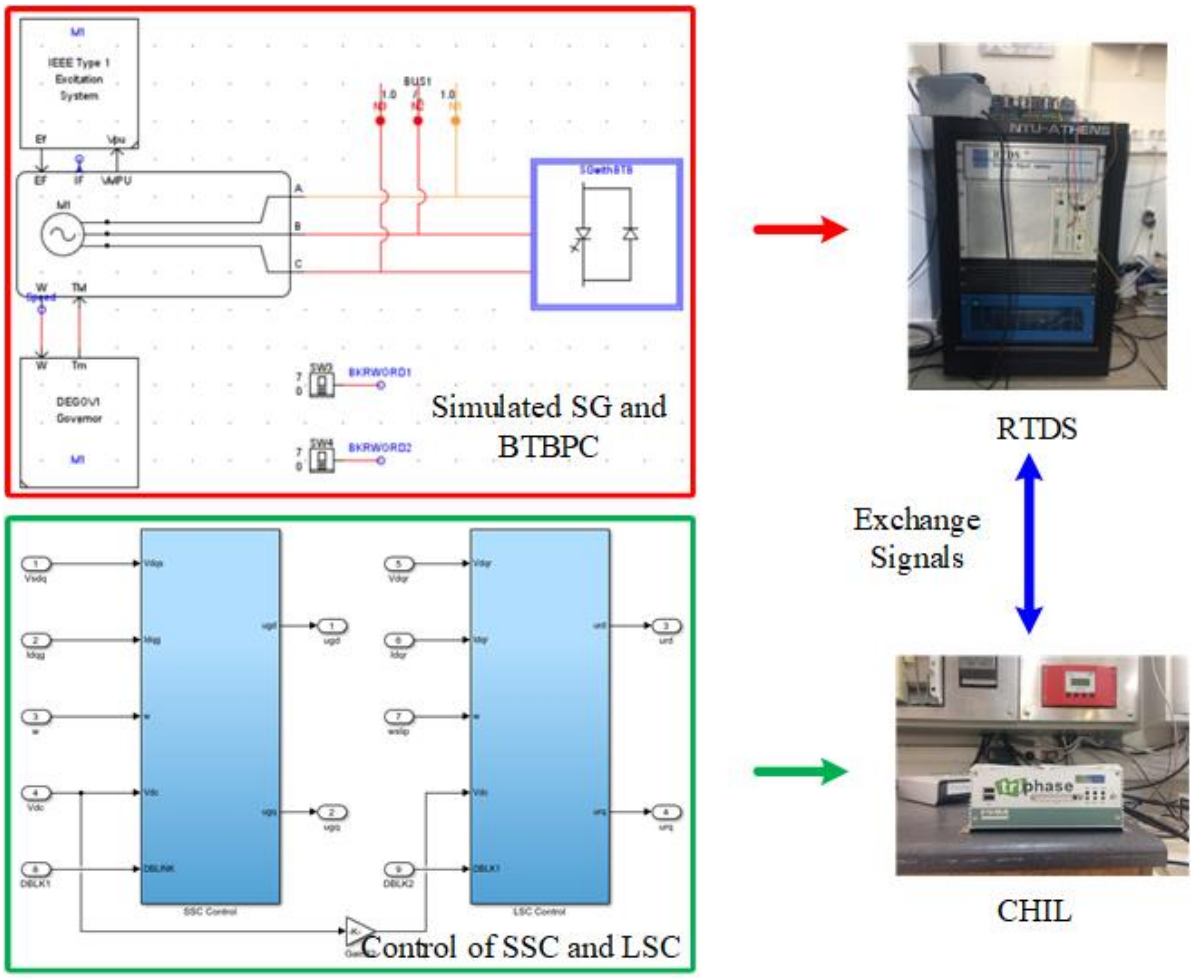

Fig. 6.9. RTDS simulation platform with CHIL setup.

The synchronous angular frequency and angle are obtained by using a phase-locked loop (PLL) for the three-phase stator voltages of SG, and the rotor angular speed and angle of DFIM are derived by PLL with the slip frequency. An IEEE Type 1 excitation system and a governor are used in RTDS software to control the SG. The Park and Inverse Park Transformation blocks are established in RTDS software, while the control blocks for BTBPC in the *dq* reference frame are built up in Simulink and implemented in the CHIL setup. The test is generally divided into three parts: 1) The control of SG connected with an SSC supplying the DC-bus capacitor is to be verified to obtain a stable DC-bus voltage and sinusoidal three-phase grid-side AC currents. 2) The control of LSC connected to a three-phase voltage source is to be verified to achieve good tracking performances for the *dq* currents and active/reactive power. 3) The SG

connected with BTBPC that supplied by a three-phase voltage source is to be controlled to achieve all the targets described in 1) and 2). With the aforementioned step-by-step simulation procedure, the performance of SG and that of BTBPC can be evaluated roundly in a nearly real operating environment to establish the basis for applying the proposed PPD-SPS in practice in the future.

The implementation of the SG connected three-phase power rectifier aims to verify the DC bus voltage control scheme in the proposed PPD-SPS, and the current control performance in the grid-connected three-phase power converter with DC voltage supply is to be demonstrated by good tracking performance. In the RTDS software, the rotor of DFIM is replaced by a three-phase voltage source with the slip frequency, and the DC bus is supplied by an SG through the SSC. Therefore, the power circuit of SG connected with BTBPC is established. The two aforementioned targets will then be achieved by tuning the controller parameters. During the controller parameter tuning process, two switches are added in the “Runtime” interface of RTDS software to enable or disable the control of the SSC and LSC. The LSC is disabled at first, and the SSC is controlled to ensure the DC-bus voltage is maintained at the rated value. Afterwards, the control of LSC is activated to achieve the desirable rotor-side active and reactive powers for DFIM.

The procedures of the RTDS simulations with CHIL setup are shown below.

1) Establish the power circuit of a three-phase AC voltage source feeding an SSC to charge the DC-bus capacitors in RTDS software.

2) Set up the voltage source, Park Transformation, Inverse Park Transformation, power calculation, PLL, D/A and A/D blocks in RTDS software for the system in 1).

3) Set up the DC-bus voltage and grid current control blocks in Simulink with Triphase input/output blocks.

4) Set appropriate values for the variable scaling used in the digital/analog (D/A) and analog/digital (A/D) blocks in RTDS software to make sure the readings of measurements in RTDS software and Simulink are the same.

5) Compile the draft in RTDS software, and build up and activate the control model in Simulink by using an external target PC.

6) Run the simulation and tune the PI control parameters to obtain acceptable control performance for the system.

7) Display the plots in the "Runtime" interface of RTDS software.

8) Implement a step change in the reference value of current during the simulation process, and then save the obtained waveforms.

9) Establish the power circuit of an SG with Type 1 exciter and governor that feeds the SSC to charge the DC-bus capacitors in RTDS software.

10) Set up the voltage source, Park Transformation, Inverse Park Transformation, power calculation, PLL, D/A and A/D blocks in RTDS software for the system in 9).

11) Repeat Steps 3) to 8) for the power system in 9).

12) Establish the power circuit of LSC with DC voltage supply that connects to a three-phase power grid in RTDS software.

13) Set up the voltage source, Park Transformation, Inverse Park Transformation, power calculation, PLL, D/A and A/D blocks in RTDS software for the system in 12).

14) Repeat Steps 3) to 8) for the power system in 12).

15) Establish the power circuit of an SG with Type 1 exciter and governor that feeds a BTBPC that connects to a three-phase power grid in RTDS software.

16) Set up the voltage source, Park Transformation, Inverse Park Transformation, power calculation, PLL, D/A and A/D blocks in RTDS software for the power system in 15).

17) Repeat Steps 3) to 8) for the power system in 15).

6.3.1 Parameter Setup

The simulation studies in RTDS are carried out by using the parameters shown in Tables 6.1 to 6.3 for the proposed power system.

Table 6.1. Parameters of SG

Description	Value	Unit
Rated apparent power	36	MVA
Rated RMS line-to-line voltage	4.16	kV
Base angular frequency	50	Hz
Inertia constant	3.5	MWs/MVA
Synchronous Mechanical Damping	0	/
Stator leakage reactance	0.075	pu
d-axis unsaturated reactance	1.321	pu
d-axis unsaturated transient reactance	0.1685	pu
d-axis unsaturated sub-transient reactance	0.105	pu
q-axis unsaturated reactance	1.173	pu
q-axis unsaturated sub-transient reactance	0.09	pu
Stator resistance	0.036	pu
d-axis unsaturated transient open-circuit time constant	6.5	Second
d-axis unsaturated sub-transient open-circuit time constant	0.0241	Second
q-axis unsaturated sub-transient open-circuit time constant	0.0464	Second

Table 6.2. Parameters of IEEE Type1 excitation system

Description	Value	Unit
Voltage transducer time constant	0.02	Second
Voltage regulator gain	300	/

Voltage regulator time constant	0.001	Second
Maximum control element output	2	pu
Minimum control element output	-2	pu
Exciter field resistance line slope margin	1	pu
Exciter field time constant	0.0001	Second
Rate feedback gain	0.0001	pu
Rate feedback time constant	0.1	Second

Table 6.3. Power circuit parameters

Description	Value	Unit
Rated apparent power	36	MVA
Rated grid line-to-line voltage	4.16	kV
Rated rotor line-to-line voltage	4.16	kV
Grid-side base angular frequency	50	Hz
Rotor-side base angular frequency	10	Hz
Resistance of reactive power compensator	160.237	Ohms
Capacitance of reactive power compensator	320474.0741	MicroF
Resistance of grid-side filter	0.0014421	Ohms
Inductance of grid-side filter	0.14421	Henries
DC-bus capacitance	10000	MicroF
Rotor resistance	0.00769	Ohms
Rotor inductance	0.0235356	Henries
Rate feedback gain	0.0001	pu
Rate feedback time constant	0.1	Second
Valve switching voltage magnitude	4	kV
Valve switching current magnitude	4	kA
Valve RLD damping factor	0.7	pu

In order to appropriately control the BTBPC in RTDS, the measurements in CHIL should correspond to those in RTDS (control signals are in either pu or SI units). The scaling for the outputs from RTDS software is displayed in Table 6.4.

Table 6.4. Scaling for the output signals from RTDS software

Description	Value
Peak value of *dq* grid voltages for 5 Volts D/A out	16.983
Peak value of *dq* grid currents for 5 Volts D/A out	24.982
Peak value of synchronous angular speed for 5 Volts D/A out	1570.796327
Peak value of DC-bus voltage for 5 Volts D/A out	33.966
Peak value of *dq* rotor voltages for 5 Volts D/A out	16.983
Peak value of *dq* rotor currents for 5 Volts D/A out	160.237
Peak value of slip angular speed for 5 Volts D/A out	1570.796327
Peak value of power converter control signal for 5 Volts D/A out	315

6.3.2 Simulation Results for Three-Phase Voltage Source Feeding SSC

At the first stage, the influence of SG parameters is not taken into account, and the SG is regarded as a stable three-phase grid voltage source that supplies power to the PPD-SPS propulsion subsystem. The control of SSC is enabled at 2s in the simulation, and the simulation results are displayed in Figs 6.10 & 6.11.

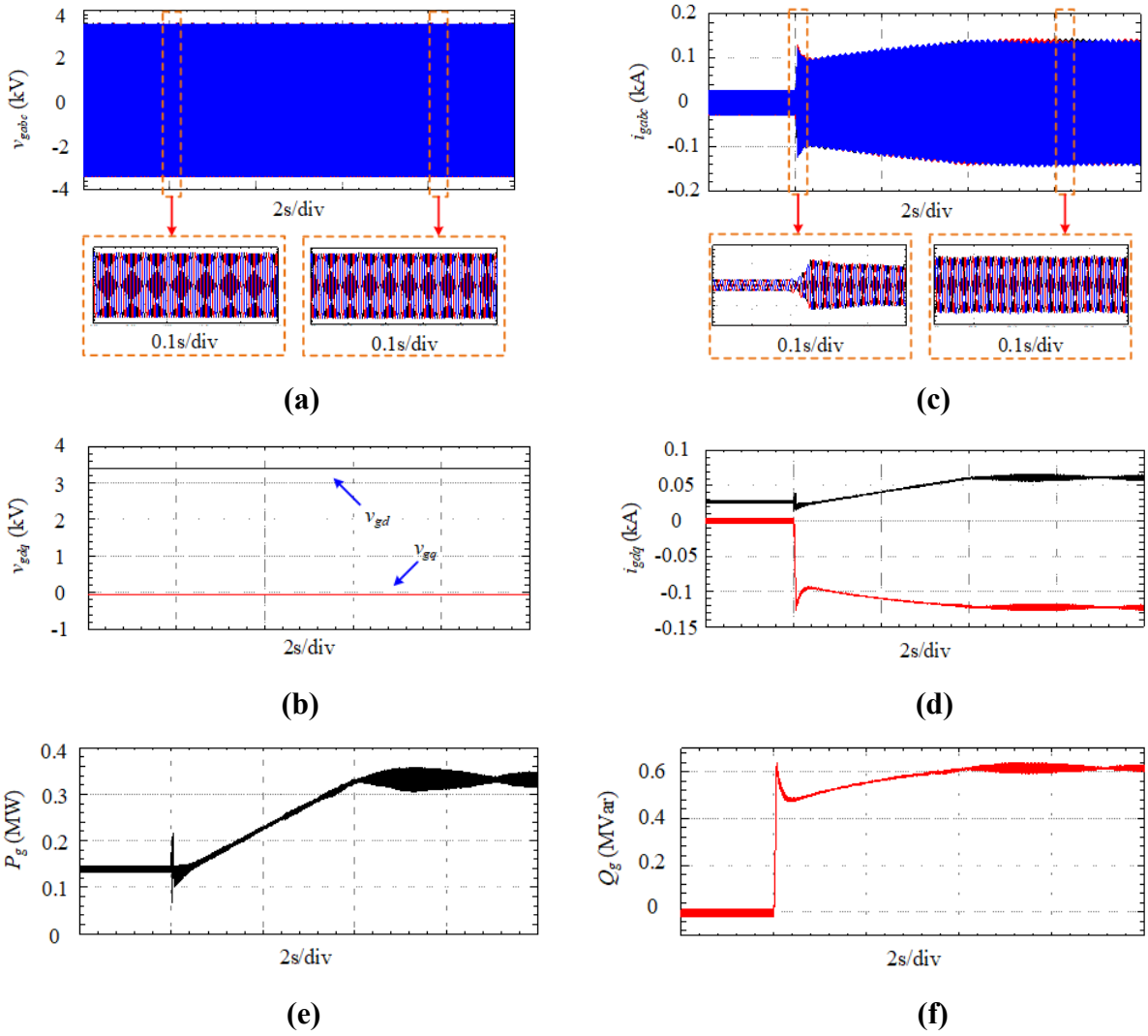

Fig. 6.10. Simulation results for the variables of three-phase voltage source by activating the SSC control at 2s.

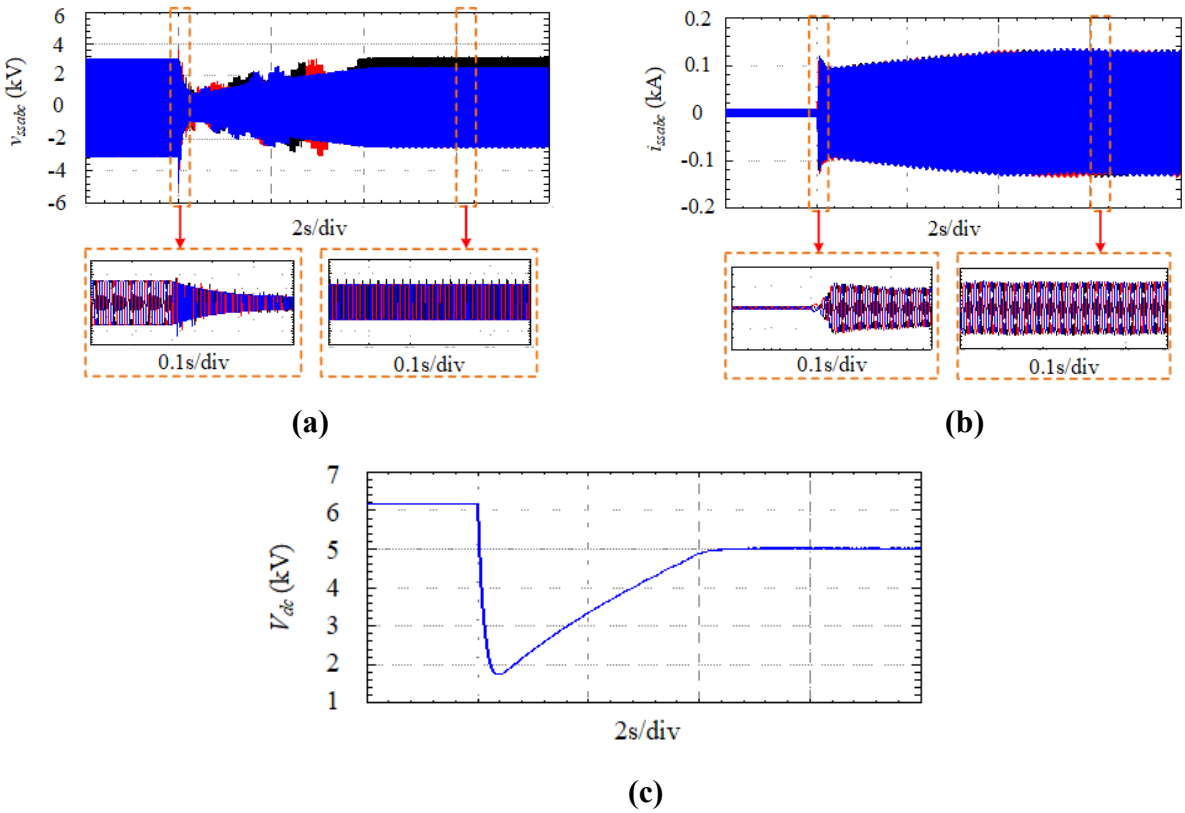

Fig. 6.11. Simulation results for the variables of SSC with a three-phase voltage supply by activating the SSC control at 2s.

It can be seen from Fig. 6.10 that the grid three-phase voltages are kept in almost sinusoidal waveforms during the whole simulation process, and the decoupling between the *dq* grid voltages v_{ssd} and v_{ssq} is perfectly completed. After activating the control of SSC, the magnitude of three-phase source-side currents keeps increasing until it reaches 0.15kA, and the waveforms are almost sinusoidal from the enlarged plots shown in Fig 6.10(c).

The performance of SSC is displayed in Fig. 6.11. The three-phase SSC voltages decline immediately after enabling the control strategy for SSC, and it takes around 4s to get to a new steady operation state. The three-phase SSC currents have the similar performance as that of the three-phase grid currents, except that the magnitude is a little bit smaller. It can be seen from Fig. 6.11(c) that the DC-bus voltage drops to a value below 2kV after activating the control of SSC, and it raises up to approximately 5kV at 6s to achieve the stable operation. This is because when the switch for SSC control is turned on with a delay after 2s in the RTDS

environment, which is caused by the effect of simulating the power circuit in RTDS, and the system becomes uncontrollable for a short period of time.

6.3.3 Simulation Results for SG Connected with SSC

Then, an SG is directly connected to the SSC to provide power. The SSC control was turned on at 2s to see the control effects, which are displayed in Figs. 6.12 & 6.13.

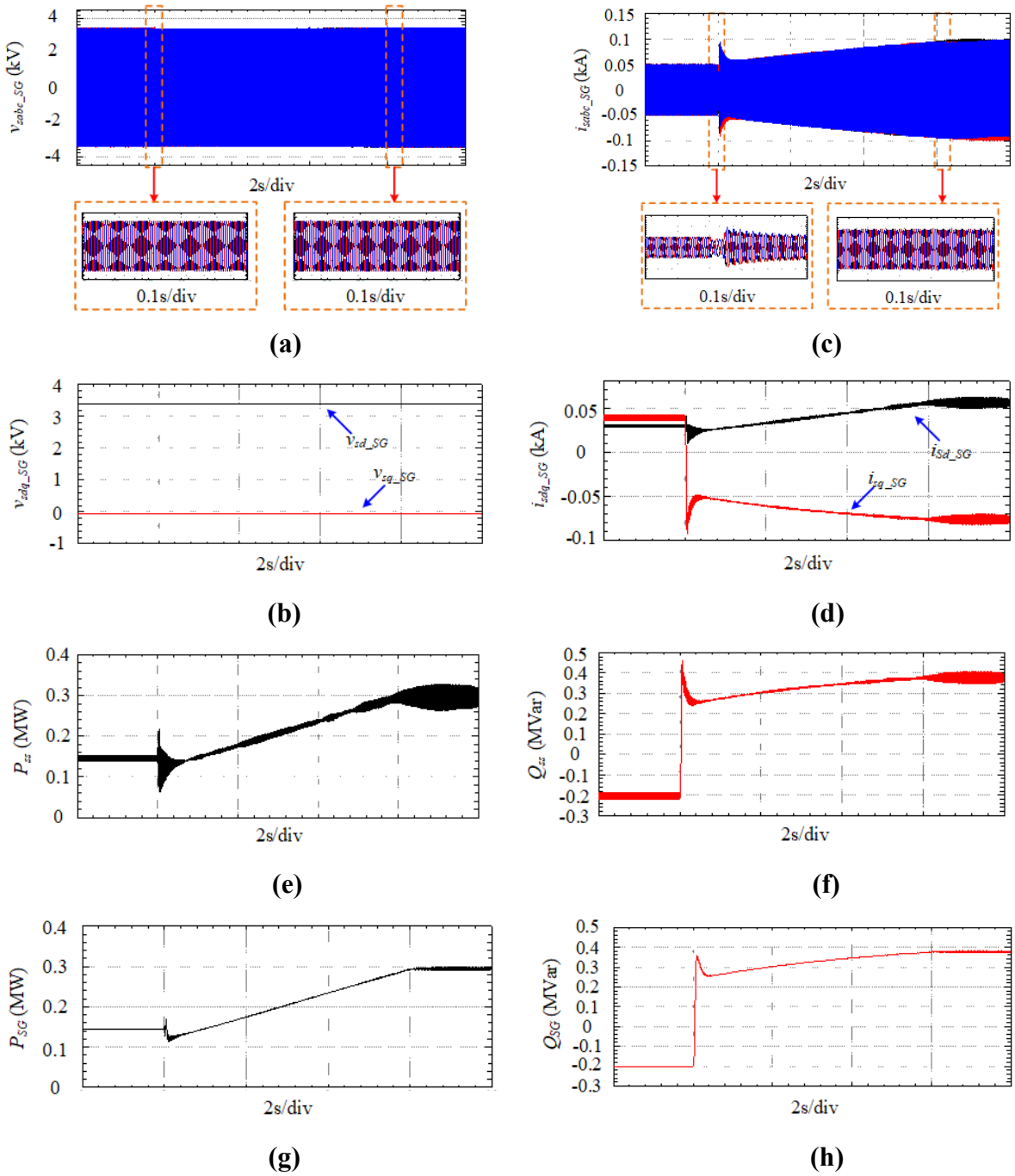

Fig. 6.12. Simulation results for the SG variables by activating the SSC control at 2s.

From Fig. 6.12, it can be seen that the three-phase voltages supplied by SG are stable during the whole process of simulation, and the *dq* grid voltages are completely decoupled. There are some ripples in the three-phase grid currents at the point of activating the SSC control, and it takes around 6s to achieve the steady operating state. In addition, the sinusoidal current waveforms are obtained as can be seen in Fig. 6.12(c). Comparing the power generated to the system (Fig. 6.12(e) & (f)) with that generated directly from SG (Fig. 6.12(g) & (h)), there are some noises owing to the use of voltage source converter interfaces between the SG and the power circuit of the rest part of the system.

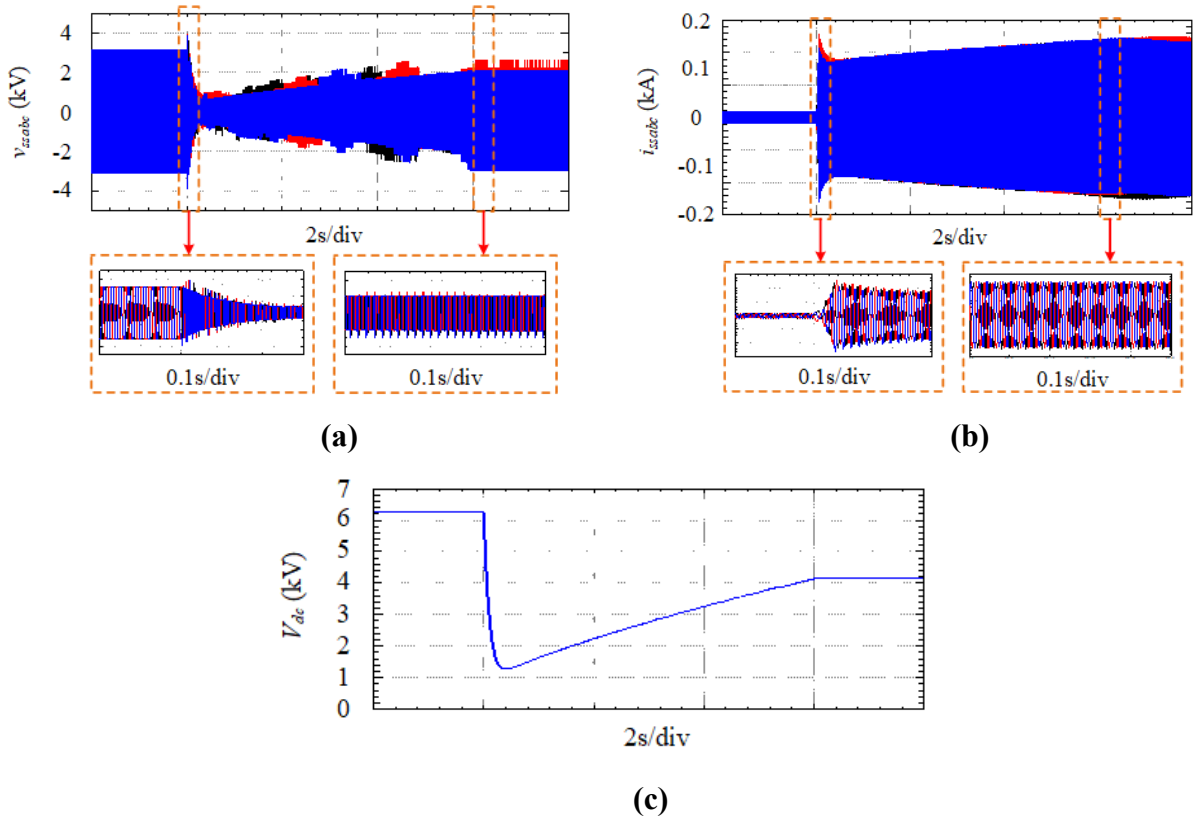

Fig. 6.13. Simulation results for the variables of SSC with an SG power supply by activating the SSC control at 2s.

The three-phase SSC voltages drop at the instant of applying SSC control, and it takes around 6s to regain the steady state of operation. From Fig. 6.13(b), the three-phase SSC currents

achieve the magnitude of around 0.17kA after 8s, and almost sinusoidal current waveforms are obtained. The DC-bus voltage drops from the nominal value to a value above 1kV, and then moderately increases back to over 4kV, as can be seen from Fig. 6.13(c).

In order to generate more power from the SG, the exciter gain was increased from 1 to 1.2. The simulation results in this case are displayed in Figs. 6.14 & 6.15.

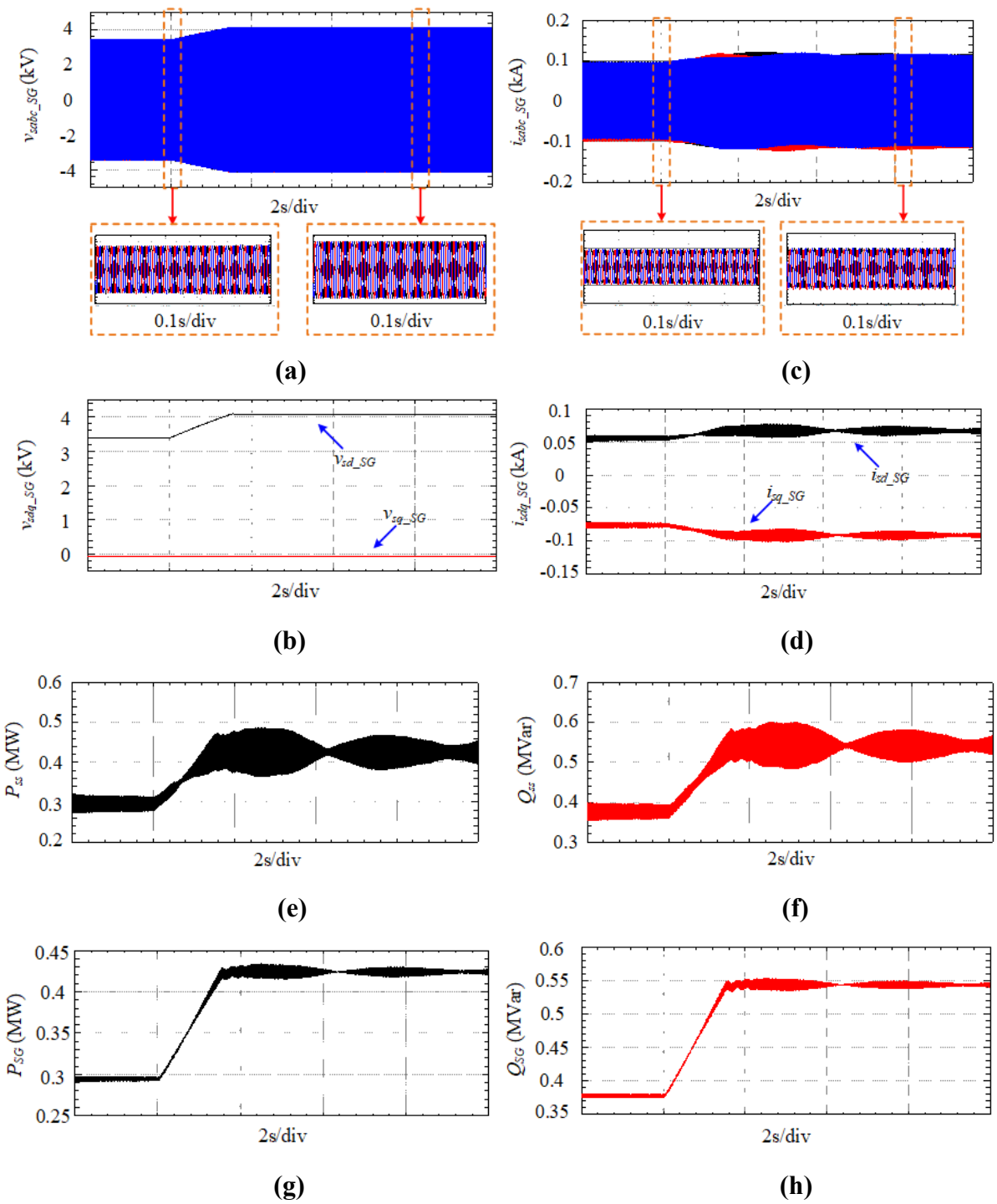

Fig. 6.14. Simulation results for the SG variables by changing the exciter gain from 1 to 1.2 at 2s.

From Fig. 6.14, it can be seen that the magnitudes of the three-phase grid voltages and current both increase, resulting from the increase in the active and reactive powers from the SSC.

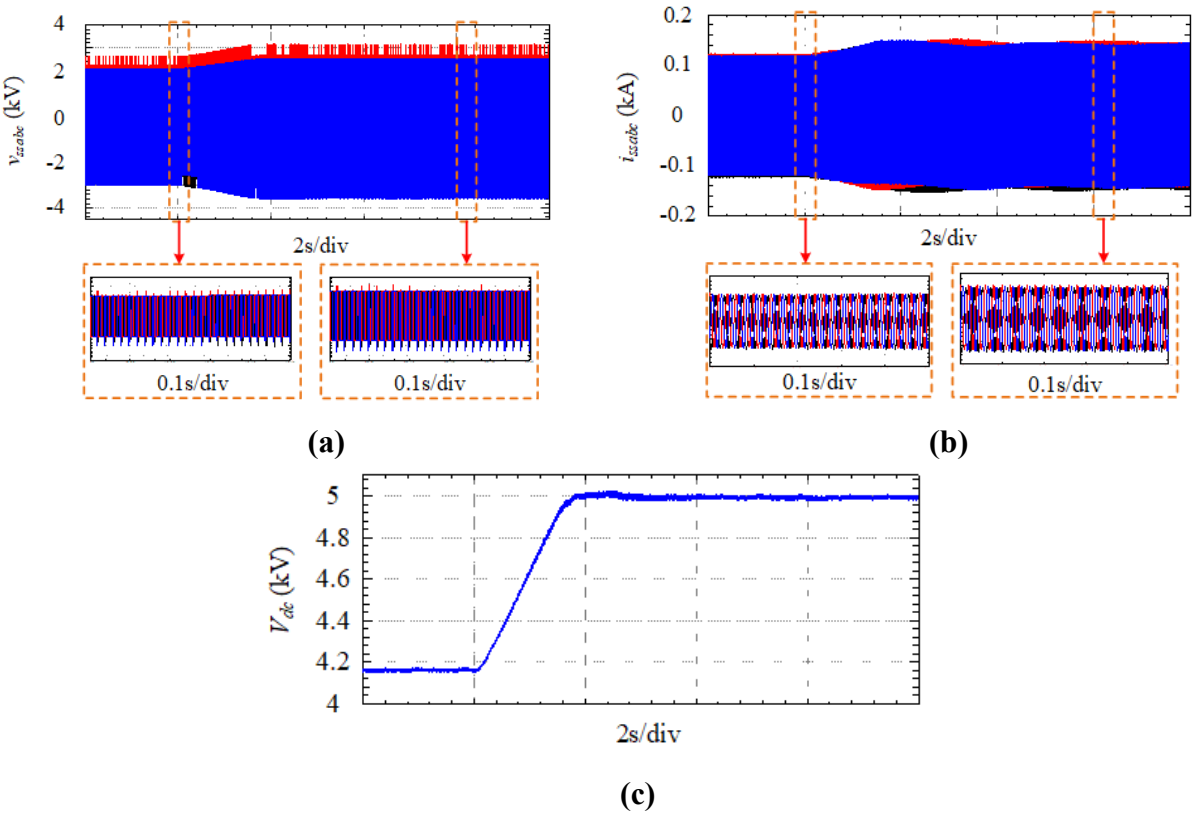

Fig. 6.15. Simulation results for the variables of SSC with an SG power supply by changing the exciter gain from 1 to 1.2 at 2s.

From Fig. 6.15, it can be seen that the magnitude of three-phase SSC voltages increases, while there is unbalance among them owing to the imperfect SSC control effect. The three-phase SSC currents still maintain in almost sinusoidal waveforms after increasing the exciter gain, and some fluctuations can be observed, which do not significantly influence the overall performance. The DC-bus voltage increases from 4.16kV to around 5kV to endow the system with a higher power rating.

The cases shown in Figures 6.12 – 6.15 are carried out by forcing the SG to operate at the synchronous speed (lock mode). For the sake of simulating a more practical case where the

rotor angular speed of SG is determined by the multi-mass model of SG (free mode), the RTDS simulation setup is modified to implement the control strategies in the free mode. The corresponding simulation results are shown in Figs. 6.16 – 6.19.

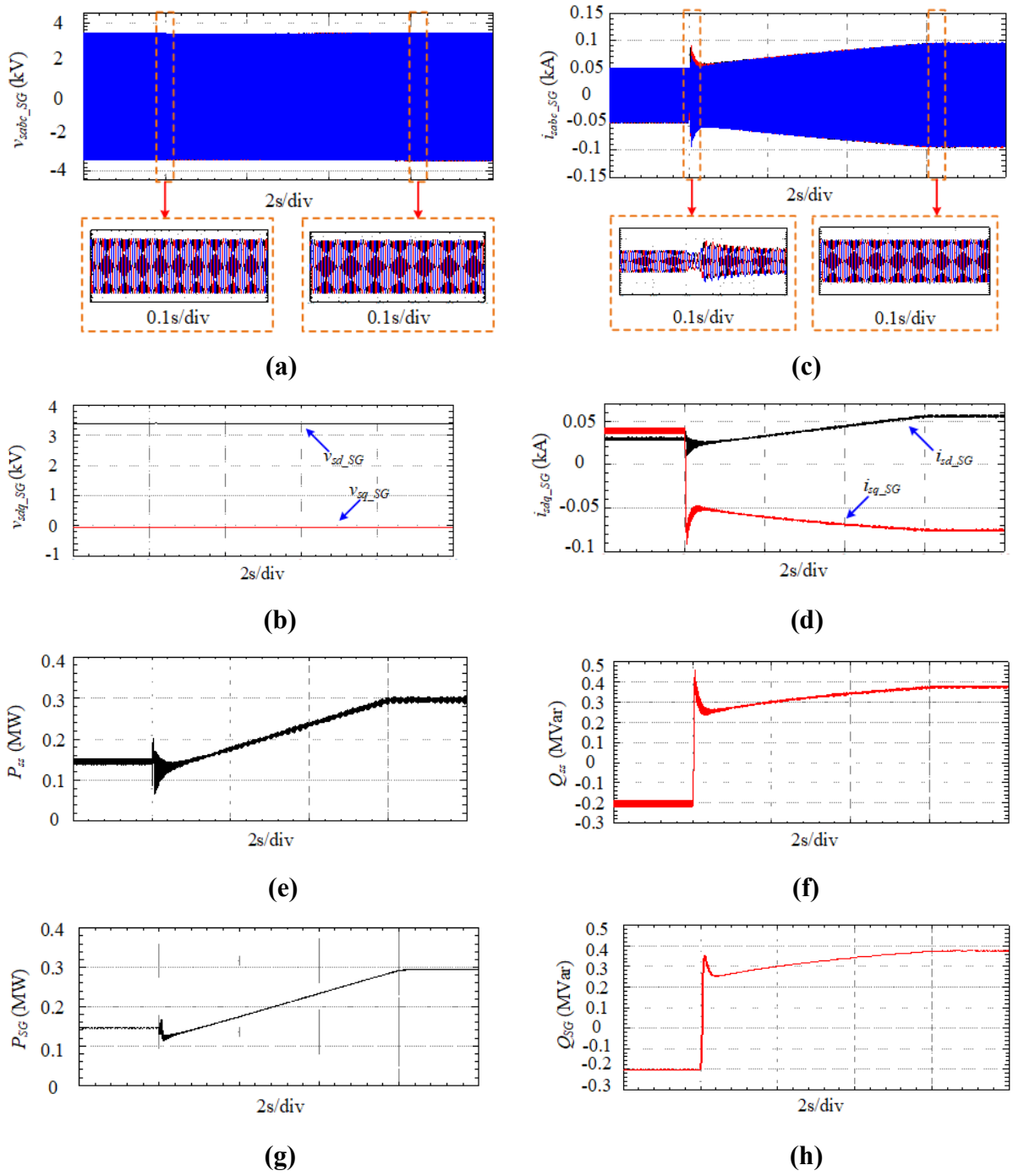

Fig. 6.16. Simulation results for the SG variables by activating the SSC control at 2s in the free mode.

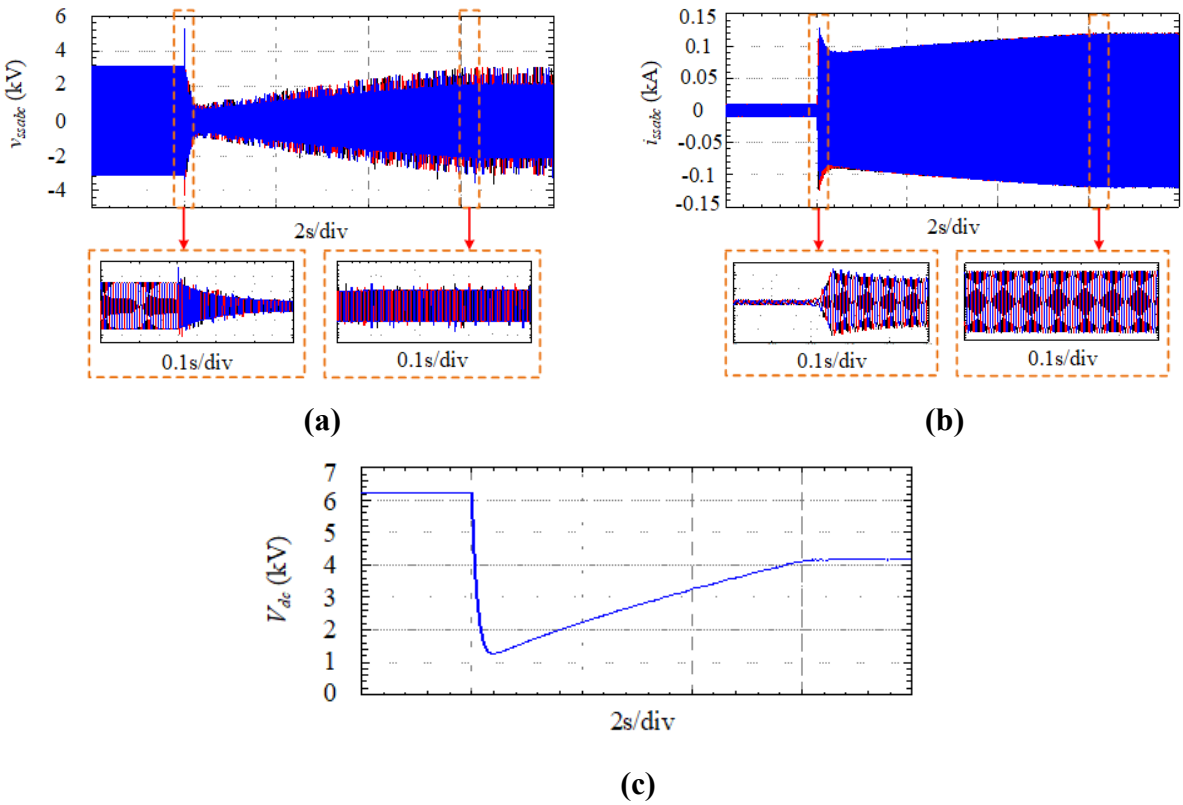

Fig. 6.17. Simulation results for the variables of SSC with an SG power supply by activating the SSC control at 2s in the free mode.

It can be seen from Figs. 6.16 and 6.17 that when the free mode is applied, there is less noise in the grid currents and power. Therefore, by applying the free mode for the power circuit of SG connected with SSC, the simulated current and power waveforms for SG can track the reference values more precisely than the case of applying the lock mode. For the SSC side, the three-phase voltages and currents become more balanced, while there are more glitches in these waveforms due to the more practical case presented by the free mode.

After increasing the exciter gain from 1 to 1.2, the magnitudes of three-phase voltages, currents and DC-bus voltage increase, and the performance of the system is similar to the previous case, as is shown in Figs. 6.18 and 6.19.

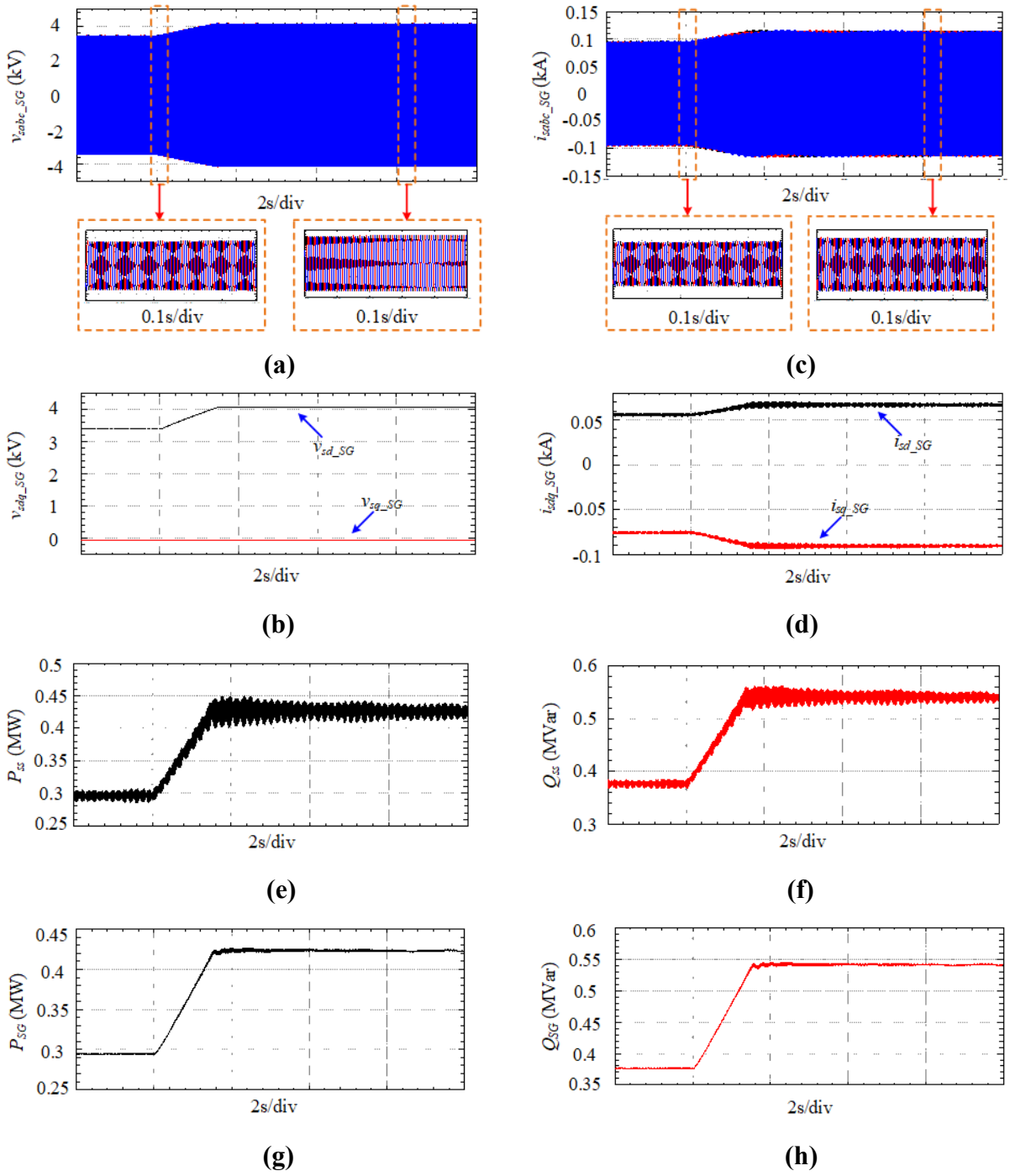

Fig. 6.18. Simulation results for the SG variables by changing the exciter gain from 1 to 1.2 at 2s with the actual rotor angular speed.

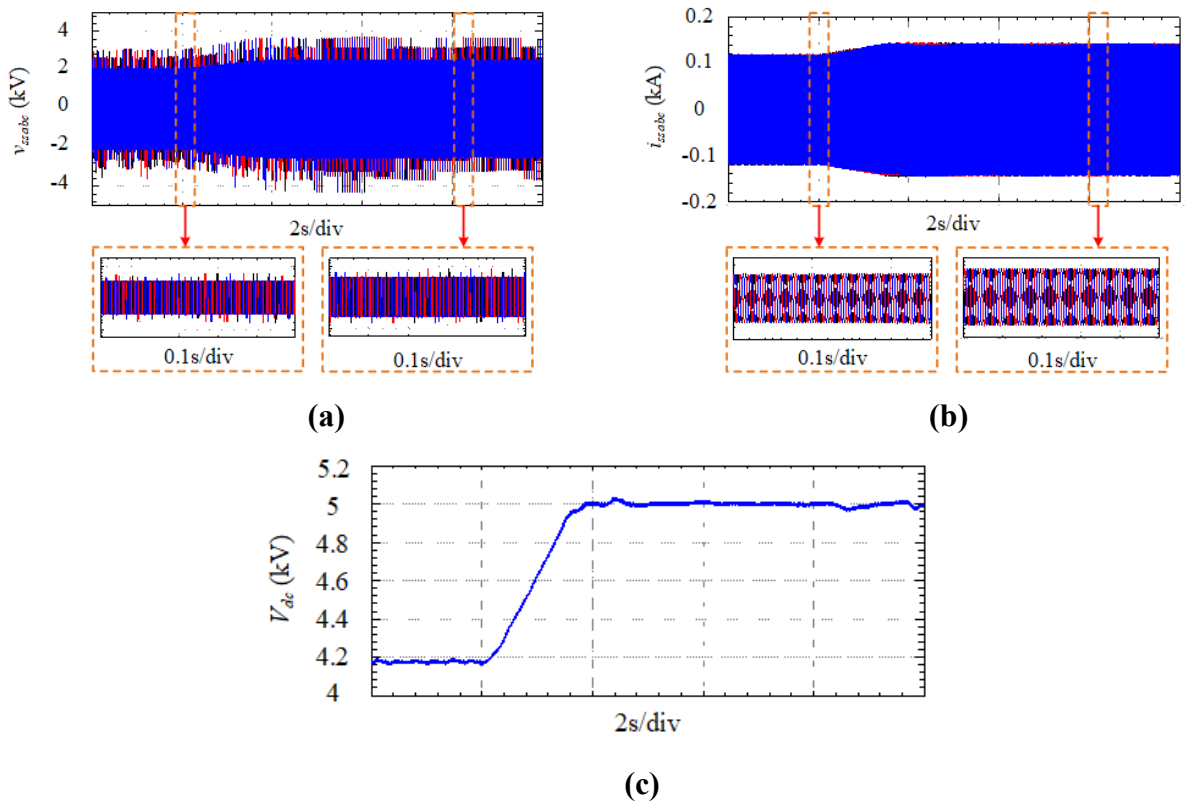

Fig. 6.19. Simulation results for the variables of SSC with an SG power supply by changing the exciter gain from 1 to 1.2 at 2s with the actual rotor angular speed.

6.3.4 Simulation Results for LSC Connected with A Three-Phase Voltage Source

The control of LSC is then evaluated by using constant DC-bus voltage supply to eliminate the power circuit at the SSC side. In the simulation, the slip is maintained at 0.2 so that the base frequency of the three-phase rotor voltages is 10Hz, and the DFIM is assumed to operate at the subsynchronous operation mode. In this case, the currents flow from the LSC to the rotor (three-phase voltage source in the RTDS simulation). The tracking performance of LSC is verified by changing the reference values of the rotor *dq* currents. In the proposed system, the vector control is based on grid voltage orientation, where the *d*-axis rotor current is controlled to regulate the active power, and the *q*-axis rotor current is controlled to regulate the reactive power. The *d*-axis current i_{rd} is first changed from 0kA to 1kA to make the rotor active power

P_r change from 0 to a positive value. Then, with i_{rd} remained at 0kA, the q-axis current i_{rq} varies from 0kA to 1kA to change the rotor reactive power. The simulation results are displayed in Figs. 6.20 and 6.21.

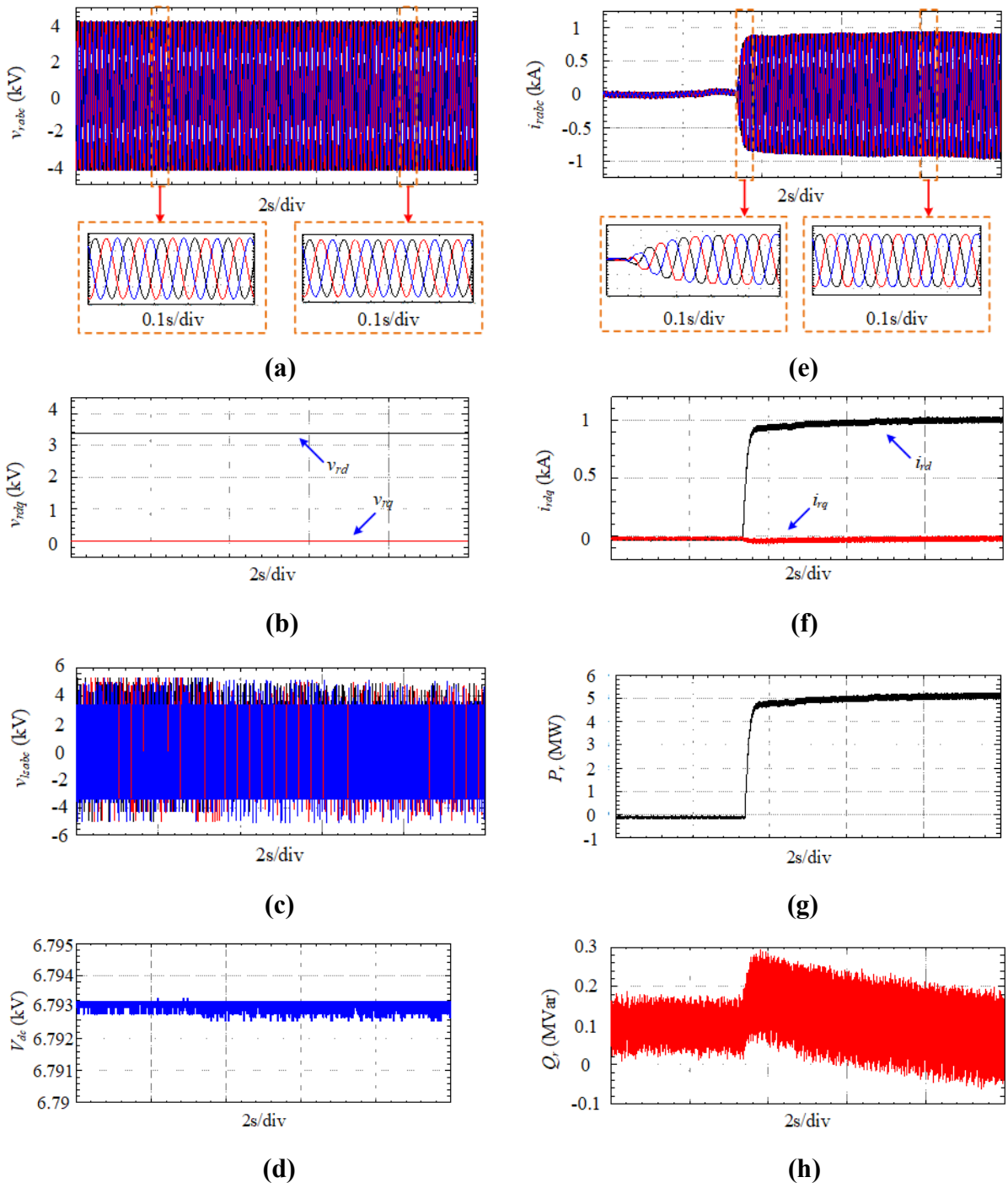

Fig. 6.20. Simulation results for LSC connected with a three-phase voltage source with *d*-axis rotor current changing from 0 to 1kA at around 3.3s.

It can be seen from Fig. 6.20 that with a constant DC-bus voltage supply, the control performance of LSC is satisfactory, and the rotor active power P_r increases at 3.3s with the change of i_{rd}, and it reaches 5MW at around 3.5s. Besides, the three-phase rotor current waveforms are almost sinusoidal, demonstrating a high current quality.

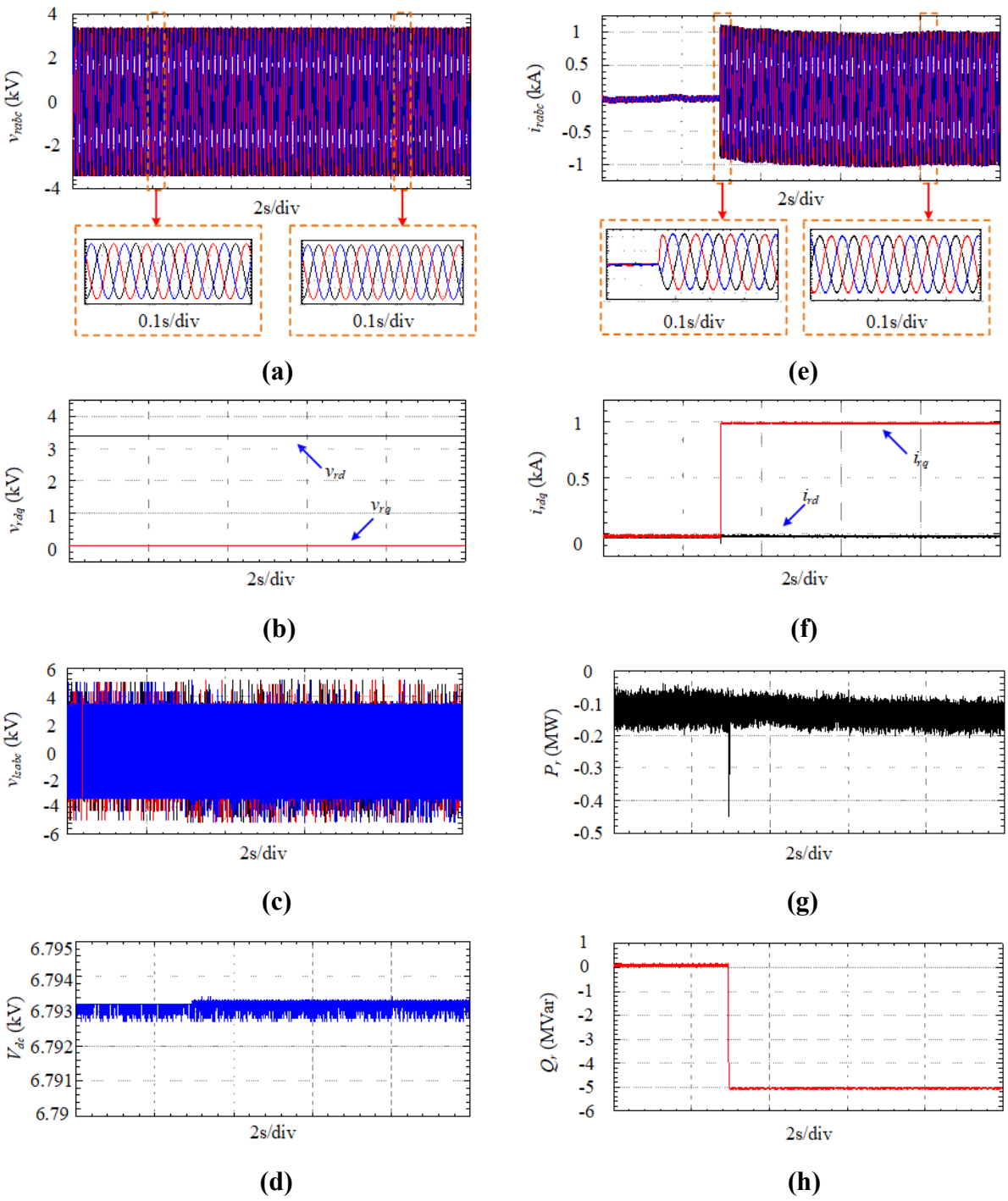

Fig. 6.21. Simulation results for LSC connected with a three-phase voltage source with *q*-axis rotor current changing from 0 to 1kA at around 3.3s.

From Fig. 6.21, similar performance to the case shown in Fig. 6.21 can be observed. The three-phase rotor voltages and DC-bus voltage are stable, and the three-phase rotor currents are in almost sinusoidal waveforms. With the change in i_{rq}, the rotor reactive power Q_r changes instantly from 0 to -5MVar, as shown in Fig. 6.21(h).

According to Figs. 6.21 and 6.22, the tracking performance of LSC is fully verified for the proposed PPD-SPS.

6.3.5 Simulation Results for SG Connected with BTBPC

From Sections 6.3.2 to 6.3.4, the simulations were conducted for the SSC and LSC separately. In this section, the BTBPC that contains both SSC and LSC is applied in the power circuit, and the control performance of the power circuit of SG connecting with BTBPC is to be verified. The exciter gain is kept at 1.2 and the control of SSC is on during the whole simulation process. The simulation results are displayed in Figs. 6.22 – 6.24 by turning the LSC control on at 4s.

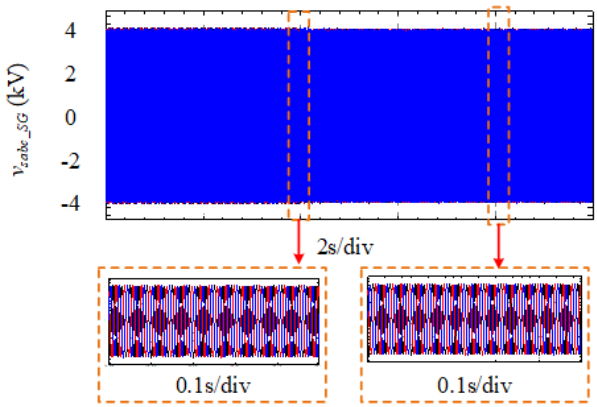

(a)

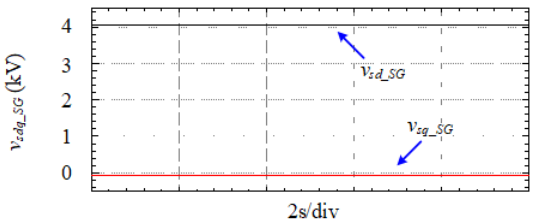

(b)

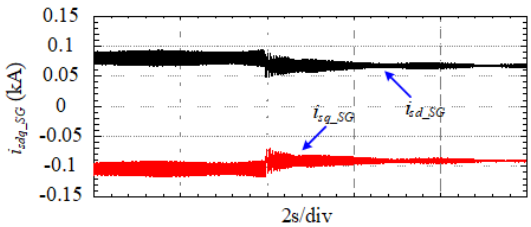

(c)

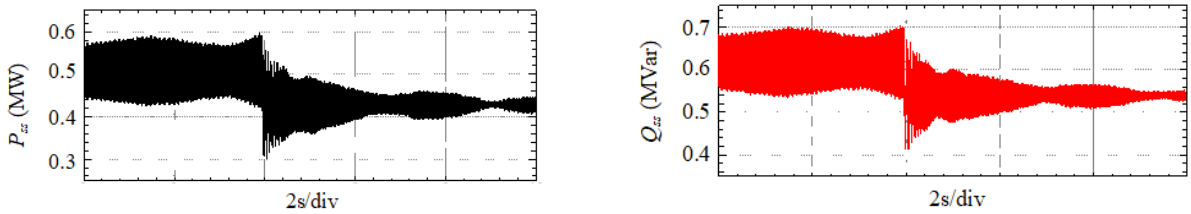

(d) **(e)**

Fig. 6.22. Simulation results for the SG variables in the power circuit of SG connected with BTBPC by turning the LSC control on at 4s.

It can be seen from Fig. 6.22 that the grid voltages are stable during the whole process. There are some fluctuations in the *dq* grid currents, which result in the fluctuations in the source-side active and reactive power.

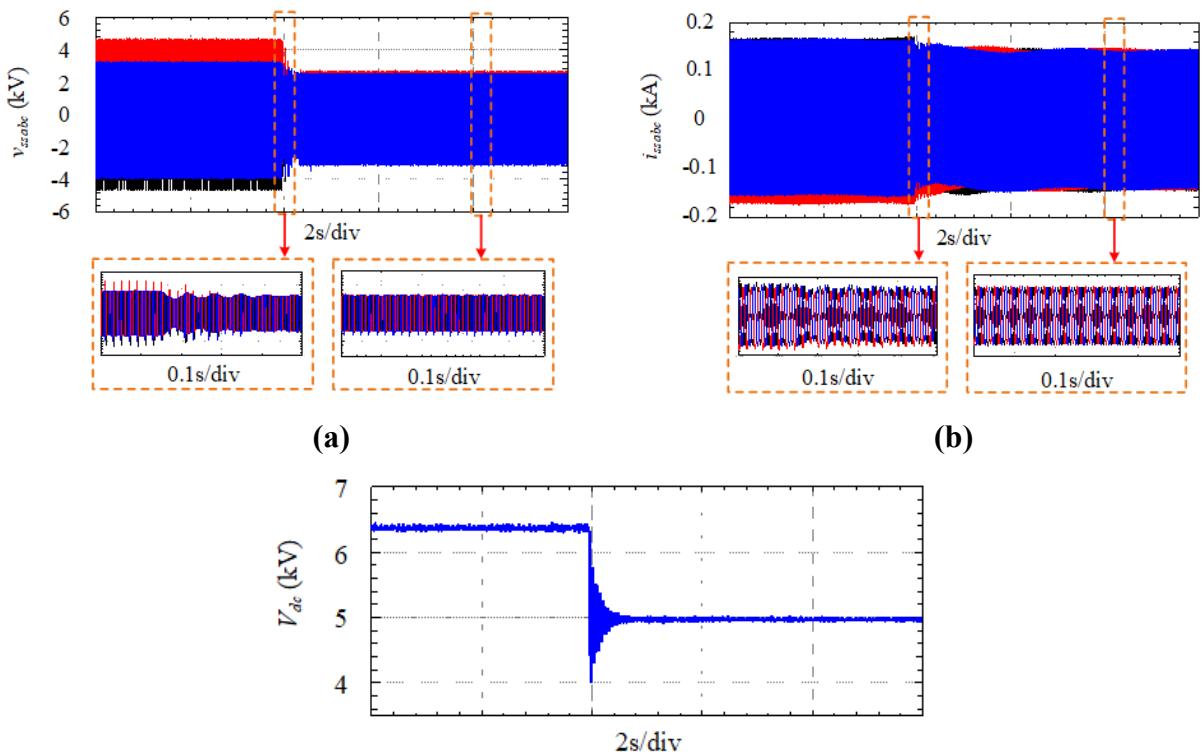

(a) **(b)**

(c)

Fig. 6.23. Simulation results for the SSC variables in the power circuit of SG connected with BTBPC by turning the LSC control on at 4s.

From Fig. 6.23, it can be seen that once the control of LSC is activated, the magnitude of DC-bus voltage declines from 6.4kV to 5kV. As a consequence, the magnitudes of SSC voltages and currents both decrease.

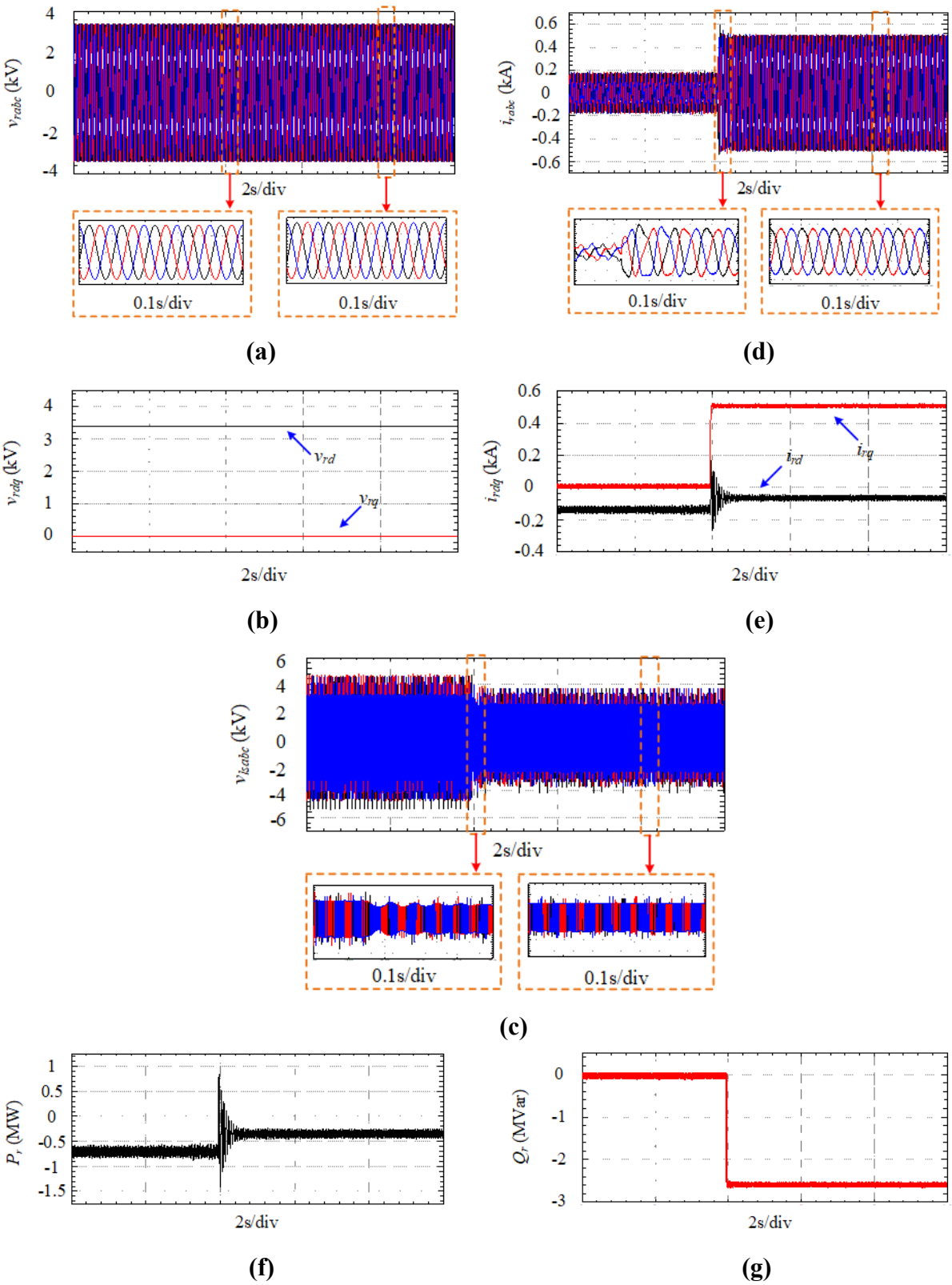

Fig. 6.24. Simulation results for the rotor-side variables in the power circuit of SG connected with BTBPC by turning the LSC control on at 4s.

From Fig. 6.24, it can be seen that the rotor voltages are always stable as the rotor of DFIM is simulated as a constant three-phase voltage source. In addition, at the instant of activating the LSC control, the magnitude of three-phase LSC voltages drops, while that of three-phase rotor currents arises from 0.2kA to around 0.5kA, and almost sinusoidal current waveforms are presented. The reference values of i_{rd} and i_{rq} are set to 0kA and 0.5kA, respectively, and it can be clearly seen from Fig. 6.24(e) that the *dq* rotor currents track these reference values appropriately. Moreover, the tracking performances of P_r and Q_r are verified in Figs. 6.24(f) and (g).

6.4 Summary

This chapter first investigates the effects of parameter deviations of PGU (including SG and its EXS) on PPD-SPS. Three PDEIs (*AVGD*, *STDEV* and *ASRQS*) are defined to respectively evaluate the average error, dispersion degree of samples, and absolute error when applying different degrees of parameter deviations for a specific parameter. 16 important SG and EXS parameters are taken for sensitivity analysis to study the effects of parameter deviations on the SG terminal voltage and output active power. The overall system performance is further investigated for the two most influential SG parameters, which are X_d' and X_q. According to the simulation results, the following points are obtained to present the vital clues on SG and EXS parameter identification for PPD-SPS. Overall, the parameter deviations of X_q have the most significant impacts on the system performance of the proposed PPD-SPS. Therefore, it is necessary to precisely identify the value of X_q to ensure the system stability.

In addition, the simulation results are derived by using RTDS with CHIL setup for the proposed PPD-SPS to investigate the system performance in almost exactly an actual operation environment. The rotor of DFIM is simulated as a three-phase voltage source with the base

frequency of the slip frequency. The power circuit is simulated in separate parts first, and then these parts are combined to form the circuit of SG connected with a BTBPC. The following power circuits have been simulated in RTDS with the corresponding control strategies implemented in CHIL setup on the target PC: 1) three-phase voltage source feeding SSC; 2) SG connected with SSC; 3) LSC connected with a three-phase voltage source; 4) SG connected with BTBPC.

Chapter 7 Conclusion, Main Contributions and Future Work

7.1 Conclusion

In this thesis, a PPD-SPS is proposed to obtain a higher SPS safety level by using less power electronics. The proposed PPD-SPS has an AC-DC hybrid power distribution architecture, which places more freedom and flexibility in allocating the volumes for on-board AC and DC power components. Compared with the popular FPD-SPS, the main differences are revealed in the following two points: 1) On-board power flows are regulated through both the AC transmission line and BTBPC based power path; 2) The DC power distribution architecture is replaced by a hybrid AC-DC power distribution one. The dominant status of power electronics in the proposed PPD-SPS is mitigated as the volume of power electronics can be greatly reduced. The main power flow is handled by the direct AC power path between the PGU and DFIM-based propulsion subsystem, while the BTBPC is only responsible for dealing with the slip power between the source and load of PPD-SPS. Under the situation of power electronic converter faults, the power delivery from the PGU to the propulsion subsystem is not suspended even if the BTBPC is cut out, in which case the PPD-SPS can continuously sail to transport the passengers and crew to safe places. This ability is critical for preventing the MES from the scenario of staying on the sea due to power shortages, which is extremely dangerous as the weather condition on the sea is usually unpredictable, and the MES that are out of power has no capability of defending severe weather on the sea. Another obvious advantage of the proposed PPD-SPS over FPD-SPS is that the fault protection requirement can be much lower. For FPD-SPS, the DC power distribution architecture is commonly used, which has high

requirements in fault detection and isolation. Specifically, the faulty section has to be detected and isolated swiftly and precisely, without influencing the normal operation of the other sections in the SPS. By applying the proposed PPD-SPS, easy fault protection in AC power system is introduced. In addition, as some of the expensive DC circuit breakers are replaced by the mature AC ones, fault protection for PPD-SPS is also cost-effective. Due to the intrinsically safe SPS architecture, the proposed PPD-SPS has a great potential in being widely accepted by the worldwide ship industry. The modelling, control and performance analysis of PPD-SPS are carried out in this thesis will provide theoretical support for the future practical application.

In Chapter 1, the challenges that impede the development and application of FPD-SPS are illustrated, which mainly correspond to the fault protection and system safety level. Although the extensive use of power electronics is beneficial for improving the controllability of the SPS, the intrinsic reliability and safety issues caused by power electronic interfaces cannot be thoroughly handled. Hence, an intrinsically safe SPS architecture with less power electronics needs to be developed. This chapter explained the necessity and urgency of carrying out the proposed research, as well as the introduction of the main work in the whole thesis.

Starting from the history of MES, Chapter 2 gives an across-the-broad review of the state-of-the-art technologies in terms of the design, control, power management, system stability and reliability for MES. The details of some representative works are illustrated with the pros and cons of different methods compared. The other researchers can refer to this chapter to find the most advanced research in the field of MES, which may help them broaden their knowledge hierarchy. In particular, this chapter can be valuable for those who are working on this topic or are going to step into this research field.

Chapter 3 presents the basic principles for modelling the main power components including the PGU, DFIM, BTBPC, and ESS in the proposed PPD-SPS. A salient-pole SG and a type

DC1A EXS are introduced as the widely used models in PGU. The *dq* model of DFIM is established in the synchronous reference frame, which consists of the voltage, flux and motion equations, and the equivalent circuit is presented in the *dq* frame. The sign of slip and the direction of power flow in the two power paths determine the operation modes of DFIM. Besides, the detailed and average models of BTBPC are respectively built by closely modelling the switching behaviour and regarding the converters as controlled voltage sources. The power loss model of BTBPC is also illustrated. For the battery, SC, and FC that are the three categories of most commonly used devices in ESS, their models are presented by the expressions of key variables.

Following the models of main power components in PPD-SPS, the corresponding control strategies are illustrated in Chapter 4. Based on the EXS control block diagram, the field voltage of SG is properly controlled. The transfer function of the input voltage of EXS to the field voltage is constructed by employing the multiplication of the regulator and exciter gains as the control variable to analyse the PGU stability. Since a PPD-SPS can be deemed as a weak micro-grid, where PLL control effects may threaten the SPS stable operation, an ESVO-VC strategy is proposed to eliminate the use of PLL, which has almost identical performance to the traditional SFO-VC. To deal with the issue that power imbalance occur between the power source and load, the SC bank is applied and the interconnected DC-DC power converter is controlled to complement the power difference.

Chapter 5 presents the small-signal models of PPD-SPS propulsion subsystem in the electromechanical control timescale to investigate the interactions between electrical and mechanical behaviours of PPD-SPS. The phase-amplitude dynamics of the specified internal voltage vectors in the proposed system are focused on to evaluate the system performance according to the effects of rotor speed control, reactive power control and PLL. Two distinct modelling schemes with respect to separate DFIM and BTBPC models, and SIVV, are

illustrated in detail with the linearization and transfer function deduction processes. The internal and external behaviours of PPD-SPS propulsion subsystem in the electromechanical control timescale can be analysed by using these two different models respectively. Moreover, the proposed ESVO-VC in Chapter 4 is applied to simplify the equivalent motion equations for the small-signal model to eliminate the stability issues caused by improperly setting the PLL controller gains.

For the purpose of evaluating the PPD-SPS performance in terms of PGU parameter deviations, Chapter 6 proposes three PDEIs to assess the system performance when different degrees of parameter deviations are presented in the PGU of PPD-SPS. The effects of parameter deviations for 16 system and control parameters in PGU on the terminal power and voltage values are focused on, and simulations are implemented in Matlab/Simulink to find the most critical parameter according to the values and increasing trends in the PDEIs when different degrees of parameter deviations are applied. With further analysis on the overall system performance, it is found that the selection of X_q is of paramount importance for the reliable operation of PPD-SPS. In addition, in the actual operation environment offered by RTDS with CHIL setup, the system performance is carried out to provide the basis of applying the proposed PPD-SPS in practice. The simulation works are presented in different circuit complexity levels to evaluate the performance of each part in detail. Good system steady-state and transient performance is validated for the power circuit of SG with BTBPC in both the lock and free modes.

7.2 Main Contributions

A comprehensive study on the modelling, control and performance analysis of PPD-SPS is carried out in this work, which establishes the basis for applying the proposed system in future

MES to achieve a higher safety level by reducing the proportion of power electronics. The proposed methods and technologies have been validated by simulation studies.

The main contributions to new knowledge are detailed as follows:

(1) The models of the main power components including the SG, DFIM, BTBPC and ESS in PPD-SPS are described in detail. In addition, the power loss model is established for BTBPC by considering source-side copper loss, load-side copper loss, DC-bus loss, switching and conduction losses. Moreover, the normal operation of the proposed PPD-SPS with both detailed switching model and average model is validated.

(2) The control strategies for the PGU, propulsion subsystem and ESS are illustrated in detail. Besides, an ESVO-VC strategy is proposed for DFIM to prevent inappropriate controller gain setup for the PLL control loop, and high quality of voltage and current waveforms is derived.

(3) Two small-signal modelling methods for the PPD-SPS propulsion subsystem are proposed in the electromechanical control timescale in this chapter to investigate the system dynamics from the internal voltage vector phase and amplitude points of view. The controller gain setup of rotor speed controller, reactive power controller and PLL is investigated for system performance analysis.

(4) A detailed analysis on the system performance of PPD-SPS is implemented with respect to PGU parameter deviations and simulation in almost exactly an actual operation environment in RTDS with CHIL setup.

7.3 Future Work

The presented work in this thesis marks the start of research activities in the proposed PPD-SPS, and further work is required to broaden the border of knowledge in this field, as well as

deepen the theoretical analysis.

- **SG Governor and EXS Saturation Effects**

  The model of PGU in the proposed PPD-SPS is only composed of SG and its EXS, as illustrated in Section 3.1 of Chapter 3. The voltage control provided by EXS is concerned, which is merely one of the important parts in the PGU control system. Under these circumstances, the input signal of SG has to be the rotor speed since the mechanical behaviour cannot be properly revealed. In order to obtain a complete model to include both the mechanical and electrical characteristics for PGU, the governor of SG needs to be integrated to implement speed control, which is significant for achieving reliable system performance. Moreover, the saturation block in EXS control diagram is neglected for simplicity in the presented work, as can be seen in Section 4.1 of Chapter 4. In the future work, the effect of EXS saturation will be considered.

- **Fault-Tolerant Control of BTBPC**

  The BTBPC is the key power component in the proposed PPD-SPS to control the power flow between the power source and load. In the presented work, the control strategies are implemented with the BTBPC in healthy state. As explained in Chapter 1, the motivation of this research is enhancing the safety of MES by applying less power electronics. Although the normal and reliable operation of the proposed PPD-SPS can be obtained with all the switches intact in BTBPC, its operation with BTBPC fault needs to be further investigated to demonstrate the merits of the proposed PPD-SPS over FPD-SPS. The faults in BTBPC can be categorized into different levels, which are switch level, converter level and system level. The corresponding fault-tolerant control strategies for different fault scenarios will be designed and implemented in the future study. As the fault level increases, the difficulty in preserving good system performance

becomes higher, and some compromises may be adopted, which are also the future research interests.

- **In-Depth Small-Signal System Stability Analysis**

According to the work in Chapter 5, the controller gain setup for the control loops of rotor speed, reactive power and PLL in the electromechanical control timescale has different degrees of impacts on the system performance. However, only the internal voltage vector phase-amplitude dynamics are studied without examining in depth the system stability analysis to explain the corresponding phenomena from the mathematical point of view. Although the transfer functions for the phase and amplitude dynamics are obtained, the small-signal system stability needs to be further studied by choosing the appropriate operation points for the proposed PPD-SPS. In addition, the derivation of the transfer functions in the presented work is based on several assumptions, which deteriorates the accuracy in the expression of these transfer functions. In the future work, a more precise small-signal model of PPD-SPS propulsion subsystem is to be derived, and the validity of this model will be compared to those with lower precision by frequency-domain stability analysis methods like Nyquist stability criterion and Bode plots.

- **Impedance Modelling of PPD-SPS for Stability Analysis**

The proposed PPD-SPS can be regarded as a system with a source output impedance and a load input impedance for system-level stability analysis by employing the impedance-based Nyquist stability criterion. For the models presented in this thesis, they are separately established with the detailed mechanical and electrical behaviours considered, which are difficult for system-level analysis. Although the small-signal models of PPD-SPS propulsion subsystem are established in Chapter 5, they do not

clearly reveal the impedance characteristics, and these models can only be used to study the controller effects in the electromechanical control timescale through internal voltage vector phase-amplitude dynamics on the propulsion subsystem performance. Since the impedance modelling method is easy to be physically understood, and the commonly used Nyquist stability criterion can be directly used, it is an excellent choice for evaluating the stability of the whole PPD-SPS. Moreover, even if some of the source or load power components are added or removed, there is no need to remodel the system.

- **Energy Management of PPD-SPS**

In Chapters 3 and 4, the modelling of the main energy storage devices and control of SC bank are illustrated. Nevertheless, these principles are basic and they are only simply applied to the proposed PPD-SPS to compensate the source-load power imbalance to a certain degree. More in-depth research is required in this field to investigate the energy management strategies for PPD-SPS in different working scenarios. The present work only employs SC bank for short-term power balance control, whose capability is limited when taking the long-term operation of PPD-SPS into consideration. Firstly, the devices used in ESS should be updated, and a hybrid ESS that consists of both batteries and SCs will be desirable. Secondly, modified power flow control and charging/discharging strategies are needed to achieve better energy and power balance performances. Thirdly, different types of service loads will be integrated into the proposed PPD-SPS, and proper power distribution strategies are to be designed to satisfy the on-board power requirement in each section of PPD-SPS.

Appendix

1) DFIM Parameters

P_{nom} = 36MVA; V_{nom} = 4.16kV; f_{nom} = 50Hz; C_{dc} = 30mF; R_s = 0.023pu; L_s = 3.08pu; R_r = 0.016pu; L_r = 3.06pu; L_m = 2.9pu; H = 3.5s; F = 0.01pu; n_p = 2; R_{ss} = 0.003pu; L_{ss} = 0.3pu.

2) SG and EXS Parameters

P_{nom} = 36MVA; V_{nom} = 4.16kV; f_{nom} = 50Hz; n_p = 20; K_a = 300; T_a = 0.001s; K_e = 1; T_e = 0.0001s; K_f = 0.0001; T_f = 0.1s; T_r = 0.02s.

For simulations in Chapter 4: $R_s = 2.85*10^{-3}$pu; $L_{ls} = 4.56*10^{-3}$pu; L_{md} = 0.1pu; L_{mq} = 0.01pu; $R_f = 10^{-3}$pu; $L_{lfd} = 2*10^{-4}$; R_{kd} = 0.0117pu; L_{lkd} = 0.0182pu; R_{kq} = 0.01; L_{lkq} = 0.0182.

For simulations in other chapters: R_s = 0.036pu; X_d = 1.321pu; X_d' = 0.1685pu; X_d'' = 0.105pu; X_q = 1.173pu; X_q'' = 0.09pu; X_l = 0.075pu; T_{do}' = 6.5s; T_{do}'' = 0.0241s; T_{qo}'' = 0.0464s.

3) Primitive Controller Parameters

rotor speed controller: $k_{p\omega}$ = 3, $k_{i\omega}$ = 0.6; reactive power control: k_{iq} = 20, k_{iv} = 10; PLL: k_{pp} = 4.5, k_{ip} = 39.27.

4) Expressions of transfer function blocks

$$G_1 = \frac{X_m(k_{p\omega}'s + k_{i\omega}')}{E_{s0}(2Hs + F)s} \tag{A-1}$$

$$G_2 = -\frac{X_m k_{iq} k_{iv}}{s^2} \tag{A-2}$$

$$G_3 = \frac{2X_m k_{iq} k_{iv}}{E_{s0} s^2} - \frac{X_s}{E_{s0} V_{s0}} \tag{A-3}$$

$$G_4 = V_{s0} \frac{k_{pp} s + k_{ip}}{s^2} \tag{A-4}$$

$$G_{\theta 1} = \frac{X_m X_t (k_{p\omega}' s + k_{i\omega}')}{X_s E_{t0} (2Hs + F) s} \tag{A-5}$$

$$G_{\theta 2} = \frac{X_t \omega_{m0}}{E_{t0} V_{s0}} \tag{A-6}$$

$$G_{\theta 3} = V_{s0} \frac{k_{pp} s + k_{ip}}{s^2} \tag{A-7}$$

$$G_{\theta 4} = \frac{g V_{s0}}{E_{t0}} \tag{A-8}$$

$$G_{E1} = \frac{k_{iq}}{s} \tag{A-9}$$

$$G_{E2} = \frac{X_t X_m k_{iv}}{X_s s} \tag{A-10}$$

$$G_{E3} = g \tag{A-11}$$

5) Coefficients in $M_\theta(s)$ and $M_E(s)$

$$B = E_{t0} X_s (E_{t0} - g V_{s0}) / X_t \tag{A-12}$$

$$K_0 = E_{t0} V_{s0} X_m k_{i\omega}' k_{ip} \tag{A-13}$$

$$K_1 = E_{t0}V_{s0}X_m(k_{i\omega}'k_{pp} + k_{p\omega}'k_{ip}) + \omega_{m0}E_{t0}FX_sk_{ip} \tag{A-14}$$

$$K_2 = E_{t0}X_mk_{i\omega}' + E_{t0}V_{s0}X_mk_{p\omega}'k_{pp} + \omega_{m0}E_{t0}X_s(2Hk_{ip} + Fk_{pp}) \tag{A-15}$$

$$K_3 = E_{t0}X_mk_{p\omega}' + \omega_{m0}gFX_s + 2\omega_{m0}E_{t0}HX_sk_{pp} \tag{A-16}$$

$$K_4 = 2\omega_{m0}gHX_s \tag{A-17}$$

$$D_1 = F \tag{A-18}$$

$$D_2 = 2H \tag{A-19}$$

$$N_0 = -X_tX_mk_{iq}k_{iv} \tag{A-20}$$

$$N_1 = gX_sk_{iq} \tag{A-21}$$

$$W = X_sE_{t0}V_{s0} / X_t \tag{A-22}$$

$$T_0 = 2HX_mV_{s0}k_{i\omega}' + X_s\omega_{m0} \tag{A-23}$$

$$T_1 = 2H(X_mV_{s0}k_{p\omega}' + FX_s\omega_{m0}) \tag{A-24}$$

References

[1] J. F. Hansen and F. Wendt, "History and State of the Art in Commercial Electric Ship Propulsion, Integrated Power Systems, and Future Trends," *Proceedings of the IEEE,* vol. 103, no. 12, pp. 2229-2242, Nov. 2015.

[2] A. Vicenzutti, D. Bosich, G. Giadrossi, and G. Sulligoi, "The Role of Voltage Controls in Modern All-Electric Ships: Toward the all electric ship," *IEEE Electr. Mag.,* vol. 3, no. 2, pp. 49-65, May 2015.

[3] E. Skjong, E. Rodskar, M. Molinas, T. A. Johansen, and J. Cunningham, "The Marine Vessel's Electrical Power System: From its Birth to Present Day," *Proceedings of the IEEE,* vol. 103, no. 12, pp. 2410-2424, Dec. 2015.

[4] *IEEE recommended practice for 1 to 35kV medium voltage DC power systems on ships.*, 2010.

[5] Z. Jin, L. Meng, J. M. Guerrero, and R. Han, "Hierarchical Control Design for a Shipboard Power System With DC Distribution and Energy Storage Aboard Future More-Electric Ships," *IEEE Trans. Ind. Informat.,* vol. 14, no. 2, pp. 703-714, Feb. 2018.

[6] G. Seenumani, J. Sun, and H. Peng, "Real-Time Power Management of Integrated Power Systems in All Electric Ships Leveraging Multi Time Scale Property," *IEEE Trans. Control Syst.Technol.,* vol. 20, no. 1, pp. 232-240, Jan. 2012.

[7] T. J. McCoy, "Integrated power systems—An outline of requirements and functionalities for ships," *Proceedings of the IEEE,* vol. 103, no. 12, pp. 2276-2284, Nov. 2015.

[8] G. Sulligoi, A. Vicenzutti, and R. Menis, "All-Electric Ship Design: From Electrical Propulsion to Integrated Electrical and Electronic Power Systems," *IEEE Trans. Transport. Electr.,* vol. 2, no. 4, pp. 507-521, Dec. 2016.

[9] F. D. Kanellos, A. Anvari-Moghaddam, and J. M. Guerrero, "A cost-effective and emission-aware power management system for ships with integrated full electric propulsion," *Electric Power Systems Research,* vol. 150, pp. 63-75, May 2017.

[10] G. Sulligoi, A. Tessarolo, V. Benucci, M. Baret, A. Rebora, and A. Taffone, "Modeling, Simulation, and Experimental Validation of a Generation System for Medium-Voltage DC Integrated Power Systems," *IEEE Trans. Ind. Appl.,* vol. 46, no. 4, pp. 1304-1310, Jul./Aug. 2010.

[11] M. Cupelli *et al.*, "Power Flow Control and Network Stability in an All-Electric Ship," *Proceedings of the IEEE,* vol. 103, no. 12, pp. 2355-2380, Nov. 2015.

[12] A. Riccobono *et al.*, "Stability of Shipboard DC Power Distribution: Online Impedance-Based Systems Methods," *IEEE Electr. Mag.,* vol. 5, no. 3, pp. 55-67, Sep. 2017.

[13] R. M. Cuzner and V. Singh, "Future Shipboard MVdc System Protection Requirements and Solid-State Protective Device Topological Tradeoffs," *IEEE J. Emerg. Sel. Topics Power Electron.,* vol. 5, no. 1, pp. 244-259, Mar. 2017.

[14] M. Saeedifard, M. Graovac, R. F. Dias, and R. Iravani, "DC Power Systems: Challenges and Opportunities," presented at the IEEE PES General Meeting, Providence, RI, USA, Jul., 2010.

[15] M. Babaei, J. Shi, and S. Abdelwahed, "A Survey on Fault Detection, Isolation, and Reconfiguration Methods in Electric Ship Power Systems," *IEEE Access,* vol. 6, pp. 9430-9441, Mar. 2018.

[16] K. Satpathi, A. Ukil, and J. Pou, "Short-Circuit Fault Management in DC Electric Ship Propulsion System: Protection Requirements, Review of Existing Technologies and Future Research Trends," *IEEE Trans. Transport. Electr.,* vol. 4, no. 1, pp. 272-291, Mar. 2018.

[17] A. A. S. Emhemed, K. Fong, S. Fletcher, and G. M. Burt, "Validation of Fast and Selective Protection Scheme for an LVDC Distribution Network," *IEEE Trans. Power Del.,* vol. 32, no. 3, pp. 1432-1440, Jun. 2017.

[18] L. L. Qi, A. Antoniazzi, L. Raciti, and D. Leoni, "Design of Solid-State Circuit Breaker-Based Protection for DC Shipboard Power Systems," *IEEE J. Emerg. Sel. Topics Power Electron.,* vol. 5, no. 1, pp. 260-268, Mar. 2017.

[19] M. Monadi, C. Gavriluta, A. Luna, J. I. Candela, and P. Rodriguez, "Centralized Protection Strategy for Medium Voltage DC Microgrids," *IEEE Trans. Power Del.,* vol. 32, no. 1, pp. 430-440, Feb. 2017.

[20] P. Cairoli and R. A. Dougal, "Fault Detection and Isolation in Medium-Voltage DC Microgrids: Coordination Between Supply Power Converters and Bus Contactors," *IEEE Trans. Power Electron.,* vol. 33, no. 5, pp. 4535-4546, May 2018.

[21] S. Yang, A. Bryant, P. Mawby, D. Xiang, L. Ran, and P. Tavner, "An Industry-Based Survey of Reliability in Power Electronic Converters," *IEEE Trans. Ind. Appl.,* vol. 47, no. 3, pp. 1441-1451, May/Jun. 2011.

[22] J. Lu, Y. Hu, X. Zhang, Z. Wang, J. Liu, and C. Gan, "High-Frequency Voltage Injection Sensorless Control Technique for IPMSMs Fed by a Three-Phase Four-Switch Inverter With a Single Current Sensor," *IEEE/ASME Trans. Mechatronics,* vol. 23, no. 2, pp. 758-768, Apr. 2018.

[23] H. Alafnan *et al.*, "Stability Improvement of DC Power Systems in an All-Electric Ship Using Hybrid SMES/Battery," *IEEE Trans. Appl. Supercond.,* vol. 28, no. 3, pp. 1-6, Apr. 2018.

[24] Y. Ji *et al.*, "Hierarchical control strategy for MVDC distribution network under large disturbance," *IET Gen. Trans. & Distrib.,* vol. 12, no. 11, pp. 2557-2565, 2018.

[25] K. Satpathi, A. Ukil, S. S. Nag, J. Pou, and M. A. Zagrodnik, "DC Marine Power System: Transient Behavior and Fault Management Aspects," *IEEE Trans. Ind. Informat.,* vol. 15, no. 4, pp. 1911-1925, Apr. 2019.

[26] V. Nougain, S. Mishra, and A. K. Pradhan, "MVDC Microgrid Protection using a Centralized Communication with a Localized Backup Scheme of Adaptive Parameters," *IEEE Trans. Power Del.,* vol. 34, no. 3, pp. 869-878, Jun. 2019.

[27] J. L. Kirtley, A. Banerjee, and S. Englebretson, "Motors for Ship Propulsion," *Proceedings of the IEEE,* vol. 103, no. 12, pp. 2320-2332, Dec. 2015.

[28] L. Huang, H. Xin, L. Zhang, Z. Wang, K. Wu, and H. Wang, "Synchronization and Frequency Regulation of DFIG-Based Wind Turbine Generators With Synchronized Control," *IEEE Trans. Energy Convers.,* vol. 32, no. 3, pp. 1251-1262, Sep. 2017.

[29] Q.-C. Zhong and G. Weiss, "Synchronverters: Inverters That Mimic Synchronous Generators," *IEEE Trans. Ind. Electron.,* vol. 58, no. 4, pp. 1259-1267, Apr. 2011.

[30] Q.-C. Zhong, P.-L. Nguyen, Z. Ma, and W. Sheng, "Self-Synchronized Synchronverters: Inverters Without a Dedicated Synchronization Unit," *IEEE Trans. Power Electron.,* vol. 29, no. 2, pp. 617-630, Feb. 2014.

[31] Q.-C. Zhong, "Virtual Synchronous Machines: A unified interface for grid integration," *IEEE Power Electron. Mag.,* vol. 3, no. 4, pp. 18-27, Dec. 2016.

[32] S. Wang, J. Hu, X. Yuan, and L. Sun, "On Inertial Dynamics of Virtual-Synchronous-Controlled DFIG-Based Wind Turbines," *IEEE Trans. Energy Convers.,* vol. 30, no. 4, pp. 1691-1702, Dec. 2015.

[33] S. Wang, J. Hu, and X. Yuan, "Virtual Synchronous Control for Grid-Connected DFIG-Based Wind Turbines," *IEEE J. Emerg. Sel. Topics Power Electron.,* vol. 3, no. 4, pp. 932-944, Dec. 2015.

[34] W. He, X. Yuan, and J. Hu, "Inertia Provision and Estimation of PLL-Based DFIG Wind Turbines," *IEEE Trans. Power Syst.,* vol. 32, no. 1, pp. 510-521, Jan. 2017.

[35] J. Hu, L. Sun, X. Yuan, S. Wang, and Y. Chi, "Modeling of Type 3 Wind Turbines With df/dt Inertia Control for System Frequency Response Study," *IEEE Trans. Power Syst.,* vol. 32, no. 4, pp. 2799-2809, Jul. 2017.

[36] J. Hu, H. Yuan, and X. Yuan, "Modeling of DFIG-Based WTs for Small-Signal Stability Analysis in DVC Timescale in Power Electronized Power Systems," *IEEE Trans. Energy Convers.,* vol. 32, no. 3, pp. 1151-1165, Sep. 2017.

[37] J. Hu, Y. Huang, D. Wang, H. Yuan, and X. Yuan, "Modeling of Grid-Connected DFIG-Based Wind Turbines for DC-Link Voltage Stability Analysis," *IEEE Trans. Sustain. Energy,* vol. 6, no. 4, pp. 1325-1336, Oct. 2015.

[38] M. Zhao, X. Yuan, and J. Hu, "Modeling of DFIG Wind Turbine Based on Internal Voltage Motion Equation in Power Systems Phase-Amplitude Dynamics Analysis," *IEEE Trans. Power Syst.,* vol. 33, no. 2, pp. 1484-1495, Mar. 2018.

[39] W. Tang, J. Hu, Y. Chang, X. Yuan, and F. Liu, "Modeling of DFIG-based WT for System Transient Response Analysis in Rotor Speed Control Timescale," *IEEE Trans. Power Syst.,* vol. 33, no. 6, pp. 6795-6805, Nov. 2018.

[40] J. Ying, X. Yuan, and J. Hu, "Inertia Characteristic of DFIG-based WT under Transient Control and Its Impact on the First-Swing Stability of SGs," *IEEE Trans. Energy Convers.,* pp. 1502-1511, Dec. 2017.

[41] J. Ying, X. Yuan, J. Hu, and W. He, "Impact of Inertia Control of DFIG-Based WT on Electromechanical Oscillation Damping of SG," *IEEE Trans. Power Syst.,* vol. 33, no. 3, pp. 3450-3459, May 2018.

[42] K. Ni, L. Xie, and Y. Hu, "Cost Effective Electric Ship Energy Regulation System Based on Asynchronized Synchronous Motor," presented at the 2018 IEEE International Conference on Electrical Systems for Aircraft, Railway, Ship Propulsion and Road Vehicles & International Transportation Electrification Conference (ESARS-ITEC), Nottingham, United Kingdom, 2018.

[43] L. Qi, J. Pan, J. Daniel, O. Apeldoorn, M. J. Li, and Z. Wang, "Integrated converter modeling for medium voltage DC shipboard distribution system simulation," presented at the 2014 IEEE PES General Meeting, National Harbor, MD, USA, Jul., 2014.

[44] L. Zhou, H. Liu, and L. Bai, "Modeling and Simulation of All-Electric Ships with Medium-Voltage DC Integrated Power System," presented at the 2014 IEEE Conference and Expo Transportation Electrification Asia-Pacific (ITEC Asia-Pacific), Beijing, China, 2014.

[45] S. Liu, W. Zhu, Y. Cheng, and B. Xing, "Modeling and Small-signal Stability Analysis of an islanded DC Microgrid with Dynamic Loads," presented at the 2015 IEEE 15th International Conference on Environment and Electrical Engineering (EEEIC), Rome, Italy, 2015.

[46] S. Chiniforoosh *et al.*, "Definitions and Applications of Dynamic Average Models for Analysis of Power Systems," *IEEE Trans. Power Del.,* vol. 25, no. 4, pp. 2655-2669, Oct. 2010.

[47] X. Wang, F. Blaabjerg, and W. Wu, "Modeling and Analysis of Harmonic Stability in an AC Power-Electronics-Based Power System," *IEEE Trans. Power Electron.,* vol. 29, no. 12, pp. 6421-6432, Dec. 2014.

[48] B. Wen, D. Dong, D. Boroyevich, R. Burgos, P. Mattavelli, and Z. Shen, "Impedance-Based Analysis of Grid-Synchronization Stability for Three-Phase Paralleled Converters," *IEEE Trans. Power Electron.,* vol. 31, no. 1, pp. 26-38, Jan. 2016.

[49] F. Yahyaie and P. W. Lehn, "On Dynamic Evaluation of Harmonics Using Generalized Averaging Techniques," *IEEE Trans. Power Syst.,* vol. 30, no. 5, pp. 2216-2224, Sep. 2015.

[50] X. Liu, A. M. Cramer, and F. Pan, "Generalized Average Method for Time-Invariant Modeling of Inverters," *IEEE Trans. Circuits Syst. I, Reg. Papers,* vol. 64, no. 3, pp. 740-751, Mar. 2017.

[51] J. Rico, E. Acha, and T. Miller, "Harmonic Domain Modelling of T Thyristor-Controlled Reactors by Mea Vectors and Discrete Convolutions," *IEEE Trans. Power Del.,* vol. 11, no. 3, pp. 1678-1684, Jul. 1996.

[52] J. J. Rico, M. Madrigal, and E. Acha, "Dynamic harmonic evolution using the extended harmonic domain," *IEEE Trans. Power Del.,* vol. 18, no. 2, pp. 587-594, Apr. 2003.

[53] J. R. C. Orillaza and A. R. Wood, "Harmonic State-Space Model of a Controlled TCR," *IEEE Trans. Power Del.,* vol. 28, no. 1, pp. 197-205, Jan. 2013.

[54] J. Kwon, X. Wang, F. Blaabjerg, C. L. Bak, A. R. Wood, and N. R. Watson, "Linearized Modeling Methods of AC–DC Converters for an Accurate Frequency Response," *IEEE J. Emerg. Sel. Topics Power Electron.,* vol. 5, no. 4, pp. 1526-1541, Dec. 2017.

[55] B. Zahedi and L. E. Norum, "Modeling and Simulation of All-Electric Ships With Low-Voltage DC Hybrid Power Systems," *IEEE Trans. Power Electron.,* vol. 28, no. 10, pp. 4525-4537, Oct. 2013.

[56] J. Shi, R. Amgai, and S. Abdelwahed, "Modelling of shipboard medium-voltage direct current system for system level dynamic analysis," *IET Electr. Syst. Transport.,* vol. 5, no. 4, pp. 156-165, Jan. 2015.

[57] U. Javaid, F. D. Freijedo, D. Dujic, and W. van der Merwe, "Dynamic Assessment of Source–Load Interactions in Marine MVDC Distribution," *IEEE Trans. Ind. Electron.,* vol. 64, no. 6, pp. 4372-4381, Jun. 2017.

[58] P. Kundur, *Power System Stability and Control*. New York, NY, USA: McGraw-Hill, 1994.

[59] F. P. DEMELLO and C. CONCORDIA, "Concepts of Synchronous Machine Stability as Affected by Excitation Control," *IEEE Trans. Power App. Syst.,* vol. PAS-88, no. 4, pp. 316-329, Apr. 1969.

[60] I. M. Canay, "I.M. Canay_Determination of model parameters of synchronous machines," *IEE Proceedings,* vol. 130, no. 2, pp. 86-94, Mar. 1983.

[61] J. Tamura and I. Takede, "A NEW MODEL OF SATURATED SYNCHRONOUS MACHINES FOR POWER SYSTEM TRANSIENT STABILITY SIMULATIONS," *IEEE Trans. Energy Convers.,* vol. 10, no. 2, pp. 218-224, Jun. 1995.

[62] J. A. Martinez, B. Johnson, and C. Grande-Moran, "Parameter Determination for Modeling System Transients—Part IV: Rotating Machines," *IEEE Trans. Power Del.,* vol. 20, no. 3, pp. 2063-2072, Jul. 2005.

[63] L. Wang, J. Jatskevich, and H. W. Dommel, "Re-examination of Synchronous Machine Modeling Techniques for Electromagnetic Transient Simulations," *IEEE Trans. Power Syst.,* vol. 22, no. 3, pp. 1221-1230, Aug. 2007.

[64] M. Giuseppe Fusco and M. Russo, "Adaptive Voltage Regulator Design for Synchronous Generator," *IEEE Trans. Energy Convers.,* vol. 23, no. 3, pp. 946-956, Sep. 2008.

[65] H. Lomei, D. Sutanto, K. M. Muttaqi, and A. Alfi, "An Optimal Robust Excitation Controller Design Considering the Uncertainties in the Exciter Parameters," *IEEE Trans. Power Syst.,* vol. 32, no. 6, pp. 4171-4179, Nov. 2017.

[66] B. Zaker, G. B. Gharehpetian, M. Karrari, and N. Moaddabi, "Simultaneous Parameter Identification of Synchronous Generator and Excitation System Using Online Measurements," *IEEE Trans. Smart Grid,* vol. 7, no. 3, pp. 1230-1238, May 2016.

[67] B. Zaker, G. B. Gharehpetian, and M. Karrari, "Improving Synchronous Generator Parameters Estimation Using d − q Axes Tests and Considering Saturation Effect," *IEEE Trans. Ind. Informat.,* vol. 14, no. 5, pp. 1898-1908, May 2018.

[68] A. K. A. Dnanes, "Maritime electrical installations and diesel electric propulsion," ABB report/Lecture note NTNU 2003.

[69] E. Skjong, R. Volden, E. Rodskar, M. Molinas, T. A. Johansen, and J. Cunningham, "Past, Present, and Future Challenges of the Marine Vessel's Electrical Power System," *IEEE Trans. Transport. Electr.,* vol. 2, no. 4, pp. 522-537, Dec. 2016.

[70] J. Chalfant, "Early-Stage Design for Electric Ship," *Proceedings of the IEEE,* vol. 103, no. 12, pp. 2252-2266, Dec. 2015.

[71] R. G. Keane and Jr., "Reducing total ownership cost: Designing inside-out of the hull," *Naval Eng. J.,* vol. 124, no. 4, pp. 67-80, 2012.

[72] E. J. Thurkins and Jr., "Development of an Early Stage Ship Design Tool for Rapid Modeling in Paramarine," Nav. E. thesis, Dept. Mech. Eng., Massachusetts Inst. Technol., Cambridge, MA, USA, 2012.

[73] D. J. Jurkiewicz, J. Chalfant, and C. Chryssostomidis, "Modular IPS machinery arrangement in early-stage naval ship design," presented at the Proc. 2013 IEEE Electr. Ship Technol. Symp. (ESTS), Arlington, VA, USA, Apr. 22–24, 2013.

[74] K. Nestoras, "A Tool to Create Hydrodynamically Optimized Hull-Forms With Geometrical Constraints From Internal Arrangements," S. M. thesis, Dept. Mech. Eng., Massachusetts Inst. Technol., Cambridge, MA, USA, 2013.

[75] B. v. Oers, D. Stapersma, and J. J. Hopman, "A 3D packing approach for the early stage configuration design of ships," presented at the Proc. Int. Conf. Comput. Appl. Inf. Technol. Maritime Ind. (COMPIT), V. Bertram, Ed., Hamburg, Germany, 2010.

[76] N. H. Doerry and D. H. Clayton, "Shipboard electrical power quality of service," presented at the Proc. IEEE Electr. Ship Technol. Symp., Philadelphia, PA, USA, 2005.

[77] P. A. Gale, "The ship design process," in *Ship Design and Construction*, vol. 1T. Lamb, Ed. Alexandria, VA, USA: Society of Naval Architects and Marine Engineers, 2003.

[78] F. Mistree, W. F. Smith, B. Bras, J. K. Allen, and D. Muster, "Decisionbased design: A contemporary paradigm for ship design," *Trans.-Soc. Naval Archit. Marine Eng.,* vol. 98, pp. 565-597, 1990.

[79] N. H. Doerry and H. Fireman, "Designing all electric ships," presented at the Proc. 9th Int. Marine Design Conf., Ann Arbor, MI, USA, 2006.

[80] A. Brown and J. Salcedo, "Multiple-objective optimization in naval ship design," *Naval Eng. J.,* vol. 115, no. 4, pp. 49-61, 2003.

[81] J. Stepanchick and A. Brown, "Revisiting DDGX/DDG-51 concept exploration," *Naval Eng. J.,* vol. 119, no. 3, pp. 67-88, 2007.

[82] H. Ali *et al.*, "Cross-platform validation of notional baseline architecture models of naval electric ship power systems," presented at the Proc. IEEE Electr. Ship Technol. Symp. (ESTS), Alexandria, VA, USA, 2011.

[83] F. Wang, Z. Zhang, T. Ericsen, R. Raju, R. Burgos, and D. Boroyevich, "Advances in Power Conversion and Drives for Shipboard Systems," *Proceedings of the IEEE,* vol. 103, no. 12, pp. 2285-2311, Dec. 2015.

[84] Z. Wang, X. Wang, J. Cao, M. Cheng, and Y. Hu, "Direct Torque Control of T-NPC Inverters-Fed Double-Stator-Winding PMSM Drives With SVM," *IEEE Trans. on Power Electron.,* vol. 33, no. 2, pp. 1541-1553, Feb. 2018.

[85] P.-H. Wu, Y.-T. Chen, and P.-T. Cheng, "The Delta-Connected Cascaded H-Bridge Converter Application in Distributed Energy Resources and Fault Ride Through Capability Analysis," *IEEE Trans. Ind. Appl.,* vol. 53, no. 5, pp. 4665-4672, Sep./Oct. 2017.

[86] M. Jankovic, A. Costabeber, A. Watson, and J. C. Clare, "Arm-Balancing Control and Experimental Validation of a Grid-Connected MMC With Pulsed DC Load," *IEEE Trans. Ind. Appl.,* vol. 64, no. 12, pp. 9180-9190, Dec. 2017.

[87] M. Jaksic *et al.*, "Medium-Voltage Impedance Measurement Unit for Assessing the System Stability of Electric Ships," *IEEE Trans. Energy Convers.,* vol. 32, no. 2, pp. 829-841, Jun. 2017.

[88] H. Liu, D. Zhang, and D. Wang, "Design Considerations for Output Capacitance Under Inductance Mismatches in Multiphase Buck Converters," *IEEE Trans. Power Electron.,* vol. 32, no. 7, pp. 5004-5015, Jul. 2017.

[89] E. A. R. Engku Ariff, O. Dordevic, and M. Jones, "A Space Vector PWM Technique for a Three-Level Symmetrical Six-Phase Drive," *IEEE Trans. Ind. Electron.,* vol. 64, no. 11, pp. 8396-8405, Nov. 2017.

[90] H. Ma, G. Chen, J. H. Yi, Q. W. Meng, L. Zhang, and J. P. Xu, "A Single-Stage PFM-APWM Hybrid Modulated Soft-Switched Converter With Low Bus Voltage for High-Power LED Lighting Applications," *IEEE Trans. Ind. Electron.,* vol. 64, no. 7, pp. 5777-5788, Jul. 2017.

[91] T. Ericsen, N. Hingorani, and Y. Khersonsky, "PEBB - Power Electronics Building Blocks from Concept to Reality," presented at the Petroleum and Chemical Industry Conference, 2006. PCIC '06. Record of Conference Papers - IEEE Industry Applications Society 53rd Annual, Philadelphia, PA, USA, 2006.

[92] J. Yu, R. Burgos, N. R. Mehrabadi, and D. Boroyevich, "DC fault current control of modular multilevel converter with SiC-based Power Electronics Building Blocks," presented at the Electric Ship Technologies Symposium (ESTS), 2017 IEEE, Arlington, VA, USA, 2017.

[93] S. Debnath, J. Qin, B. Bahrani, M. Saeedifard, and P. Barbosa, "Operation, Control, and Applications of the Modular Multilevel Converter: A Review," *IEEE Trans. Power Electron.,* vol. 30, no. 1, pp. 37-53, Jan. 2015.

[94] M. A. Perez, S. Bernet, J. Rodriguez, S. Kouro, and R. Lizana, "Circuit Topologies, Modeling, Control Schemes, and Applications of Modular Multilevel Converters," *IEEE Trans. Power Electron.,* vol. 30, no. 1, pp. 4-17, Jan. 2015.

[95] R. M. Cuzner, R. Soman, M. M. Steurer, T. A. Toshon, and M. O. Faruque, "Approach to Scalable Model Development for Navy Shipboard Compatible Modular Multilevel Converters," *IEEE J. Emerg. Sel. Topics Power Electron.,* vol. 5, no. 1, pp. 28-39, Mar. 2017.

[96] R. Mo and H. Li, "Hybrid Energy Storage System With Active Filter Function for Shipboard MVDC System Applications Based on Isolated Modular Multilevel DC/DC Converter," *IEEE J. Emerg. Sel. Topics Power Electron.,* vol. 5, no. 1, pp. 79-87, Mar. 2017.

[97] Y. Chen, S. Zhao, Z. Li, X. Wei, and Y. Kang, "Modeling and Control of the Isolated DC–DC Modular Multilevel Converter for Electric Ship Medium Voltage Direct Current Power System," *IEEE J. Emerg. Sel. Topics Power Electron.,* vol. 5, no. 1, pp. 124-139, Mar. 2017.

[98] Y. Chen, Z. Li, S. Zhao, X. Wei, and Y. Kang, "Design and Implementation of a Modular Multilevel Converter With Hierarchical Redundancy Ability for Electric Ship MVDC System," *IEEE J. Emerg. Sel. Topics Power Electron.,* vol. 5, no. 1, pp. 189-202, Mar. 2017.

[99] J. Millan, P. Godignon, X. Perpina, A. Perez-Tomas, and J. Rebollo, "A Survey of Wide Bandgap Power Semiconductor Devices," *IEEE Trans. Power Electron.,* vol. 29, no. 5, pp. 2155-2163, May 2014.

[100] J. Biela, M. Schweizer, S. Waffler, and J. W. Kolar, "SiC versus Si—Evaluation of Potentials for Performance Improvement of Inverter and DC–DC Converter Systems by SiC Power Semiconductors," *IEEE Trans. Ind. Electron.,* vol. 58, no. 7, pp. 2872-2882, Jul. 2011.

[101] U. K. MISHRA, P. PARIKH, and Y.-F. WU, "AlGaN/GaN HEMTs—An Overview of Device Operation and Applications," *Proceedings of The IEEE,* vol. 90, no. 6, pp. 1022-1031, Jun. 2002.

[102] T. A. Baginski and K. A. Thomas, "A robust one-shot switch for highpower pulse applications," *IEEE Trans. Power Electron.,* vol. 24, no. 1, pp. 253-259, Jan. 2009.

[103] P. Mitra and G. K. Venayagamoorthy, "An Adaptive Control Strategy for DSTATCOM Applications in an Electric Ship Power System," *IEEE Trans. Power Electron.,* vol. 25, no. 1, pp. 95-104, Jan. 2010.

[104] E. Skjong, J. A. Suul, A. Rygg, T. A. Johansen, and M. Molinas, "System-Wide Harmonic Mitigation in a Diesel-Electric Ship by Model Predictive Control," *IEEE Trans. Ind. Electron.,* vol. 63, no. 7, pp. 4008-4019, Jul. 2016.

[105] W.-S. Im, C. Wang, L. Tan, W. Liu, and L. Liu, "Cooperative Controls for Pulsed Power Load Accommodation in a Shipboard Power System," *IEEE Trans. Power Syst.,* vol. 31, no. 6, pp. 5181-5189, Nov. 2016.

[106] D. Dong, Y. Pan, R. Lai, X. Wu, and K. Weeber, "Active Fault-Current Foldback Control in Thyristor Rectifier for DC Shipboard Electrical System," *IEEE J. Emerg. Sel. Topics Power Electron.,* vol. 5, no. 1, pp. 203-212, Mar. 2017.

[107] C. Yan, G. K. Venayagamoorthy, and K. Corzine, "Hardware Implementation of an AIS-Based Optimal Excitation Controller for an Electric Ship," *IEEE Trans. Ind. Appl.,* vol. 47, no. 2, pp. 1060-1070, Mar./Apr. 2011.

[108] Y. d. Valle, G. K. Venayagamoorthy, S. Mohagheghi, J. C. Hernandez, and R. G. Harley, "Particle swarm optimization: Basic concepts, variants and applications in power systems," *IEEE Trans. Evol. Comput.,* vol. 12, no. 2, pp. 171-195, Mar. 2008.

[109] C. Yan, G. K. Venayagamoorthy, and K. Corzine, "AIS-Based Coordinated and Adaptive Control of Generator Excitation Systems for an Electric Ship," *IEEE Trans. Ind. Electron.,* vol. 59, no. 8, pp. 3102-3112, Aug. 2012.

[110] F. Zheng, Q.Wang, T. H. Lee, and X. Huang, "Robust PI controller design for nonlinear systems via fuzzy modeling approach," *IEEE Trans. Syst., Man, Cybern. A, Syst., Humans,* vol. 31, no. 6, pp. 666-675, Nov. 2001.

[111] A. Karimi and A. Feliachi, "PSO-tuned adaptive backstepping control of power systems," presented at the Proc. IEEE Power Syst. Conf. Expo., 2006.

[112] S. Mohagheghi, Y. d. Valle, G. K. Venayagamoorthy, and R. G. Harley, "A proportional–integrator type adaptive critic design-based neurocontroller for a static compensator in multimachine power systems," *IEEE Trans. Ind. Electron.,* vol. 54, no. 1, pp. 86-96, Feb. 2007.

[113] Z. Jin, G. Sulligoi, R. Cuzner, L. Meng, J. C. Vasquez, and J. M. Guerrero, "Next-Generation Shipboard DC Power System: Introduction Smart Grid and dc Microgrid Technologies into Maritime Electrical Netowrks," *IEEE Electr. Magn.,* vol. 4, no. 2, pp. 45-57, Jun. 2016.

[114] S. R. Rudraraju, A. K. Srivastava, S. C. Srivastava, and N. N. Schulz, "Small signal stability analysis of a shipboard MVDC power system," in *Proc. IEEE Electric Ship Technol. Symp.*, 2009, pp. 135-141.

[115] X. Liu, H. Li, and Z. Wang, "A Start-Up Scheme for a Three-Stage Solid-State Transformer With Minimized Transformer Current Response," *IEEE Trans. Power Electron.,* vol. 27, no. 12, pp. 4832-4836, Dec. 2012.

[116] S. Xu, A. Q. Huang, and R. Burgos, "Review of Solid-State Transformer Technologies and Their Application in Power Distribution Systems," *IEEE J. Emerg. Sel. Topics Power Electron.,* vol. 1, no. 3, pp. 186-198, Sep. 2013.

[117] L. J. Petersen, D. J. Hoffman, J. P. Borraccini, and S. B. Swindler, "Nextgeneration power and energy: Maybe not so next generation," *J. Naval Eng.,* vol. 122, no. 4, pp. 59-74, 2010.

[118] N. Doerry and J. Amy, "MVDC shipboard power system considerations for electromagnetic railguns," in *Proc. 6th DoD Electromagn. Railgun Workship*, Laurel, MD, USA, 2015, pp. 15-16.

[119] G. Sulligoi, A. Tessarolo, V. Benucci, A. Millerani Trapani, M. Baret, and F. Luise, "Shipboard Power Generation: Design and Development of a Medium-Voltage dc Generation System," *IEEE Ind. Appl. Mag.,* vol. 19, no. 4, pp. 47-55, Apr. 2013.

[120] F. D. Kanellos, J. Prousalidis, and G. J. Tsekouras, "Onboard DC grid employing smart grid technology: challenges, state of the art and future prospects," *IET Electr. Syst. Transport.,* vol. 5, no. 1, pp. 1-11, 2015.

[121] P. Kankanala, S. C. Srivastava, A. K. Srivastava, and N. N. Schulz, "Optimal Control of Voltage and Power in a Multi-Zonal MVDC Shipboard Power System," *IEEE Trans. Power Syst.,* vol. 27, no. 2, pp. 642-650, May 2012.

[122] *IEEE Recommended Practice for 1 kV to 35 kV Medium-Voltage DC Power Systems on Ships*, 2010.

[123] M. Farasat, A. Arabali, and A. M. Trzynadlowski, "Flexible-Voltage DC-Bus Operation for Reduction of Switching Losses in All-Electric Ship Power Systems," *IEEE Trans. Power Electron.,* vol. 29, no. 11, pp. 6151-6161, Nov. 2014.

[124] C.-L. Su, K.-L. Lin, and C.-J. Chen, "Power Flow and Generator-Converter Schemes Studies in Ship MVDC Distribution Systems," *IEEE Trans. Ind. Appl.,* vol. 52, no. 1, pp. 50-59, Jan./Feb. 2016.

[125] G. Seenumani, J. Sun, and H. Peng, "A numerically efficient iterative procedure for hybrid power system optimization using sensitivity functions," in *Proc. Amer. Control Conf.*, 2007, pp. 4738-4743.

[126] X. Feng, K. L. Butler-Purry, and T. Zourntos, "Multi-Agent System-Based Real-Time Load Management for All-Electric Ship Power Systems in DC Zone Level," *IEEE Trans. Power Syst.,* vol. 27, no. 4, pp. 1719-1728, Nov. 2012.

[127] X. Feng, K. L. Butler-Purry, and T. Zourntos, "A Multi-Agent System Framework for Real-Time Electric Load Management in MVAC All-Electric Ship Power Systems," *IEEE Trans. Power Syst.,* vol. 30, no. 3, pp. 1327-1336, May 2015.

[128] F. D. Kanellos, "Optimal Power Management With GHG Emissions Limitation in All-Electric Ship Power Systems Comprising Energy Storage Systems," *IEEE Trans. Power Syst.,* vol. 29, no. 1, pp. 330-339, Jan. 2014.

[129] F. D. Kanellos, G. J. Tsekouras, and N. D. Hatziargyriou, "Optimal Demand-Side Management and Power Generation Scheduling in an All-Electric Ship," *IEEE Trans. Sustain. Energy,* vol. 5, no. 4, pp. 1166-1175, Oct. 2014.

[130] T. A. Johansen, T. I. Bo, E. Mathiesen, A. Veksler, and A. J. Sorensen, "Dynamic Positioning System as Dynamic Energy Storage on Diesel-Electric Ships," *IEEE Trans. Power Syst.,* vol. 29, no. 6, pp. 3086-3091, Nov. 2014.

[131] S. Mashayekh and K. L. Butler-Purry, "An Integrated Security-Constrained Model-Based Dynamic Power Management Approach for Isolated Microgrids in All-Electric Ships," *IEEE Trans. Power Syst.,* vol. 30, no. 6, pp. 2934-2945, Nov. 2015.

[132] T. M. Masaud, K. Lee, and P. K. Sen, "An overview of energy storage technologies in electric power systems: What is the future?," presented at the North American Power Symposium (NAPS), Arlington, TX, USA, 2010.

[133] C.-L. Su, X.-T. Weng, and C.-J. Chen, "Power generation controls of fuel cell/energy storage hybrid ship power systems," presented at the Transportation Electrification Asia-Pacific (ITEC Asia-Pacific), 2014 IEEE Conference and Expo, Beijing, China, 2014.

[134] M. M. S. Khan, M. O. Faruque, and A. Newaz, "Fuzzy Logic Based Energy Storage Management System for MVDC Power System of All Electric Ship," *IEEE Trans. Energy Convers.,* vol. 32, no. 2, pp. 798-809, Jun. 2017.

[135] E. A. Sciberras, B. Zahawi, D. J. Atkinson, A. Breijs, and J. H. van Vugt, "Managing Shipboard Energy: A Stochastic Approach Special Issue on Marine Systems Electrification," *IEEE Trans. Transport. Electr.,* vol. 2, no. 4, pp. 538-546, Dec. 2016.

[136] A. Tashakori Abkenar, A. Nazari, S. D. G. Jayasinghe, A. Kapoor, and M. Negnevitsky, "Fuel Cell Power Management Using Genetic Expression Programming in All-Electric Ships," *IEEE Trans. Energy Convers.,* vol. 32, no. 2, pp. 779-787, Jun. 2017.

[137] M. R. Banaei and R. Alizadeh, "Simulation-Based Modeling and Power Management of All-Electric Ships Based on Renewable Energy Generation Using Model Predictive Control Strategy," *IEEE Intell. Transp. Syst. Mag.,* vol. 8, no. 2, pp. 90-103, Apr. 2016.

[138] P. Cairoli and R. A. Dougal, "New Horizons in DC Shipboard Power Systems: New fault protection strategies are essential to the adoption of dc power systems," *IEEE Electr. Mag.,* vol. 1, no. 2, pp. 38-45, Dec. 2013.

[139] J. G. Ciezki and R. W. Ashton, "Selection and Stability Issues Associated with a Navy Shipboard DC Zonal Electric Distribution System," *IEEE Trans. Power Del.,* vol. 15, no. 2, pp. 665-669, Apr. 2000.

[140] G. Sulligoi, D. Bosich, G. Giadrossi, L. Zhu, M. Cupelli, and A. Monti, "Multiconverter Medium Voltage DC Power Systems on Ships: Constant-Power Loads Instability Solution Using Linearization via State Feedback Control," *IEEE Trans. Smart Grid,* vol. 5, no. 5, pp. 2543-2552, Sep. 2014.

[141] K. P. Logan, "Intelligent Diagnostic Requirements of Future All-Electric Ship Integrated Power System," *IEEE Trans. Ind. Appl.,* vol. 43, no. 1, pp. 139-149, Jan./Feb. 2007.

[142] P. Mitra and G. K. Venayagamoorthy, "Implementation of an Intelligent Reconfiguration Algorithm for an Electric Ship's Power System," *IEEE Trans. Ind. Appl.,* vol. 47, no. 5, pp. 2292-2300, Sep./Oct. 2011.

[143] S. Bose, S. Pal, B. Natarajan, C. M. Scoglio, S. Das, and N. N. Schulz, "Analysis of Optimal Reconfiguration of Shipboard Power Systems," *IEEE Trans. Power Syst.,* vol. 27, no. 1, pp. 189-197, Feb. 2012.

[144] E. Christopher, M. Sumner, D. W. P. Thomas, X. Wang, and F. de Wildt, "Fault Location in a Zonal DC Marine Power System Using Active Impedance Estimation," *IEEE Trans. Ind. Appl.,* vol. 49, no. 2, pp. 860-865, Mar./Apr. 2013.

[145] A. K. Adnanes, "Maritime electrical installations and diesel electric propulsion," ABB2003.

[146] *IEEE Recommended Practice for Excitation System Models for Power System Stability Studies*, 1992.

[147] F. Baneira, J. Doval-Gandoy, A. G. Yepes, O. Lopez, and D. Perez-Estevez, "Comparison of Postfault Strategies for Current Reference Generation for Dual Three-

Phase Machines in Terms of Converter Losses," *IEEE Trans. Power Electron.,* vol. 32, no. 11, pp. 8243-8246, Nov. 2017.

[148] C. Abbey and G. Joos, "Supercapacitor Energy Storage for Wind Energy Applications," *IEEE Trans. Ind. Appl.,* vol. 43, no. 3, pp. 769-776, May/Jun. 2007.